JAERI-Review
2004-017

ACTIVITY REPORT OF THE FUSION NEUTRONICS SOURCE FROM APRIL 1, 2001 TO MARCH 31, 2004

July 2004

Fusion Neutron Laboratory

日本原子力研究所
Japan Atomic Energy Research Institute

本レポートは，日本原子力研究所が不定期に公刊している研究報告書です。
入手の問合わせは，日本原子力研究所研究情報部研究情報課（〒319-1195　茨城県那珂郡東海村）あて，お申し越しください。なお，このほかに財団法人原子力弘済会資料センター（〒319-1195　茨城県那珂郡東海村日本原子力研究所内）で複写による実費頒布をおこなっております。

This report is issued irregularly.
Inquiries about availability of the reports should be addressed to Research Information Division, Department of Intellectual Resources, Japan Atomic Energy Research Institute, Tokai-mura, Naka-gun, Ibaraki-ken, 319-1195, Japan.

編集兼発行　　日本原子力研究所

JAERI-Review 2004-017

Activity Report of the Fusion Neutronics Source from April 1, 2001 to March 31, 2004

Fusion Neutron Laboratory

Department of Fusion Engineering Research
(Tokai Site)
Naka Fusion Research Establishment
Japan Atomic Energy Research Institute
Tokai-mura, Naka-gun, Ibaraki-ken

(Received June 1, 2004)

The Fusion Neutronics Source (FNS) is an accelerator based 14 MeV neutron generator established in 1981. FNS is a powerful tool for neutronics research aiming the fusion reactor development such as neutron cross section measurements, integral experiments and blanket neutronics experiments. This report reviews the FNS activities in the period from April 1, 2001 to March 31, 2004, including collaboration with universities and other research institutes.

Keywords: Fusion Neutronics, D-T Neutrons, Blanket, Integral Experiment, Neutron Cross Section, Neutron Detection, Skyshine, FNS

Editor : Takeo NISHITANI

2001~2003年度における核融合中性子工学用中性子源の活動報告

日本原子力研究所那珂研究所核融合工学部
核融合中性子工学研究室

(2004年6月1日受理)

核融合中性子工学用中性子源FNSは1981年に完成した、加速器型の14MeV中性子源である。FNSは中性子断面積測定、積分実験、ブランケット中性子工学実験等の核融合炉開発を目的として中性子工学実験にとって強力な研究手段である。本報告書は大学及び他の研究機関との協力研究も含めて、2001～2003年度のFNSの活動をまとめたものである。

那珂研究所（東海駐在）：〒319-1195 茨城県那珂郡東海村白方白根2-4
編集者：西谷健夫

Contents

JP0450648

1. Overview of the FNS Activity

Takeo NISHITANI

Fusion Neutron Laboratory, Japan Atomic Energy Research Institute, Tokai, Ibaraki

FNS was established in 1980 as an accelerator based intense neutron source through D-T reactions. Figure 1.1 shows a bird's eye view of the FNS facility. FNS is a cascaded transformer type accelerator. Maximum voltage is 400 kV for deuterons. FNS has two target rooms; the target room I has a fixed tritium target including 3.7×10^{11} Bq tritium and the target room II has a rotating tritium target including 3.7×10^{13} Bq tritium. In the target room I, a maximum neutron yield of 3×10^{11} n/s is available with a beam current of 2 mA. Also a maximum neutron yield of 4×10^{12} n/s is available with a beam current of 20 mA in the tagerget room II. Those neutron yields are monitored by the associated alpha particle measurement with a silicon surface barrier diode installed in the beam line.

FNS has been operating since 1981 for 14 MeV neutron cross section measurements, cross section integral benchmark experiments, blanket characteristics experiments and other fusion neutronics. In 1999, FNS joined to the Department of Fusion Engineering Research. After then, the major research subject has been shifted to neutronics for the International Thermonuclear Experimental Reactor (ITER) and power demonstration fusion reactors.

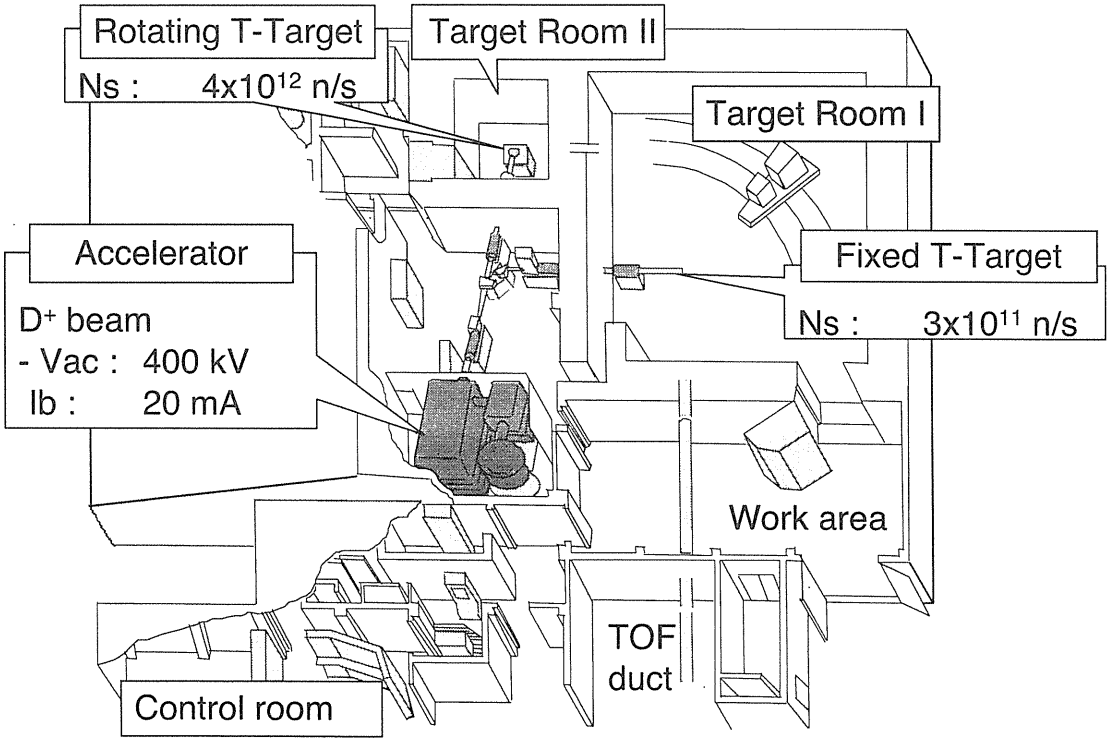

Fig. 1.1 Bird's eye view of the FNS facility.

This report reviews the FNS activities in the period of April 2001 – March 2004 including the results of collaborations with many universities. Highlights in the period are as follows:

Blanket neutronics experiments has been carried out using a mockup of the solid breeder blanket consisting of F82H blocks, Li_2TiO_3 blocks with a ^6Li enrichment of 40 and 95 %, and beryllium blocks, where calculated values of the tritium production rate agreed with the measured ones using Li_2CO_3 and Li_2TiO_3 pellet detectors within about 10% uncertainty. Also the effects of impurities in the beryllium on the tritium production rate were investigated with a pulsed neutron technique and a ICP mass spectroscopy. Finally, it was found that the impurities might reduce the tritium production rate only a few percent.

The effective activation cross sections via Sequential Charged Particle Reactions (SCPRs) induced by secondary charged particles have been measured to estimate the induced activities and dose rates of structure materials. We confirmed that enhancement of the radioactivity production due to recoiled proton from cooling water would make corrosion products more activated around the surface of cooling pipe in D-T fusion reactors.

The D-T neutron skyshine experiments were carried out with a port at the roof in March 2002 and March 2003. The highest total dose rate measured was about 0.5 μSv/h at a distance of 30 m from the D-T target point and the dose rate was attenuated to about 0.02μSv/h at a distance of 550 m for the neutron intensity of 1.7×10^{11} n/s. The MCNP calculation agreed well both neutron and secondary gamma-ray dose rate distributions.

A micro-fission chamber of ^{235}U has been developed for the ITER in-vessel neutron monitor. Excellent linearities of count rates and square of Campbelling voltage to neutron fluxes were confirmed in the temperature range from 20°C(room) to 250°C. As a result, it was concluded that the present micro-fission chamber is applicable to ITER.

Distributions of deuterium and tritium in the JT-60 diverter tiles have been measured employing the Nuclear Reaction Analysis (NRA) method using D-beam of FNS for understanding plasma-wall interactions. The result suggests that the retained tritium in the diverter tiles is implanted by energetic tritons produced by D-D reactions in the plasma.

New large rotating tritium target with a diameter of 310 mm was developed, which enables us an increase in neutron yield of FNS.

2. Status of the FNS Machine

2.1 Overview of the Machine Operation

Shigeru TANAKA
Fusion Neutron Laboratory, Japan Atomic Energy Research Institute, Tokai, Ibaraki

FNS introduced a newly developed large rotating tritium target facility for the target room I in 2001, which provided the improvement in the neutron intensity and the lifetime of the target. In the period of April 2001 – March 2004, FNS has been operated without any big trouble. The operation time in the period is summarized in Table 2.1. The target room II is used mainly for the material irradiation experiments. The target room I is used for the blanket neutronics experiments, cross-section measurements and other experiments.

Table 2.1 (a) Operation time in 2001 fiscal year.

Period / Target room	The first quarter	The second quarter	The third quarter	The fourth quarter	Total
Target room I	33:21	113:32	79:29	100:12	326:34
Target room II	172:13	75:47	128:39	25:14	401:53
Total operation time	205:34	189:19	208:08	125:26	728:27

Table 2.1 (b) Operation time in 2002 fiscal year.

Period / Target room	The first quarter	The second quarter	The third quarter	The fourth quarter	Total
Target room I	20:25	134:45	106:31	101:38	363:19
Target room II	184:54	64:21	145:16	46:49	441:20
Total operation time	205:19	199:06	251:47	148:27	804:39

Table 2.1 (c) Operation time in 2003 fiscal year.

Period / Target room	The first quarter	The second quarter	The third quarter	The fourth quarter	Total
Target room I	118:10	139:23	75:56	132:09	465:38
Target room II	47:03	86:39	99:02	87:58	320:42
Total operation time	165:13	226:02	174:58	220:07	786:20

2.2 Development of the Large Rotating Tritium Target

Yuichi ABE, Masakazu SEKI, Shigeru TANAKA, Yoshikazu OGINUMA,
Chuzo KUTSUKAKE,
Fusion Neutron Laboratory, Japan Atomic Energy Research Institute, Tokai, Ibaraki

By FNS users, much higher neutron intensity has been desired in FNS for a long time, because it will bring us more varieties of experiments. A key subject to attain the intense neutron source is how much the deuteron beam current can be increased through the improvement of the cooling performance of the target. The several modifications were conducted on the target system to meet the demand.

First, the area of the new target disk was made twice larger than that of the old target. The size of the new target disk is 310 mm in diameter as shown in Fig.2.2-1, while that of the old target disk was 230 mm. The enlargement of the disk helps the heat generated by the beam hit diffuse more efficiently, and enables to produce more intensive neutron source accompanied by more heat generation.

Second, the rotating speed of the target was made faster through the mechanical improvement of the rotating system. The higher speed provides the more efficient heat removal ability to the target. The cross sectional view of the new target system is shown in Fig. 2.2-2. In order to keep the vacuum insulation, the rotor was sliding on the facing surface of the fixed target assembly in the previous target system. On the other hand, non-contact seal system was developed for the new target system. The rotor is separated by about 15 μm from the facing surface by the compressed air of about 500 kPa. The air is exhausted through differential pumping system. The rotating target assembly is supported with mechanical ball bearings to be properly arranged and adjusted. Thus, the mechanism made possible to attain the extreme high speed up to 2000 rpm for the rotating target assembly, which is not disturbed by resisting friction. Compared with the old type with a fixed revolution speed at 1000 rpm, the new type can provide variable speed in the range of 0 - 2000 rpm. In addition, the life of the seal became longer from 250 hours to over 1000 hours due to the above- mentioned improvement along with the exchange of the vacuum seal to that of higher grade.

Third, a cooling water flow regulator was installed at the center of the rotating target disk cover. The structure makes the water flow uniformly to the very rim of the rotating target disk to carry away the heat more efficiently from the disk.

As a result of the work mentioned above, the neutron source was improved to produce twice larger intensity than before. In addition, the exposure dose for workers to suffer during the maintenance activity around the target was considerably decreased due to the modified sealing design adopting the new type of seal with the extended lifetime.

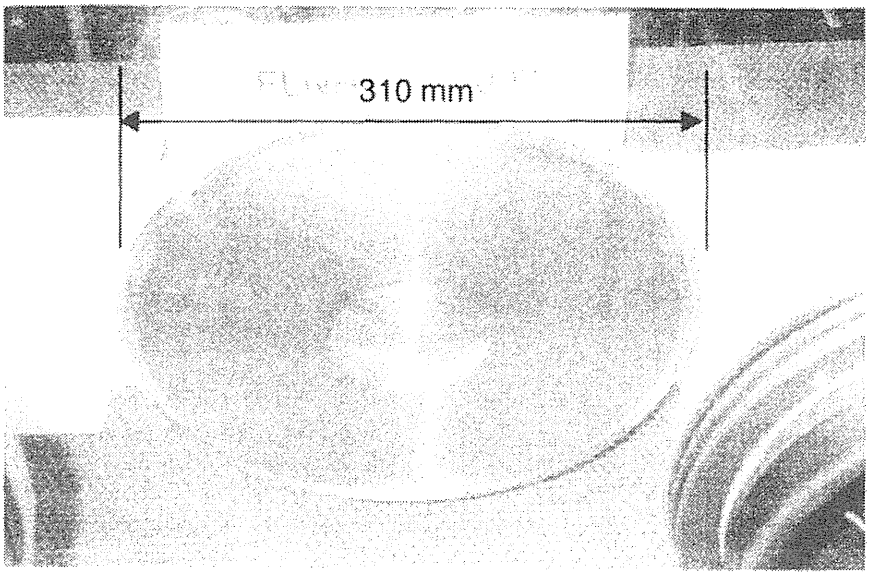

Fig. 2.2-1 Picture of new large target disc.

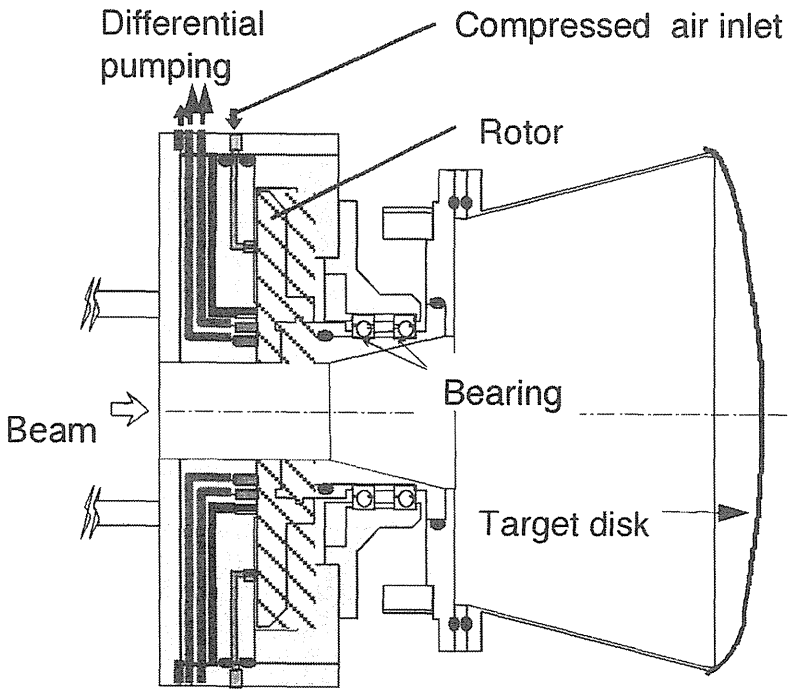

Fig. 2.2-2 Schematic view of the new target system.

2.3 Tritium Profile Measurement of Large Rotating Target

Chuzo KUTSUKAKE, Shigeru TANAKA, Yuichi ABE, Masakazu SEKI,
Yoshikazu OGINUMA, Takeo NISHITANI
Fusion Neutron Laboratory, Japan Atomic Energy Research Institute, Tokai, Ibaraki

2.3.1 Introduction

It is important to obtain the knowledge as to the amount of remaining tritium and the tritium distribution in the accelerator target in order to optimize the neutron production condition. Therefore, the measurement by imaging plates was adopted as a convenient method for the case. Here in the present study, the applications to the measurement of residual tritium inventory and tritium distribution were studied.

2.3.2 Surrounding conditions of Imaging Plate

FNS uses rotating type (RNT) target and stationary type of tritium target. The shape of rotating target is a part of spherical surface and made from copper about 1 mm in thickness with a 3 – 5 μm thick evaporated titanium layer on the surface facing deuteron beam. Tritium is impregnated in the titanium layer, and the initial amount is about 30 TBq. Figure 2.3-1 indicates an overall rotating target system. The RNT target disk rotates keeping vacuum of the inside chamber and cooling outside the target by the water flow. The beam scans a concentric circle of the RNT target. The RNT target operation conditions are as follows;

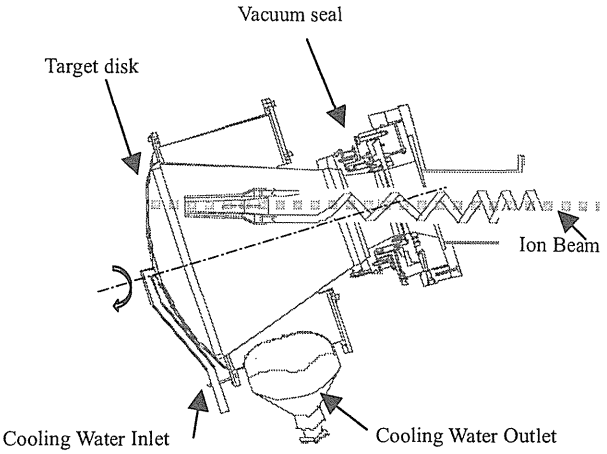

Fig.2.3-1 RNT target system

Baem size:	smaller than 15 mm in diameter
Rotation speed:	1600 r.p.m.
Swing speed:	12 min./swing
Beam power:	7 kW
Water flow:	23 litter/min.
Vacuum:	-5×10^{-3} Pa

Electrons emitted by tritium generate characteristic and bremsstrahrung X rays through reactions with titanium. The spectrum was measured by a lithium drift type silicon detector and shown in Fig. 2.3-2. The prominent peak represents characteristic X ray at 4.5 keV and 4.9 keV. In order to detect these X rays, an imaging plate which is composed of BaFBr:Eu^{2+} and base material were employed. They were enclosed in dual laminated sheets consisting of 3 materials (k-nylon 15μm, aluminum 12μm and polyethylene 70 μm in thickness respectively) to shield from light and prevent tritium contamination. On the other hand, titanium targets were also wrapped with polyethylene sheet (100 μm thick) to confine tritiated titanium flakes.

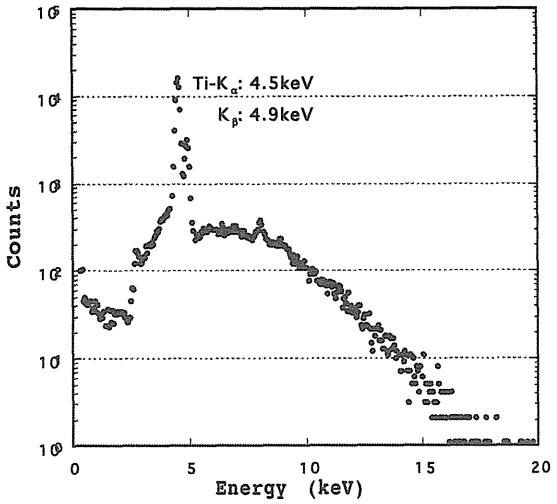

Fig. 2.3-2 X ray energy spectrum emitted from target and measured by silicon detector

The enclosed imaging plates were closely attached on the surface of the tritiated titanium target. This arrangement means two laminated sheets and one polyethylene sheet were interposed between the plate and the target.

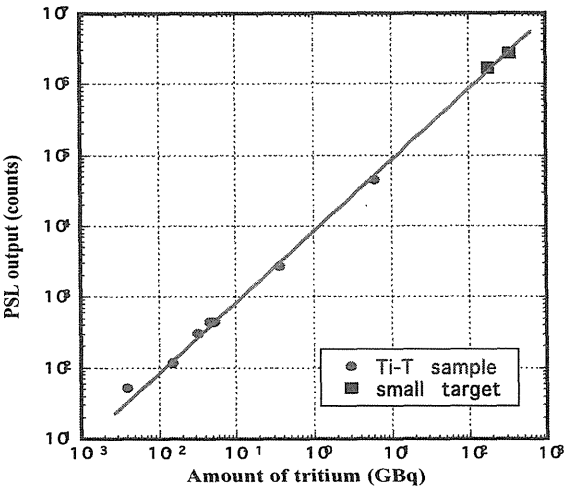

Fig.2.3-3 Tritium calibration curve between PSL output and amount of tritium

2.3.3 Procedure of the Measurement

The imaging plates were exposed to tritium target for a few minutes. The plate after exposure causes photo-stimulated luminescence (PSL) when it is irradiated by laser light of image reader. The intensity of the luminescence is expected to be proportional to the exposure dose to tritium, and the correlation was measured by photo-multiplier. The signals were processed digitally to present tritium distribution. The system gave the resolution of a measurement point at 50 micrometers.

Prior to the measurement of the tritium target, the PSL response was calibrated with a small tritium sample containing known amount of tritium that had been measured by calorimetry and an ion chamber. The calibration curve is shown in Figure 2.3-3. An excellent linearity is observed between the PSL output of the imaging plate and tritium inventory in the range from 10 MBq to 300 GBq.

2.3.4 Tritium Distributions in RNT target

Major conditions of RNT target measured in the present study are as follows.

Titanium area : 333.4 cm^2 (63.5 mm ϕ to 209.6 mm ϕ in diameter)
Titanium thickness: 1.6 mg/cm^2
Tritium inventory (initially): 19.6 TBq
Incident deuterons: 2300 Coulombs

Since the surface of RNT target is spherical, flat plate cannot be closely attached on it. In the present work, imaging plates were cut into rectangles 13 by 200 mm in size and fixed across the target surface to measure the tritium distribution on RNT. The obtained images are shown in Fig. 2.3-4. The upper is for the target before irradiation and the lower after irradiation. The darker the more tritium exists, therefore the white zone inside the circle does not contain tritium and concentric circles of lower image represent the traces where the target was irradiated and the tritium was consumed.

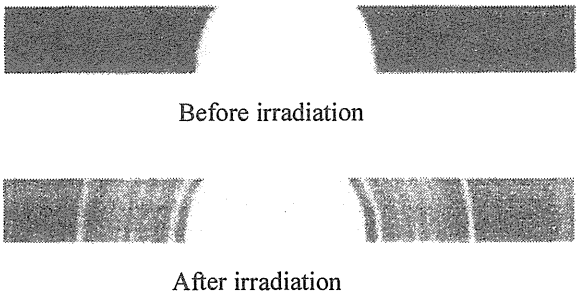

Fig.2.3-4 Image of tritium distribution

The tritium distributions before and after the irradiation were compared along one of the traverses in Fig. 2.3-5.

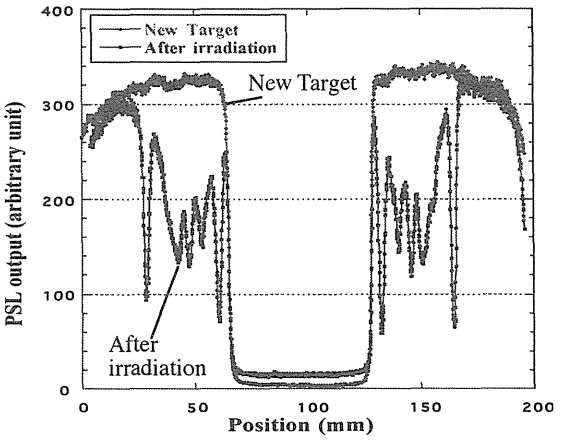

Fig. 2.3-5 Tritium distribution before and after irradiation across the RNT target

In case of the target that has not been irradiated yet, the tritium distribution around central non-tritiated part forms moderate hills in both sides. On the other hand, several sharp gutters are observed in same regions for the irradiated target. The gutters represent the traces where deuteron ion beam swept. The discrepancies show the tritium consumption by the beam irradiation.

By subtracting the tritium distribution of irradiated RNT target from that before irradiation, the consumed tritium distribution was estimated and is shown in Figure 2.3-6 Since the amount of tritium decreases through reactions with deuteron, the distribution represents focusing performance of deuteron ion beam. The width of the focusing was

estimated to be 2.5 mm at FWHM on the basis of the distribution shown in the figure. This shows the beam power losses about 44 kW/cm^2 at the D-T beam reaction area.

Figure 2.3-7 shows the tritium distribution of the other RNT target after 1.1x10^4 coulomb incidence deuterons irradiation. This shows the beam scans full of the tritium titanium area.

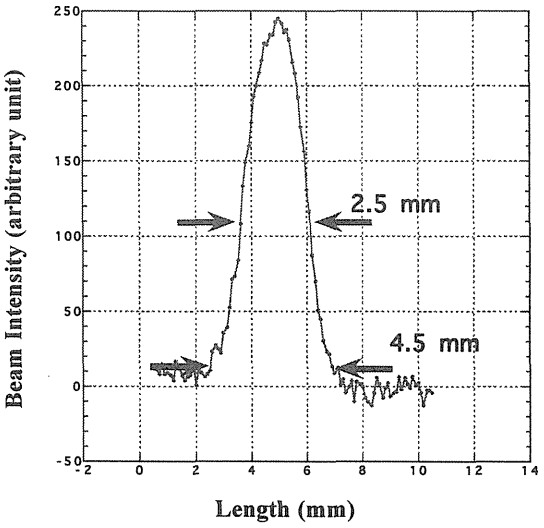

Fig. 2.3-6 Consumed tritium distribution across a scanned path by deuteron beam on a rotating target

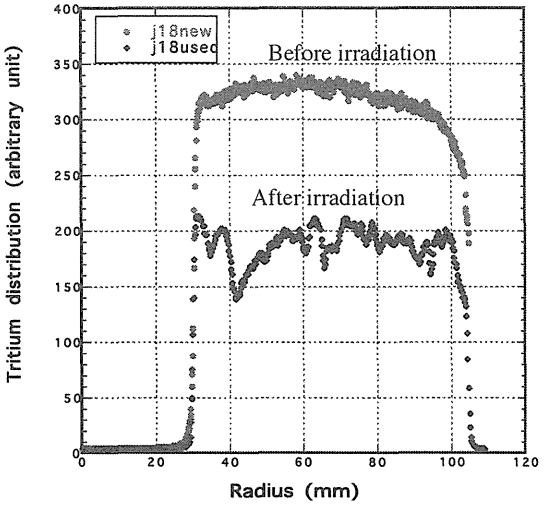

Fig 3.2-7 Tritium distribution of RNT target number 18 before and after irradiation.

References

[1] K.Takahashi et al., "Mechanism of Photostimulated Luminescence in BaFX:Eu(X=Cl,Br) Phosphers", Journal of Luminescence, **31&32**, 266-288, (1984).

[2] H. von Seggern, "Physical Model of Photo stim- ulated Luminescence of X-ray irradiated BaF Br:Eu^{2+}", Journal of Applied Physics, **64**, 1405- 1412, (1988).

[3] T. Sanami et al., "Fast Neutron Profiling with Im- aging Plate", KEK Proc. **97-8**, 74-81, (1997).

[4] H. Sakane et al., "A Study on 14 MeV Neutron Beam Characteristics and its Applications", Reactor Dosimetry: Radiation Methodology and Assessment, 375-382, (2001).

3. Blanket Neutronics Experiments

3.1 Tritium Breeding Experiments with Lithium Titanate in Thermal-type Mockups

Axel KLIX, Kentaro OCHIAI[1], Takeo NISHITANI[1], Akito TAKAHASHI
Department of Nuclear Engineering, Osaka University, Suita, Osaka
[1]*Fusion Neutron Laboratory, Japan Atomic Energy Research Institute, Tokai, Ibaraki*

3.1.1 Introduction

Tritium is a fuel for fusion reactors based on the Deuterium-Tritium (DT) fusion reaction. It must be produced artificially in a lithium compound in the breeding blanket which surrounds the fusion zone. A sufficiently high tritium production performance is an important design parameter for the breeding blanket. To maximize the tritium production rate (TPR), the lithium in the blanket is usually enriched in ^{6}Li in current conceptual designs since the reaction cross section for the tritium production is so high for low energy neutrons compared to that of ^{7}Li which is a threshold reaction, see Fig. 3.1-1. Therefore, the blanket designs contain also neutron moderating and -multiplying materials for enhancing the tritium production. A primary candidate for moderation and multiplication is beryllium. But other materials in the blanket, such as structural materials (steel) and impurities may reduce the TPR by neutron capture reactions such as (n,γ) and (n, c.p.*[1]).

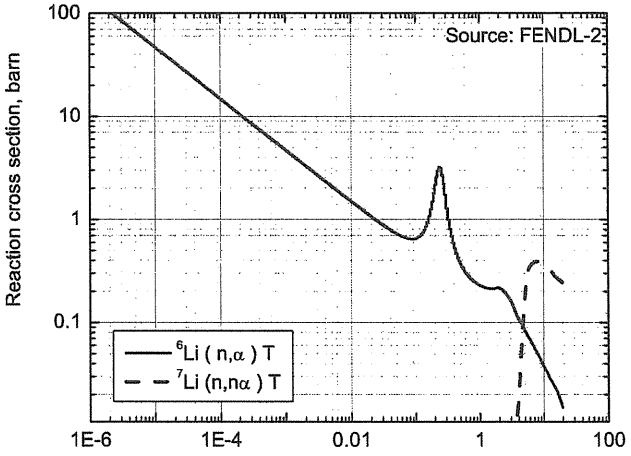

Figure 3.1-1 Cross section of tritium production reactions in lithium.

Mock-up experiments with blanket materials are therefore conducted which allow to study the effects on the TPR experimentally and also to validate computer code and nuclear cross section data which are essential tools for the R&D work.

Recently, integral mock-up experiments with candidate materials for the future DEMO fusion reactor have been done at Fusion Neutronics Source (FNS) of JAERI. The breeding assemblies consisted of layers of low activation ferritic steel F82H, lithium titanate enriched in

*[1]c.p.: charged particle

^{6}Li, and beryllium. They were irradiated with the DT neutron source of the 80 degree beam line.

3.1.2 Local TPR measurement

A method has been developed which allows to measure tritium directly in lithium titanate by means of small pellet detectors which can be inserted into holes in blocks of lithium titanate used to build the breeding layers, see Figure 3.1-2. It is expected that the application of TPR detectors made of the same material as the breeding layers will reduce uncertainties in the measured TPR caused by inhomogeneities especially in the ^{6}Li concentration. This is important because in such a thermal-type blanket (most of the TPR from thermal and epithermal neutrons), the thermal neutron spectrum and hence the TPR change substantially within short distances due to the presence of strong neutron absorbers (^{6}Li). The method is described in more detail in Refs. [1,2].

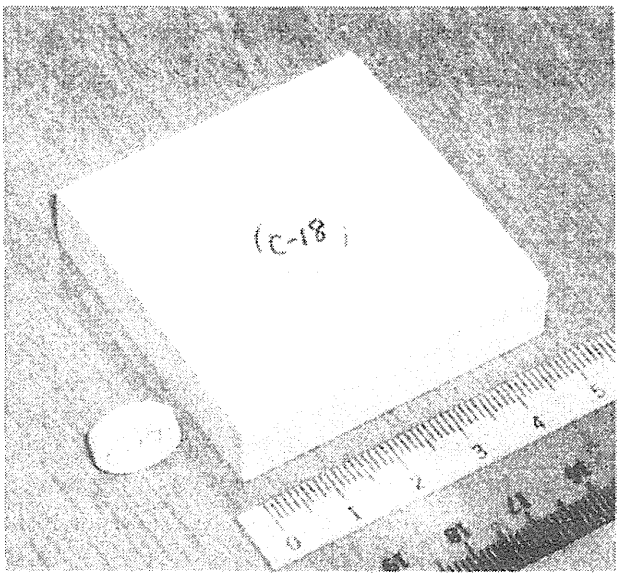

Fig.3.1-2 A block of lithium titanate and a pellet detector.

3.1.3 Application in mock-up experiments

A typical setup for the initial series of experiments with one breeding layer (40% and 95% ^{6}Li enriched lithium titanate) is shown in Fig. 3.1-3. A more detailed description of the experiments can be found in Refs. [3-4]. The assembly consisted of sheets of F82H steel, beryllium blocks and lithium titanate blocks. It was surrounded by lithium carbonate blocks for shielding off room-returned neutrons. Measured TPR profiles are shown in Fig. 3.1-4.

The obtained TPR profile is typical for a thermal-type blanket. It can be seen that the TPR on the surface of the breeding layer next to the beryllium is substantially higher than in the middle of the breeding layer. This difference is caused by a self-shielding effect, the very high macroscopic cross section for tritium production causes the absorption of neutrons entering the layer with energies below 1 eV so that they cannot contribute to the TPR deeper in the breeding layer. These neutrons produce tritium near the surface instead.

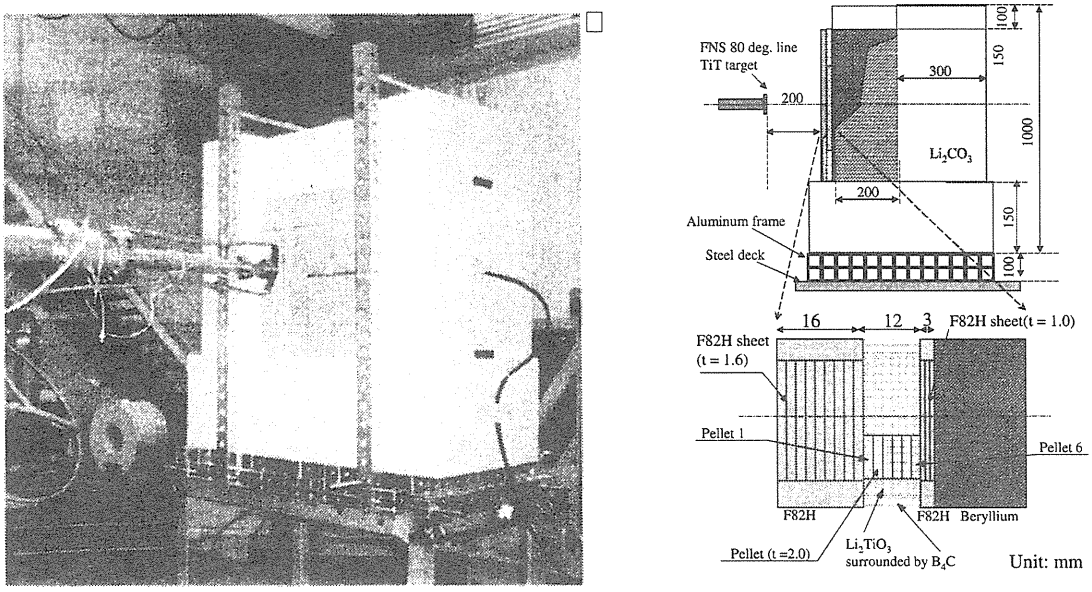

Fig. 3.1-3 Photograph and cross sectional view at the experimental assemblies with one breeding layer.

Table 3.1-1 The layer configurations used in the experiments. All thicknesses in mm.

Configuration	^{6}Li enrichment	F82H	Be	F82H	Lithium titanate	F82H	Be
a)	95.00%	0	0	16	12	3	200
b)		0	0	16	12	9	200
c)		16	50	3	12	9	150
d)	40.00%	16	50	3	12	9	150

3.1.4 Analysis

The TPR in the pellet next to the beryllium layer is about five times higher than in the deeper positions in the breeding layer. This illustrates the self-shielding effect which is especially pronounced in case of the 95% enriched lithium titanate. After changing the F82H sheet between the breeding layer and beryllium from 3 mm to 9 mm the surface TPR drops to four times the value inside the layer. This effect is caused by absorption of thermal neutrons in the F82H ferritic steel which containes absorbers such as tungsten (2%) and chromium (8%). In case of the breeding layer sandwiched between beryllium, the TPR on both surfaces is higher than inside the breeding layer due to thermal neutrons entering from both sides now.

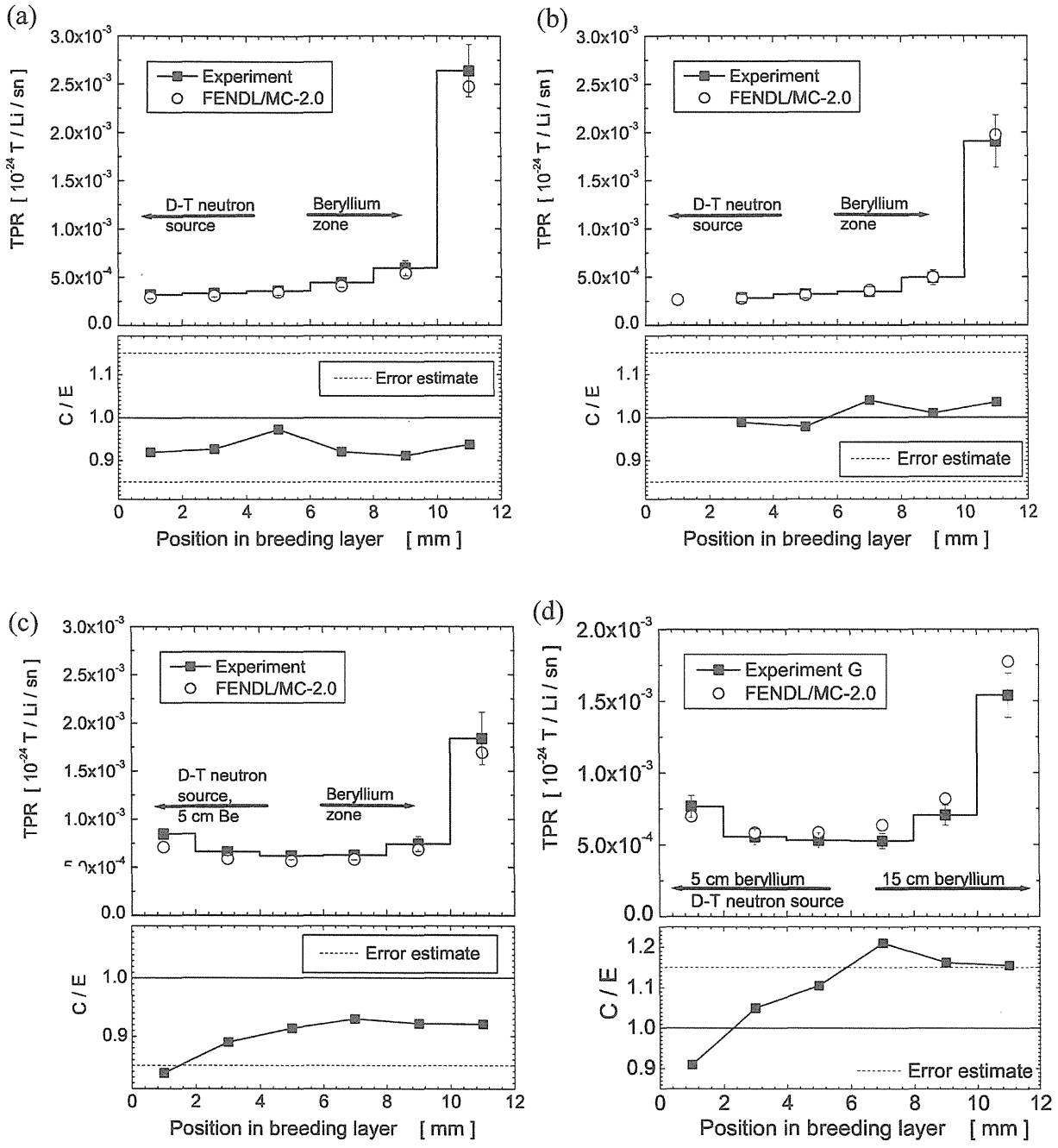

Fig. 3.1-4 Tritium production rates measured in assemblies with 95 % (a-c) and 40% (d) enriched lithium titanate, F82H, and beryllium. For configuration see Table 3.1-1

The spatial TPR profile looks similar for 40% enriched lithium titanate. However, it can be seen, that the profile is more flat since thermal and epithermal neutrons can penetrate deeper into the breeding layer.

Numerical simulations were done with MCNP-4C [5], the library FENDL/MC-2.0 [6] and the dosimetry file JENDL-DOS91 [7]. For the lithium density, a value of 9.4 wt% and 11.8 wt% for 40% and 95% enriched lithium titanate, repectively, was used as obtained from an ICP mass spectroscopy analysis performed at JAERI. The ^{6}Li concentration in the material was calculated from the enrichment given on the data sheet of the manufacturer. The measured and calculated tritium production rates are also shown in Fig. 3.1-4. The calculation/experiment ratio (C/E) was within the error estimate of 15% (combined experimental and calculation error) for the mock-ups with 95% 6Li enrichment in the breeding layer. Larger discrepancies were seen for the mock-ups with 40% enriched lithium titanate.

3.1.5 Summary

Lithium titanate, an advanced tritium breeding material, is currently investigated in integral mock-up experiments at FNS. A method was developed which allows to measure low tritium concentrations directly in this material. The local tritium production rate was obtained by small lithium titanate pellet detectors inserted into the breeding layers which are dissolved after irradiation of the assemblies, and the accumulated tritium was counted by liquid scintillation techniques.

The measurement method was applied in mock-up experiments with candidate materials for the future DEMO reactor breeding blanket. Experimental assemblies consisted of sheets of low activation ferritic steel F82H, lithium titanate, and beryllium. Tritium production rate profiles were obtained and compared with results from calculations with the Monte Carlo neutron transport code MCNP-4C. In case of the mock-ups with 95% enriched lithium titanate, the C/E ratios were within the error estimate while larger discrepancies were observed in case of 40% enriched lithium titanate.

References

[1] A. Klix et al., Fus. Sci. Techol. **41**, 1040 (2002).
[2] A. Klix et al., Proc. CBBI-11 workshop, Tokyo, Dec. 2003.
[3] S. Sato et al., Nucl. Fusion **43**, 527 (2003).
[4] A. Klix et al., J. Plasma Fus. Res., SERIES, **5**, 565 (2002).
[5] J. F. Briesmeister (Ed.), LA-13709-M, LANL, (2000).
[6] H. Wienke and M. Herman, IAEA-NDS-176 Rev. 0, IAEA, (1998).
[7] M. Nakazawa et al., JAERI 1325, JAERI, (1992)

3.2 Tritium Breeding Experiments of Three Layers Mockup experiments

Kentaro OCHIAI, Axel KLIX, Yury VERZILOV, Satoshi SATO, Masayuki WADA,
Takeo NISHITANI,
Fusion Neutron Laboratory, Japan Atomic Energy Research Institute, Tokai, Ibaraki

3.2.1 Introduction

In order to examine the accuracy of the TBR calculations, neutronics experiments have been performed with D-T neutrons at FNS by using a three-layer mockup of the solid breeder blanket consisting of the tritium breeder, the neutron multiplier and the structural material. The tritium production rates (TPR) were measured by Li_2CO_3 pellet detectors embedded in the breeding layers. Measured TPR was analyzed by the Monte Carlo code MCNP-4B[1] with the nuclear data libraries JENDL-3.2, JENDL-Fusion File (JENDL-FF) [2], ENDF/B-VI and FENDL-2.0 [3]. Also impurity effect in the beryllium neutron multiplier has been investigated.

3.2.2 Mockup Assembly with Three Layers

The blanket mockup consisting of three breeder layers was employed. Fig.3.2-1 shows a schematic view of the experimental assembly. The size of the assembly is about ϕ 600 mm^2 wide with a total thickness of 350 mm. The first layer facing to the neutron source is simulating a first wall of F82H. Three 12-mm thick ceramics layers consisting of 40% enriched $^6Li_2TiO_3$ with a thin F82H layer are set up between 100- and 50-mm thick layers of beryllium in the assembly. The assembly was enclosed in a cylindrical stainless steel (SS-316) reflector to shield the neutrons reflected by the experimental room walls. The tritium target was also surrounded by a cylindrical stainless steel with a 100-mm thick beryllium reflector in order to simulate the energy spectrum of the incoming neutron flux in the blanket.

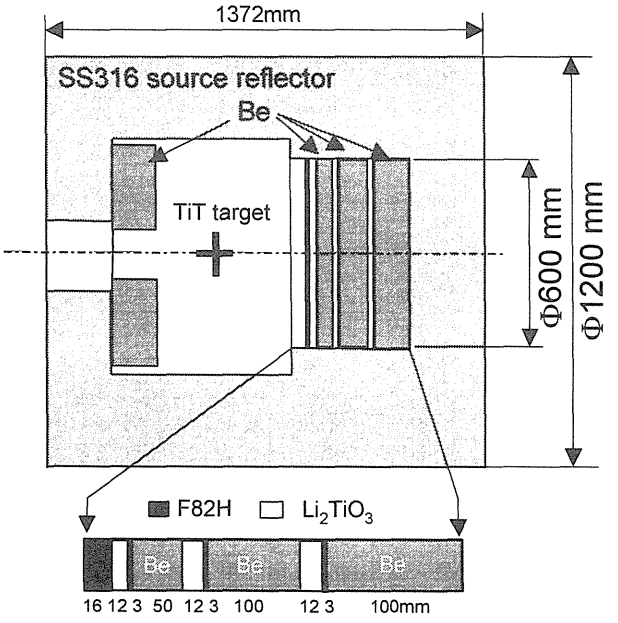

Fig. 3.2-1 Schematic view of the experimental assembly consisting of three layers of the breeding blanket mockup.

50-% enriched $^{6}Li_2CO_3$ pellets, with sizes of ϕ13 mm in diameter and thickness between 0.5-2 mm, were used as the tritium detectors in each $^{6}Li_2TiO_3$ ceramics layers to measure the produced tritium. As a neutron counting monitor, 3.5 MeV associated α particles was counted by SSBD was used. And Nb, In and Au foils were also set up at important positions in the assembly to verify the neutron field.

3.2.3 Measurement and procedures

The liquid scintillation counting technique was employed to measure the tritium [4]. After irradiation, Li_2CO_3 pellets were taken out of the assembly and were dissolved with the weak acid liquid and neutralized. Finally, it was mixed to produce the scintillation liquid and neutralized liquid. The tritium concentration in each of pellet was measured by determining the activity of the accumulated tritium. Fig. 3.2.2 shows a scheme of the procedure for the tritium measurement of the irradiated pellet [5]. The activities of solutions were evaluated from the measured counts with the liquid scintillation spectrometer Aloka 5500, where the internal standard method was used. The samples were counted, then a small amount of tritium standard solution was added and the sample was counted again. Also the calibration of the TPR of the pellet was carried out with 99.5-% enriched $^{7}Li_2CO_3$ pellet irradiated with virgin 14 MeV neutrons near the FNS target. From the calibration, it was found that the accuracy of the tritium measurement is about 10 % including the accuracy of the source neutron intensity.

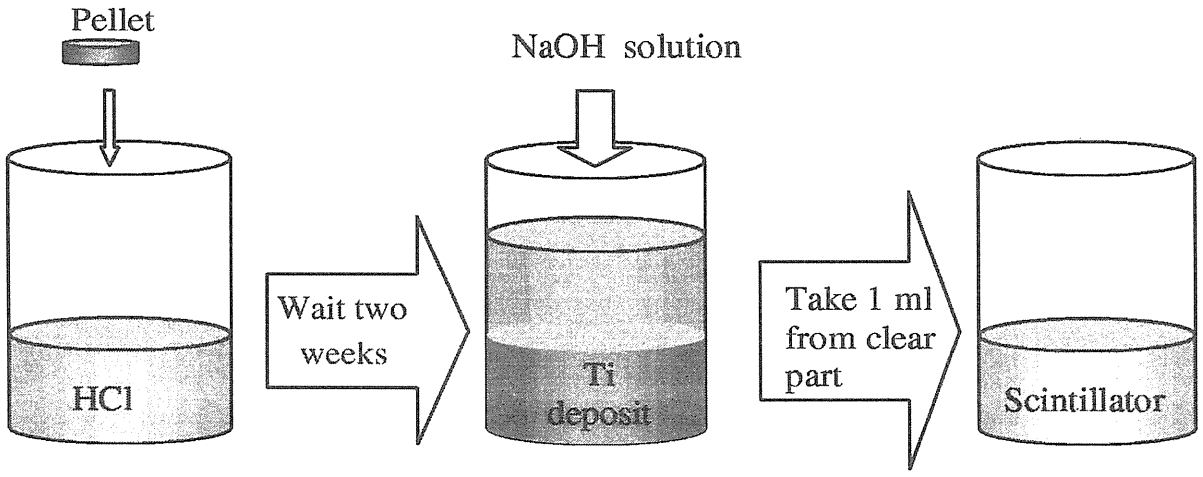

Fig. 3.2.2 Scheme of the procedure for the tritium measurement of the irradiated pellet

3.2.4 Results

Fig. 3.2-3 shows the TPR for Li_2CO_3 pellet obtained by the experiment and calculations and the ratio of the calculated results to the experimental results in the three layers experiment. The calculation of TPR is overestimated by 5% to 25% in this experiment. C/E of the 1st breeding layer is much larger than that of the single layer experiment. The layer-average TPR was about 1.21, 1.12 and 1.09 in 1st, 2nd and 3rd breeding layer, respectively. C/E of the integrated TPR for three layers was about 1.15, which is a little bit larger than the present design margin for the tritium breeding performance. The reason for this overestimation in TPR is not clear. The value of C/E decrease toward unity with the distance from the assembly surface. The fast neutron fluxes measured with Nb and In foils agreed well with the calculation in any layer. So it is considered that the calculated neutron influx to the surface of the assembly is not accurate in the low energy range. The candidates of the reason of the discrepancy are the inaccuracies of the double differential cross section of beryllium and SS316 stainless steel constituting the source reflector can.

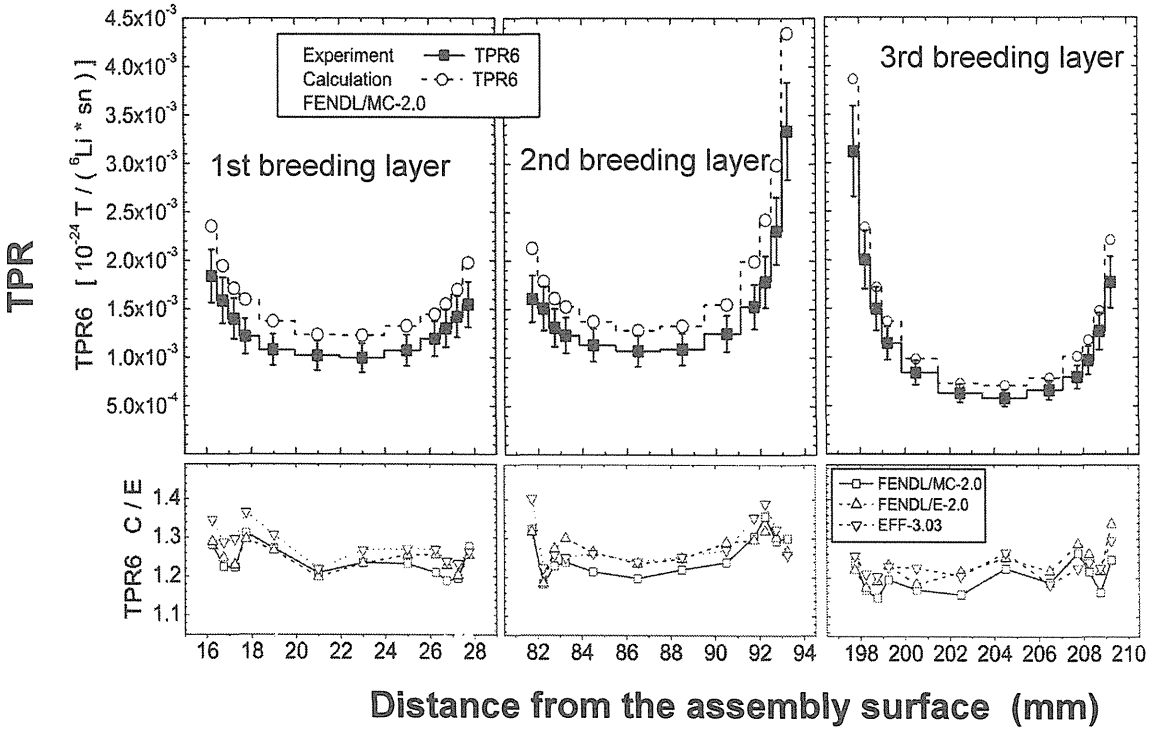

Fig.3.2-3 TPR for Li_2TiO_3 pellets obtained by the experiment and calculations and the ratio of the calculated results to the experimental results in the three layers experiment.

3.2.5 Summary and Conclusion

In order to examine the accuracy of TPR calculations, neutronics experiments have been performed with D-T neutrons by using a mockup of the solid breeder blanket concept. TPR in the pellets were measured by liquid scintillation counting methods. The TPR was calculated by the Monte Carlo codes MCNP-4B and –4C with the nuclear data libraries JENDL-3.2, ENDF-VI and FENDL-2. The C/E values of the TPR were on average 1.15. We confirm the existence of impurities in beryllium blocks, which increases the macroscopic absorption cross section by 30%. However, it is found that such amount of impurities does not affect TPR significantly. Other possible reason of the discrepancy is uncertainties in the double differential cross sections of beryllium and/or SS316.

Reference

[1] J.F. Briesmeister (Ed.), MCNP - a general Monte Carlo n-particle transport code, version 4B, Los Alamos National Laboratory Report, LA-12625-M, 1997.

[2] T. Nakagawa, K. Shibata, S. Chiba, et al., "Japanese evaluated nuclear data library version 3 reversion-2: JENDL-3.2", J. Nucl. Sci. Technol., **32**, (1995) 1259.

[3] H. Wienke and M. Herman, "FENDL/MG-2.0, and FENDL/MC-2.0, The processed cross-section libraries for neutron-photon transport calculations, version 1 of February 1998, IAEA-NDS-176 Rev.1, IAEA, 1998.

[4] A. Klix, K. Ochiai, Y. Terada, Y. Morimoto, M. Yamauchi, J. Hori, and T. Nishitani, "Tritium measurement for ^{6}Li-Enriched Li_2TiO_3 breeding blanket experiments with D-T neutrons" , Fusion Sci. Tech. **41** (2002) 1040.

3.3 Experiment for the Assembly with Tungsten Armor

Satoshi SATO, Makoto NAKAO, Yury VERZILOV, Kentaro OCHIAI, Takeo NISHITANI
Fusion Neutron Laboratory, Japan Atomic Energy Research Institute, Tokai, Ibaraki

3.3.1 Introduction

In fusion DEMO reactors, the blanket is required to provide a tritium breeding ratio (TBR) of more than unity by neutron induced reactions in lithium in the blanket. The solid breeder blanket being developed by JAERI for tokamak-type DEMO reactors consists of Li_2TiO_3 or other lithium ceramics as the tritium breeder material, beryllium as the neutron multiplier material, reduced activation ferritic steel F82H as the structural material and water as the coolant [1]. Neutronics experiments had been conducted in the previous studies using blanket mockups composed of these materials to verify the accuracy of the tritium production rate (TPR), where the calculation results agreed with experimental values within about 10 % [2]. In the blanket design proposed by JAERI, the local TBR is around 1.4 - 1.5 for the case without an armor on the first wall. From the view point of sputtering damage of the first wall, tungsten (W) armors are the effective protection. However, from the view point of nuclear responses, W armors may reduce the TBR, and TBR might not satisfy the requirement in case [3]. There are a number of scattering and resonance capture reactions in W. No experimental studies have been reported so far about the impact of the W armor on the TBR. Therefore experimental studies are very important for the evaluation of nuclear responses of the blanket in the presence of the W armor. In order to evaluate this issue experimentally, neutronics experiments have been performed by using DT neutrons at FNS.

3.3.2 Experiments

A breeding blanket mockup, composed of a set of slabs of 16 mm thick F82H, 12 mm thick Li_2TiO_3 (^6Li enrichment of 40 %) and 200 mm thick Be with about 660 mm height and about 660 mm width each, was installed at about 450 mm distant from the DT neutron source, and DT neutron irradiation experiments were conducted by using FNS 80° beam line. In the experiments three types of mockups were tested: without the armor; with 12.6 mm thick W armor; and with 25.2 mm thick W armor. Figure 3.3-1 shows a configuration of the mockup for the case with the 25.2 mm thick W armor and the installation position of the detector. DT neutron yield at the target was about 1×10^{11} neutrons/s on average, which was monitored by the associated alpha particle measurement with a silicon surface barrier diode installed in the beam line. Three continuous irradiation experiments, each for ten hours, were performed, with the integrated irradiation period of 30 hours in total. Metal foils of Nb, Al, Au, with 10 mm in diameter and 1 – 100 μm in thickness, were installed at the boundary surfaces inside the

mockup. In addition to the Au foils without a cover, the Au foils with a Cd cover were also installed. After the irradiation, induced radioactivities were measured by decay gamma ray intensity with a high purity Ge detector, and neutron fluxes corresponding to each reaction rate were evaluated. Fifteen slices of Li_2CO_3 pellets, with a ^6Li enrichment of 40 %, 13 mm in diameter and 0.5 - 2 mm in thickness, were embedded inside the Li_2TiO_3. After the irradiation, induced radioactivities were measured by beta ray intensity of these pellets with production rate (TPR) was evaluated.

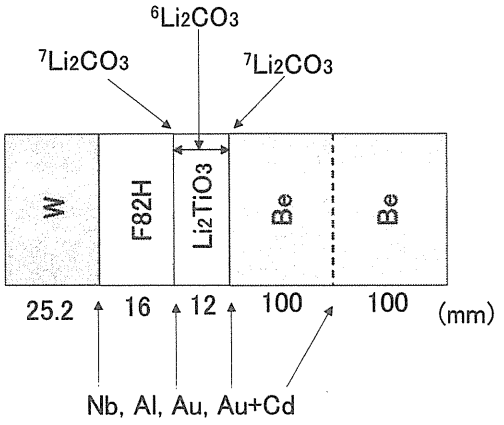

Fig. 3.3-1 The configuration of the mockup and the installation position of the detector.

3.3.3 Results and Discussions

Figure 3.3-2 shows the experimental results of the Nb reaction rate which corresponds to the neutron flux with the energy above about 9 MeV. The circles denote the experimental data with 25.2 mm armor, the squares without armor, the solid line the ratio of those with 25.2 mm armor to without armor, and the broken line the ratio of those with 12.6 mm armor to without armor. By installing the 25.2 mm thick W armor, the reaction rates of Nb, Al and Au inside the Li_2TiO_3 were reduced by 20 – 30, 30 and 10 – 30 %, respectively. Both of the fast and thermal neutron fluxes were reduced by installing the W armor. Figure 3.3-3 shows the experimental results of the TPR which corresponds to the ^6Li reaction rate. By installing the 25.2 and 12.6 mm thick W armors, the TPRs were reduced by 19 and 18 %, respectively, in maximum, and the integrated TPRs in the Li_2TiO_3 were reduced by 8 and 3 % relative to the case without the armor, respectively.

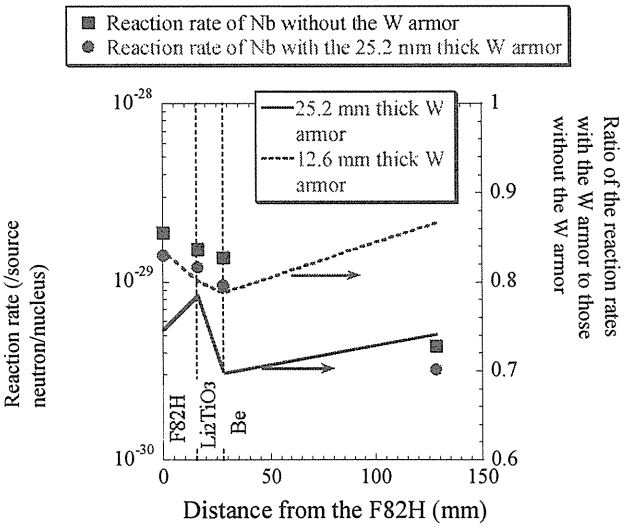

Fig. 3.3-2 The experimental results of the Nb reaction rate.

Numerical analyses were conducted by using the Monte Carlo neutral particle transport code MCNP-4C and the fusion evaluated nuclear data library FENDL-2. The calculation results almost showed the same tendency as the experiment ones with the C/E

ratios below 1.15 for the integrated TPRs, which is probably due to complex cross sections of tungsten, such as giant resonance capture reactions. Figure 3.3-4 shows the neutron spectra at the front surface of the F82H without the armor and with 25.2 mm armor. Similarly to the experiment results, both of the fast and thermal neutron fluxes were reduced by installing the W armor at all boundary surfaces. It is expected that the fast neutron fluxes are reduced by the scattering of the W, therefore the thermal neutron fluxes are reduced by the reduction of neutron multiplying reactions between Be and the fast neutron. In addition, capture reactions of the W itself are also expected to contribute to reduction of thermal neutron fluxes.

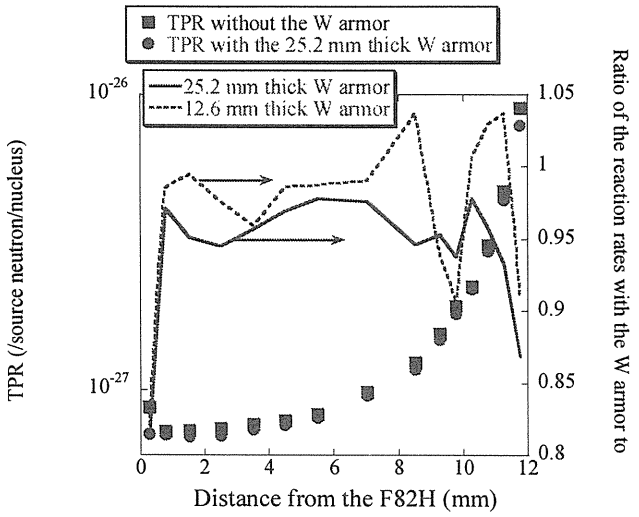

Fig. 3.3-3 The experimental results of the TPR.

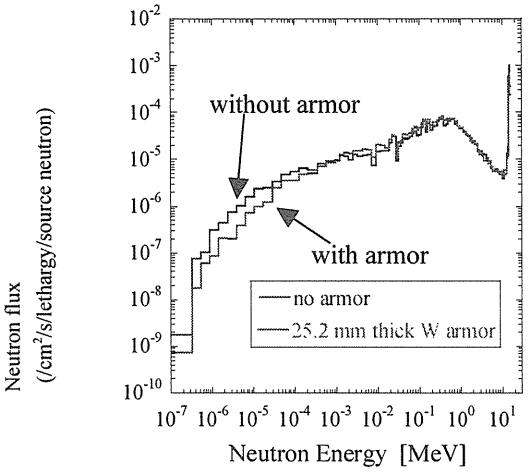

Fig. 3.3-4 The neutron spectra at the front surface of the F82H without the W armor and with the 25.2 mm thick one.

3.3.4 Conclusion

It can be concluded that the TPRs were reduced by above-mentioned effect, while W has large neutron multiplier reactions itself,. In the blanket design proposed by JAERI, it is expected that the reduction of the TBR is less than 2 % as the thickness of the W armor is less than 5 mm. Further experiment is to be performed using the mockup with 5 mm thick W armor.

References

[1] M. Enoeda, et al., Nucl. Fusion **43**, 1837 (2003).

[2] S. Sato, et al., Nucl. Fusion **43**, 527 (2003).

[3] S. Sato, et al., J. Nucl. Mater., **313-316**, 690-695 (2002).

3.4 Impurities in Beryllium

Yury VERZILOV, Kentaro OCHIAI, Michinori YAMAUCHI, Axel Klix,
Masayuki WADA* and Takeo NISHITANI
Fusion Neutron Laboratory, Japan Atomic Energy Research Institute, Tokai, Ibaraki
** Startcom Co. Ltd., Tokyo*

3.4.1 Introduction

Beryllium is a high priority material utilized in the field of fusion technologies. In most conceptual fusion power reactor designs, it is proposed to use beryllium as a neutron multiplier in the blanket [1]. Researching the chemical composition of beryllium in detail is important from two points of view:

- ✓ estimating the activation and transmutation of beryllium in the reactor;
- ✓ evaluation of the tritium breeding ratio.

The activation behavior of beryllium in a fusion reactor strongly depends on presence of impurities in the metal, thus affecting the choice of conditioning methods for beryllium waste from fusion reactors. Estimations [2] show, that the radiotoxicity, and the actinide inventory of the fusion beryllium waste, are strongly associated with the initial concentration of uranium and thorium.

Beryllium is an excellent neutron moderator with an extremely low absorption cross section for thermal neutrons. In such conditions, tritium production mostly occurs through absorption of thermal neutrons by lithium-6, according to the reaction $^{6}Li(n,\alpha)^{3}H$. However, thermal neutrons can be easily absorbed by other elements as well, if they are presented in beryllium as impurities that increase the absorption cross section. At a maximum, the impurities in beryllium can increase the absorption cross section by up to 30 times [3]. This impurity effect decreases the number of thermal neutrons, and as a result, the tritium production is decreased.

In the present paper, special attention was paid to a detailed analysis of impurities in beryllium, relevant to the tritium breeding ratio evaluation. Considering that such impurities can exist in structural beryllium grades, beryllium blocks (S-200F, Brush Wellman Inc.) used for the blanket benchmark experiments were studied with the purpose of qualification and validation. Two different methods were used for the study of impurities: an analysis of the local sample by the ICP-MS method, and an integral analysis of the beryllium assembly, using the pulsed neutron method. The latter method was proposed as the most effective way of analyzing the integral effect of impurities in beryllium on production of the tritium on the lithium-6. Generally, the inductively coupled plasma mass spectrometry method is suitable for the study, however, due to the wide spectrum and range of expected impurities, and their non-uniform distributions in beryllium, the study would be quite a lengthy and laborious

procedure. In such circumstances, it is useful to have a method which is able to quickly, easily and precisely evaluate the integral effect of impurities affecting evaluation of the tritium breeding ratio.

3.4.2 Chemical composition of structural beryllium grades (Brush Wellman Inc.)

Structural grades S-65C, S-200F and S-200E are being considered for use in ITER [4]. Manufacturer information concerning the composition of these grades, is shown in Table 3.4-1. In typical specifications, the main impurity elements are characterized by a high concentration, about 1000 ppm. Minor impurities are commonly not specified in detail. Instead, the total impurity level, of about 400 ppm, is shown in the last row of Table. This level isn't dependent on the beryllium grade. Very limited information concerning the content of minor impurities is available. Various studies [5,6] have shown that impurities can include elements such as Li, B, Cl, Cr, Mn, Co, Cd, Dy, Th, U and others. Some of the elements tend to have a significant effect on the absorption cross section of thermal neutrons, in spite of the low impurity level, caused by a high value of their absorption cross sections. It is possible to estimate the significance of the effect, using the impure beryllium to pure beryllium ratio of the total macroscopic absorption cross sections, R. Results of calculations of R for impurities, which are characterized by a high absorption cross section, are presented in Table 3.4-2. As indicated

Table 3.4-1 Specification of chemical compositions for structural beryllium grades

Chemical composition	S-65B / S-65C	S-200F	S-200E
Be, min %	99.0	98.5	98.0
BeO, max %	1.0	1.5	2.0
Al, max ppm	600	1000	1600
C, max ppm	1000	1500	1500
Fe, max ppm	800	1300	1800
Mg, max ppm	600	800	800
Si, max ppm	600	600	800
Other max ppm	400	400	400

Table 3.4-2 The effect of minor impurities on the ratio of macroscopic absorption cross section of impure to pure beryllium, R.

Composition			R
Be, %	Impurity		
	Element	Level, ppm	
100	---	0	1.00
99.99	B	5	1.43
99.99	Gd	5	2.78
99.99	Cd	5	1.15
99.99	Li	5	1.06
99.99	Cl	100	1.11
99.99	Co	100	1.08
99.99	Mn	100	1.03
99.99	All the above	320	3.63

in this table, even a small amount of impurities, less than 10 ppm, can increase the total absorption cross section in beryllium.

3.4.3 Impurity effect on tritium production

The influence of the impurity effect on tritium production depends on the blanket design, the volumetric ratio of lithium and beryllium, and enrichment of lithium [7]. Nonetheless, the beryllium mock-up will be most affected by the impurity effect. As an example of the parasitic absorption influence in the beryllium on tritium production, an estimation of the tritium production rate on lithium-6, was performed for the beryllium assembly, irradiated by D-T neutrons. The parasitic absorption was simulated by boron at a level of 5 ppm, a concentration corresponding to a 40% increase of the absorption cross section. The ratio of TPR-6 in the impure beryllium to pure beryllium is presented in Fig. 3.4-1. The parasitic absorption decreases the TPR-6 by about 5% on the surface of the assembly. This effect has a tendency to decrease the TPR-6 to a deeper location, due to the moderation and thermalization of neutrons, as a result of the increasing absorption cross section, which follows the 1/v-law.

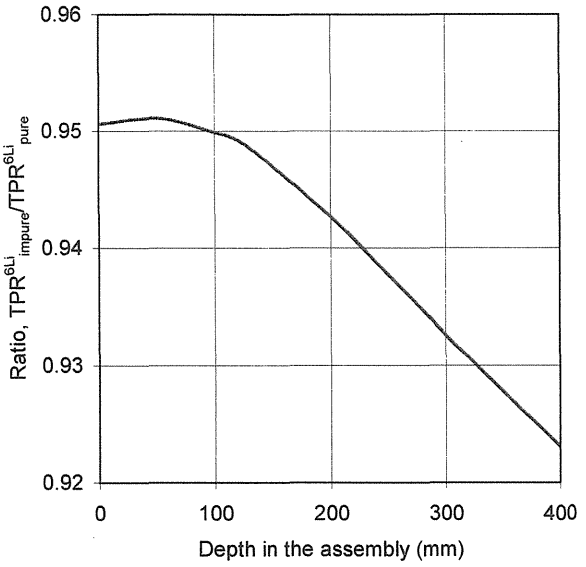

Fig. 3.4-1 The calculated effect of the parasitic absorption of thermal neutrons in beryllium blocks on the tritium production rate.

3.4.4 Impurity Analyses of Beryllium

3.4.4.1 Sample analysis by ICP-MS Method

In order to expand knowledge, concerning minor impurities in beryllium, the inductively coupled plasma mass spectrometry (ICP-MS) method was used for analysis of the sample. The study was completed by the Analytical Chemistry Laboratory (Department of Material Science) in JAERI [6]. Results of the analysis are presented in Table 3.4-3. Some of the elements were detected, though their quantities were not measured absolutely (indicated by symbol "S"). Results obtained from the spectroscopic study, can introduce some uncertainties to calculations of the tritium production rate, due to the sensitivity level of the technique, therefore not being able to meet the benchmark requirements for the integral experiment. Besides, additional uncertainties can exist as well, due to the non-uniform impurity distribution, since only one sample of the beryllium material was analyzed. In such

circumstances, for qualification and validation purposes, measurements of the integral effect seem very useful.

Table 3.4-3 Chemical composition of the S-200-F standard grade Be measured with the ICP-MS method

Element	Content	Element	Content
Be, %	97.9±0.8	Ni, ppm	250±30
Li, ppm	< 1	Zr	S
B, ppm	< 3	Nb	S
Mg, ppm	110±5	Mo	S
Al, ppm	570±50	Cd, ppm	< 1
Sc	S	Dy	S
Ti	S	Ta	S
V	S	W	S
Cr	S	Hg	S
Mn, ppm	96±5	Pb	S
Fe, ppm	1300±70	Th, ppm	1.5±0.1
Co	S	U, ppm	82±3

3.4.4.2 Integral Analyses by Pulsed Neutron Method

The non-destructive, pulsed neutron method was chosen with the following constrains in mind. First, it is useful to estimate the total effect of impurities, which increase the macroscopic absorption cross section of thermal neutrons, since the effect directly affects the tritium breeding ratio on lithium-6. Secondly, it is reasonable to measure the integral effect of impurities, in order to avoid a future problem concerning uniformity of impurity distributions. The effectiveness of this method is based on the following facts:

- ✓ all beryllium blocks, used for the benchmark experiments are suitable for estimation of the integral impurity effect;
- ✓ the total macroscopic absorption cross section for thermal neutrons can be measured;
- ✓ high accuracy of experimental results;
- ✓ fast and simple experimental procedures.

The integral effect was evaluated from time behavior observations of the neutron flux, following the injection of a burst of D-T neutrons into the beryllium assembly. The assembly was constructed from the structural beryllium grade S-200F (Brush Wellman Inc.). The pulsed neutron source experiment on beryllium performed at the FNS facility is described in detail in Ref. [8]. Experimental data were compared with the reference data and MCNP-4B calculations. Results show that the measured absorption cross section of thermal neutrons in beryllium blocks is approximately 30% larger than the calculated value, based on the data, specified by the manufacturing company. This result is consistent with the sample analysis.

3.4.5 Conclusions

Structural beryllium (S-65C, S-200F, S-200E from Brush Wellman Inc.), which is considered for use in ITER, contains less than 400ppm of unspecified impurities in total. The impurities composition contains a variety of elements, such as the Li, B, Cl, Cr, Mn, Co, Cd, Dy, Th, U and others. Due to the parasitic absorption of thermal neutrons in beryllium

material, some elements can affect the tritium breeding ratio. Impurities such as U and Th affect the choice of conditioning methods for fusion reactor beryllium waste. In order to evaluate the integral effect of impurities relevant to the tritium breeding ratio evaluation, a non-destructive, pulsed neutron method was applied. The measurements demonstrated the usefulness of the pulsed neutron method, as a tool ideal for fast and simple determination of the integral effect of impurities. It has been experimentally proven that the effective absorption of thermal neutrons in structural beryllium (S-200F) is approximately 30% higher than the calculated value, based on the data specified by the manufacturing company. For the pure beryllium assembly, such effect will decrease the tritium production rate by at least 5 %. In the blanket of a fusion reactor, the effect will depend on the blanket design, volumetric ratio of lithium and beryllium, and enrichment of the lithium. The estimation should be completed in each case.

Acknowledgements

The authors gratefully acknowledge M. Ito for analysis of the beryllium sample, C. Kutsukake, S. Tanaka, Y. Abe, M. Seki and Y. Oginuma, for their excellent operation of the D-T pulsed neutron source at the FNS facility.

References

[1] M. Enoeda, Y. Kosaku, T. Hatano, T. Kuroda, N. Miki, T. Honma, and M. Akiba, Design and technology development of solid breeder blanket cooled by supercritical water in Japan, Proc. 19th Fusion Energy Conference, Lyon, France, 14-19 October 2002.

[2] F. Druyts, P. Van Iseghem, Conditioning methods for beryllium waste from fusion reactors, Fusion Eng. Des. **69**, 607-610 (2003).

[3] C.R. Tipton (Ed.), Reactor handbook, second ed., Interscience Publishers, Inc., New York, 897-898 (1960).

[4] D. E. Dombrowski, Manufacture of beryllium for fusion applications. Fusion Eng. Des. **37**, 229-242 (1997).

[5] D. Webster, G.J. London (Eds.), Beryllium Science and Technology, V. 1, Plenum Press, New York, 34-36 (1979).

[6] M. Ito, JAERI, private communication, June 2003.

[7] M. Yamauchi, K. Ochiai, Y. Verzilov, M. Ito and T. Nishitani, Influence of Impurities in Beryllium on Tritium Breeding Ratio, Proc. Of 6th International Workshop on beryllium technology for Fusion, BeWS-6, Miyazaki, Japan, December 2-5, 2003.

[8] Y. Verzilov, K. Ochiai, S. Sato, M. Wada, M. Yamauchi and T. Nishitani, Analysis of Impurities in Beryllium, Affecting Evaluation of the Tritium Breeding Ratio, Japan Atomic Energy Research Institute Report, JAERI-Research 2004-005, 2004.

4. Cross Section Measurement

4.1 Sequential Charged Particle Reaction

Jun-ichi HORI[†], Kentaro OCHIAI, Satoshi SATO, Michinori YAMAUCHI and
Takeo NISHITANI
Fusion Neutron Laboratory, Japan Atomic Energy Research Institute, Tokai, Ibaraki

4.1.1 Introduction

It is important to precisely estimate the induced activities and dose rates in structural materials in view of safety designs of D-T fusion reactors. Recently it was pointed out that the activation processes via not only primary neutron reactions but also sequential reactions should be considered in activation calculations [1-2]. A sequential charged particle reaction (SCPR) is defined as the reaction induced by secondary charged particles, so that the contribution of SCPRs to the induced radioactivity is ordinarily much smaller than that of the primary reactions. However, the productions of radioactivity via SCPRs would influence severely on the total induced activity in the following two cases: (1) SCPRs produce undesirable long-lived radioactive nuclei in low-activation materials and (2) charged particles emitted from nearby another material promote the sequential reaction rates in a boundary region locally. Therefore, we focused on two special cases and carried out experimental studies on the effective cross sections or reaction rates of the SCPRs [3-5].

In the former case, we aimed at measuring the effective cross-sections for the production of radioactivity via SCPRs in the low-activation candidate materials, such as low-activation steel (F82H), pure vanadium and LiF. LiF is a composition of the candidate breeding materials such as FLIBE (LiF, BeF_2) and FLINABE (LiF, NaF and BeF_2). In the latter case, we simulated the surface of a cooling pipe in a D-T fusion reactor where many recoiled protons are generated in cooling water irradiated with high-energy neutrons. The enhancement of the radioactivity production around the surface of a cooling pipe makes corrosion products more activated. It gives rise to critical safety issue because the corrosion products are carried along cooling loops into ex-vessel regions. In order to obtain the distribution of sequential reaction rates with the distance from the attached hydrogen compound, we selected natural Fe, Cu, V, Ti, W, Pb and low-activation ferrite steels F82H as samples.

[†]*Present address: Research Reactor Institute, Kyoto University, Kumatori-cho, Osaka*

4.1.2 Experiments

Neutron irradiation experiments have been performed at the FNS facility. D-T neutrons were generated by bombarding a Ti-^{3}H rotating target with a deuteron beam of 350 keV at 20 mA. We prepared two kinds of sample and set it in front of the D-T neutron target. Typical arrangements of the irradiated samples are shown in Fig. 4.1-1. A typical distance between those samples and the target outer surface was 30 mm.

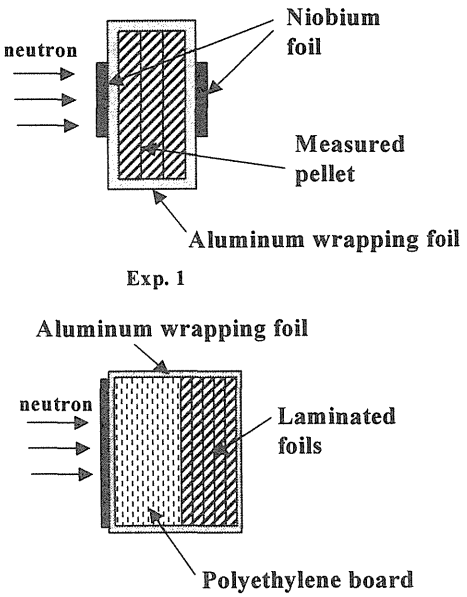

Fig. 4.1-1 Typical arrangements of the irradiated samples

In the Exp, three pellets were stacked and wrapped with aluminum foil as shown in Fig.4.1-1. The size of each pellets was 10mmϕ × 1mm. The purities of vanadium and LiF were 99.9 % and 99.99 %, respectively. The gamma rays emitted from the irradiated center pellets were measured by a HPGe detector for the following nuclei: ^{56}Co($T_{1/2}$=77.27d) via the ^{nat}Fe(p,n) reaction in F82H, ^{51}Cr($T_{1/2}$=27.7d) via the ^{nat}V(p,n) and ^{54}Mn($T_{1/2}$=312d) via the ^{nat}V(α,n) reaction in pure vanadium, and ^{7}Be($T_{1/2}$=53.12 d) via the ^{7}Li(p,n) and ^{22}Na($T_{1/2}$=2.6y) via the ^{19}F(α,n) reaction in LiF.

In the Exp. Ⅱ, several sheets of thin foil were laminated on a polyethylene board 3 mm in thickness which simulated water flowing inside a cooling pipe as shown in Fig. 4.1-1. Note that the range of proton recoiled by 14-MeV neutron in polyethylene is less than 3 mm. The size of the foil was 10×10×0.05-0.25 mm^{3}. We have measured the distribution of sequential reaction rates with the distance from the attached polyethylene board for seven materials (Fe, Cu, V, Ti, W, Pb and F82H). We measured the gamma-rays emitted from the irradiated samples by a HPGe detector for the following nuclei: ^{56}Co, ^{65}Zn, ^{51}Cr, ^{48}V, ^{184}Re, ^{206}Bi via the (p,n) sequential reactions in iron, F82H, copper, vanadium, titanium, tungsten and lead.

In order to determine the neutron flux incident on each stack, niobium foils were attached on both sides of it. A ^{232}Th fission chamber located at the ceiling of the target room was used as a monitor for generated neutrons. The counts per 10 sec were recorded by using multi-channel scaling (MCS) and the recorded history was used to make corrections for the fluctuations of neutron flux.

4.1.3 Results and Discussion

The observed gamma-ray spectra from the irradiated pure V and LiF pellets were shown in figs 4.1-2 and 3, respectively. The effective cross-sections with respect to 14.9-MeV neutrons for producing ^{56}Co in F82H, ^{51}Cr, ^{54}Mn in pure vanadium and ^{7}Be, ^{22}Na in LiF were derived from the activities and neutron flux. The data processing and estimation method have been in detail elsewhere [3], so it is omitted. The estimation was performed by using the values from the European Activation Files [6] (EAF_XN-97, EAF_SPEC-97, EAF_STOP-97). The cross sections for proton and alpha emission from Li isotopes were quoted from the reference [7]. The comparison between the experimental and the estimated values are shown in Table 4.1-1. The effective cross sections for the reaction induced by proton were overestimated by a factor 1.5-3. For alpha induced reactions, the range of discrepancy was large. We have to improve the data associated with alpha especially.

Figure 4.1-4 shows the obtained distribution of the reaction rates for producing ^{56}Co in F82H foils with respect to the distance from the surface of the polyethylene board. With coming closer to the polyethylene board, an exponential increase of the effective reaction rate is clearly observed. In the closest region, the reaction rate for producing ^{56}Co reached about 3 % of that for producing the main product ^{54}Mn. The contribution of ^{56}Co to the special radiation dose rate would reach about 10 % of that of ^{54}Mn since the contact

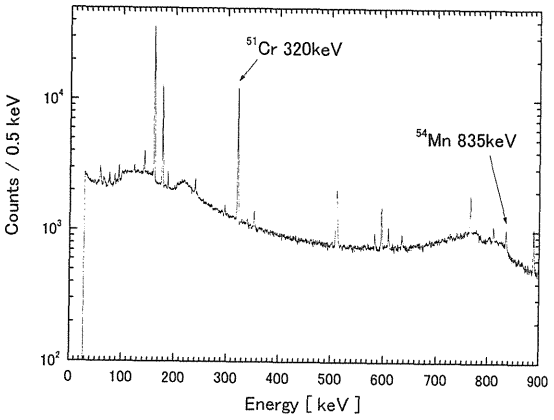

Fig. 4.1-2 The gamma-ray spectrum from the irradiated pure V

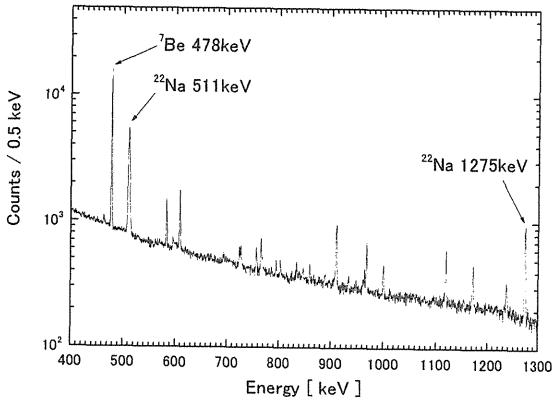

Fig. 4.1-3 The gamma-ray spectrum from the irradiated LiF

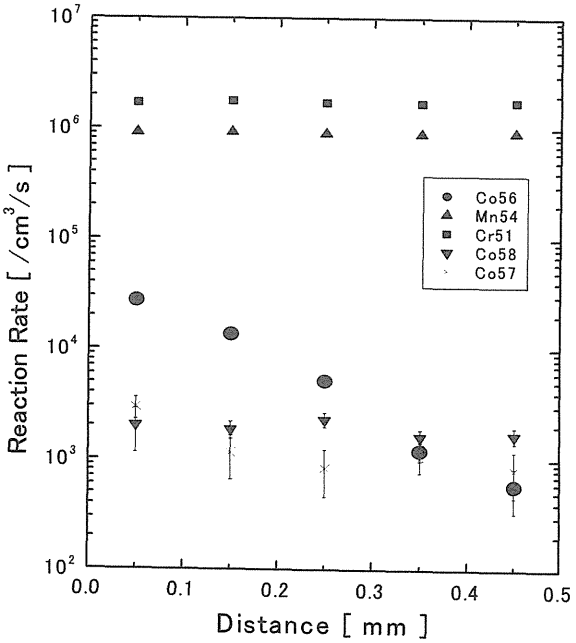

Fig. 4.1-4 The distribution of the reaction rate for producing ^{56}Co in F82H with respect to the distance from the surface of polyethylene board.

dose rate factor per unit activity for ^{56}Co is about 4 times larger than that for ^{54}Mn. During the operation before the equilibrium is attained, the contribution must be larger than the values, so that it cannot be neglected in the safety design.

Table 4.1-1 Measured and estimated effective cross-section for the sequential reaction

Sample	Reaction	Product	Effective Cross Section [μb]		
			Measured	Estimated	Ratio
F82H	^{56}Fe(p,n)	^{56}Co	8.0±0.9	24.2	3.0
Pure V	^{51}V(p,n)	^{51}Cr	25.7±1.6	38.7	1.5
	^{51}V(α,n)	^{54}Mn	1.1±0.3	0.30	0.3
LiF	^{7}Li(p,n)	^{7}Be	20.6±1.3	32.6	1.6
	^{19}F(α,n)	^{22}Na	3.7±0.3	25.4	6.9

4.1.4 Conclusion

The effective cross sections for producing the sequential reaction products in F82H, pure vanadium and LiF with respect to the 14.9-MeV neutron were obtained and compared with the estimation ones. Since the sequential reactions depend on the secondary charged particles behavior, the effective cross sections are corresponding to the target nuclei and the material composition. The effective cross sections were also estimated by using the EAF-libraries and compared with the experimental ones. There were large discrepancies between estimated and experimental values.

Additionally, we showed the contribution of the sequential reaction on the induced activity and dose rate in the boundary region with water. From the present study, it has been clarified that the sequential reactions are of great importance to evaluate the dose rates around the surface of cooling pipe and the activated corrosion products.

References

[1] S. Cierjacks and Y. Hino, J. Nucl. Mat. **170**, 134 (1990).

[2] S. Cierjacks, P. Oblozinsky, S. Kelzenberg, B. Rzehorz, Fus. Technol. **24**, 277 (1993).

[3] J. Hori, F. Maekawa, et al., Fus. Eng. Des. **63-64**, 271 (2002).

[4] J. Hori, S. Satoshi M. Yamauchi, K. Ochiai, T. Nishitani, JAERI-Research 2003-002 (2003).

[5] S. Sato, K. Ochiai, J. Hori, et al., Nucl. Fusion **43**, 527 (2003).

[6] J-Ch. Sublet, J. Koppecky, R. A. Forrest, UKAEA Fusion Report, UKAEA FUS 351 (1997).

[7] F. Maekawa, Y. M. Verzilov, D. L. Smith, Y. Ikeda, J. Nucl. Mater. **283-287**, 1448 (2000)

4.2 ^{18}F Production using Sequential Charged Particle Reaction

Jun-ichi HORI†, Kentaro OCHIAI, Ryohei TANAKA, Michinori YAMAUCHI,
Takeo NISHITANI
Fusion Neutron Laboratory, Japan Atomic Energy Research Institute, Tokai, Ibaraki

4.2.1 Introduction

In a diagnostic nuclear medical field, the significance of Positron Emission Tomography (PET) is increasing. Positron emitting nuclei such as ^{18}F ($T_{1/2}$=1.83h), ^{11}C ($T_{1/2}$=20.39m) and ^{13}N ($T_{1/2}$=9.97m) are commonly utilized as Pet-nuclei and ^{18}F with a longer half-life is the most useful nuclide.

Three methods were generally applied to the production of ^{18}F: (1) highly enriched ^{18}O-water are irradiated with proton beam and ^{18}F is produced via the ^{18}O(p,n) reaction, (2) Ne gas is irradiated with deuteron beam and ^{18}F is produced via the ^{20}Ne(d,α) reaction and (3) lithium-6 oxide is irradiated with thermal neutrons in a fission reactor and tritons emitted from the ^{6}Li(n,α) reaction produce ^{18}F via the ^{16}O(t,n) sequential reaction. As regards the methods of (1) and (2), an accelerator such as a cyclotron is needed in each medical facility. Moreover, the volume of product is limited by the irradiation area and charged particle range. In the case of (3), the sequential reaction as described in chapter 4.1 is utilized to producing ^{18}F. Since the ^{6}Li(n,α) reaction has large capture cross-sections in a low-energy region and neutron flux is also high in a fission reactor, it is possible to produce a lot of ^{18}F enough to use for a medical purpose. However, the irradiated samples should be solved to water and separated with an ion-exchanging method after an irradiation.

In this study, we aimed at implying a new and simple method for producing ^{18}F in a D-T fusion reactor. Around the first wall of a D-T fusion reactor, neutron flux would be reached the order of 10^{14} cm^{-2} s^{-1} and generate many recoil protons in irradiated water. Recoiled protons could cause the ^{16}O(p,α)^{13}N and ^{18}O(p,n)^{18}F sequential reactions, since the threshold proton energies for those reactions are not so high, which are 5.66 and 2.58 MeV, respectively [1]. Therefore, we have measured the effective cross-sections for the ^{16}O(p,α)^{13}N and ^{18}O(p,n)^{18}F reactions in irradiated water by using a D-T neutron source and showed the possibilities to produce PET nuclei as a potential applications of a D-T fusion reactor.

4.2.2 Experiments

Three irradiation samples of pure water and ^{18}O enriched-water (^{18}O:95% and ^{18}O:32%, ^{17}O:20%) were prepared. A thin cylindrical polyethylene case of 1 cm in diameter was filled

---

†*Present address: Research Reactor Institute, Kyoto University, Kumatori-cho, Osaka*

with each liquid sample. Net weight of the irradiated water was estimated to be about 1 g by subtracting the weight of the empty case from that of the case filled with water. Each sample was set in front of the D-T neutron target by using a pneumatic sample transport system.

Irradiations with D-T neutrons were performed at a place of about 8×10^{8} cm^{-2} s^{-1} neutron flux in the second target room at the FNS/JAERI. Irradiation time was typically about 7 hours. Additional irradiations with an empty case and an aluminum foil of 0.5 mm in thickness were also performed for 7 hours and 10 minutes, respectively. By irradiating the empty case and measuring it after irradiation, we confirmed that the activities of the irradiated case could not influence on the measurement of the sequential reaction rate. The averaged neutron flux at the sample position was determined from the standard cross section of the $^{27}Al(n,p)^{27}Mg$ reaction [2] and the observed activity of ^{27}Mg.

After irradiation, we pull the sample back to the measurement room by a pneumatic sample transport system and started measuring the annihilation gamma rays from the sample with a HPGe detector rapidly. Measurements were divided into a suitable period and repeated until count rate of the annihilation gamma-rays decreases to be a few counts per minute.

4.2.3 Results and Discussion

The curves for the count rate of annihilation gamma rays are shown in Fig. 4.2-1. The two components were observed in the curve of the irradiated pure water. It is confirmed that the fast decay component is due to ^{13}N and slow decay component is due to ^{18}F by fitting the curves. In the case of ^{18}O-enriched water, the component of ^{18}F could be observed.

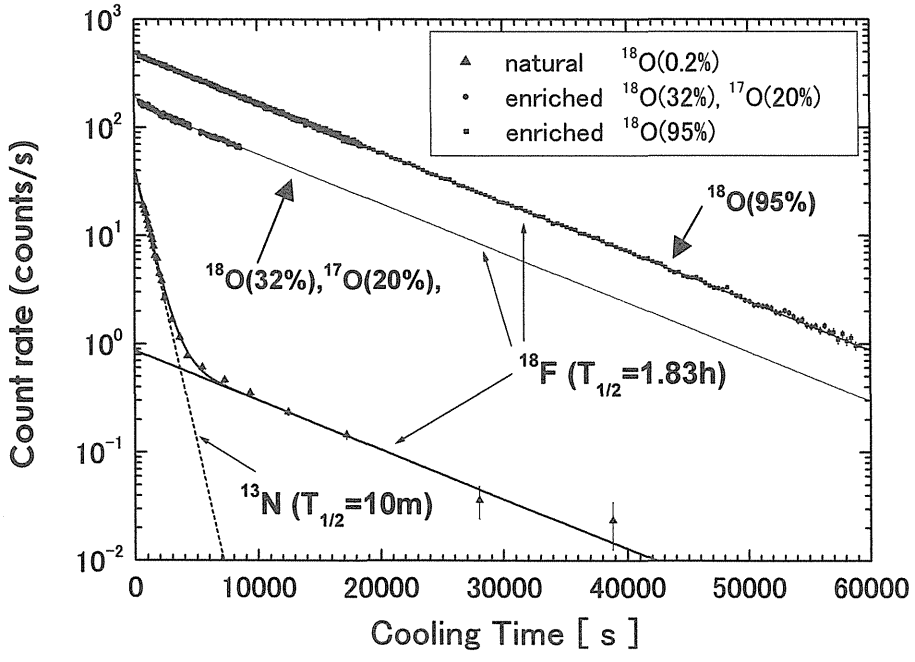

Fig. 4.2-1 The fitted curves for the count rate of annihilation gamma ray as a function of cooling time.

The effective reaction rates for the $^{18}O(p,n)$ and $^{16}O(p,\alpha)$ sequential reactions were derived from those activities and incident neutron flux. The saturated activities of ^{18}F were estimated from the obtained reaction rate. Figure 4.2-2 shows the saturated activities of ^{18}F under the irradiation with 10^{14} cm^{-2} s^{-1} 14-MeV neutron flux as a function of the degree of ^{18}O enrichment. The linearity between the saturated activity and the degree of ^{18}O enrichment was clearly observed. When a wall road of 14 MeV neutron of 1 MW/m^2 and ^{18}O 95% enriched water loop are assumed, the saturated activity would be reach more than 1 GBq/g as shown in Fig.4.2-2. This activity level could be satisfied with the recommendation in the medical field.

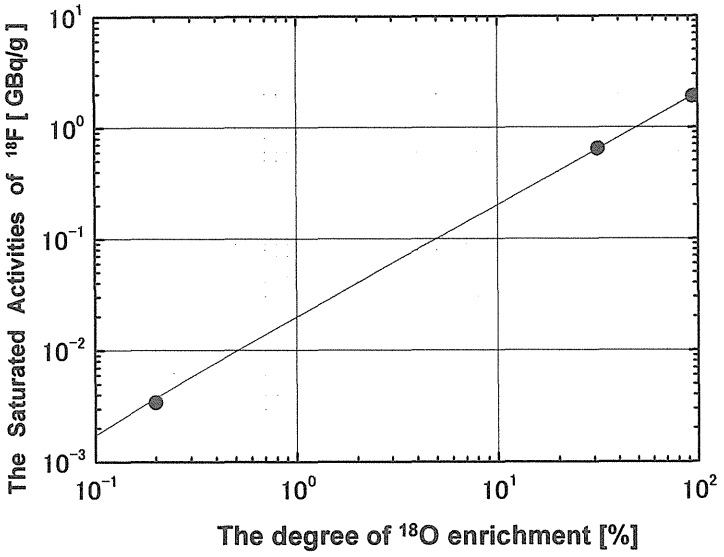

Fig.4.2-2 The relation between the saturated activity and the degree of ^{18}O enrichment

The effective cross-sections for producing ^{18}F and ^{13}N were also estimated by using the evaluated $^{1}H(n,n)^{1}H$ reaction cross section at 14.9 MeV taken from JENDL-3.2 [3], proton stopping power in water [4], and the evaluated (p,n) or (p,α) cross-sections [1]. The experimental and calculated effective cross-sections are shown in Table 4.2-1. The C/E values corresponding to the production of ^{18}F and ^{13}N are 1.1 and 1.3, respectively. Although the calculated values are larger than the experimental ones, the agreement between them is fairy good in spite of simple estimation. According to the present results, we estimated the saturated activity of ^{18}F under the irradiation with D-T neutron in a fusion reactor.

Table 4.2-1 Measured and estimated effective cross-sections for the sequential reactions

Sample	Reaction	Product	Effective Cross Section [μb]		
			Measured	Estimated	Ratio
Water	$^{16}O(p,\alpha)$	^{13}N	43 ± 2	55	1.3
	$^{18}O(p,n)$	^{18}F	656 ± 41	706	1.1

4.2.4 Conclusion

D-T neutron irradiation experiments were carried out at FNS and the effective cross-sections for producing ^{18}F and ^{13}N via the $^{18}O(p,n)$ and $^{16}O(p,\alpha)$ sequential reactions were obtained. Moreover, the effective cross-sections were estimated by using a $^{1}H(n,n)^{1}H$ reaction cross-section at 14.9 MeV, proton stopping power, and evaluated (p,n) or (p,α) cross-sections. The agreement between the experimental and calculated values was fairy good. We also considered the possibilities of producing ^{18}F-water to utilize to medical diagnostic nuclear medical field in a D-T fusion reactor. The present works implied that the activity of ^{18}F produced in a D-T fusion reactor would reach the reasonable level.

References

[1] D. L. Aldama, "Formatting of cross sections for production of diagnostic radionuclides" , IAEA-NDS-210 (2003).

[2] Y. Ikeda et al., "Activation Cross Section Measurements for Fusion Reactor Structural Materials at Neutron Energy from 13.3 to 15.0 MeV Using FNS facility", JAERI. 1312 (1988).

[3] T. Nakagawa et al., J. Nucl. Sci. Technol., **32**, 1259 (1995).

[4] H. H. Andersen, J. F. Ziegler, Hydrogen Stopping Powers and Ranges in All Elements, Pergamon, New York, 1977.

4.3 Measurement of Activation Cross Sections with d-D Neutrons in the Energy Range of 2.1 to 3.1 MeV.

Toshiaki SHIMIZU, Hitoshi SAKANE*, Itaru MIYAZAKI, Michihiro SHIBATA**, Kiyoshi KAWADE, Jun-ichi HORI[1***], Kentaro OCHIAI[1], and Takeo NISHITANI[1]

Department of Energy Engineering and Science, Nagoya University, Nagoya 464-8603
[1]Fusion Neutronics Laboratory, Japan Atomic Energy Research Institute, Tokai-mura

4.3.1. Introduction

A database of activation cross sections for neutron energies of up to 20 MeV is required for the design of a D-T fusion reactor, for neutron dosimetry and neutron shielding in an accelerator facility, and to confirm predictions based on nuclear reaction calculations. A number of cross section data have been reported at energies of around 14 MeV with d-T neutrons [1]. These data have been compiled in several evaluated-data libraries, such as JENDL-3.3 [2]. The data in those libraries are evaluated mainly on the basis of theoretical calculations. Experimental data, if available, are used to normalize the calculated excitation functions and to improve the accuracy and reliability of those functions. In case no measurements have been made, the systematics for the majority of reactions are used to predict unmeasured cross sections. The systematics of (n, p), (n, α), (n, 2n), and (n, np) in the neutron energy range between 13.4 and 14.9 MeV have been proposed on the basis of our experimental data [3 - 5]. At present, the prediction ability of these systematics is estimated to be $\pm(20 \sim 30)\%$. The experimental data below 13 MeV are, however, still incomplete, owing to the lack of available neutron sources that have intense neutron fluence rates. The systematics in this neutron energy range have not been studied. In order to propose the systematics around 3 MeV, we measured 14 (n, p), 2 (n, α), and 15 (n, n') reaction cross sections in the energy range of 2.1 to 3.1 MeV.

4.3.2. Experiment and Results

The d-D neutrons were generated by bombarding a deuterated titanium (Ti-D) target with a 350 keV d^+-beam at the 80-degree beam line of the FNS at the JAERI. The incident d^+-beam intensity was typically 1 - 2 mA.

Present address: Japan Nuclear Cycle Development Institute, Tokai-mura, Ibaraki

**Present address: Radioisotope Research Center, Nagoya University, Nagoya*

***Present address: Resarch Reactor Institute, Kyoto University, Kumatori-cho, Osaka*

In order to measure short-lived nuclei with half-lives down to several seconds, a pneumatic sample transport system was used to send samples to the irradiation position and return them to the measurement position quickly [6]. The typical transfer time was about 2 - 3 s. Figure 4.3-1 shows the layout of the pneumatic sample transport system. The angles of the irradiation positions with respect to the incident d^+-beam were 0°, 45°, 70°, 95°, 120°, and 155°, which covered the neutron energies ranging from 2.1 to 3.1 MeV. The distances between the Ti-D target and the irradiation position were 20 mm at 0°, 45°, 70°, and 95°, 42 mm at 120°, and 65 mm at 155°. The typical neutron fluence rate was $6 \times 10^6 \sim 1 \times 10^8$ n/cm^2/s.

When we measure short-lived nuclei with half-lives less than 1 s, we set a detector at an irradiation room. In order to get rid of prompt γ-ray backgrounds, pulsed neutron beam were used. The arrangement of the apparatus that irradiation angle with respect to the incident d^+-beam was 0° (neutron energy; 3.1 MeV), is shown in Fig. 4.3-2. The distance between the neutron source and the sample was 45 cm, and that between the sample and the detector was 2 cm. The sample was set in 45° to the detector. The typical neutron fluence rate was 2×10^5 n/cm^2/s. The neutron shield consists of 30 cm thick polyethylene, 1 cm thick B_4C as absorber of thermal neutrons, and 5 cm thick lead as γ-rays shielding. Since using B_4C, γ-rays via (n, γ) reaction whose cross section was large against thermal neutron were reduced to about 1/5. The detail of experiments were described elsewhere [6-10].

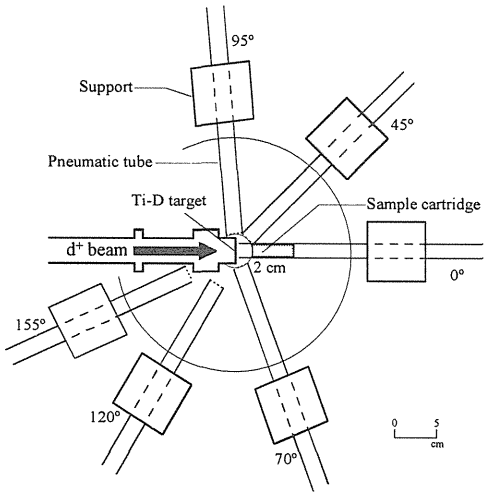

Fig.4.3-1 The layout of the pneumatic sample transport system.

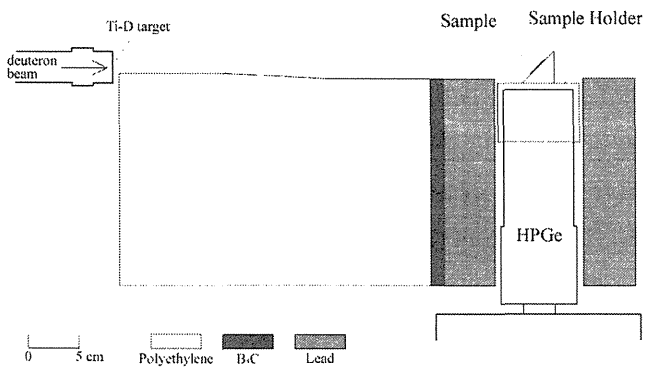

Fig. 4.3-2 Schematic view of experimental arrangement for the measurement with pulsed neutron beam.

The cross section data of 14 (n, p), 2 (n, α), and 15 (n, n') reactions were obtained in the energy range of 2.1 to 3.1 MeV as shown in Fig. 4.3-3. The half-life of measured reactions was between 0.8 s and 312 d. The half-life of 15 reactions was less than 1 h.

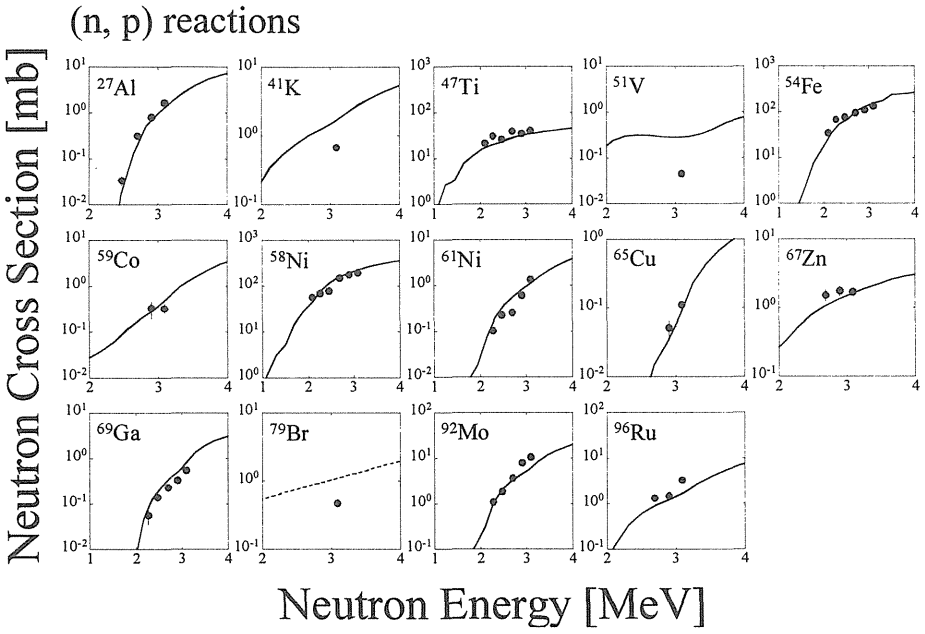

Fig.4.3-3(1) Cross section data for (n, p) reactions. Solid line and broken lines are evaluated data in JENDL-3.3 and FENDL/A-2.0 [11], except for ^{51}V (JENDL-3.2 [12]), ^{67}Zn, ^{69}Ga and ^{92}Mo (JENDL-AF96 [13]).

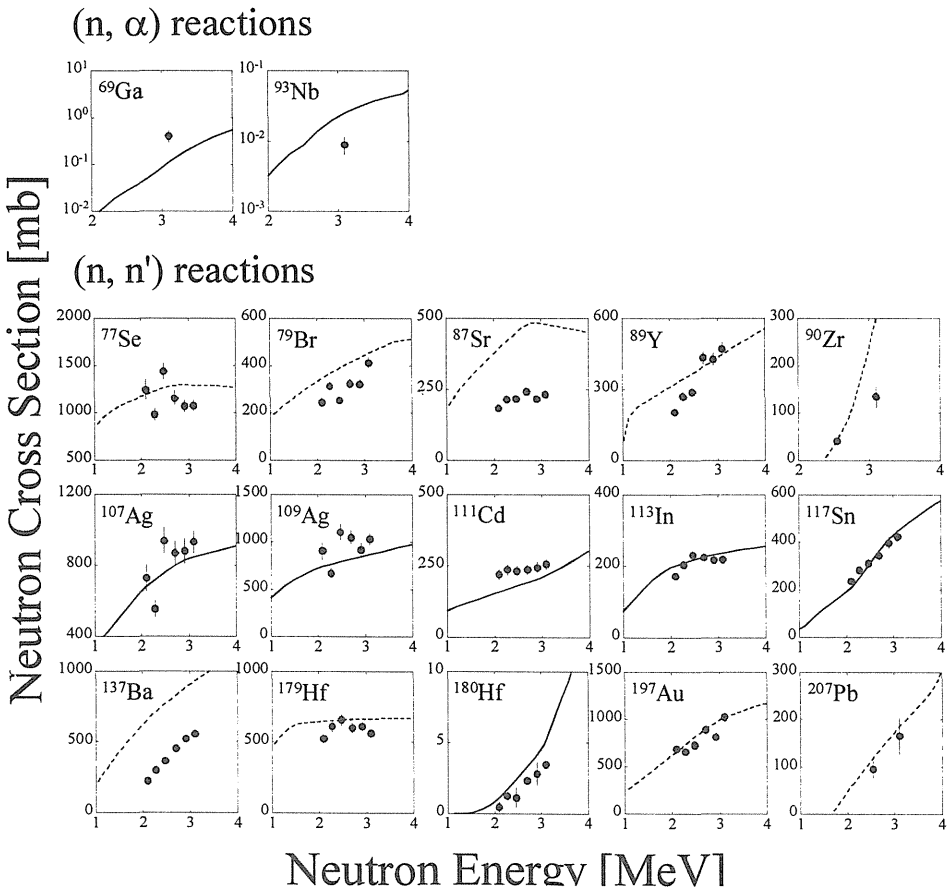

Fig. 4.3-3(2) Cross section data for (n, α) and (n, n') reactions. Solid line and broken lines are evaluated data in JENDL-AF96 and FENDL/A-2.0, except for ^{69}Ga (JENDL-3.3). The data for ^{90}Zr and ^{207}Pb were obtained by using pulsed neutron beam.

4.3.3. Conclusion

We could measure activation cross sections down to the level of sub-millibarns by using the pneumatic sample transport system, those down to about 50 mb by using pulsed neutron beam. The present results will soon be used for a proposal of the (n, p), and (n, n') systematics.

References

[1] OECD Nuclear Energy Agency (NEA), "CINDA 2003 (1988-2003)" France (2003).
[2] K. Shibata, T. Kawano, T. Nakagawa, et al., J. Nucl. Sci. Technol. **39**, 1125 (2002).
[3] Y. Kasugai, Y. Ikeda, H. Yamamoto, and K. Kawade, Ann. Nucl. Energy, **23**, 1429 (1996).
[4] Y. Kasugai, Y. Ikeda, H. Yamamoto, and K. Kawade, Ann. Nucl. Energy, **25**, 421 (1998).
[5] H. Sakane, M. Shibata, K. Kawade, Y. Kasugai, and Y. Ikeda, JAERI-conf 2000-005, 202 (2000).
[6] T. Shimizu, H. Sakane, S. Furuichi, et al., Nucl. Instr. Methods in press.
[7] T. Shimizu, H. Yamamoto, M. Kasaishi, et al., JAERI-Conf 2003-006, 138 (2003).
[8] T. Shimizu, H. Sakane, M. Shibata, K. Kawade, T. Nishitani, Ann. Nucl. Energy **31**, 975 (2004).
[9] T. Shimizu, H. Sakane, M. Shibata, K. Kawade, T. Nishitani, submitted to Ann. Nucl. Energy.
[10] K. Kawade, H. Sakane, Y. Kasugai, et al., Nucl. Instr. Methods **A496**, 183 (2003).
[11] A. B. Pashchenko, Summary Report for IAEA Consultants' Meeting on Selection of Evaluations for the FENDL/A-2.0 Activation Cross Section Library. INDC (NDS)-341, International Atomic Energy Agency (1996).
[12] T. Nakagawa, K. Shibata, S. Chiba, et al., J. Nucl. Sci. Technol., **32**, 1259 (1995).
[13] Y. Nakajima, Proc. 1990 Symposium on Nuclear Data, JAERI-M 91-032, 43 (1991).

4.4 Measurement of (n,2n) Reaction Cross Sections by Coincidence Detection of Emitted Two Neutrons with A Pencil-Beam DT Neutron Source

Isao MURATA, Motoyuki MITSUDA[1], Takashi NISHIO*, Yasuaki TERADA**, Akito TAKAHASHI, Kentaro OCHIAI[1], Fujio MAEKAWA[1], Takeo NISHITANI[1]

Department of Electronic, Information Systems and Energy Engineering, Osaka University, Suita, Osaka

[1]*Fusion Neutron Laboratory, Japan Atomic Energy Research Institute, Tokai-mura, Ibaraki*

4.4.1 Introduction

The (n,2n) reactions are of primary interest in the design of fusion reactor, because it is a neutron multiplication reaction and has a large cross section value in the energy range of several to 14 MeV. In the previous experiments, the cross section was measured mainly by the foil activation method. However, the measurement often became difficult unless appropriate radioisotopes were produced by the reaction. In other words, if a sample element includes isotopes of which the difference of the neutron number between any two isotopes is unity, the measurement is impossible in principle. To overcome this difficulty, there are some other methods available to obtain the cross section value. The most famous method is to measure neutron multiplication using a very large schintillator [1]. However, at present the accuracy of the method is not better than the foil activation method. Also the method is normally available for elements, i.e., an enriched sample should be prepared for measuring an isotope. Nevertheless, it can be said that mostly the cross sections of (n,2n) can be measured with this somewhat old method, unless minding the accuracy.

The focused point in the present study is the differential cross section, i.e., energy spectrum and angular distribution. With the above method, it is not possible to measure the neutron spectrum and angular distribution of neutrons emitted through (n,2n) reaction. Fortunately, the energy spectrum of the two neutrons is mostly predicted by an evaporation spectrum. But, for light elements, the energy spectrum might become complicated because the evaporation process may not be assumed for small cluster nuclei. For 14 MeV neutrons, it is generally known that there is weak angular dependence, i.e., forward oriented distribution on the angular differential cross section. However, for lights elements the detailed angular dependence is not yet found out. It must be crucial information to find out the nuclear reaction mechanism. The problem is that it is quite hard to extract and measure only the two neutrons emitted from (n,2n) reaction out of all the measured signals including strong background neutrons and other particles.

---

* *Present Adress: Kobe Steel, Ltd., Nada-ku, Kobe*

** *Present Adress: Siemens-Asahi Medical Technologies Ltd., Shinagawa, Tokyo*

In the present study, using a newly developed pencil-beam DT neutron source at fusion neutronics source (FNS), JAERI [2], a method was established to accurately measure the energy and angle dependent neutron spectrum of only the emitted two neutrons as well as its cross section with the coincidence detection technique, especially for light elements to examine their (n,2n) reaction mechanism. The method was at first validated by an experiment with a manganese sample [3,4], because the emitted neutron spectrum from ^{55}Mn(n,2n) reaction can be assumed to be an evaporation spectrum and the cross section value was well known by various experimental studies carried out so far. In the present paper a preliminary result of measurement for beryllium was also described. Beryllium is known to be the most important neutron multiplication material for the fusion reactor.

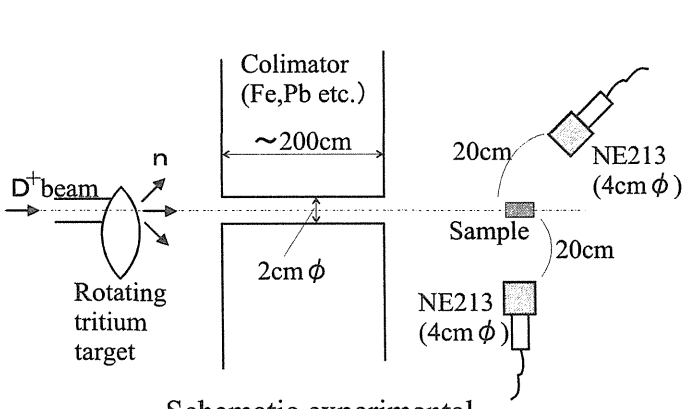

Schematic experimental arrangement.

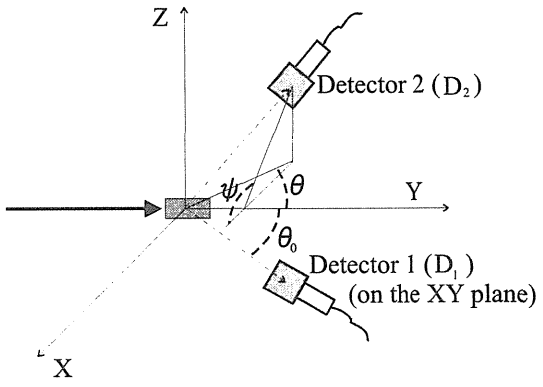

Details of the detector arrangement.

Fig. 4.4-1 Experimental arrangement.

4.4.2 Experimental

Measurement of (n,2n) reaction cross section is possible in principle with the coincidence detection technique for two neutrons emitted simultaneously. However, it is not easy to attain an acceptable signal to noise (S/N) ratio, because isotropically produced source neutrons, the great majority of which does not bombard the sample, act as a large amount of background signals in the measurement. One must shield detectors to prevent such neutrons from bombarding the detectors directly and/or indirectly. Thus it means that detectors cannot be arranged close to the sample. This is a significant problem to realize efficient coincidence detection of the two neutrons. The newly developed pencil-beam (2 cmϕ-collimated) DT neutron source at Fusion Neutronics Source (FNS) [2] of Japan Atomic Energy Research Institute (JAERI) can realize the measurement. The details of the experimental procedure can be found elsewhere [3,4]. A brief description is hence given here.

The schematic experimental arrangement is shown in Fig. 4.4-1. A small sample was positioned on the beam line at ~60 cm from the collimator, meaning that the sample was

placed at ~350 cm from the neutron source. The dimensions of the sample are 1.5 cmϕ3 cm long, so that the sample can be arranged just inside the neutron beam region. The neutron flux intensity at the sample, determined by Al foil, was 1×10^6n/sec/cm^2. Two spherical NE213 (4cmϕ) detectors were arranged on a spherical shell, the center of which is the sample, in order to measure simultaneously emitted two neutrons. The distance between the sample and the detector is 20 cm.

The measurement was carried out with the coincidence detection technique and n/γ pulse shape discrimination technique to exclude other pairs of simultaneously emitted particles than the two neutrons of (n,2n) reaction. The former is a technique to selectively measure two neutrons emitted simultaneously through the (n,2n) reaction by coincidence detection. The latter technique was employed to exclude coincident signals of n γ and γ γ pairs through nuclear reactions such as (n,n' γ), (n,2n γ) by discriminating the rise time spectrum of dynode signals.

As for the angular dependence, it is known that a slightly forward oriented distribution can be obtained if simultaneously emitted two neutrons are not distinguished. However, in the present measurement, the angular correlation of the two neutrons could be taken into account to yield accurate (n,2n) cross section because the two neutrons are measured separately with two detectors.

4.4.3 Data processing and correction

The net raw neutron spectrum is deduced by the following equation:

$$y=(y_{in,FG}-\alpha \cdot y_{in,BG})-\beta\,(y_{out,FG}-\alpha \cdot y_{out,BG}), \qquad (1)$$

where, y is the net raw FG spectrum, $y_{in,FG}$ and $y_{in,BG}$ the raw FG and BG spectra in sample-in measurement, $y_{out,FG}$ and $y_{out,BG}$ the raw FG and BG spectra in sample-out measurement, α the ratio of the gated width in the time difference spectrum of two anodes signals of the detectors, and β the normalization factor between the sample-in and -out measurements, respectively. This equation can be used for both detectors. Then the cross section can be obtained by the next equations:

$$N\,\sigma\,\phi\,\eta\,(d\Omega_1/4\pi)(d\Omega_2/4\pi)f_1 f_2' R_1 = y_1, \text{ for detector 1,} \qquad (2)$$
$$N\,\sigma\,\phi\,\eta\,(d\Omega_1/4\pi)(d\Omega_2/4\pi)f_2 f_1' R_2 = y_2, \text{ for detector 2,} \qquad (3)$$

where, N is the number of sample atoms, σ the (n,2n) cross section, ϕ the neutron flux at the sample, η the neutron multiplicity of (n,2n) reaction, = 2, $d\Omega_1$ and $d\Omega_2$ the solid angles of the detectors (1 and 2), f_1 and f_2 the efficiencies of the detectors, f_1' and f_2' the conditional

efficiencies of the detectors, R_1 and R_2 the response functions of the detectors, y_1 and y_2 the pulse height spectra of the detector (identical to y in Eq.(1)), respectively.

The obtained cross section should be corrected for the following problems. One is neutron multiple-scattering in the sample. Multiple-scattering due to incident neutrons as well as emitted neutrons through (n,2n) reaction should be taken into consideration. And the other is inter-detector scattering of neutrons produced in the sample. This means that sequential detections of a neutron in the two detectors can be recognized as a coincidence signal. These correction calculations were carried out with the Monte Carlo code MCNP-4B[5] and the correction factor was estimated to be about 10%.

More details about the data processing and correction are given in Refs. [3,4].

4.4.4 Results and discussion

4.4.4.1 Validation of the method with the result of Mn [3,4]

Figure 4.4-2 shows time difference spectrum between anode signals of the two NE213 detectors. A large peak corresponding to the FG signals is found at around 200 ns in the sample-in spectrum. Since correlated signals are detected almost simultaneously, a 200 ns delay is artificially added to one anode signal. In the sample-out spectrum, a very small peak around the same position as the FG peak is seen. This corresponds to detection of two coincident neutrons due to (n,2n) reaction induced at materials surrounding the sample and detectors or inter-detector scattering of neutron between the two detectors. The BG counts are successfully suppressed and a good S/N ratio is therefore achieved.

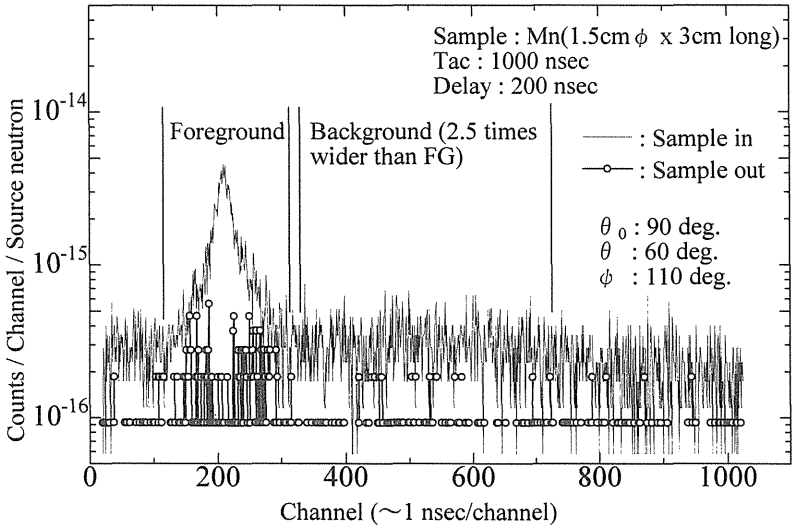

Fig. 4.4-2 Time difference spectrum between two NE213 detectors.

Figure 4.4-3 shows angular distribution for axial direction compared with the nuclear data of JENDL fusion file. It seems that one can see a slightly forward oriented distribution.

However, the accuracy is not so good as to conclude it. Nevertheless, the integral value, that is (n,2n) reaction cross section, is acceptable. This indicates that the present new measurement method is significantly successful. From the result of angular distribution for circumferential direction, it seems that there is no angular dependence. From these results, it is confirmed that the angular dependence is, if any, very weak. Thus, it is expected that one complete measurement for a medium-heavy element would become possible by several measurements.

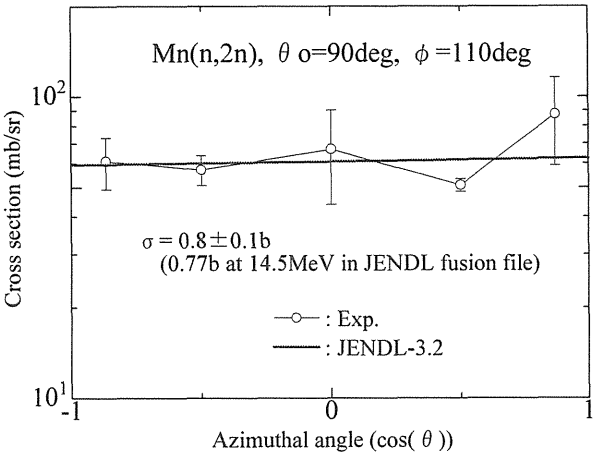

Fig. 4.4-3 Angular differential cross section of Mn(n,2n).

4.4.4.2 Test measurement of beryllium [6]

A measurement for beryllium was preliminarily carried out to roughly see the angle dependence of the energy spectrum. The results will be helpful for the coming next experiment. Figure 4.4-4 shows some neutron spectra for various angle pairs under the condition that one detector is fixed at 45 deg. The energy spectra did not vary very much with respect to the scattering angle. Also the estimated angular differential cross section at 45 deg. was fairly larger than the evaluation as in Fig. 4.4-5. The latter result seems to be a serious problem. However, the circumferential angle difference, ϕ , of two detectors is 180 deg. in the measurement, meaning that the cross section may become its maximum considering the circumferential symmetry. In this case, the experimental value can be larger than the evaluation. Another problem is the extrapolation of cross section in Fig. 4.4-5. From this figure, there exists a quite strong angular dependence, i.e., strong forward angle oriented spectrum. However, no measured values are given in this experiment around

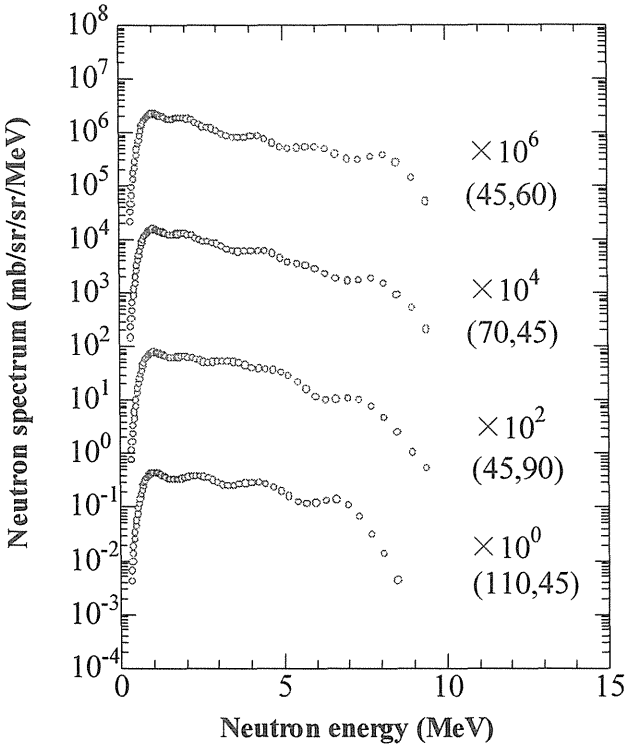

Fig. 4.4-4 Double angular differential neutron emission cross section of Be(n,2n) reaction. (θ_1, θ_2) means azimuthal angles of two NE213. detectors.

forward scattering angles. The extrapolation can thus cause a critical overestimation on the experimental value. It is concluded that more precise experiments of angular dependence are indispensable in the next machine time.

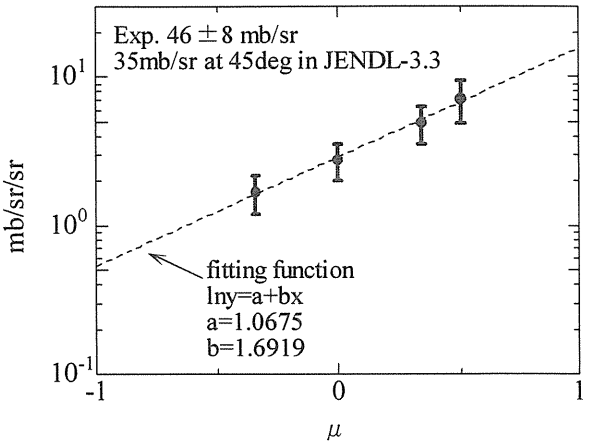

Fig. 4.4-5 Double angular differential cross section of Be(n,2n).

4.4.5 Conclusion

Using a newly developed pencil-beam DT neutron source at FNS, the method has been established to measure (n,2n) reaction cross section and its energy and angular distributions of simultaneously emitted two neutrons with the coincidence detection technique. In the present measurement, a cylindrical manganese, the (n,2n) cross section of which had been measured precisely with the foil activation method, was used to check the experimental method. From the results, it was confirmed that the present new method was basically functioning to measure only two neutrons emitted through (n,2n) reaction. Also, it was found that for Mn not so strong angular dependence was observed. It is therefore expected that complete measurement for a medium-heavy element and for stable-isotope producing element by (n,2n) reaction would become possible by several measurements. Also preliminary measurement was carried out for beryllium sample. As a result, the angular dependence of the cross section was quite large, however, the shape of the energy spectrum had little angular dependence. For beryllium further experiments are indispensable for more precise discussion.

References

[1] J. Frehaut, Nucl. Instr. Meth., **135**, 511 (1976).

[2] H. Sakane et al, Reactor Dosimetry: Radiation Metrology and Assessment, ASTM STP 1398, 375 (2001).

[3] I. Murata et al., Proc. 2000 Symposium on Nucl. Data, Tokai, JAERI-Conf 2001-006, 184 (2001).

[4] I. Murata el al., J. Nucl. Sci. and Technol., **Sup. 2**, 433 (2002).

[5] Briesmeister, J. F. (Ed.), "MCNP- A General Monte Carlo N-Particle Transport Code, Version 4B," LA-12625-M (1997).

[6] M. Mitsuda et al., Proc. 2002 Symposium on Nucl. Data, Tokai, JAERI-Conf 2003-006, 144 (2003).

4.5 DT Neutron Induced Charged-Particle Emission DDX of Beryllium

Isao MURATA, Keitaro KONDO, Satoshi TAKAKI, Hiroyuki MIYAMARU,
Akito TAKAHASHI, Kentaro OCHIAI[1], and Takeo NISHITANI[1]
Department of Electronic, Information Systems and Energy Engineering, Osaka University, Suita, Osaka
[1]*Fusion Neutron Laboratory, Japan Atomic Energy Research Institute, Tokai, Ibaraki*

4.5.1 Introduction

DT neutron induced double-differential charged-particle emission cross sections (DDXc) of fusion reactor materials are very important to evaluate the nuclear heating and material damages. However, only a few data have been accumulated since the measurement is difficult due to small cross sections of the reactions and high background. For fusion reactor development we should make a great deal of efforts to prepare DDXc data.

Up to this time several measurements have been carried out. Also in our group, measurements of DDXc of various materials for fusion reactor had been carried out continuously using the charged-particle spectrometer based on the two-dimensional analysis of energy and time-of-flight of emitted charged-particle at OKTAVIAN in Osaka University [1].

However, generally the experiments using an isotropic neutron source are very difficult, because background levels of neutron and secondary particles are considerably high. A detector must be shielded severely and set at a long interval from a measuring sample. As a result the S/N ratio becomes bad and the count rate decreases. Thus the new measurement technique to obtain more accurate data is needed.

In this study we developed a new measurement technique of DDXc using the pencil-beam DT neutron source in FNS. Using the present method we measured charged-particle emission DDX of beryllium, which was one of very important material for the blanket of a fusion reactor.

4.5.2 Experimental procedure

The pencil-beam DT neutron source in FNS realizes a perfectly collimated 2cm-ϕ neutron beam. An accelerated deuterium beam bombers a tritium target and 14-MeV neutrons are generated. A large shield structure consisted of Fe, Pb, Cd, and polyethylene is embedded into a concrete wall with a thickness of 2m in order to collimate the neutrons. There is a hole of 2cm in diameter pierced through the shield structure and the 2cm-ϕ neutron beam is extracted. Characteristics of the beam, such as beam intensity, beam profile and neutron background, were well investigated [2]. The neutron flux at the outside of the beam is about

1×10^{5}~10^{6} times lower than at the inside of the beam. Thus we can arrange a detector very close to a measurement sample without shield and therefore high S/N ratio and high counting rate can be achieved.

A measuring sample and detectors were located in an experimental vacuum chamber of 40cm-ϕ by 30cm in height. The chamber was set at the outlet of neutron beam. The distance of the neutron source and the sample was 380cm. We used a metal beryllium disc of 100μm in thickness and 3cm in diameter as the sample. Fig.4.5-1 shows the experimental arrangement.

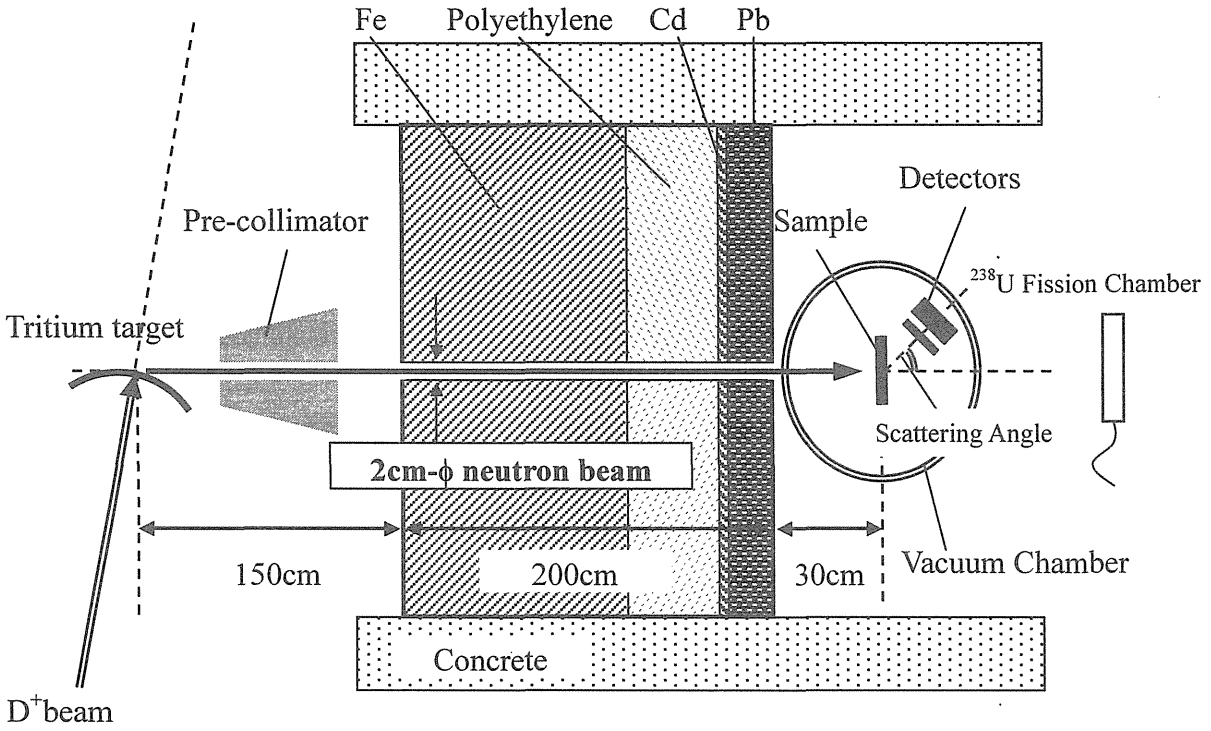

Fig. 4.5-1 Experimental arrangement

In the measurement of DDXc, we have to discriminate types of charged particles. We chose a telescope system with two silicon SSDs of ΔE and E for particle discrimination. The significantly low neutron background condition became possible to use SSD. The thicknesses of the ΔE and E detectors were 9.6μm and 700μm, respectively. The energy ratio of ΔE detector to E detector changes depending on type of charged-particles and their energy which relate to stopping power. A two-dimensional MCA was used in order to distinguish signals of interest. When measured pulses are plotted in two-dimensional space where the axes represent ΔE energy and E energy, the signals theoretically appear on specific lines for respective charged-particle types. Fig4.5-2 shows ideal two-dimensional plots according to energy distributions calculated by Bethe Formula for three different types of charged-particle.

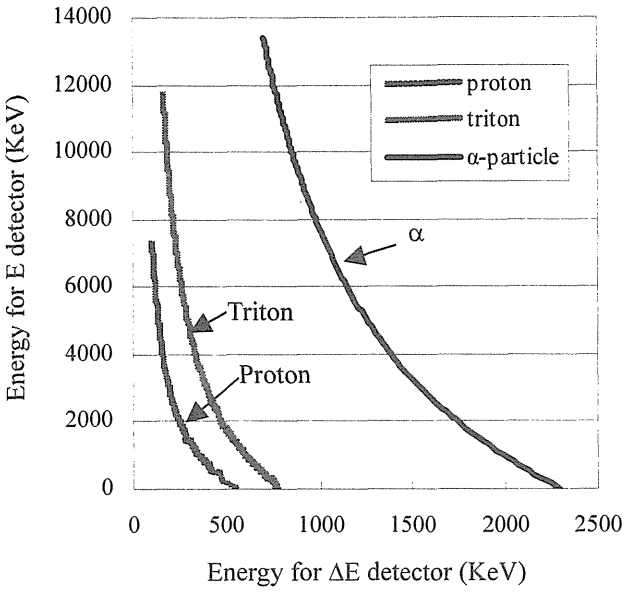

Fig. 4.5-2 Ideal 2D-plots for three different types of charged-particle.

Extracting the signals of interest and adding detected energies of two detectors we obtained the measured energy spectrum.

Because we use the coincidence detection technique, lower limit of the measurable energy for α-particle corresponds to lower threshold energy to penetrate ΔE detector. For the present ΔE detector the energy is around 2.3 MeV. In order to lower the energy, we utilized the anticoincidence alpha spectrum of ΔE detectors as the spectrum below the lower limit of coincidence measurement. The reasons why we could use the anticoincidence alpha spectrum was following;

1. The thickness of ΔE detector was extremely thin and therefore the detection energy for proton was up to about 600 KeV.
2. The background signals of α-particle in case of sample-out measurement were exceptionally low, which were only 10~15 counts per hour, although the background signals of ^{9}Be particles form elastic scattering couldn't be neglected and we had to subtract.

4.5.3 Data Analysis

In order to obtain the actual energy spectrum of emitted charged-particle the measured spectrum must be corrected for energy loss in the sample. The relationship between the actual spectrum and the measured spectrum is expressed in the following matrix equation;

$$\mathbf{A} = \mathbf{R} \cdot \mathbf{M}$$

where, **A** is the actual spectrum, **M** is the measured spectrum, **R** is the response function that represents effects of energy loss in the sample and broadening of angular resolution,

respectively. In the first we calculated the matrix **R** by using SRIM-2003 code [3] combined with our own making codes. Then the spectrum unfolding was carried out using our own making code based on *the spectrum type Bayes estimation method* and the actual energy spectrum was obtained [4][5].

The absolute DDX $\sigma(E_n \rightarrow E,\theta)$ [barn/sr/eV] is obtained by the following equation;

$$\sigma(E_n \rightarrow E,\theta) = \frac{R(E,\theta)}{k_{\Delta E} \cdot k_E \cdot \phi_n \cdot N \cdot d\Omega_{\Delta E} / 4\pi}$$

where, $R(E,\theta)$ is the energy spectrum, $k_{\Delta E}$ and k_E is the efficiency of the detectors (for charged-particle, $k \cong 1$), ϕ_n is the neutron flux at the sample, N is the number of beryllium atoms, $d\Omega_{\Delta E}$ is the solid angle of the ΔE detector, respectively. In the present study, ϕ_n was monitored with ^{238}U Fission Chamber relatively and determined absolutely by the foil activation method with Al and Nb.

4.5.4 Results and discussions

The measured 2D-spectrum at scattering angle of 30 degree in LAB-system is shown in Fig.4.5-3. Since detectors have finite energy resolution, the measured 2D-spectrum has also a broad energy resolution. The counting rate of sample-out measurement was only a few counts per hour so that it was not necessary to subtract the signals of sample-out measurement from the total signals. We can clearly extract α signals from ^{9}Be(n,xα) reactions. We can also observe tritium signals from ^{9}Be(n,t) reaction distinguished from α signals. Using the present method we can measure such a small DDXc for ^{9}Be(n,t) reaction. This fact suggests the superiority of the present method to other conventional methods.

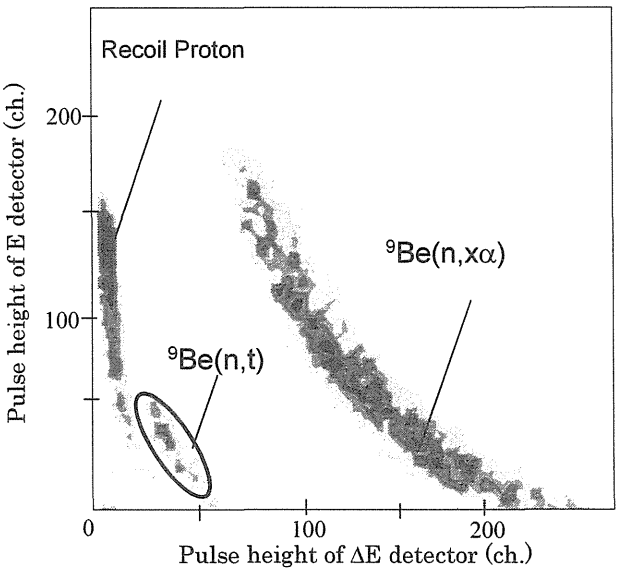

Fig.4.5-3 Measured 2-D spectrum of 9Be(n,CP) reactions at 30 deg.

Measured energy spectrum was obtained by extracting signals of interest. For lower energy spectrum, anti-coincidence spectrum was used. Fig. 4.5-4 shows the obtained measured spectrum.

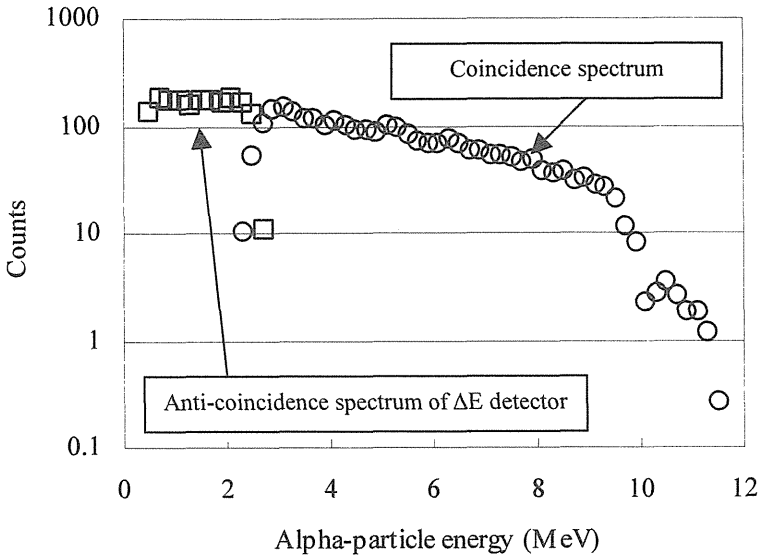

Fig. 4.5-4 Obtained measured spectrum for ^{9}Be(n,xα) reaction at 30deg

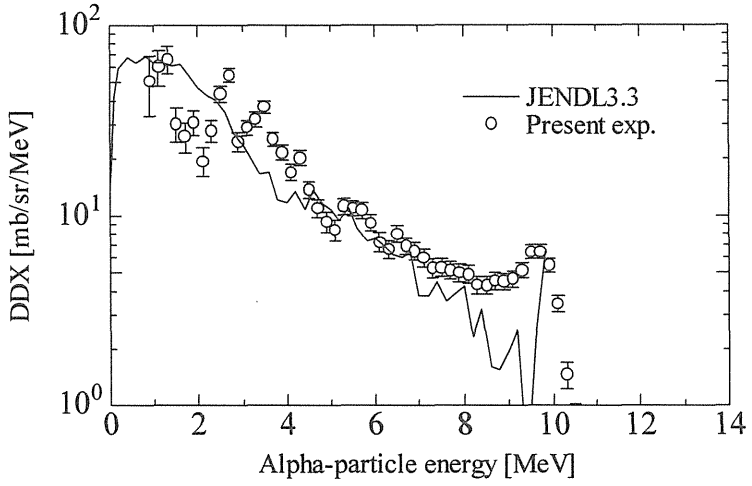

Fig. 4.5-5 Unfolded DDXc for ^{9}Be(n,xα) reaction at 30deg.

Figure 4.5-5 shows the unfolded DDXc for ^{9}Be(n,xα) reaction at 30deg. The evaluated data in JENDL 3.3 is also shown. Although the unfolded DDXc appears slightly different in the detail of structure, the ADX obtained by integrating DDXc over the energy well agrees with JENDL 3.3.

4.5.5 Conclusions

We developed a new measurement technique of DDXc using the pencil-beam DT neutron source and the counter telescope system with two silicon SSDs of ΔE and E for

particle discrimination. We carried out measurement of charged-particle emission DDX of beryllium and confirmed the superiority of the present method to other conventional methods. We are now analyzing the obtained data and comparing them with evaluated data and other experimental data.

References

[1] Takahashi, A., et al., "A Time-of-Flight Spectrometer with Pulse-Shape Discrimination for the Measurement of Double-Differential Charged-Particle Emission Cross Sections", Nucl. Instr. Meth., **A401**, 93(1997)

[2] Sakane, H., et al., "A Study on 14 MeV Neutron Beam Characteristics and its Applications", Reactor Dosimetry: Radiation Metrology and Assessment, ASTM STP 1398, John G. Williams, et al., Eds., American Society for Testing and Materials, West Conshohocken, PA,(2001).

[3] SRIM.EXE, (C) 1984-2000, International Business Machines Corporation, James F. Ziegler. http://www.srim.org/

[4] Iwasaki, S., "A New Approach for Unfolding PHA Problems Based Only on the Bayes' Theorem", Proc. 9th International Symposium on Rector Dosimetry, Prague, Chezk Republic, Sep. 2-6, 1996, p.245, World Scientific (Singapore, 1998).

[5] Takagi, H., et al., "Measurement of Double Differential Cross Section of Charged Particle Emission Reactions by Incident DT neutrons -Correction for Energy Loss of Charged Particle in Sample Materials-", Proc. 1999 Symposium Nucl. Data, Nov. 18-19, 1999, JAERI, Tokai, JAPAN, JAERI-Conf 2000-005 (2000).

4.6 Measurement of deuteron-induced activation cross section for IFMIF accelerator structural materials in 22-40 MeV region

Makoto NAKAO, Jun-ichi HORI, Kentaro OCHIAI, Satoshi SATO, Michinori YAMAUCHI, Noriko S. ISHIOKA[1], Takeo NISHITANI

Fusion Neutron Laboratory, Japan Atomic Energy Research Institute, Tokai, Ibaraki

[1]Department of Ion-beam-applied Biology, Japan Atomic Energy Research Institute Takasaki, Gunma

4.6.1 Introduction

The IFMIF (International Fusion Materials Irradiation Facility) is an accelerator-based D-Li neutron source designed to produce an intense neutron field for testing fusion reactor candidate materials. The IFMIF has two 40 MeV deuteron linear accelerators with each 125 mA beam current [1]. In the design of the IFMIF, long-term operation with total facility availability of at least 70 % is conceived. However, activation of the structural materials along the beam transport lines by deuteron beam loss limits maintenance and makes long-term operation difficult. Thus the accurate estimation of deuteron-induced activity and the selection of structural materials are important in order to determine the beam loss criteria.

In this work, measurements of deuteron-induced activation cross sections for aluminum, copper and tungsten were performed. Aluminum is the main component of the beam tube and chamber. Copper is used in the cavity walls, electrodes and magnetic conductors. For beam slits and coating to protect the beam facing materials, high-Z materials (tantalum, gold, tungsten, etc) are candidate materials.

4.6.2 Experiment and Data processing

Activation cross sections were measured by using a stacked-foil technique. The stacked-foils consisted of natural composition aluminum, copper and tungsten with chemical purity more than 99.95 %. Each thickness of foil was 200 μm for Al, 25 μm for Cu and 20 μm for W. The stacked-foils were wrapped in aluminum sheet with a thickness of 10 μm and irradiated with 35 MeV and 50 MeV deuteron beam (current=0.1 μA) at the AVF cyclotron in TIARA facility, JAERI. After suitable cooling time, the decayed gamma rays emitted from the irradiated foils were measured by a calibrated Ge detector and the induced activities were obtained for ^{27}Mg, ^{24}Na, $^{61, 64}$Cu. $^{62, 63}$Zn, $^{181\text{-}184, 186}$Re, ^{187}W and ^{65}Zn.

The energy degradation along the stack and the effective deuteron energy at the middle position of each foil were estimated by IRACM code [2]. The number of incident deuteron on each stacked-foil was determined from ^{65}Zn activities observed by the ^{nat}Cu(d,x)^{65}Zn reaction cross section data reported by Takács et al.[3]. The elemental cross sections were derived

from the induced activities and the number of incident deuteron.

4.6.3 Results

The cross sections for the twelve radioactive nuclei were measured and compared with previous ones by other groups and the data in ACSELAM library calculated by ALICE-F code [4]. Because the cross sections in ACSELAM library are given for each isotope target, the cross sections measured in this work were normalized by weighting with natural abundance.

The comparison of the present cross sections with other experimental ones and the data in ACSELAM library for ^{27}Mg and ^{24}Na are shown in Figure 4.6-1 and 2. For ^{27}Mg, there is only one experimental data reported by Wilson et al. [5] in low energy region. ACSELAM were smaller than the present result by a factor of 1.3-2.0. For ^{24}Na, the present results were in agreement with the data by Takács et al.[3], Martens et al.[6], and Michel et al.[7] within experimental error. On the other hand the data in ACSELAM were about 1 order lower than the experimental ones.

Figure 4.6-3,4,5,6 show the present results for the ^{nat}Cu(d,x)^{61}Cu($T_{1/2}$=3.33h), ^{64}Cu($T_{1/2}$=12.7h), ^{62}Zn($T_{1/2}$=9.19h) and ^{63}Zn($T_{1/2}$=38m) reactions with other experimental ones and the data in ACSELAM library. There are two experimental data reported by Bartell et al.[8] and Fulmer et al.[9] on those reactions. The data reported by Flumer and ACSELAM resembled the present results in shape. In the case of ^{61}Cu and ^{62}Zn the values of these become higher than the present results by a factor of 2-4. In the case of ^{64}Cu and ^{63}Zn the values of these and the present results were in agreement within 40 %.

Figure 4.6-7,8,9,10,11,12 show the present results for the ^{nat}W(d,x)^{181}Re($T_{1/2}$=19.9h), ^{182g}Re($T_{1/2}$=2.67d), ^{182m}Re($T_{1/2}$=12.7h), ^{183}Re($T_{1/2}$=70d), ^{184g}Re($T_{1/2}$=38d), ^{184m}Re($T_{1/2}$=169d), ^{186}Re($T_{1/2}$=3.78d) and ^{187}W($T_{1/2}$=23.72h) reactions with other experimental ones and the data in ACSELAM library. In the energy region of 22-40MeV, there is no experimental data. For ^{181}Re, $^{182m+g}$Re and ^{183}Re, the present data and the data in ACSELAM were about same shapes and in agreement within 30 %. For $^{184m+g}$Re, the present data were different from ACSELAM in shape and became higher than ACSELAM by a factor of 1.5-7. For ^{186}Re, the present results showed decreasing tendency above 24 MeV and were 3 times as low as the data in ACSELAM at the maximum though the experimental ones reported by Pement et al.[10], Nassiff et al.[11], and Zhenlan et al.[12] were close to ACSELAM below 10 MeV. For ^{187}W, the present data and other experimental data reported by Baron et al.[13] and Andelin et al.[14] were different from the data in ACSELAM in shape. The reason of this difference is that ^{187}W could be produced by not only ^{186}W(d,p) but also ^{186}W(n,γ) reaction and the latter reaction was occurred by secondary low-energy neutron. The experimental results obtained by adopting an activation method include the component via the (n, γ) reaction. On the other

hands, the data in ACSELAM were calculated for only (d,p) reaction.

4.6.4 Summary

The activation cross-sections for the deuteron-induced reactions have been obtained for Al, Cu and W in 22-40 MeV regions and compared with previous experimental ones and the data in ACSELAM library. For ^{27}Mg, ACSELAM were smaller than the present result by a factor of 1.3-2.0. For ^{24}Na, ACSELAM resembled experimental values in shape but were lower than these by about 1 order. For ^{61}Cu, ^{64}Cu, ^{62}Zn and ^{63}Zn, the present results resembled other experimental data and ACSELAM in shape. In the case of ^{61}Cu and ^{62}Zn, ACSELAM became higher than the present results by a factor of 2-4. In the case of ^{64}Cu and ^{63}Zn, ACSELAM and the present results were in agreement within 40 %. For ^{181}Re, $^{182m+g}$Re and ^{183}Re, the present data and the data in ACSELAM were about same shapes and in agreement within 30 %. For $^{184m+g}$Re, ^{186}Re and ^{187}W, the data in ACSELAM were different from the present data about 1.5-7 times.

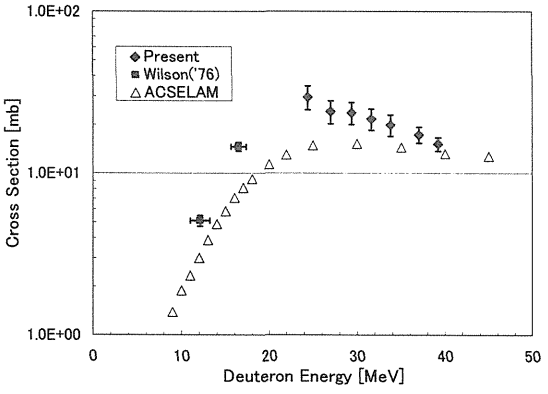

Fig. 4.6-1 Cross sections for the ^{27}Al(d,2p)^{27}Mg

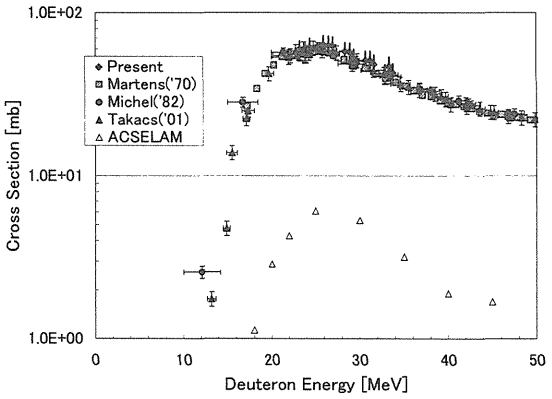

Fig. 4.6-2 Cross sections for the ^{27}Al(d,x)^{24}Na

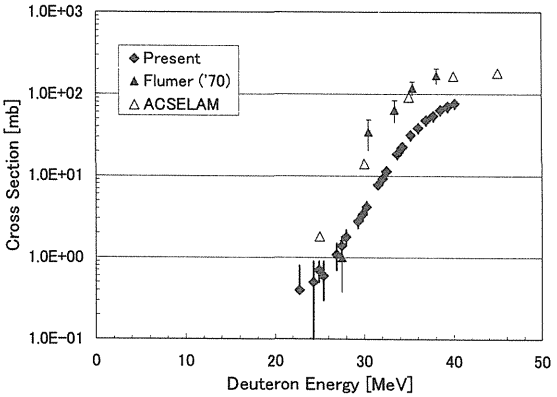

Fig. 4.6-3 Cross sections for the ^{nat}Cu(d,x)^{61}Cu

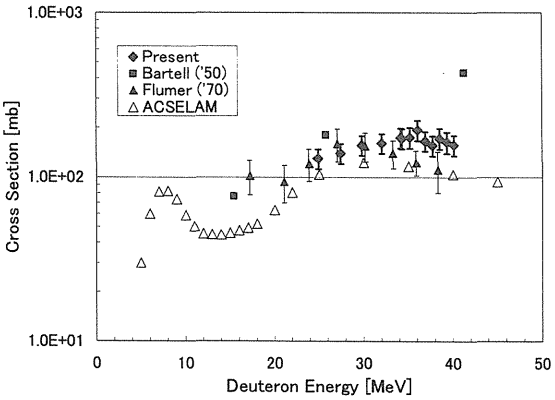

Fig. 4.6-4 Cross sections for the ^{nat}Cu(d,x)^{64}Cu

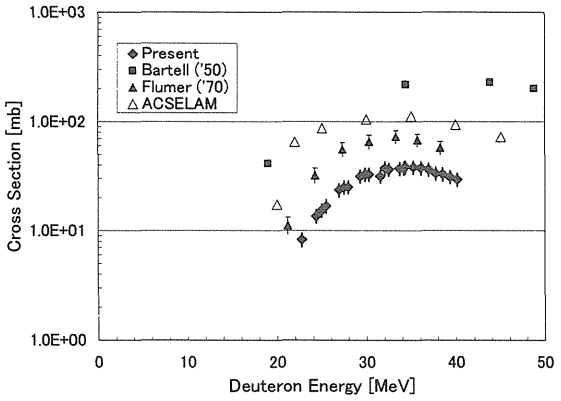

Fig. 4.6-5 Cross sections for the $^{nat}Cu(d,x)^{62}Zn$

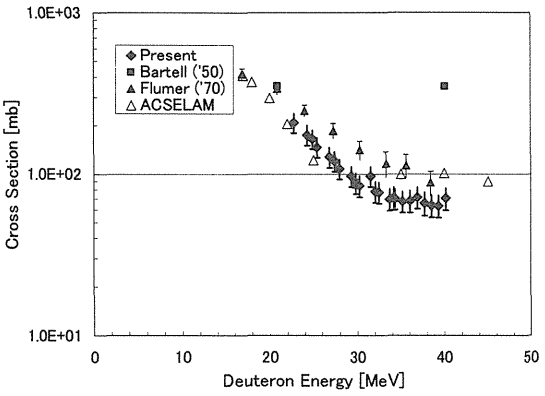

Fig. 4.6-6 Cross sections for the $^{nat}Cu(d,x)^{63}Zn$

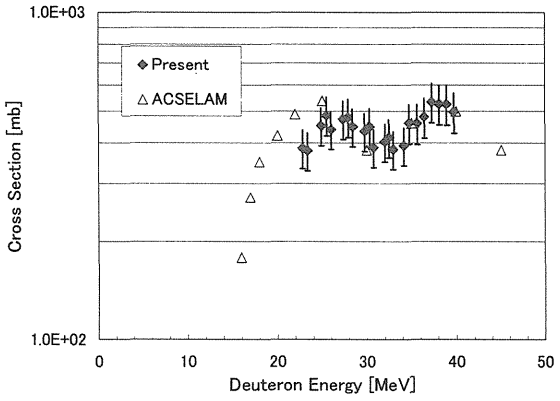

Fig. 4.6-7 Cross sections for the $^{nat}W(d,x)^{181}Re$

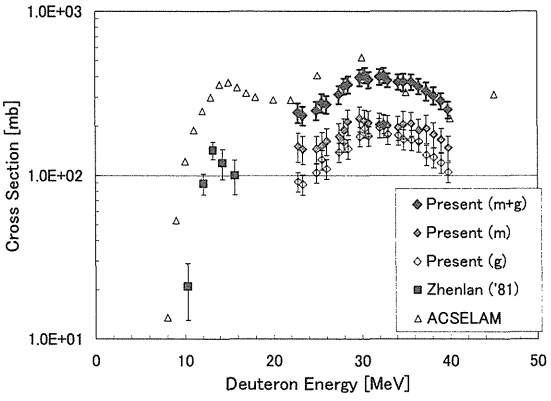

Fig. 4.6-8 Cross sections for the $^{nat}W(d,x)^{182}Re$

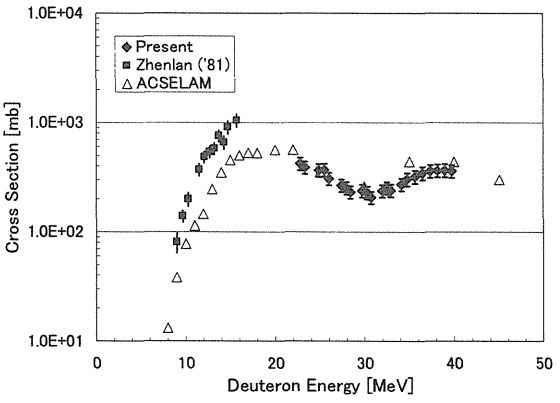

Fig. 4.6-9 Cross sections for the $^{nat}W(d,x)^{183}Re$

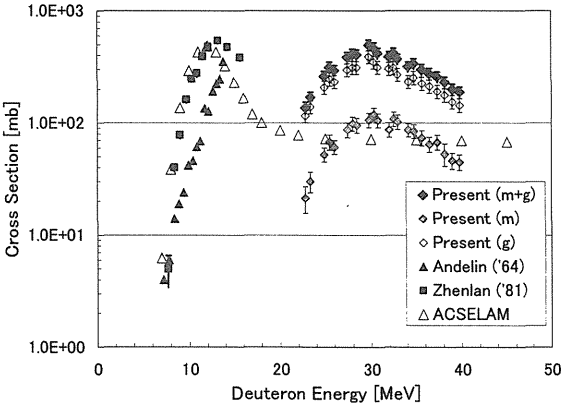

Fig. 4.6-10 Cross sections for the $^{nat}W(d,x)^{184}Re$

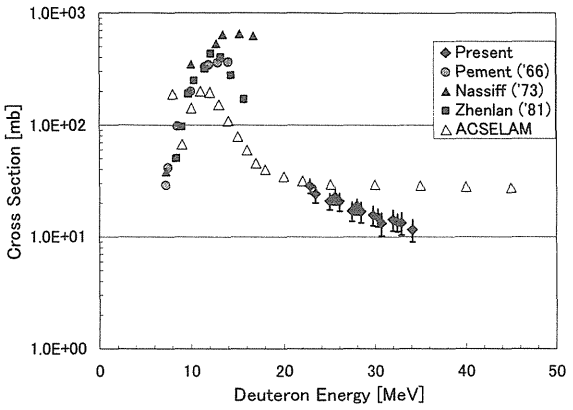

Fig. 4.6-11 Cross sections for the $^{nat}W(d,x)^{186}Re$

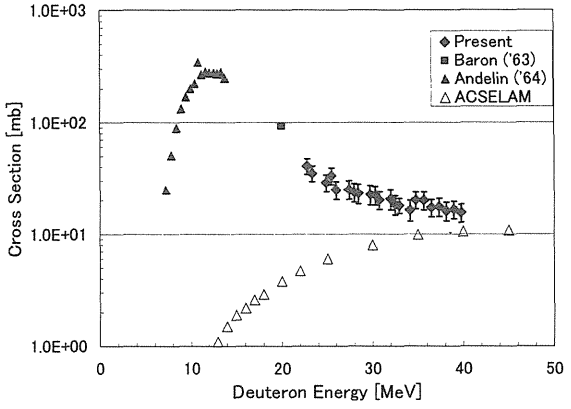

Fig. 4.6-12 Cross sections for the $^{nat}W(d,x)^{187}W$

References

[1] IFMIF International Team, "IFMIF-KEP; International Fusion Materials Irradiation Facility key element technology phase report," JAERI-Tech 2003-005 (2003).

[2] S. Tanaka, M. Fukuda, K. Nishimura, *et al.*, "IRACM: A Code System to Calculate Induced Radioactivity Produced by Ions and Neutrons," JAERI-Data/Code 97-019 (1997).

[3] S. Takács, et al., Nucl. Inst. Meth., **B 174**, 235-258 (2001).

[4] T. Fukahori, Proc. of the Specialists' Meeting on High Energy Nuclear Data, Tokai, October 3-4, 1991, JAERI-M 92-039. 114-122 (1992)

[5] R. L. Wilson, et al., J. Phys. Rev., **C13**, 976 (1976).

[6] U. Martens, G. W. Schweimer, J. Zeitschrift für Physik, **233**, 170 (1970).

[7] R. Michel, et al., EXFOR No. A0158 (1982).

[8] F. O. Bartell, et al., Phys. Rev., **80**, 1006 (1950).

[9] C. B. Fulmer, et al., Nucl. Phys., **A155**, 40 (1970).

[10] F. W. Pement and R. L. Wolke, Nucl. Phys., **86**, 429 (1966).

[11] S. J. Nassiff and H. Munzel, Radiochim. Acta., **19**, 97 (1973).

[12] T. Zhenlan, et al., Chinese Nucl. Phys., **3**, 242 (1981).

[13] N. Baron, B. L. Cohen, Phys. Rev., **129**, 2636 (1963).

[14] R. L. Andelin, et al., EXFOR C0722 (1964).

4.7 Lifetime Measurement of Excited States in ^{68}Cu

Tetsuro ISHII, HOU Long, Jun-ichi HORI[1], Masato ASAI, Kengo OGAWA[2], Hitoshi NAKADA[2]

Advanced Science Research Center, Japan Atomic Energy Research Institute, Tokai, Ibaraki

[1]Fusion Neutron Laboratory, Japan Atomic Energy Research Institute, Tokai, Ibaraki

[2]Department of Physics, Chiba University, Inage, Chiba

4.7.1 Introduction

The $^{68}_{28}Ni_{40}$ nucleus has doubly magic properties, and thus, nuclei around ^{68}Ni provides important knowledge of the nuclear shell structure.[1,2] In the $^{68}_{29}Cu_{39}$ nucleus, the proton(π) $p_{3/2}$ and the neutron(ν) $p_{1/2}$ orbitals lie near the Fermi surface. Therefore, the 1^+ ground state and the 2^+ first excited state in ^{68}Cu are expected to have a large component of the $\pi p_{3/2}\nu p_{1/2}^{-1}$ configuration. This simple configuration gives an insight into the nuclear structure in the neutron-rich Ni region. In particular, the reduced M1 transition probability between the 2^+ and the 1^+ states, B(M1;$2^+\rightarrow1^+$), provides a good test of a shell model calculation. Furthermore, this B(M1) value gives information on the core excitation.

In the present study, we have carried out a decay experiment of ^{68m}Cu produced by the ^{68}Zn(n,p) reaction using 14 MeV neutrons. By measuring the lifetime of the first excited state in ^{68}Cu, we obtained a small B(M1;$2^+\rightarrow1^+$) value. We show that this B(M1) value can be reproduced by a parameter-free shell model calculation taking the inert core as ^{68}Ni.

4.7.2 Experiments

The ^{68m}Cu source ($T_{1/2}$=3.75 min) was produced by the ^{68}Zn(n,p) reaction at FNS. Three ^{68}Zn metal targets of 0.2 g and 10 mm in diameter were prepared from the 99.4% enriched ^{68}ZnO powder by electrolysis. The ^{68}Zn target was irradiated by 14 MeV neutrons at a place of about 5×10^9 cm^{-2}s^{-1} neutron flux. The target was irradiated for 10 min and then transferred through a pneumatic tube to the outside of the irradiation room. The irradiated target was cooled for about 2min. Thus, the cycle of 10 min-irradiation, 2 min-cooling, and 8 min-measurement was repeated using three ^{68}Zn targets. Since the production cross section of ^{68m}Cu is 5 mb [3], the activity of the ^{68m}Cu source was about 30 kBq at the beginning of the measurement.

Lifetimes of excited states in ^{68}Cu were measured using two BaF_2 detectors of 25 mm in diameter and 10 mm in thickness. These detectors were placed face to face at a distance of 20 mm and the ^{68m}Cu source was placed at the center between them. A β-ray absorber made of a 3.5 mm-thick aluminum plate was attached to both of the detectors. The lifetimes were also measured by another detector configuration to reduce backscattering γ rays

between the BaF_2 detectors; the BaF_2 detectors were placed at 90° and a 3 mm thick lead absorber was placed between them.

The BaF_2 scintillator was mounted on a Hamamatsu-H3378 photomultiplier tube and the time pickoff signals were generated by an ORTEC-583 constant fraction discriminator. An ORTEC-567 TAC was employed and was calibrated using an ORTEC-462 time calibrator. The γ-γ-t coincidence data were recorded event by event. An energy resolution was 9% for the 570 keV γ ray of ^{207}Bi. A typical time resolution of this system was 130 ps at FWHM for the 1173-1332 keV γ-ray cascade of ^{60}Co.

A γ-ray singles measurement was also performed in order to obtain the γ-ray energies and intensities in ^{68}Cu using an n-type Ge detector of 33% relative efficiency. The distance between the source and the surface of the detector was 102 mm. No β-absorber was placed on this detector. The detection efficiency of the Ge detector was calibrated using a standard source of ^{152}Eu, ^{133}Ba, and ^{207}Bi, and was corrected for the self absorption in the ^{68}Zn target.

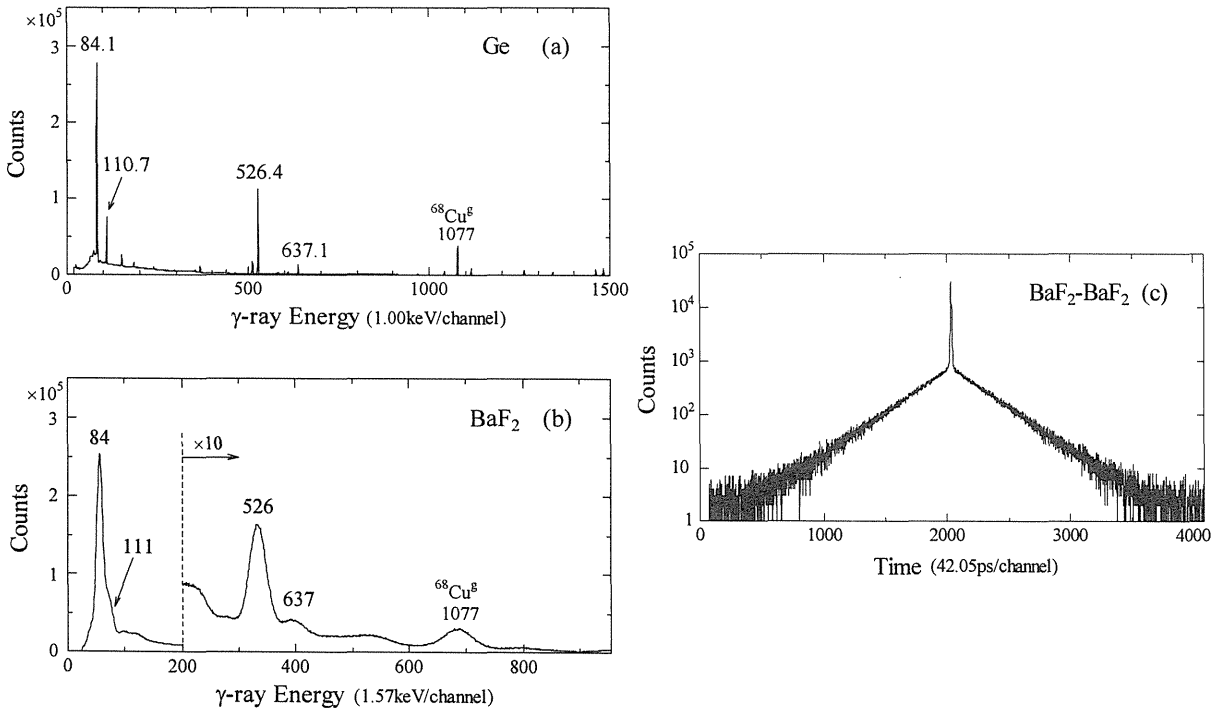

Fig. 4.7-1 (a) A γ-ray singles spectrum measured with a Ge detector. The γ-ray energies are depicted for the transitions descending from ^{68m}Cu. The 1077 keV γ ray follows the β decay of the ground state in ^{68}Cu.

(b) A γ-ray singles spectrum measured with a BaF_2 detector.

(c) A time spectrum measured by the BaF_2- BaF_2-t coincidence with no gates on γ rays.

4.7.3 Results

Figures 4.7-1(a) and -1(b) show γ-ray singles spectra measured with the Ge detector and with the BaF_2 detector, respectively. Figure 4.7-1(c) shows a time spectrum measured with the BaF_2 detectors. The decay scheme of ^{68m}Cu is shown in Fig. 4.7-2. Coincidence relationships measured in the present work are consistent with the previous scheme.[4,5]

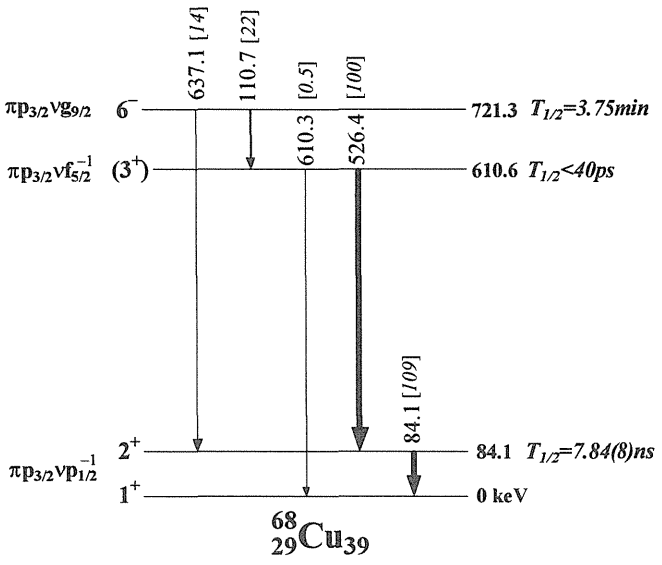

Fig. 4.7-2 A decay scheme of ^{68m}Cu. Relative intensities are shown in brackets.

Decay curves for the 84 keV level were obtained by setting gates on a combination of γ-ray energies measured with the BaF_2 detectors, shown in Figure 4.7-3(a). The experimental data were fitted with an exponential decay curve by a least squares method and the fitted lines are drawn in Fig. 4.7-3(a) in the range where the experimental data were used as the input values. We deduced the lifetime of the 84 keV level from the slopes of these fitted lines as well as from those of the decay curves gated on 111-84 keV. All the values of the slopes for the six decay curves are the same within measured uncertainties. Consequently, we determined that the lifetime of this level is $T_{1/2}$=7.84(8) ns. This error was estimated from the spread of all the values obtained in the experiment and from the variation of the values resulting from changing the fitting range.

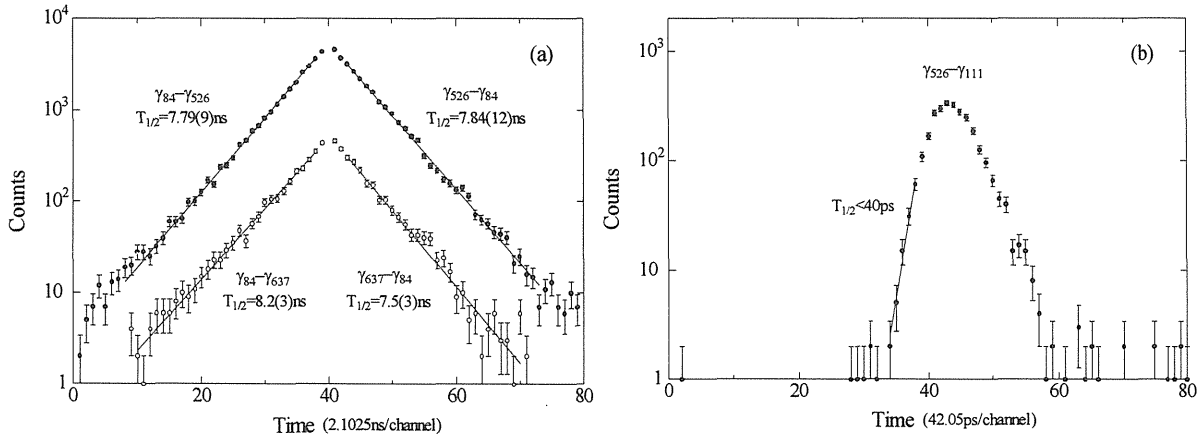

Fig. 4.7-3 (a) Decay curves due to the lifetime of the 84 keV level. The lines fitted to an exponential decay are drawn in the fitting ranges. (b) A time spectrum for the 611 keV level. The slope of the line drawn in this figure gives an upper limit for the lifetime of the 611 keV level.

Figure 4.7-3(b) shows a time spectrum obtained by setting the gate on the combination of the 526 keV energy (start signal) and the 111 keV energy (stop signal). The slope of the line drawn in this figure allows us to deduce an upper limit of 40 ps for the halflife of the 611 keV level.

4.7.4 Discussion

The B(M1;$2^+ \rightarrow 1^+$) value of the 84 keV transition is derived from the measured lifetime and the M1/E2 mixing ratio of this transition. The internal conversion coefficient of the 84keV transition is obtained as α_T=0.05(4) from the γ-ray intensity balance measured in the present work. Thus, we regard this transition as a pure M1 multipolarity; a theoretical α_T is 0.086 and 1.18 for a pure M1 and E2 transition, respectively. Then, the B(M1;$2^+ \rightarrow 1^+$) value is obtained as 0.00777(8) μ_N^2, or 1/230 W.u.

This B(M1) value is compared with a shell model calculation which takes the core to be ^{68}Ni and uses experimental g-factors of neighboring nuclei. The B(M1) value of the 84 keV transition between the $\pi p_{3/2} \nu p_{1/2}^{-1}$ doublets is calculated as [6]
B(M1;$2^+ \rightarrow 1^+$) =$3/(4\pi) \times 3/8 \times (g_\pi - g_\nu)^2$ =0.043 μ_N^2, where g_π=1.893 μ_N and g_π=1.202 μ_N are taken from the experimental values of the $3/2^-$ ground state in $^{69}_{29}Cu_{40}$ and the $1/2^-$ ground state in $^{67}_{28}Ni_{39}$, respectively.[7] This calculation reproduces a small B(M1) value, which originates from the cancellation of $g_\pi - g_\nu$.

The g-factor of the 1^+ ground state in ^{68}Cu was also measured recently by a laser-ion-source technique to be +2.48(2)(7) μ_N.[8] This g-factor is calculated as
g(1^+) =$1/4 \times (5g_\pi - g_\nu)$ =+2.07 μ_N. Thus, the calculation in the $\pi p_{3/2} \nu p_{1/2}^{-1}$ model space provides a good description of these M1 matrix elements in ^{68}Cu, using no free parameters. However, it is difficult to adjust the calculation more accurately for both the B(M1) value and the g-factor by only changing the g_π and g_ν effectively. This difficulty indicates a limit of this calculation using a minimum model space.

We have further studied the nuclear structure of ^{68}Cu by a shell model calculation in a fp model space $f_{7/2}^{(-r)} p_{3/2} f_{5/2} p_{1/2}^{(n+r)}$ (r=0,1). In this calculation, two-body interactions derived from the folded diagram theory were used and single particle energies were adjusted to reproduce low-lying levels in ^{67}Ni, $^{68, 69}$Cu. This calculation gives a small B(M1) value of 0.070 μ_N^2 and a large g(1^+) value of 2.60 μ_N. Although the experimental B(M1) value is still smaller than this calculated result, the calculation may be improved by extending the model space to include the excitation to a $g_{9/2}$ orbital.

4.7.5 Conclusion

We have measured the lifetime of the first excited state in ^{68}Cu through the γ decay of ^{68m}Cu produced by the ^{68}Zn(n,p) reaction using 14 MeV neutrons. We obtained a small B(M1) value between the $\pi p_{3/2}\nu p_{1/2}^{-1}$ doublet states in ^{68}Cu. A parameter-free shell model calculation taking the core as ^{68}Ni gives a good prediction of this B(M1) value by using experimental g-factors of the neighboring nuclei.

References

[1] T. Ishii, M. Asai, I. Hossain, et al., Phys. Rev. Lett. **81**, 4100 (1998).
[2] T. Ishii, M. Asai, A. Makishima, et al., Phys. Rev. Lett. **84**, 39 (2000).
[3] K. Kawade, H. Yamamoto, T. Yamada, et al., JAERI-M **90-171**, 1 (1990).
[4] D.L. Swindle, N.A. Morcos, T.E. Ward, et al., Nucl. Phys. **A185**, 561 (1972).
[5] V.K. Tikku and S.K. Mukherjee, J. Phys. G **1**, 446 (1975).
[6] R.D. Lawson, Theory of the Nuclear Shell Model (Clarendon press, Oxford, 1980).
[7] J. Rikovska, T. Giles, N.J. Stone, et al., Phys. Rev. Lett. **85**, 1392 (2000).
[8] L. Weissman, U. Köster, R. Catherall, et al., Phys. Rev. C **65**, 024315 (2002).

5. Shielding Experiments and Analyses

5.1 Double Bent Duct Streaming Experiment and the Analysis

Michinori YAMAUCHI, Kentaro OCHIAI, Yuichi MORIMOTO, Masayuki WADA, Satoshi SATO and Takeo NISHITANI

Fusion Neutronics Laboratory, Japan Atomic Energy Research Institute, Tokai, Ibaraki

5.1.1 Introduction

There are several penetrations such as diagnostics port, neutral beam injector (NBI) port, divertor port etc. through the shield in fusion reactors. From the viewpoint of the global shield of the reactors, it is important to investigate the influence of neutron streaming through those ports on the radiation dose. Previously, streaming experiments for straight ducts were successfully conducted with the FNS (Fusion Neutronics Source) facility at the Japan Atomic Energy Research Institute (JAERI) for the shielding design of ITER/EDA[1-3], however, the streaming effects of a bent duct had not been investigated. Thus, in order to study the behavior of the neutrons streaming through a dogleg duct, an experiment was conducted for a doubly bent duct with the rotating neutron target (RNT) of the FNS/JAERI.

Analyses of the experiment were carried out with the continuous energy Monte Carlo codes MCNP-4C[4], which had been used for miscellaneous radiation shielding calculations in the design of ITER/EDA. The aim of the analyses was to study the dogleg duct streaming effect on the local nuclear responses, and demonstrate the capability of the Monte Carlo transport calculations in the design of the fusion reactor shielding. Two sets of nuclear data FENDL/2 [5] and JENDL-3.3[6] were employed for the study. This report describes the experimental procedures, the measured data and the results of the analysis.

5.1.2 Experiment

(1) Arrangement and measurement

The experiment was conducted with the FNS facility at JAERI. The target could provide a neutron yield as large as about 4×10^{12} n/s at full beam current. The layout of the room and the experimental assembly are shown in Fig.5.1-1. A doubly bent duct 300mm × 300mm in cross section was formed through the assembly. The first horizontal leg of the duct was set as high as the D-T neutron source. The second leg was connected vertically to the first with a right angle, and the third was horizontally to the second. The lengths of the legs were 1150 mm, 600 mm and 650 mm respectively.

Neutron spectra above 2MeV were measured at several positions by a spherical NE213 scintillation spectrometer 40 mm in diameter. The pulse height spectrum of recoil protons

which represent neutron events was unfolded with the FORIST code[7] to obtain the neutron energy spectrum. The reactions of $^{93}Nb(n,2n)^{92m}Nb$, $^{115}In(n,n')^{115m}In$ and $^{197}Au(n,\gamma)^{198}Au$ were employed as neutron activation dosimeters. The first reaction is effective to evaluate the 14 MeV neutron flux, the second is sensitive to fast neutrons above 1 MeV, and the third helps to understand the amount of the thermal and epithermal neutron flux.

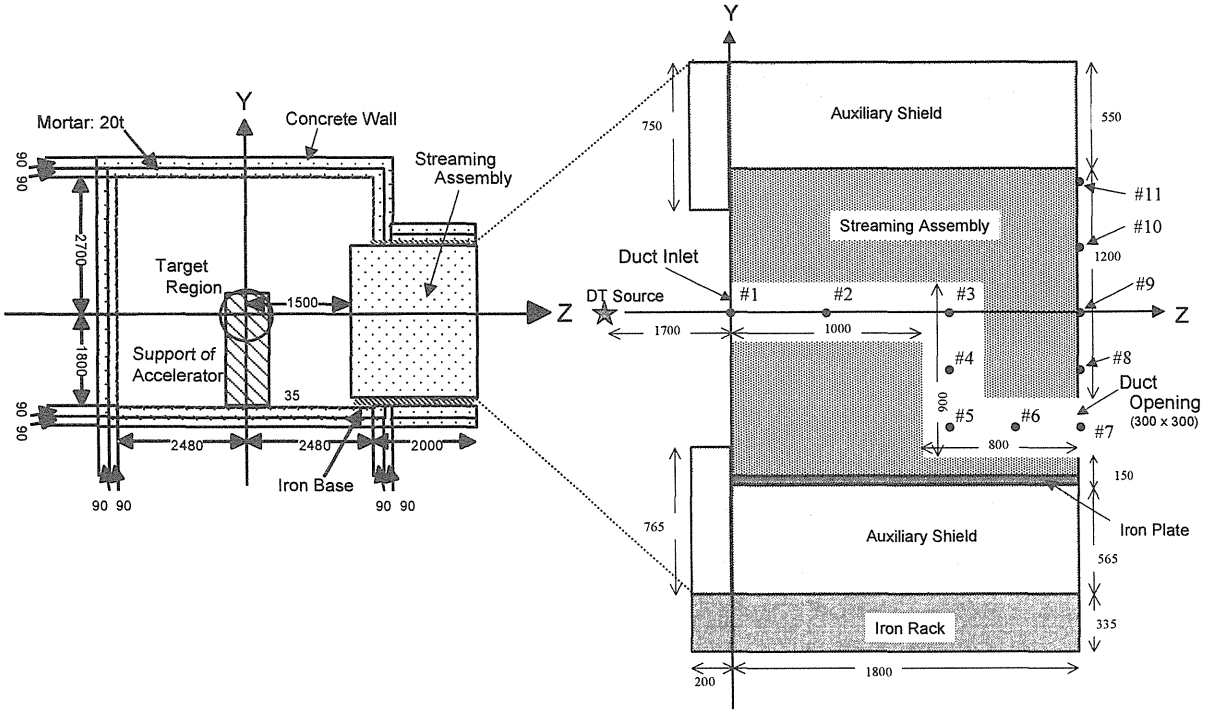

Fig. 5.1-1 Schematic view of the target room and the experimental assembly.

(2) Measured results

Measured neutron spectra are shown in Fig.5.1-2. The D-T neutron source intensity was normalized to unity.

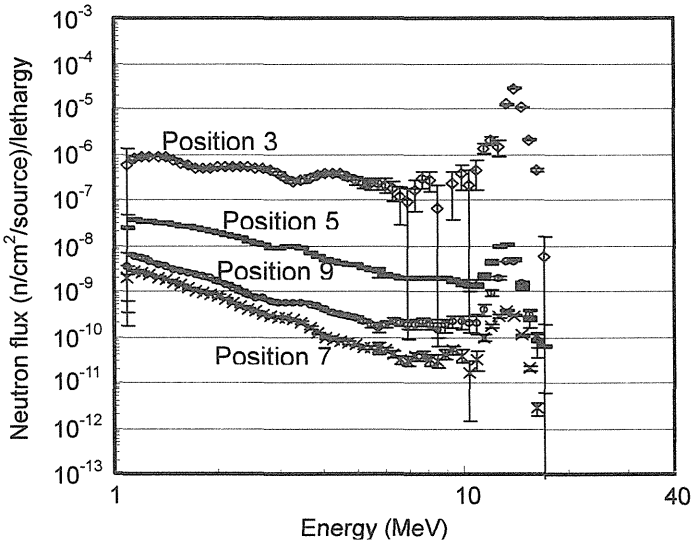

Fig. 5.1-2 Neutron spectra measured at positions #3, #5, #7 and #9.

Positions of #3, #5 and #7 are located in the duct, and the spectrum becomes softer as the path along the duct from the inlet grows larger. As for the spectrum at the position #9, it is higher than that at the position #7, because the position #9 is located on the extension of the first leg and the shield between positions #3 and #9 is only 50 cm.

Reaction rates measured with activation foils in the bent duct and on the back surface of the assembly are shown in Fig.5.1-3 under the same normalization as the spectrum. It is observed that the reaction rates of ^{93}Nb(n,2n)^{92m}Nb and ^{115}In(n,n')^{115m}In caused mainly by fast neutrons prominently decrease after the duct bends, while those of ^{197}Au(n,γ)^{198}Au do not show clear change around the bends.

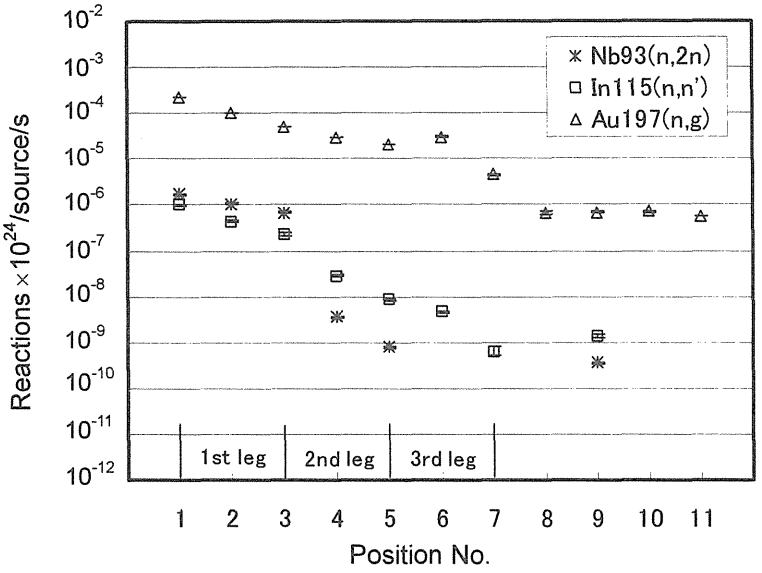

Fig. 5.1-3 Reaction rates measured in the duct and behind the assembly.

5.1.3 MCNP analysis

(1) Calculation procedure

All of the structures in the target room used for the experiment illustrated in Fig.5.1-1 were accurately modeled in the calculation. The Monte Carlo transport codes MCNP-4C with a special routine to generate D-T neutrons were used for the calculations. The source routine consists of a simulation program for deuterons slowing down in the titanium-tritium target and the kinematics of the ^{3}T(d,n)^{4}He reaction. The nuclear data libraries FENDL/2 and JENDL-3.3 were employed for the present study. Both calculated neutron spectra and reaction rates were normalized so that the ^{93}Nb(n,2n)^{92m}Nb reaction rate is consistent with the measured value at the duct inlet.

(2) Neutron Spectrum

Neutron spectra calculated by the Monte Carlo method with FENDL/2 nuclear data are compared with measured spectra above 1 MeV in Fig.5.1-4 at positions #3, #5, #7 and #9,

respectively. Although the comparisons are only in the higher energy range, the agreements are excellent except for 20 - 30 % underestimation at position #3. The discrepancy was made by the difficulty in the unfolding of the almost monochromatic spectrum data measured at the position where the target assembly can be directly observed, however, the bumps are relatively small compared with 14 MeV peak. As a general result of the spectra analysis, the calculation by MCNP-4C code together with FENDL/2 or JENDL-3.3 data was found suitable for the design calculation of ITER.

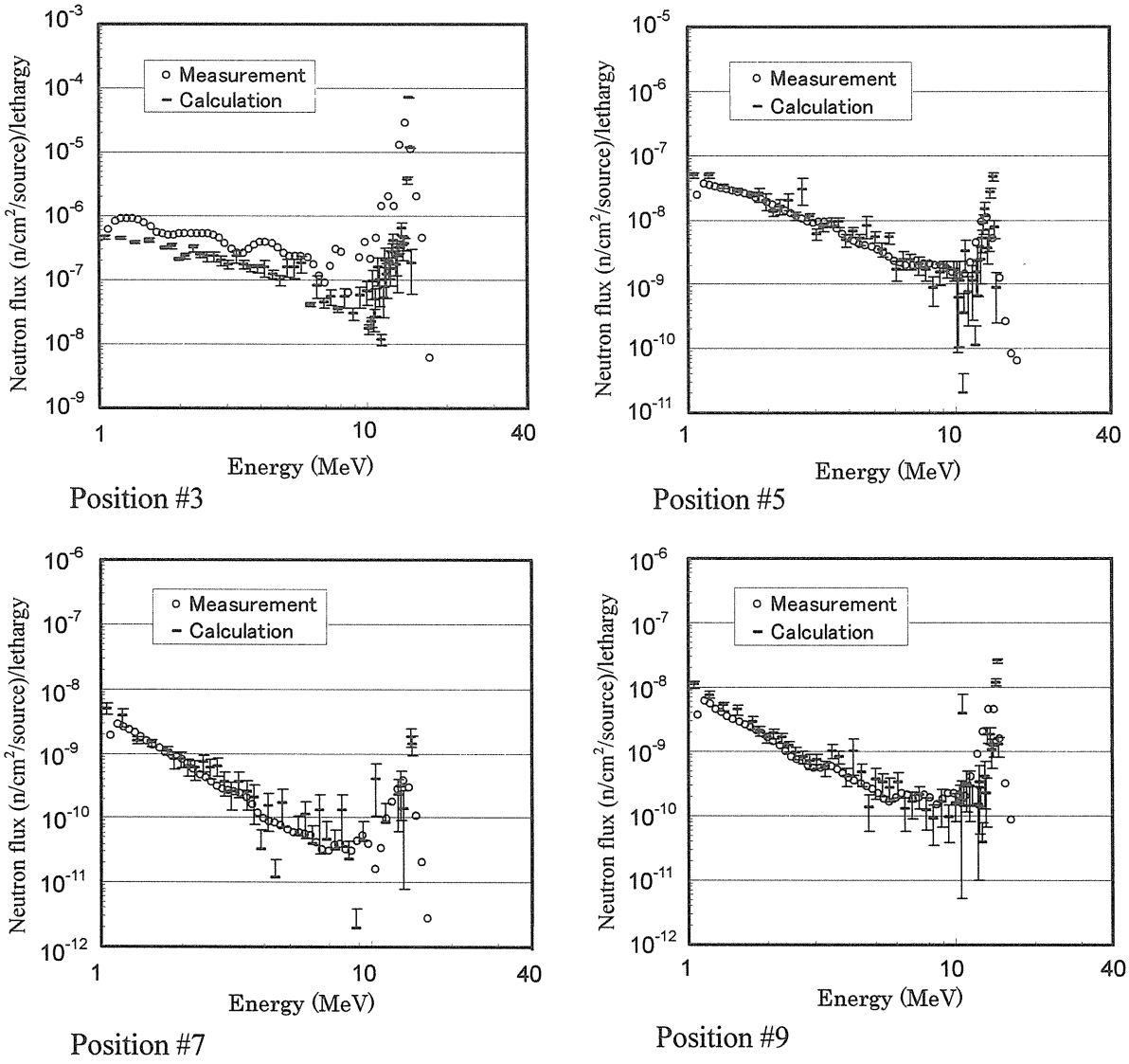

Fig. 5.1-4 Spectra measured and calculated with FENDL/2.

(3) Reaction rates

Ratios of calculated and measured reaction rates in the duct and behind the assembly for $^{93}Nb(n,2n)^{92m}Nb$, $^{115}In(n,n')^{115m}In$ and $^{197}Au(n,\gamma)^{198}Au$ are shown in Figs.5.1-5 - 5.1-7, respectively. In addition to the normal calculations, a calculation was done neglecting the wall

reflection of neutrons in the target room, and the reaction rates obtained under the condition agreed well with the results of the normal condition except the value in the first leg.

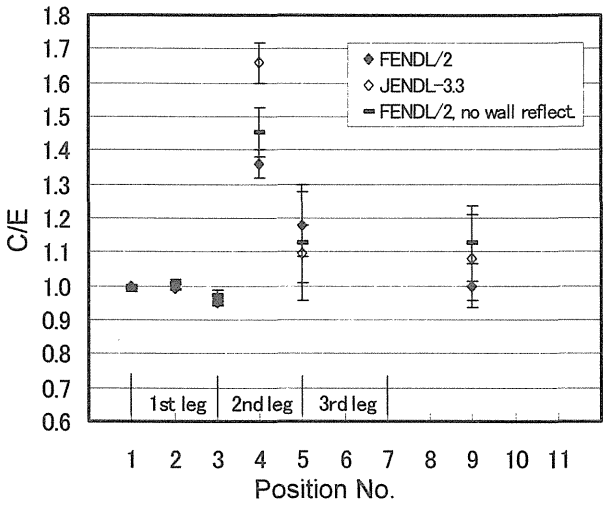

Fig. 5.1-5 C/E values of $^{93}Nb(n,2n)^{92m}Nb$ reaction rates in the duct and behind the assembly.

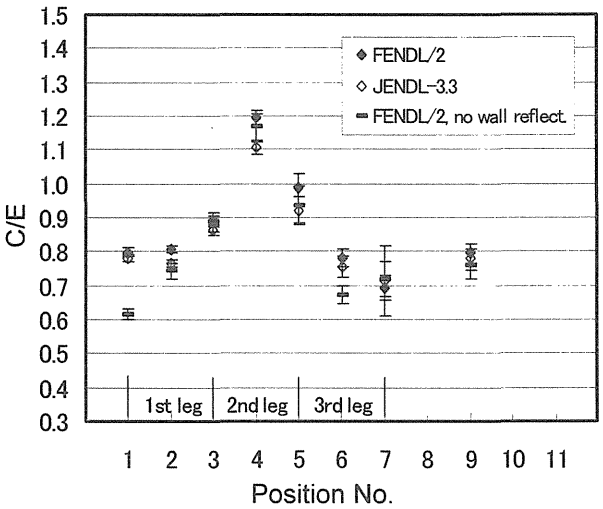

Fig. 5.1-6 C/E values of $^{115}In(n,n')^{115m}In$ reaction rates in the duct and behind the assembly.

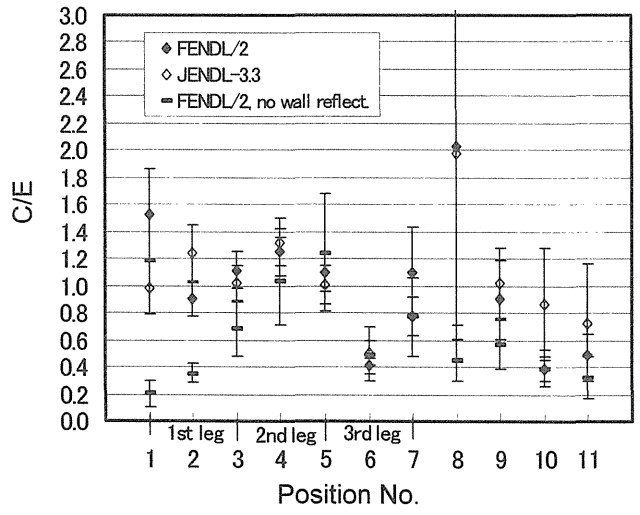

Fig. 5.1-7 C/E values of $^{197}Au(n,\gamma)^{198}Au$ reaction rates in the duct and behind the assembly.

The calculated reaction rates of $^{93}Nb(n,2n)^{92m}Nb$ agreed well with measured values except for those at positions #4 and #5, where the reaction rates become above 2 orders of magnitude smaller than that at position #3 due to the duct bend as was shown in Fig. 5.1-3. The reaction rates of $^{115}In(n,n')^{115m}In$ were generally underestimated except for those at positions #4 and #5. The underestimation may have been caused by the difficulty in dealing with the anisotropy of angular neutron flux. The calculated reaction rates of $^{197}Au(n,\gamma)^{198}Au$ generally agreed with measured values, however, the calculation made clear the difficulty to obtain accurate results with sufficiently small statistical errors in low energy range.

5.1.4 Conclusion

A doubly bent duct streaming experiment was conducted at the FNS facility of JAERI in order to estimate the streaming effect through dogleg ducts upon shielding performance and evaluate the accuracy of calculation tools for the design of a fusion reactor such as ITER. The experiment was performed with a duct 30cm × 30cm in cross section penetrating an iron assembly 1.8 m in thickness. Neutron spectra above 2MeV and reaction rates for $^{93}Nb(n,2n)^{92m}Nb$, $^{115}In(n,n')^{115m}In$ and $^{197}Au(n,\gamma)^{198}Au$ were measured, and the experiment was analyzed by the Monte Carlo code MCNP, nuclear data libraries FENDL/2 and JENDL-3.3. The agreements between calculated and measured values were generally within the statistical errors of the Monte Carlo calculations, and the results show that the code and the nuclear data libraries are sufficiently reliable means to provide values accurate enough for estimating the streaming effects in the shielding design of fusion reactors.

References

[1] F. Maekawa, C. Konno, et al., "Investigation of Prediction Capability of Nuclear Design Parameters for Gap Configuration in ITER through Analysis of the FNS Gap Streaming Experiment", J. Nucl. Sci. Technol., **Supplement 1**, 263 (2000).

[2] C. Konno, F. Maekawa, et al., "Experimental Investigation on Streaming due to a Gap between Blanket Modules in ITER", J. Nucl. Sci. Technol., **Supplement 1**, 540 (2000).

[3] C. Konno, F. Maekawa, et al., "Overview of Straight Duct Streaming Experiments for ITER", Fusion Eng. Des., **51-52**, 797 (2000).

[4] J.F. Briesmeister (Ed.), MCNP - a general Monte Carlo n-particle transport code, version 4C, LA-13709-M, Los Alamos National Laboratory (2000).

[5] A. B. Pashchenko, Summary Report of IAEA Consultants' Meeting on Selection of Basic Evaluations for the FENDL-2 Library, INDC(NDS)-356 (1996).

[6] K. Shibata, et al., "Japanese Evaluated Nuclear Data Library Version 3 Revision-3: JENDL-3.3," J. Nucl. Sci. Technol., **39**, 1125 (2002).

[7] M. Matzke and K. Weise, "Neutron spectrum unfolding by the Monte Carlo method", Nucl. Inst. Meth., **A234**, 324 (1985).

5.2 Neutron Shield Experiment of Boron-doped Resin using D-D Neutron Source

Atsuhiko MORIOKA, Satoshi SATO[1], Kentaro OCHIAI[1], Junichi HORI[1], Michinori YAMAUCHI[1], Takeo NISHITANI[1], Makoto MATSUKAWA, Hiroshi TAMAI
Tokamak Program Division, Japan Atomic Energy Research Institute, Naka, Ibaraki
[1]Fusion Neutron Laboratory, Japan Atomic Energy Research Institute, Tokai, Ibaraki

5.2.1 Introduction

JT-60SC, presently identified as the National Centralized Tokamak, has been designed for the superconducting modification of JT-60U [1, 2]. The D-D neutron emission rate in the JT-60SC is estimated to increase by a factor of two compared to that in the JT-60U [3]. For the stable operation of the superconducting coils, it is important to suppress the nuclear heating of the toroidal field (TF) coils due to the D-D neutron irradiation. The environment between a vacuum vessel and the TF coils becomes around 200 degree-C during the port baking. So, the resin is planned as the shielding material of the vacuum vessel port in JT-60SC because of its advantage in applicable temperature. In the present study, the resin, KRAFTON-HB4, is proposed instead of the polyethlene from a viewpoint of the applicable temperature. The applicable temperature is the range of -30 to 150 degree-C for the resin, though -30 to 70 degree-C for the polyethlene. Furthermore, it is proposed to add boron carbide (B_4C) in the resin to enhance the neutron shielding performance. The shielding design is carried out using the boron-doped regin. Based on the design, we performed the DD neutron transmission experiment using the Fusion Neutron Source (FNS) .

5.2.2 Shielding design

The neutron and gamma-ray fluxes were calculated using the one dimensional transport code, ANISN [4], with a group constant set FUSION-40 [5], which consists of 42 neutron and 21 gamma-ray groups, based on JENDL3.1 [6]. Multiplying these fluxes by the KERMA factor [7] based on FUSION-40, the nuclear heating of the TF coil was estimated. The nuclear heating rate at the front surface of the TF coil was calculated as a function of the boron density. Then we have developed the boron-doped resin with 2 wt % boron to satisfy the design target of 2.4 mW/cm^3 for the nuclear heating of superconducting TF coil [8].

5.2.3 Experiment

The chemical compositions of the improved boron-doped resin are summarized in Table.5.2-1. Figure 5.2-1 shows the experimental assembly used for D-D neutron

transmission experiments. The test block is composed of 1.6 cm thick F82H, 10.0 cm thick resin and 5.0 cm thick SS316, with the size of about 40 × 40 cm^2 square.

The assembly is surrounded by SS316 to decrease the neutrons scattered by the experimental room walls, and to increase the low energy neutron at the F82H surface for simulating the neutron spectrum in the vacuum vessel port in the JT-60SC.

The neutron transmission experiment was carried out using the FNS facility. The incident deuteron beam current and energy were about 2 mA and 350 keV, respectively. Neutron fluxes were measured by the activation foil method using the indium and the gold. Fast neutron flux was detected by the reaction rate of $^{115}In(n,n')^{115m}In$, and thermal neutron flux was detected by $^{197}Au(n,\gamma)^{198}Au$. These foils were placed at 0, 1.6, 6.6, 11.6 and 16.6 cm distance from the front surface along the central axis of the assembly. After irradiation, the induced radioactivities of the foils were measured by gamma-ray spectroscopy with Ge detectors during cooling times for several hours. The experimental results were compared with the analysis using the two-dimensional transport code DOT3.5[9] with the FUSION-40 and the Monte Carlo Code MCNP-4C2 [10] with the continuous energy cross section data sets based on the JENDL-3.2 [11].

The measured reaction rates and the ratio of the calculation result by DOT3.5 and MCNP to the experimental one, C/E, is shown in Figure 5.2-2 for the fast neutron in the resin with 2 wt% boron. Most of the calculation results agree with the experimental results within 20 %. The estimated values of C/E by MCNP for the resin with 0.8 wt% boron were nearly the same as those for the resin with 2 wt% boron.

Table 5.2-1 Chemical compositions of the boron-doped resin

Element	Concentration (wt.%)	
	HB-4	Improved
H	10.59	10.49
C	75.37	74.46
B	0.77	1.99
O	10.71	10.55
N	2.17	2.13
Si	0.39	0.38
density (g/cm^3)	1.08	1.09

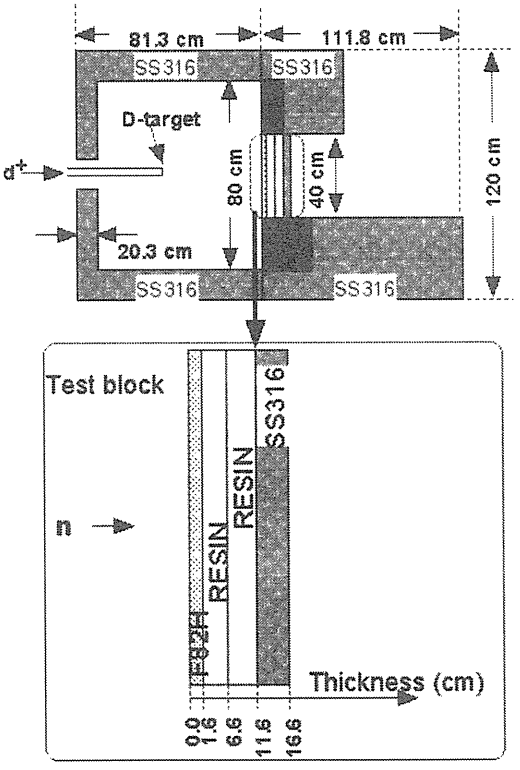

Fig. 5.2-1 Experimental assembly used for D-D neutron transmission experiments.

The reaction rates of thermal neutrons measured by In-foil for the resin with 0.8 wt% and 2 wt% boron on the experimental assembly are shown in Figure 5.2-3. The results show that the fast neutron flux through the boron-doped resin does not depend on the boron density.

The reaction rates of thermal neutron measured by Au-foils for the resin with 0.8 wt% and 2 wt% on the experimental assembly are shown in Figure 5.2-4. The neutron flux for the resin with 2 wt% boron were 10 - 25% lower than that with 0.8 wt% at the thickness of 6.6 cm and 11.6 cm. Thus, it was experimentally clarified that the boron-doped resin is effective to reduce the transmission of the thermal neutron flux.

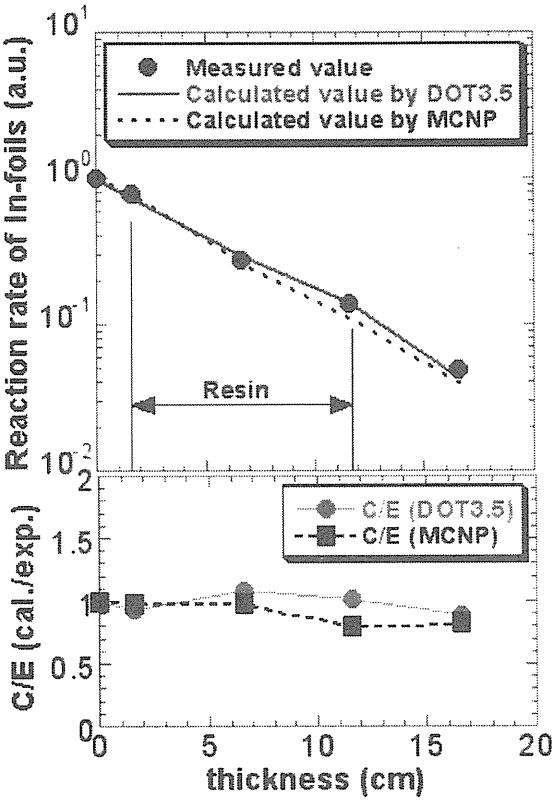

Fig. 5.2-2 Comparison between measured and calculated reaction rates of fast neutron.

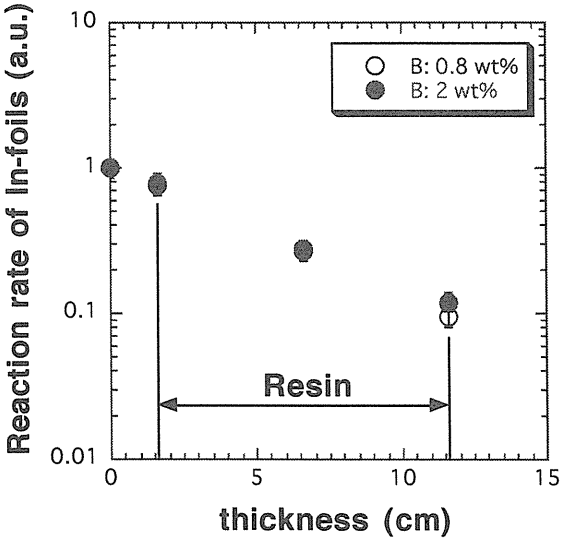

Fig.5.2-3 Reaction rates of the fast neutron measured by In-foils

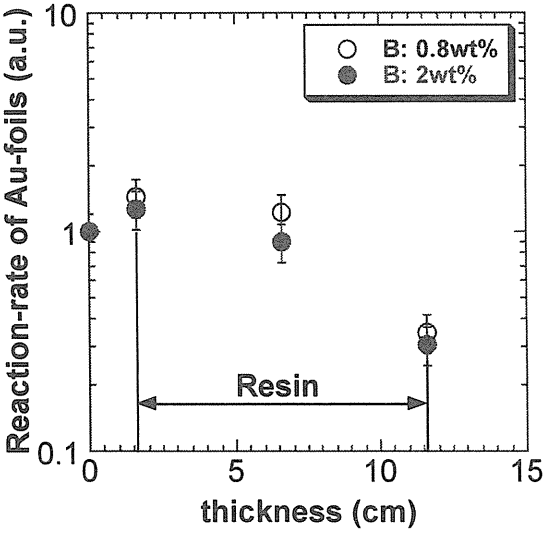

Fig.5.2-4 Reaction rates of the thermal neutron measured by Au-foils

5.2.4. Conclusion

Based on the shielding design of the JT-60, the boron-doped resin has been developed to satisfy the neutron shielding requirements for the JT-60SC, the former design of the JT-60 superconducting modification. For the boron-doped resin, the neutron transmission experiment has been carried out with 2.45 MeV neutron source. The results are summarized as follows:

- The fast neutron flux through the boron-doped resin does not depend on the boron density, which indicates that the boron doping is less effective for the fast neutron shielding.
- The thermal neutron flux in the resin with 2 wt% boron were 10 - 25% lower than that with 0.8 wt% at the thickness of the 6.6cm and the 11.6 cm.

The gamma ray heating, which is induced by the thermal neutron through (n, γ) reaction, is dominant in the nuclear heating of the TF coil, so the reduction of nuclear heating rate can be expected with using the boron-doped resin as shielding material. Therefore, the boron-doped resin will be attractive for the shielding material in the JT-60 superconductiong modification.

Reference

[1] S. Ishida et al., Nucl. Fusion **43**, 606-613 (2003).
[2] M. Matsukawa et al., Fus. Eng. Des. **63-64**, 519-529 (2002).
[3] A. Morioka et al., Fus. Eng. Des. ,**63-64**, 115-120 (2002).
[4] Engle, W. A. Jr., K-1693 (1967).
[5] K. Maki et al., JAERI-M 91-072 (1991).
[6] K.Shibata et al., JAERI 1319 (1990).
[7] K. Maki et al., JAERI-M 91-073 (1991).
[8] A. Morioka et al., ISORD-2, Sendai, (2003), to be published in J. Nucle. Sci. Technol.
[9] W. A. Rhoades, et al., CCC-276 (1977).
[10] J. F. Briesmeister., LA-13709-M (2000).
[11] IAEA-NDS-110. Rev.5, Japan, 1994.

5.3 Neutron Irradiation Experiments of Boron-doped Low Activation Concrete

Atsuhiko MORIOKA, Sstoshi SATO[1], Kentaro OCHIAI[1], Masaharu KINNO[2], Junichi HORI[1], Michinori YAMAUCHI[1], Takeo NISHITANI[1], Makoto MATSUKAWA, Hiroshi TAMAI
Tokamak Program Division, Japan Atomic Energy Research Institute, Naka, Ibaraki
[1]*Fusion Neutron Laboratory, Japan Atomic Energy Research Institute, Tokai, Ibaraki*
[2]*Fujita Corporation, Shibuya*

5.3.1. Introduction

Reduction of the activation of structural materials such as concrete in nuclear facilities is the important issue in terms of maintenance and decommissioning after shut down. In the fission reactor, the low activation concrete made of white Portland cement and special limestone [1] is used for the shielding material, in which the concentrations of silicon, aluminum, iron, magnesium, sodium, potassium, manganese, titanium, and phosphorus are very few compared to the standard concrete [2]. On the other hand, the reduction of thermal neutrons should be also considered in the design for JT-60 superconducting modification (former JT-60SC) [*see 5.2 in this Report*]. The annual neutron emission in JT-60SC plasma is estimated to increase by about 6 times as that in the present JT-60U [3, 4]. In order to shield the thermal neutrons and reduce the induced activities caused by the thermal neutrons, we have developed the shielding materials doping with boron.

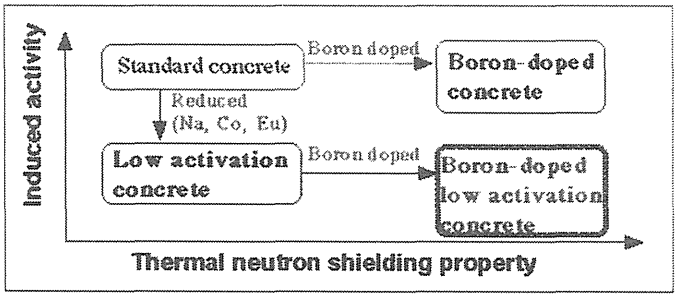

Fig. 5.3-1 Concept of boron-doped low activation concrete

The boron-doped low activation concrete is to be adopted as the cryostat for the bio-shield in JT-60SC. The concept is shown in Figure 5.3-1. The activity of ^{41}Ar nuclide, which is produced by ^{40}Ar(n,γ) reaction, in the JT-60 torus hall with the boron-doped concrete has been estimated to reduce by about 90 % compared to that with the standard concrete [5].

In order to investigate the neutron penetration and the activation characteristics of the boron-doped low activation concrete, irradiation test of 2.45 and 14 MeV neutrons is performed at FNS facility [6,7]. The penetration experiments were compared to the calculation results to using Monte Carlo calculation code, MCNP-4C2 [8], with the continuous energy cross section data sets based on the JENDL-3.2 [9].

5.3.2. Neutron penetration tests

The boron-doped low activation concrete including the natural boron with 1 wt% (B1) and 2 wt% (B2) concentrations were prepared. The chemical compositions of B1 and B2 are summarized in **Table 5.3-1**. Test pieces are 40 cm x 40 cm x 10 cm in size, 36.5 kg in weight. The experimental assembly used for the irradiation test of the fast and thermalized DD neutrons is illustrated in **Fig. 5.3-2**, and **Fig. 5.3-3**, respectively. The collimated neutrons are irradiated to the assembly in the first target room at FNS. The penetration experiments of the thermal neutron were performed by placing the polyethlene plate of 20cm thickness in front of the test concrete. The neutron flux through the boron-doped low activation concrete was measured by ^{238}U fission chamber for fast neutrons with energy above about 1 MeV and by ^{3}He proportional counter for thermal neutrons. ^{238}U fission chambers and ^{3}He proportional counter were placed at 0, 10, and 20 cm from the surface of the test piece along the central axis of the assembly.

Table. 5.3-1 Chemical composition of B1 and B2 (wt %)

	1 wt% Boron (B1)	2wt% Boron (B2)
H	1.5	1.5
Si	2.9	2.9
Ca	36	36
Al	0.65	0.65
Fe	0.063	0.062
Mg	0.26	0.26
Na	0.04	0.04
K	0.029	0.029
Mn	6.3×10^{-4}	6.4×10^{-4}
Ti	5.0×10^{-3}	4.9×10^{-3}
P	3.7×10^{-4}	3.6×10^{-6}
C	7.3	7.4
S	0.28	0.28
B	1.0	2.1
O	50	49

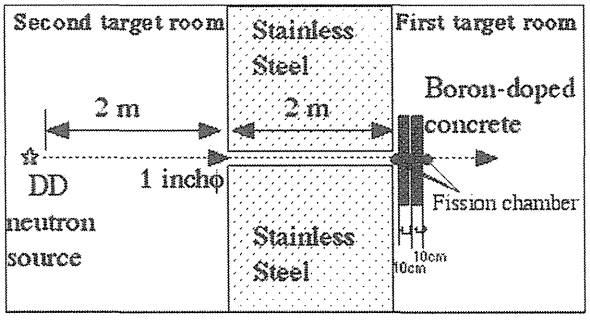

Fig. 5.3-2 Experimental assembly used for the fast DD neutron penetration experiment

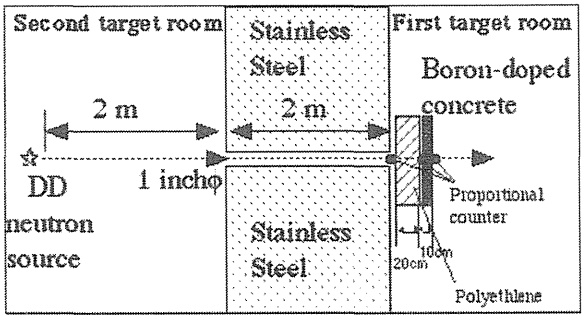

Fig. 5.3-3 Experimental assembly used for the thermal DD neutron penetration experiment

5.3.3. Results and discussions

The count rates measured by ^{238}U fission chamber in B1 and B2 concrete are shown in Fig. 5.3-4 together with the MCNP calculation of B1 concrete. The circle and triangle keys indicate the measured results for the B1 and B2, respectively. The results show that the fast

neutron shielding property of B2 is almost same as B1 within experimental error. Calculated result for B1 by MCNP-4C2 is also shown by the solid line, which agrees with the experimental results within 15 %. Calculated result for B2 by MCNP was nearly the same as that for B1. Those results strongly indicate that the shielding property of the boron-doped low activation concrete for fast neutron flux does not depend on the boron density.

Figure 5.3-5 shows the count rates of the thermal neutron flux measured by the ^{3}He proportional counter for B1 (circles) and B2 (triangles). It was experimentally clarified that the reaction rate of the thermal neutron flux of B2 was about a half of B1. The result indicates that the shielding property of the boron-doped low activation concrete for thermal neutron flux is superior in higher density of boron doping.

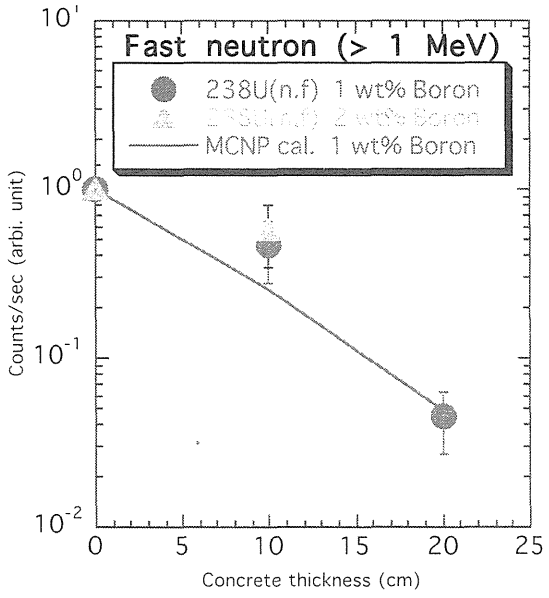

Fig. 5.3-4 Count rates measured by ^{238}U fission chamber in B1 and B2 concretes, and MCNP calculation in B1 experiment

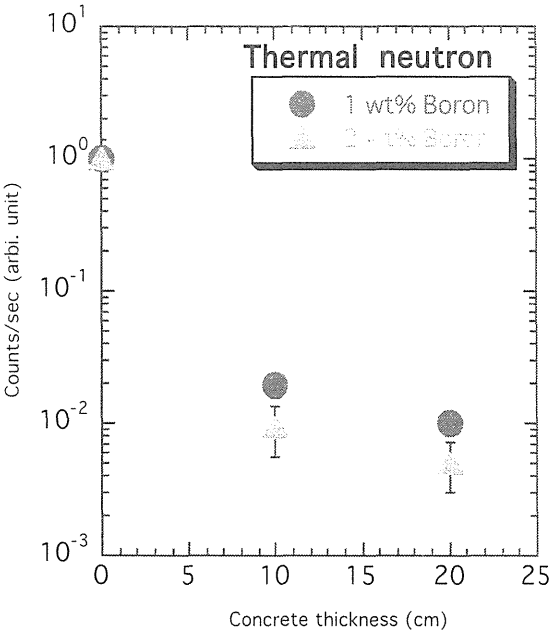

Fig. 5.3-5 Count rates measured by ^{3}He proportional counter in B1 and B2 concretes

5.3.4.Conclusion

The DD neutron irradiation tests were performed in order to evaluate the shielding property of the boron-doped low activation concrete. The shielding property of the 2 wt% boron-doped low activation concrete is superior to that of the 1 wt% boron for the thermal neutron. On the contrary, there exists no clear dependence on the boron density for the fast neutron. It can be concluded that the boron-doped low activation concrete is very attractive as the shielding material of the thermal neutron such as the cryostat of the JT-60 superconducting modification.

References

[1] M. Kinno et. al, Nucl. Sci. Technol., Sup.1, 821-826 (2000)

[2] N. Imai, et al., Geostandards Newsletter, 19,135 (1995)
http://www.aist.go.jp/RIODB/geostand/igneous.html

[3] S. Ishida et al., Nucl. Fusion 43 (2003) 606-613

[4] M. Matsukawa et al., Fus. Eng. Des. ,**63-64** (2002) 519-529

[5] A. Morioka et al., Fus. Eng. Des. ,**63-64** (2002) 115-120

[6] S. Sato et al., 2nd-ISORD, Sendai, (2003), to be published in J. Nucle. Sci. Technol.

[7] A. Morioka et al., 11th-ICFRM-2, Kyoto, (2003), to be published in J. Nucle. Mater.

[8] Judith F. Briesmeister., LA-13709-M (2000)

[9] IAEA-NDS-110. Rev.5, Japan, 1994Rev.5, Japan, 1994.

6. Irradiation Effects of Fusion Neutrons

6.1. Point Defect in Room and High Temperatures

Yoshiharu SHIMOMURA, Kenjiro SUGIO[1], Hideaki OHKUBO[1], Ichiro MUKODA[1], Chuzo KUTSUKAKE[2]

Hiroshima Institute of Technology, Hiroshima

[1]Hiroshima University, Higashi-Hiroshima

[2]Fusion Neutron Laboratory, Japan Atomic Energy Research Institute, Tokai, Ibaraki

6.1.1 Introduction

Previously, D-T neutron irradiations on fcc metals were performed at RTNS-II[1] in LLNL. In fee metals such as gold, silver and copper, an average PKA energy forming damage cascades are 100, 200 and 400 keV, respectively. In these specimens, which were irradiated below 20 K, only interstitial clusters were observed at 20 K with a cryo-transfer technique to an electron microscope [2]. A group of stacking fault tetrahedral (sft) was observed in specimens irradiated at room temperature [3]. The formation of groupings of sft was observed in D-T neutron-irradiated Au at room temperature of the neutron fluence range of 10^{22} n/m^2 at RTNS-II. Such groups were explained previously to be formed by nucleation of vacancy clusters at vacancy core of sub-cascade [4]. Present experiments were carried out to be complementary experiment to the previous one at RTNS-II to cover the relatively low fluence regime of irradiation.

6.1.2 Experiments

Irradiated specimens were Au, Ag and Cu discs of 50 μm in thickness and 3 mm in diameter. These are mounted in an irradiation chamber evacuated with a turbo-molecular pimp to be a pressure of 10^{-6} Pa. The irradiation chamber was located just in front of the rotating tritium target of FNS as shown in Fig. 6.1-1. The temperature of specimens were controlled to be 288 K during irradiation. Irradiated neutron fluence for each specimen was measured with activation dosimetry foils of Nb. After cooling down of radioactivity, specimens were observed by an electron microscope.

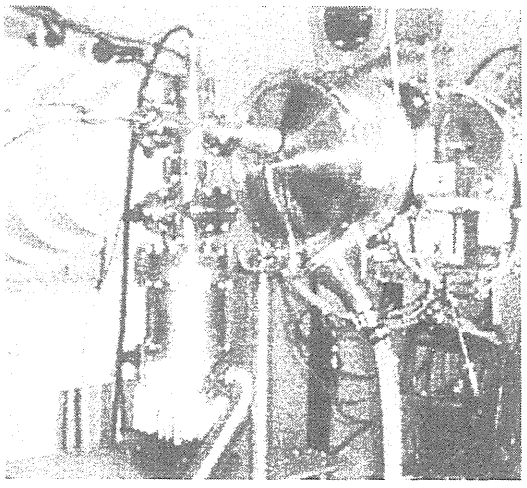

Fig. 6.1-1 Picture of the irradiation chamber installed at FNS

6.1.3 Results

Figures 6.1-2(a), (b) and (c) show the defects observed in gold specimens irradiated D-T neutrons with the fluence of 2.6×10^{18}, 2.6×10^{19} and 3.2×10^{20} n/m^2, respectively. An isolated defects as seen Fig. 6.1-2(a) is an interstitial cluster. In the present work, the nature of defects were determined by TEM annealing experiments. When the TEM specimens were annealed at 573 K for 10 min, vacancy cluster grew to sft. Disappeared defects were taken as an interstitial cluster. An Interstitial cluster disappears by absorbing vacancies. Vacancy clusters in Au irradiated up to 2.6×10^{18} n/m^2 were not observed, which was probably because those structure did not relax to TEM visible ones. In Figs. 6.1-2(b) and (c), some defects show a triangular shape which indicating vacancy type defects. We count the number density of dot defect rather than the cascade damage.

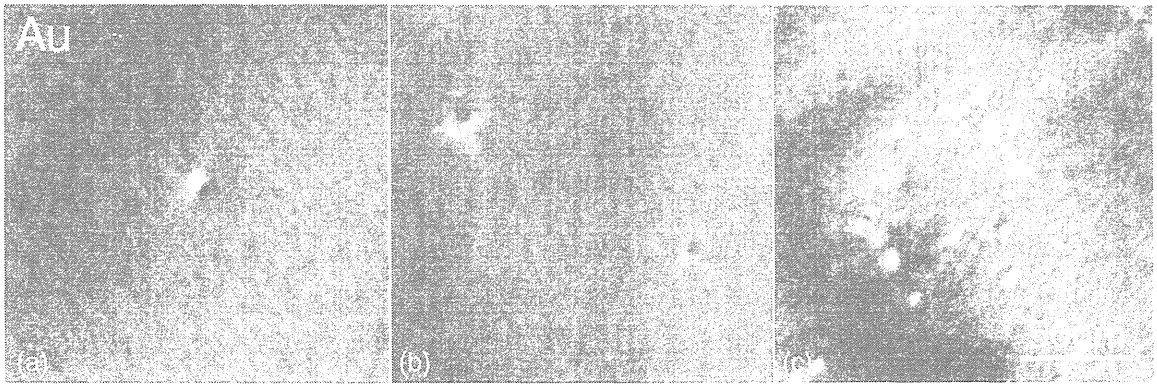

Fig. 6.1-2 Point defect cluster observed in Au at 288 K irradiated D-T neutrons with the fluence of (2) 2.6×10^{18}, (b) 2.6×10^{19} and (c) 3.2×10^{20} n/m^2, respectively.

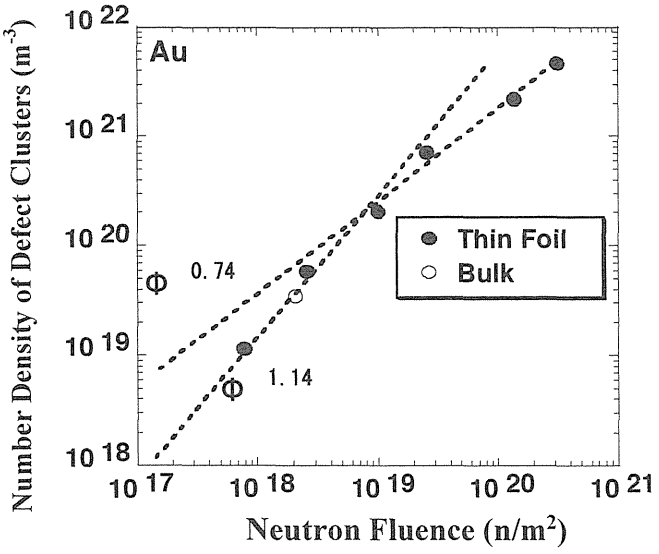

Fig. 6.1-3 Number density of dot defects in Au as a function of the neutron fluence.

Fig. 6.1-3 shows the relation of number density of dot defects in Au as a function of the neutron fluence. Defects tend to form grouping with increasing in neutron fluence as seen in Figs.6.1-2(a), (b) and (c).

6.1.4 Discussion and Conclusion

The present experimental results were explained by a following model. A large part of point defect cluster formed in displacement damage cascades are TEM invisible. At room temperature, those move as cluster. Such movements of point defect cluster were shown by computer simulation previously [5]. At low fluence, those are attracted near dislocations. Interstitial clusters are ejected from damage cascade, move in a vacancy and may be able to form isolated immovable small clusters at a vacancy cluster formed previously. By this mechanism, interstitial clusters form in crystalline grain. In Au, the number of difects is proportional to 1.14 power of the neutron fluence in low fluence regime. In high fluence regime, it is proportional to 0.74 power of the neutron fluence. In low fluence regime, invisible defects move in crystal and meet another defect with the same nature. Then, those relax to visible structure. At high fluence regime, defects of same nature agglomerate to grow to a large defect. The mutual annihilation of interstitial clusters and vacancy ones decrease also the number of defects. A 0.74 power dependence of the neutron fluence for the number density of dot defects in high fluence regime

References

[1] M. Kiritani, N. Yoshida, and S. Ishino, J. Nucl. Mater. **133-134**, 85 (1985).
[2] Y. Shimomura, M.W. Guinan, et al., J.Nucl. Mater. **155-157**, 1181 (1988).
[3] M. Kiritani, J.Nucl. Mater. **138**, 261 (1986).
[4] M. Kiritani, N. Yoshida, and S. Kojima, J. Nucl. Mater. **141-143**, 860 (1986).
[5] P. Zhao and Y. Shimomura, Jap. J. Appl, Phys. **36**, 7291 (1997)

6.2. Neutron Spectrum Effects of the Defect Production in Fusion Reactor Candidate Alloys

Toshimasa YOSHIIE, Koichi SATO, Qiu XU, Eiichi WAKAI[1], Chuzo KUTSUKAKE[2], Takeo NISHITANI[2]

Research Reactor Institute, Kyoto University, Kumatori, Osaka

[1]*Department of Effects and Analysis Material Laboratory, Japan Atomic Energy Research Institute, Tokai, Ibaraki*

[2]*Fusion Neutron Laboratory, Japan Atomic Energy Research Institute, Tokai, Ibaraki*

6.2.1 Introduction

As irradiation with fusion neutrons to high doses is not available at present, the irradiation effects on the material properties at high doses must be derived from fission neutron irradiation experiments. Therefore an understanding of the fission-fusion correlation is important. The fission-fusion correlation of defect structural evolutions was investigated for several metals and alloys by comparing the damage structures in the specimens irradiated in fission reactors with those irradiated in the Rotating Target Neutron Source (RTNS-II) at the Lawrence Livermore National Laboratory (LLNL) [1]. Recent developed fusion reactor candidate materials were not examined in the studies at that time. Vanadium alloys and ferritic/martensitic steels are recognized as attractive candidate materials for neutron interactive structural components of fusion energy systems. Vanadium alloys have high temperature strength, high thermal stress factor and low activation property. Reduced activation martensitic steels have good dimensional stability under high irradiation doses and are suitable for commercial production without a large industrial investment.

In the present work, irradiation effects of fission and fusion neutrons on fusion reactor candidate alloys, V-4Cr-4Ti and F82H were studied using the FNS facility and the Kyoto University Reactor (KUR). As the irradiation dose was low in the present study, defect structures were compared with the results of positron annihilation spectroscopy.

6.2.2 Experiments

High purity V-4Cr-4Ti alloy of NIFS-HEATs [2] was used for a vanadium alloy. The specimens for positron annihilation spectroscopy were prepared from cold-rolled sheets by punching followed by annealing at 1373K for 2 hours in vacuum. F82H alloy prepared by JAERI [3] was used after cutting and chemical polishing to remove the deformed area.

Fusion neutron irradiation was performed by a rotating tritium target in the target room II of the FNS facility at room temperature. Fission neutron irradiation was performed by the KUR, 5MW light water reactor, at room temperature using the Hydraulic Conveyer. For

irradiation at room temperature, the reactor power was reduced to 300 kW to avoid the increase of specimen temperature by nuclear heating.

Positron annihilation lifetime measurements were performed at room temperature using the fast-fast coincidence system, whose lifetime resolution FWHM is 190 ps. The counting rate is about 80 cps. The lifetime spectra were collected with a total count of about 1 to 3 × 10^6. The positron lifetime spectra were analyzed using the Resolution and Positronfit programs [4].

6.2.3 Results and Analyses

The results of positron lifetime measurement of specimens irradiated at room temperature are shown in Fig. 6.2-1 and Fig. 6.2-2 for V-4Cr-4Ti, and in Fig. 6.2-3 and Fig. 6.2-4 for F82H. After neutron irradiation, the mean lifetime is longer than that before irradiation. The effect of neutron irradiation on positron annihilation lifetime was detected even at a low irradiation dose of 10^{-6}dpa. In both alloys, the effect of neutron irradiation on positron lifetime by fusion neutrons and fission neutrons is almost the same, if we compare them by dpa.

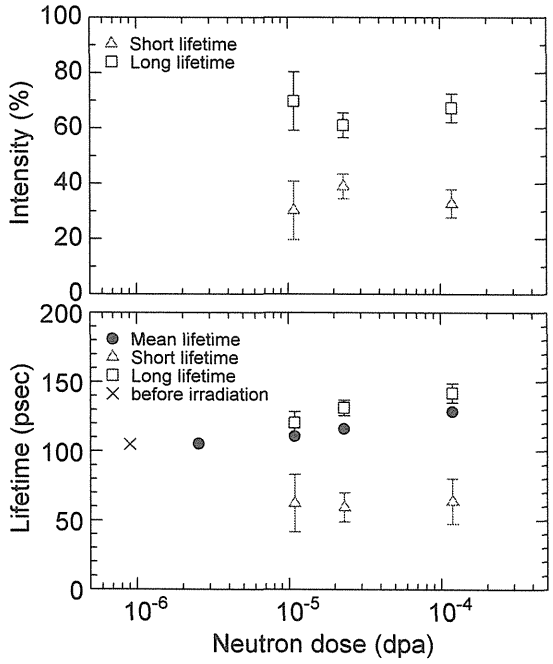

Fig. 6.2-1 Variation in the positron long, mean and short lifetimes and their intensities in V-4Cr-4Ti irradiated at room temperature in FNS. × denotes bulk lifetime (105 psec).

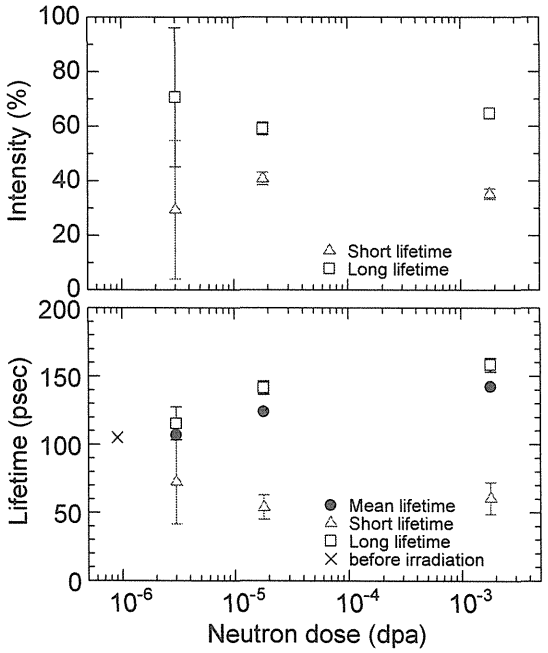

Fig. 6.2-2 Variation in the positron long, mean and short lifetimes and their intensities in V-4Cr-4Ti irradiated at room temperature in KUR (Hyd.). × denotes bulk lifetime (105 psec).

This can be explained as follows. The large cascade is divided into subcascades. If the subcascade energy is below 20keV, the number of subcascades is roughly proportional to the displacement damage measured by dpa in the case of intermediate weight atoms like Ni and Fe [5]. The subcascade energy of Fe is calculated to be 10keV [6]. It is concluded that the same number of freely migrating defects is generated from each subcascade and the same number of defects remains in each subcascade in fission and fusion neutron irradiated F82H. The situation is the same in the case of V-4Cr-4Ti, though we have not calculated the subcascade energy.

6.2.4 Conclusion

The comparison of defect structures in two fusion reactor candidate alloys between fusion neutron irradiation and fission neutron irradiation was performed. Even though the irradiation doses were low, the defect formation was detected by positron annihilation spectroscopy. Higher irradiation doses and different irradiation temperatures are required to detect the effects of neutron spectra more precisely.

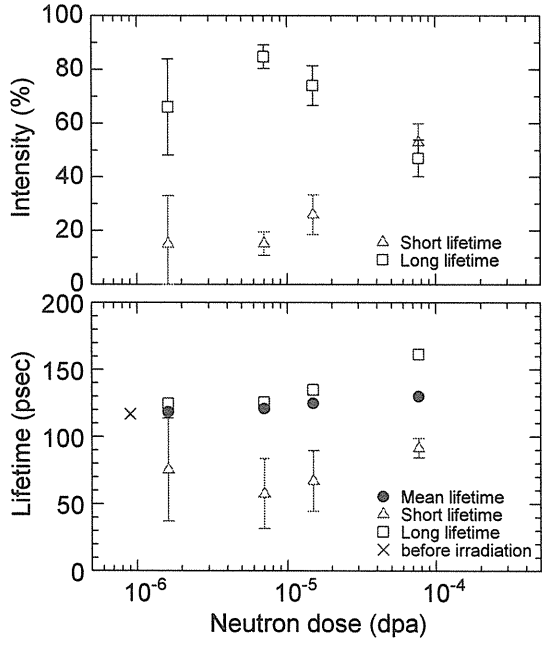

Fig. 6.2-3 Variation in the positron long, mean and short lifetimes and their intensities in F82H irradiated at room temperature in FNS. × denotes bulk lifetime (117 psec).

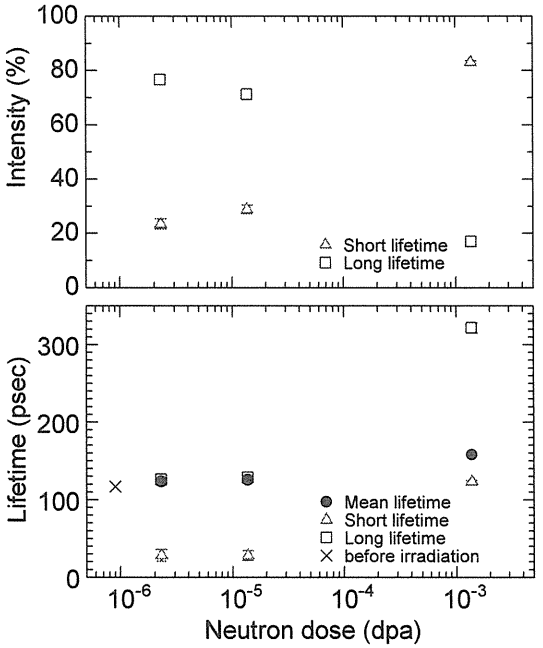

Fig. 6.2-4 Variation in the positron long, mean and short lifetimes and their intensities in F82H irradiated at room temperature in KUR (Hyd.). × denotes bulk lifetime (117 psec).

References

[1] M. Kiritani, T. Yoshiie, S. Kojima, Y. Satoh and K. Hamada, J. Nucl. Mater. **174**, 327 (1990).

[2] T. Muroga, T. Nagasaka, A. Iiyoshi, A. Kawabata, S. Sakurai, M. Sakata, J.Nucl. Mater. **283-287**, 711 (2000).

[3] E. Wakai, Y. Miwa, N. Hashimoto, J.P. Robertson, R.L. Klueh, K. Shiba, K. Abiko, S. Furuno and S. Jitukawa, J.Nucl. Mater. **283-287**, 203 (2000).

[4] P. Kirkegaard, M. Eldrup, O.E. Mogensen, N.J. Peterson, Comp Phys Commun. **23**, 307 (1981).

[5] T. Yoshie, Y. Satoh and Q. Xu, J.Nucl. Mater. to be published.

[6] T. Yoshiie, X. Xu, Q. Xu, S. Yanagita and Y. Satoh, Reactor Dosimetry: Radiation Metrology and Assessment, ASTM STP **398**, 625 (2001).

6.3 Neutron Induced Current in MI cable

Toshiyuki IIDA, Fuminobu SATO, Teruya TANAKA[1], Kentarou OCHIAI[2],
Takeo NISHITANI[2]

Department of Electronic, Information Systems and Energy Engineering, Osaka University, Suita-shi, Osaka

[1]*National Institute for Fusion Science, Toki-shi, Gifu*

[2]*Fusion Neutron Laboratory, Japan Atomic Energy Research Institute, Tokai, Ibaraki*

6.3.1 Introduction

Mineral-insulated (MI) cables are expected to be helpful for instrumentation system of a fusion reactor because of their good properties of high electrical insulation, heat resistance and mechanical strength. In severe radiation environment of high dose rate, however, the insulation of an MI cable degrades because electric charge is induced in its insulator by radiations. Some experiments on electrical degradation of MI cables have been performed [1-6]. More detailed irradiation data on electrical properties of MI cables are required for the evaluation of the reliability of the system with MI cables for fusion reactors. This section describes the degradation of electrical insulation of MI cables under fusion neutron irradiation.

6.3.2 Experiment

Fusion neutron effects on MI cables were examined by use of Fusion Neutronics Source (FNS). Figure 6.3-1 shows a schematic drawing of the experimental arrangement and the block diagram of the measurement system. Two types of MI cables were prepared for irradiation. The MI cables had a coaxial structure consisting of a Cu central wire, sintered MgO insulator and a stainless steel sheath. Both ends of the cables were sealed with glass to protect them against humidity. Cross sections of the cables and their dimensions are shown

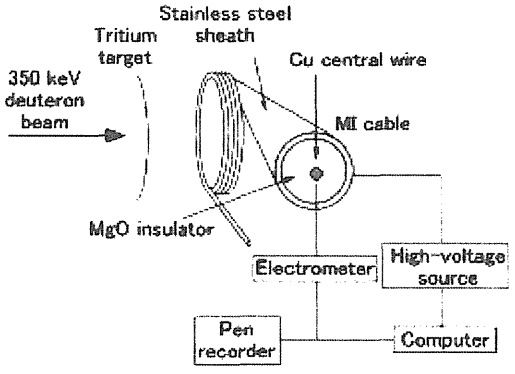

Fig. 6.3-1 Schematic drawing of experimental arrangement and block diagram of measuring system

in Fig. 6.3-2. The cables were 2.0 m in length and were bent into rings. The diameter of the ring was 26 cm (cable-a) and 14 cm (cable-b), respectively. The cables were placed in front of the tritium target and were irradiated with DT fusion neutrons. The bias voltage was applied to the sheath of the cable and the central wire was connected to an electrometer. Changes in the current flowing into the central wire were measured at room temperature as an effect of neutron-induced conduction. The neutron flux was monitored with a ^{238}U fission detector. The maximum flux of DT neutrons was 5.6×10^7 and 3.6×10^8 n/cm^2/s for the cable-a and -b, respectively. Fifteen minutes irradiation and 15 min cooling-off period was repeated to observe the transient response.

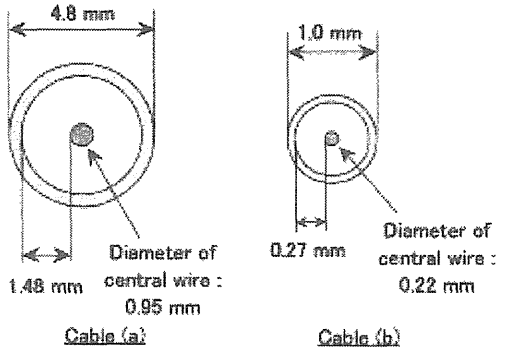

Fig. 6.3-2 Dimensions of irradiated MI cables

6.3.3 Results and discussion

Figure 6.3-3 shows an example of an increase in the leakage current induced by DT neutron irradiation for the cable-a. A large peak of transient current was observed at the start of the irradiation. After several minutes, the leakage current settled down to a steady state. At the stop of the irradiation, the transient current flowed in the reverse direction. In the present paper, the steady currents measured during irradiations were examined as the induced currents.

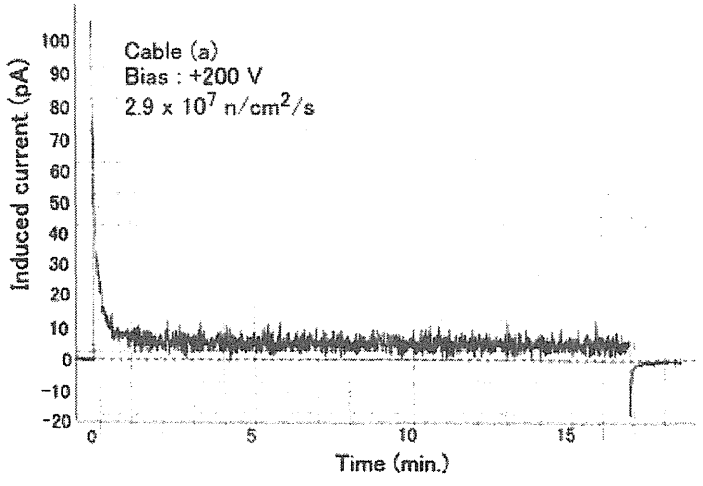

Fig. 6.3-3 Example of increase in leakage current flowing in MI cable under irradiation.

The relation between the bias voltage and the induced current and that between the neutron flux and the induced current are shown in Figs. 6.3-4 and6.3-5. As shown in the figures, the induced current was approximately proportional to the bias voltage and neutron flux. This indicates that the degradation of the insulation property was dominated by the production rate and drift of electric charge in the insulator.

Under the condition of the same bias voltage, the induced current in the thicker cable-a was about five times larger than the thinner cable-b as shown in Fig. 6.3-5. The amount of the neutron-induced electric charge in the insulator of the cable-a was estimated to be 27 times larger than the cable-b from the point of the volume. On the other hand, the strength of the electric field in the insulator of the cable-a was calculated to be about 1/5 of that of the cable-b. The difference in the radiation susceptibility between the cables -a and -b can be explained from the product of the production rate of the electric charge and the strength of the electric field.

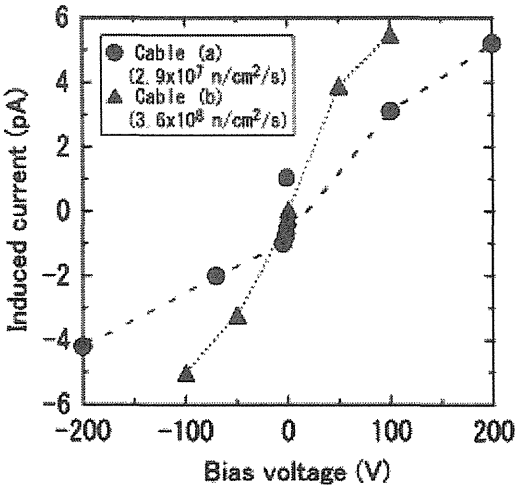

Fig. 6.3-4 Relation between bias voltage and induced current

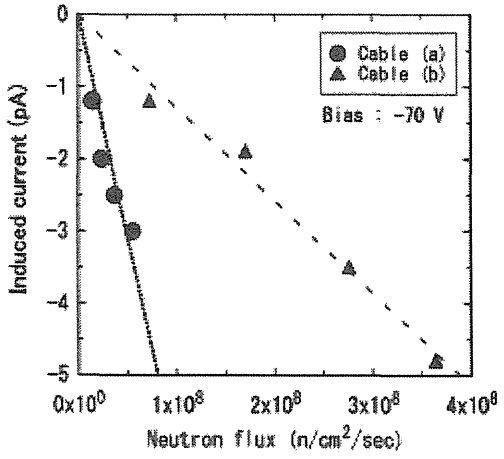

Fig. 6.3-5 Relation between neutron flux and induced current

Similar transient peaks of the leakage currents at the start of irradiations were observed in our previous experiments on sapphire plate specimens [7]. Furthermore, the reverse peak at the stop of the irradiation was observed for the experiments on MI cables. As to the sapphire specimens, the leakage current after the stop recovered slowly to the level before irradiation [7,8]. For the MI cables, the strength of the electric field around the central wire was much larger than that near the sheath. Therefore, the unbalanced distribution of the trapped electric charge may cause the pullback of the leakage current at the stop of the irradiation. For the quantitative analysis of the experimental results, we need further detailed data on the behavior of electric charge in the insulator.

6.3.4 Conclusion

Fusion neutron irradiation experiments on MI cables were performed for the examination of the degradation of their insulation property. The neutron-induced leakage current was approximately proportional to the neutron flux and bias voltage. This result indicates that the degradation of insulation property of the cable is dominated by the production rate and drift of electric charge in the insulator. The appearance of the large peaks of the transient leakage current immediately after the start and stop of the irradiation may be related to the distribution of electric charge trapped in the insulator. Further data on the behaviors of electric charge in the insulator are required for the quantitative analysis of the experimental results.

References

[1] H.D. Warren, D.P. Bozarth, Proc. of the 2nd ASTM-EURATOM Symp. on Reactor Dosimetry, Dosimetry Method for Fuels, Cladding and Structural Materials, Palo Alto, CA, (1997).

[2] E.H. Farnum, T. Shikama, M. Narui, T. Sagawa and K. Scarborough, Nucl. Mater. **228**, 117 (1996).

[3] T. Shikama, M. Narui and T. Sagawa, Nucl. Instrum. Method **B 122**, 650 (1997).

[4] D.P. White, L.L. Snead, S.J. Zinkle and W.S. Eatherly, J. Appl. Phys. **83**, 1924 (1998).

[5] T. Nishitani, T. Shikama, M. Fukao, H. Matsuo, R. Snider, J. Broesch, N. Sagawa, H. Kawamura and S. Kasai, Fusion Eng. Des., **51**, 153 (2000).

[6] T. Nishitani, T. Shikana, M. Fukao, R. Reichele, T. Sugie, T. Kakuta, S.Kasai, R. Snider and S. Yamamoto, Fusion Eng. Des. **56**, 905 (2001).

[7] T. Iida, F. Sato, H. Sato, F. Maekawa, H. Takeuchi, Proc. of the 1st International Symp. on Supercritical Water-Cooled Reactors, Design and Technology, SCR-2000, 251 (2000).

[8] W. Kesternich, J. Appl. Phys. **85**, 748 (1999).

6.4 Activation experiments on vanadium alloy NIFS-HEAT-2

Teruya TANAKA, Satoshi SATO[1], Takuya NAGASAKA, Takeo MUROGA,
Kentaro OCHIAI[1], Takeo NISHITANI[1]
Fusion Engineering Research Center, National Institute for Fusion Science, Toki, Gifu
[1]Fusion Neutron Laboratory, Japan Atomic Energy Research Institute, Tokai, Ibaraki

6.4.1 Introduction

Vanadium alloys are attractive low activation structural materials for advanced fusion reactors. Since radioactive nuclides transmuted from constituent elements, i.e. V, Ti and Cr, under fusion neutron environment have relatively short half-lives, the V-Cr-Ti ternary alloys have inherent potential for recycling in ~100 years after reactor shutdown [1,2]. For achievement of the advantage, activation level originated with impurity elements should be kept lower than or comparable to that of pure vanadium alloy. Therefore, in the development of vanadium alloys for fusion reactors, reduction of impurity concentrations to allowable levels is one of important issues [3,4].

In the National Institute for Fusion Science (NIFS), fabrication of large ingots of high-purity V-4Cr-4Ti alloy (NIFS-HEAT-1, 2) has been conducted for establishment of industrial-scale method [5-7]. According to chemical analysis, impurity levels in NIFS-HEATs were successfully reduced compared with those in other vanadium alloy ingots. However, considering the importance of impurity control, activation experiments were required for complementary analysis of impurities and direct evaluation of dose rate and decay heat after fusion neutron irradiation.

In the present study, activation analysis of impurities and evaluation of activation properties were performed on NIFS-HEAT-2 by DT neutron irradiation at FNS facility. Similar analysis and evaluation were performed on US and Chinese V-4Cr-4Ti samples for comparison.

6.4.2 Experiment

Thin foils of 10 × 10 × 0.1 mm^3 were prepared from an ingot of NIFS-HEAT-2. Specimens of same dimensions were prepared also from Round-Robin samples provided by the US (DOE 832665) [8] and China (South West Institute of Physics) [9]. DT neutron irradiations on the vanadium alloy specimens were performed at FNS facility. The specimens were located on the surface of the tritium target bombarded with 350 keV D^+ beam. Irradiations of 10 minutes (~2.5 × 10^{12} n/cm^2), 25 minutes (~6.5 × 10^{12} n/cm^2), 7 hours (~2.5 × 10^{14} n/cm^2) and 15 days (~1.2 × 10^{16} n/cm^2) were performed for detection of radioactive nuclides with different order of half-lives.

After irradiations, gamma-ray spectra were measured with a high-purity Ge detector. Especially in the 10 and 25 minutes irradiations, a pneumatic tube system connecting between the irradiation position and a measurement room was used for start of measurement within 1 minute after irradiation. Concentrations of impurities were evaluated from the areas of gamma peaks observed in the spectra.

Decay heat of the irradiated NIFS-HEAT-2 specimen was measured with Whole Energy Absorption Spectrometer (WEAS) developed in FNS facility [10]. The WEAS system consists of two large BGO scintillation detectors facing each other and detects both of gamma and beta rays with efficiency of higher than ~75%. Results of the decay heat measurement were compared with values calculated using MCNP-4C transport code [11] and ACT-4 activation code [12] for verification of the estimation accuracy. Nuclear data library used for the transport calculation was JENDL-3.2 [13] and that used for the activation calculation was JENDL Activation File [14], respectively.

6.4.3 Results and Discussion

Fig. 6.4-1 shows examples of gamma-ray spectra of NIFS-HEAT-2. During ~1 year after irradiations, eight radioactive nuclides of ^{24}Na, ^{28}Al, ^{54}Mn, ^{56}Mn, ^{57}Co, ^{58}Co, ^{89}Zr and ^{92m}Nb were identified from analysis of the gamma peaks. The sources of the nuclides were considered to be Al, Si, Mn, Fe, Ni, Co, Zr, Nb and Mo. Results of the analysis were listed in Table 6.4-1 with evaluated concentrations. The values in parenthesis are those obtained by chemical analysis. The source of ^{92m}Nb could not be identified distinctively since the nuclide could be produced through both of ^{93}Nb(n,2n)^{92m}Nb and ^{92}Mo(n,p)^{92m}Nb reactions. Therefore

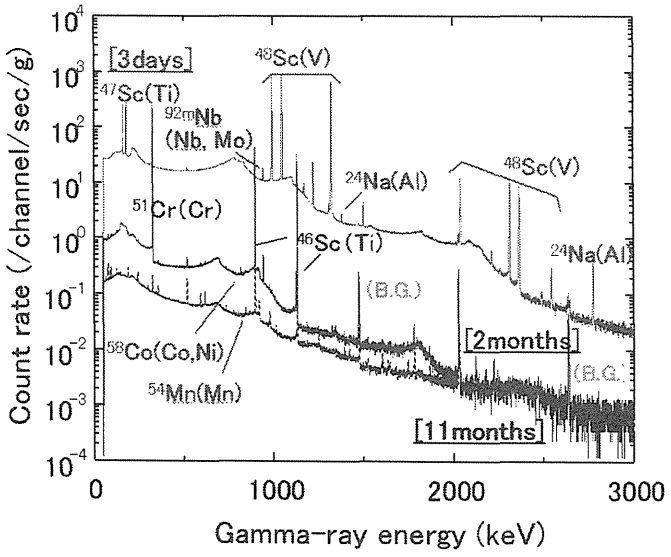

Fig. 6.4-1 Examples of gamma-ray spectra of NIFS-HEAT-2 after DT irradiation. Detected nuclides were shown with source elements in parentheses.

Table. 6.4-1 Impurity concentrations in vanadium alloys evaluated in present activation analysis.

Detected nuclide	Impurity element	Evaluated concentration (wppm)		
		NIFS-HEAT-2	US	CN
^{24}Na	Al	70 (59)*	171 (190)	384 (340)
^{28}Al	Si	271 (270)	908 (730)	129 (150)
^{54}Mn	Mn	2.0 (< 1)	2.0 (< 1)	11 (17)
^{56}Mn	Fe	53 (49)	255 (200)	559 (650)
^{57}Co	Ni	6.4 (7)	20 (9)	10 (9)
^{58}Co	Co	1.0 (0.7)	0.2 (0.2)	0.4 (0.2)
^{89}Zr	Zr	5.3-5.8 (2.5)	30-36 (40)	14 (< 10)
^{92m}Nb	Nb	< 7 (0.8)	< 70 (54)	< 1.6 (0.2)
	Mo	< 54 (24)	< 542 (300)	< 11 (4)

* Values in parentheses are concentrations obtained by chemical analysis.

maximum possible values were evaluated for Nb and Mo impurities. Also in analysis of ^{89}Zr, two paths through ^{90}Zr(n,2n)^{89}Zr and ^{92}Mo(n,α)^{89}Zr reactions were considered. Although Zr impurity could evaluated by subtracting the contribution from the ^{92}Mo(n,α)^{89}Zr reaction, the concentrations have spread due to unfixed Mo concentrations described above.

The results of present activation analysis were almost consistent with those obtained by chemical analysis. For material recycling, Aluminum is one of harmful impurities due to production of ^{26}Al with half-life of 7.4×10^5. It is confirmed that the concentration of Al in NIFS-HEAT-2 satisfied the criteria of 91 ppm proposed by Dolan et al.[1]. Unexpected impurity element, which was difficult to be detected in the chemical analysis, has not been found in the gamma-ray spectrum analysis.

Fig.6.4-2 shows an example of spectra obtained with the WEAS in decay heat measurement of NIFS-HEAT-2. Peaks corresponding to beta and gamma rays from ^{48}Sc were

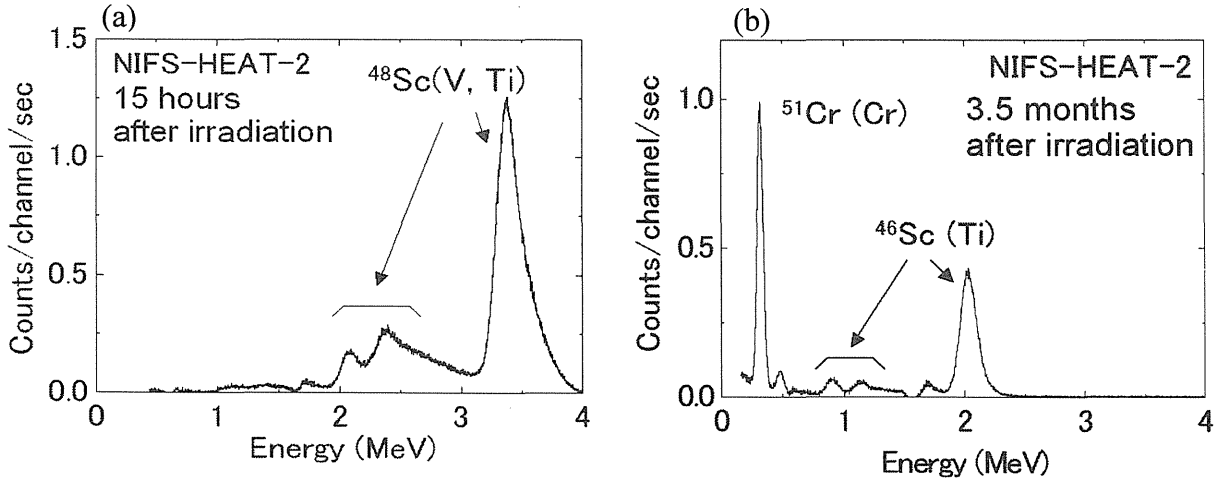

Fig. 6.4-2 Examples of spectra obtained with Whole Energy Absorption Spectrometer (WEAS) at (a) 15 hours and (b) 3.5 months after irradiation.

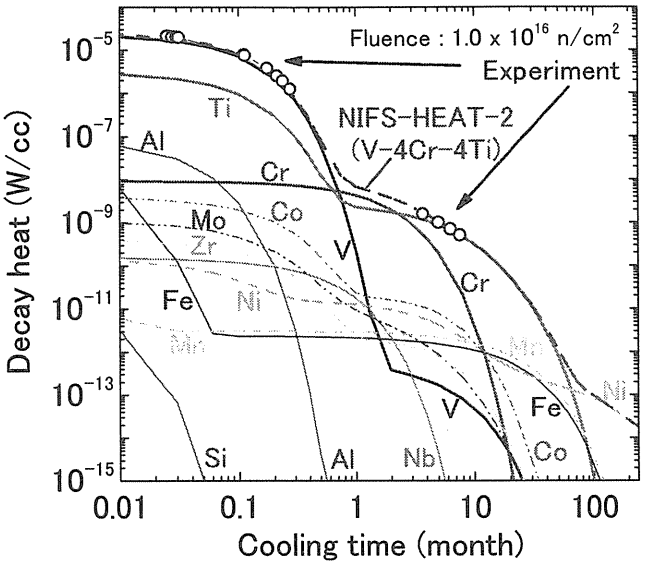

Fig. 6.4-3 Comparison between experimental and calculated values of decay heat of NIFS-HEAT-2. Decay heat calculation was performed considering impurity concentrations evaluated in the present activation analysis.

observed after cooling time of 15 hours. In the spectra obtained at 3.5 months after irradiation, peaks from ^{46}Sc and ^{51}Cr were dominant components. Significant influence of impurity elements was not observed in the measurement until 8 months after irradiation. Decay heat was evaluated by integrating energies of detected radiations. Uncertainty in the measurement was estimated to be ~10 % mainly due to correction of detection efficiency, fluctuation of background radiations and slight shift of detector bias voltage.

Evaluated values are plotted in Fig. 6.4-3 with calculated lines of decay heat. Impurity concentrations evaluated in the activation analysis were considered in the calculation. During 0.7-8 days after irradiation, values calculated with ACT-4 and JENDL Activation File were ~10% lower than those evaluated from the measurement. During 3-8 months after irradiation, calculated values were ~15% higher than experimental results. The decay curves in Fig. 6.4-3 indicated that activation of impurities will be dominant at ~6 years after irradiation mainly due to ^{60}Co transmuted from Ni. Decay heat measurement will be continued for confirmation of the present estimation.

6.4.4 Conclusion

For impurity analysis and direct evaluation of activation properties of vanadium alloys, activation experiments with DT neutron irradiations were performed on NIFS-HEAT-2 and Round-Robin samples from the US and China. Eight nuclides of ^{24}Na, ^{28}Al, ^{54}Mn, ^{56}Mn, ^{57}Co, ^{58}Co, ^{89}Zr and ^{92m}Nb were identified from analysis of the gamma peaks and concentrations of Al, Si, Mn, Fe, Ni, Co, Zr, Nb and Mo were evaluated. It was confirmed that the concentration of Al in NIFS-HEAT-2, which is harmful for low activation property, was

lower than the criteria required for recycling of used material after reactor shutdown. The results were almost consistent with those by chemical analysis.

Until ~8 months after irradiation, significant influence of impurities was not observed in the decay heat measurement. Results of decay heat measurement with the Whole Energy Absorption Spectrometer and those of calculation with MCNP-4C, ACT-4 and JENDL Activation File were consistent within ~15%. Activation calculation considering impurity concentrations from the present analysis indicated that decay heat of ^{60}Co transmuted from Ni impurity will be dominant ~6 years after irradiation.

References

[1] T. J. Dolan and G. J. Butterworth, Fusion Technol., **26**, 1014-1020 (1994).

[2] E. T. Cheng and T. Muroga, Fusion Technol., **39**, 981-985 (2001).

[3] M. L. Grossbeck, R. L. Klueh, E. T. Cheng, J. R. Peterson, M. R. Woolery and E. E. Bloom, J. Nucl. Mater., **258-263**, 1778-1783 (1998).

[4] E. T. Cheng, J. Nucl. Mater., **258-263**, 1767-1772 (1998).

[5] T. Nagasaka, T. Muroga, M. Imamura, S. Tomiyama and M. Sakata, Fusion Technol., **39**, 659-663 (2001).

[6] T. Muroga, T. Nagasaka, K. Abe, V. M. Chernov, H. Matsui, D. L. Smith, Z.-Y. Xu and S. J. Zinkle, J. Nucl. Mater., **307-311**, 547-554 (2002).

[7] T. Nagasaka, T. Muroga, Y. Wu, Z. Xu and M. Imamura, J. Plasma Fusion Res. SERIES, **5**, 545-550 (2002).

6.5 Evaluation of Radiation Induced Conductivities of Ceramic Coating Materials for Li/V blanket system

Teruya TANAKA, Akihiro SUZUKI[1], Ryo NAGAYASU[2], Takeo MUROGA, Satoshi SATO[3], Kentaro OCHIAI[3], Fuminobu SATO[2], Toshiyuki IIDA[2], Takeo NISHITANI[3]

Fusion Engineering Research Center, National Institute for Fusion Science, Toki, Gifu

[1]Nuclear Engineering Research Laboratory, University of Tokyo, Tokai, Ibaraki

[2]Department of electronic, information systems and energy engineering, Osaka University, Suita, Osaka

[3]Fusion Neutron Laboratory, Japan Atomic Energy Research Institute, Tokai, Ibaraki

6.5.1 Introduction

In the development of Li/V blanket system, MHD pressure drop of liquid Li coolant crossing magnetic field is one of important issues to be solved [1]. Since the phenomenon is caused by induced electrical current flowing between liquid Li and metal duct wall, fabrication of thin insulating coating on the duct wall has been studied for reduction of the pressure drop [2-4]. As candidate materials for the coating, nonconventional ceramics have been selected by focusing on their chemical stability in highly corrosive liquid Li. Recently, it was confirmed that ceramic materials such as Y_2O_3, Er_2O_3, $CaZrO_3$ etc. were stable in liquid Li of 1073K for 1000 h [5, 6].

As to electrical property of the insulating coating, the required conductivity for effective reduction of the MHD pressure drop was estimated to be $< 1.0 \times 10^{-2}$ S/m [6]. However, the insulating performance of the materials will be degraded due to the radiation induced conductivity (RIC) effect in an intense radiation environment [7]. Examination of electrical properties under radiations is indispensable in development of insulating materials for fusion reactors. Various data on the RIC effect have been evaluated mainly for Al_2O_3 and MgO. However, almost no data are available for the candidate materials.

In the present study, radiation induced conductivities of the candidate materials for the insulating coating were examined under DT neutron irradiations at FNS facility.

6.5.2 Experiment

Radiation induced conductivities were examined for both of bulk and coated specimens. Bulk specimens were an Y_2O_3 plate of $5.0 \times 5.0 \times 1.0$ mm^3 (supplied from TEP Corp., 3.3×10^{-13} S/m), an Er_2O_3 disc of 7.5 mm$\phi \times$ 1.0 mm (TYK Corp., 5.0×10^{-14} S/m) and a $CaZrO_3$ disc of 15 mm$\phi \times$ 3.5 mm (TYK Corp., 8.8×10^{-13} S/m) made by sintering method. On both sides of the specimens, Pt electrodes of ~200 nm in thickness were made by sputter deposition. As shown in Fig.6.5-1 (a), a guard electrode was made around a center electrode

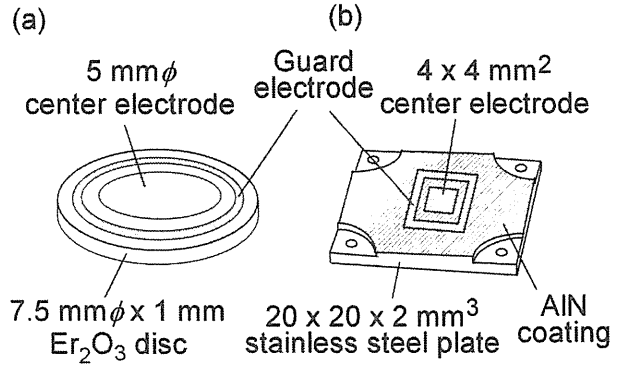

Fig. 6.5-1 Schematic drawing of irradiated specimens. (a) Er_2O_3 bulk specimen and (b) AlN coated specimen.

to prevent surface leakage current. Coated specimens of AlN and Y_2O_3 were prepared on stainless steel plates of 2 mm in thickness by RF sputtering method [8]. Thickness of the coating layers were 2.5 μm and 7.0 μm for AlN specimens (1.1×10^{-13} S/m and 1.0×10^{-13} S/m) and 2.5 μm for Y_2O_3 specimen (8.0×10^{-13} S/m). A center electrode of 4 x 4 mm^2 and a guard electrode were made by sputter deposition of Pt or painting of silver paste (Fig.6.5-1 (b)). Bias voltages were applied to the stainless steel plates.

Schematic arrangement of measurement system is shown in Fig.6.5-2. Specimens were located close to the tritium target bombarded with 350 keV D^+ beam. A lead wire for leakage current measurement was connected to the specimen through an acrylic pipe to prevent the influence of electric charges accumulated in a coaxial cable. A high resistance meter (Keithley 6517A) was used for both of voltage supply and current measurement. Insulating properties of the specimens were evaluated from changes in currents flowing into the center electrodes under DT neutron irradiations. The present measurements were performed at room temperature. Neutron flux was changed by adjustment of D^+ beam current.

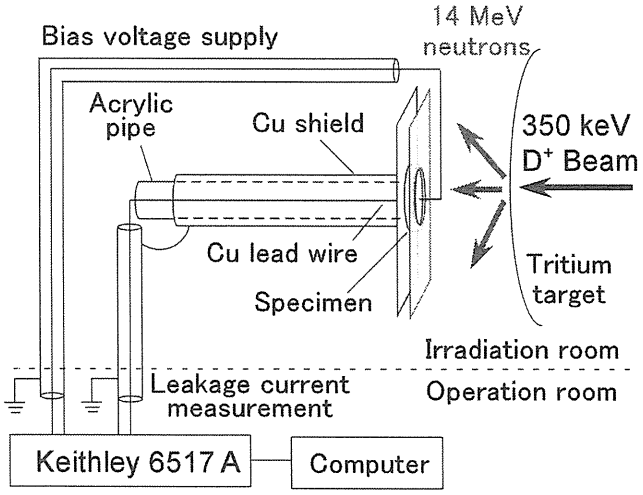

Fig. 6.5-2 Schematic arrangement of measurement system for examination of insulating properties of coating materials

The maximum neutron flux was 8.0×10^9 n/cm^2/s for the $CaZrO_2$ specimen and 4.2-7.8 $\times 10^8$ n/cm^2/s for other specimens. Contribution of induced gamma rays to total dose rate (Gy/s) was estimated to be ~30% for the Er_2O_3 specimen and ~10% for the others by transport calculation using MCNP code [9].

6.5.3 Results and Discussion

Fig.6.5-3 shows changes in neutron flux and current flowing through the AlN coated specimen. The current changed coincidentally with the neutron flux. Similar responses were observed for all of the bulk and coated specimens. Radiation induced conductivities were evaluated from the flux dependences in the current measurements. The values extrapolated or interpolated to dose rate of 0.01 Gy/s were 1.3×10^{-10} S/m (Y_2O_3), 5.3×10^{-11} S/m (Er_2O_3) and 3.1×10^{-11} S/m ($CaZrO_3$) for the bulk specimens, and 7.6×10^{-12} S/m (AlN, 2.5 μm), 1.9 $\times 10^{-11}$ S/m (AlN, 7.0 μm) and 6.3×10^{-12} S/m (Y_2O_3, 2.5 μm) for the coated specimens.

The present results were plotted in Fig.6.5-4 with previous evaluations for Al_2O_3 [10]. Close and open symbols are the results for the bulk and coated specimens, respectively. The radiation induced conductivities for the ceramic coating materials were the same level or one order higher compared with those for Al_2O_3. At first wall in fusion reactors with Li/V blanket system, dose rate is considered to be several kGy/s for the ceramic coating materials [11]. The extrapolation of the results indicates that the degradation of insulating properties should be within allowable level for application to Li/V blanket system, i.e. $< 10^{-2}$ S/m, in the present experimental condition.

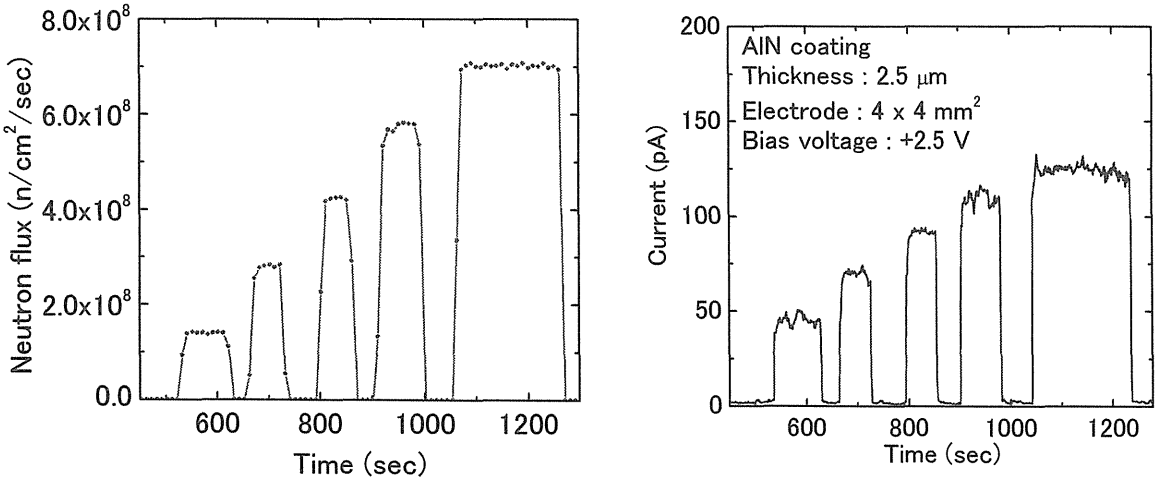

Fig. 6.5-3 Example of current measurements under DT neutron irradiations.
(a) Change in neutron flux. (b) Change in current flowing through AlN coated specimen.

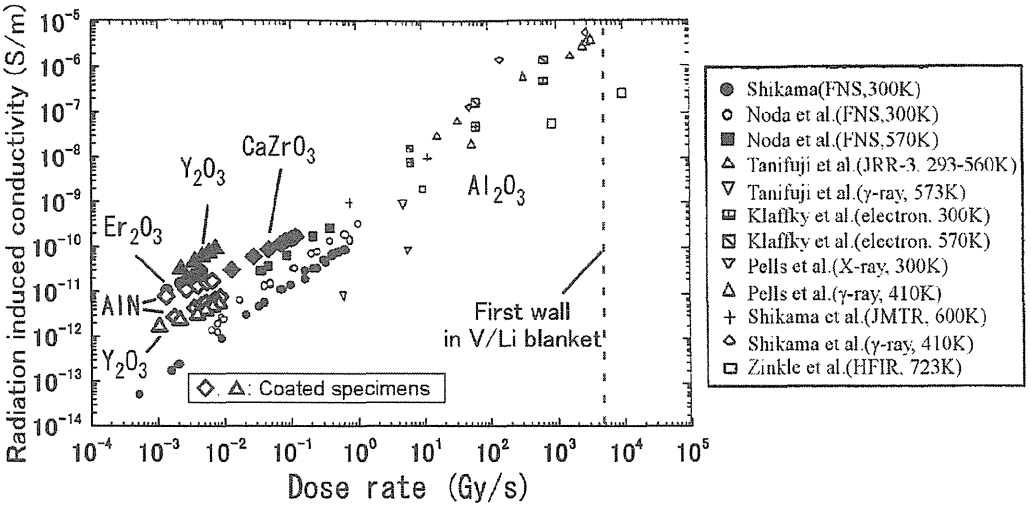

Fig. 6.5-4 Radiation induced conductivities of ceramic coating materials evaluated by the present DT neutron irradiations. Close and open symbols are results for bulk and coated specimens, respectively. Plots of Al_2O_3 are extracted from Ref. 10 for comparison.

6.5.4 Conclusion

Insulating properties of the coating materials for Li/V blanket system were examined under DT neutron irradiations. Evaluated radiation induced conductivities of the bulk and the coated specimens were 3.1×10^{-11} - 1.3×10^{-10} S/m and 6.3×10^{-12} - 1.9×10^{-11} S/m for dose rate of 0.01 Gy/s, respectively. The extrapolation of the results indicated that the degradation of insulating properties due to RIC should be within allowable level for application to Li/V blanket system. Further evaluation is planed at higher temperature.

References

[1] S. Malang, P. Leroy, G. P. Casini, et al., Fus. Eng. Des. **16**, 95-109 (1991).

[2] K. Natesan, C. B. Reed, D. L. Rink, et al., J. Nucl. Mater. **258-263**, 488-494 (1996).

[3] D. L. Smith, K. Natesan, J. -H. Park, et al., Fus. Eng. Des. **51-52**, 185-192 (2000).

[4] T. Terai, A. Suzuki, T. Yoneoka, et al., J. Nucl. Mater. **283-287**, 1322-1325 (2000).

[5] B. A. Pint, J. H. DeVan and J. R. DiStefano, DOE / ER-0313 / 31. Dec, 2001, Fusion Materials Semi-Annual Progress Reports, pp.132-133.

[6] A. Suzuki, T. Muroga, B. A. Pint, et al., Fus. Eng. Des. **69**, 397-401 (2003).

[7] V. A. J. van Lint, J. W. Harrity, et al., IEEE Trans. Nucl. Sci., **NS-15**, 194-204 (1968).

[8] A. Sawada, A. Suzuki, T. Terai and T. Muroga, will be published in J. Nucl. Mater..

[9] J. F. Briesmeister, MCNP-A general Monte Carlo n-particle transport code, LA-12625-M, 2000.

[10] T. Shikama, JAERI-Research 98-053 (1998), pp.11-18.

[11] L. A. El-Guebaly and The ARIES Team, Fus. Eng. Des. 38 (1997) 139-158.2", J. Nucl. Sci. Technol., **32**, 1259 (1995).

6.6 Radiation Hardness of Pre-annealed Optical Fibers

Kentaro TOH, Tatsuo SHIKAMA, Shinji NAGATA, Bun TSUCHIYA, Tetsuya SUZUKI, Keiji OKAMOTO, Michinori YAMAUCHI[1], Takeo NISHITANI[1], Masahiro ISHIHARA[2]
Institute for Materials Research, Tohoku University, Sendai
[1]*Fusion Neutron Laboratory, Japan Atomic Energy Research Institute, Tokai, Ibaraki*
[2]*department of JMTR, Japan Atomic Energy Research Institute, Oarai, Ibaraki*

6.6.1 Introduction

Optical devices are candidate for the signal transmission devices and as dosimeters in radiation environment, because these devices have several advantages over electrical measurements. Advantages include no electrical noises, no transmission of electrical signals, wide optical signal bands, etc. However, Optical fibers have the disadvantage that an increase of the radiation induced transmission loss as the irradiation time elapsed. This loss varies in a complicated way with the optical fiber's composition, temperature, dose rate, total absorbed dose, and wavelength of transmitted light.

It will be necessary to take account of the generation of the color centers, which is origin of radiation induced transmission loss, in the optical fiber induced by radiations, because the radiation resistance of optical fiber is strongly depend on the color centers. In radiation environment, electron-hole pairs are generated by radiation and the color centers are generated by the defect in the fibers captured the electron-hole pairs. Therefore, it is necessary to decrease the intrinsic defect for developing the radiation resistance of the fiber. The fused silica optical fiber has intrinsic defects induced by the fiber drawing process [1,2]. Therefore, we considered the reduction of the intrinsic defect after drawing process.

In this paper, fused silica optical fiber is pre-annealed before irradiation after drawing process. After the heat-treatment, irradiation test is carried out at the cobalt-60 gamma-ray irradiation facility and fast neutron source.

6.6.2 Experiments

The material used in this experiment was fused silica core optical fiber. The main component of the fiber was SiO_2 and the diameter of core/clad was 0.2/0.25 mm. The mother rod of the fiber was KS-4V fabricated by the Fibre Optic Research Centre (FORC-Moscow) and the rod was drawn by Fujikura Corp. in Japan. The fiber was coiled with diameter 100 mm for the irradiation, and the length of the coiled optical fiber was 10 m. The coiled optical fibers were annealed before irradiation at 140, 160, 180, 200, 220 and 300°C in the air for 3 hours. The heating and cooling rates were not controlled precisely.

The transmission light in the optical fiber was observed using a white light source

(Ando Electric, AQ-4303B) and optical spectrum analyzer (Ando Electric, AQ-6315A). The optical detector can measure optical signals with wavelength range from 400 to 1700 nm.

The irradiation test was performed at a Co-60 gamma-ray irradiation facility in Tohoku University and a fast neutron irradiation facility of the Fusion Neutronics Source (FNS) in Japan Atomic Energy Research Institute (JAERI). The intensity of the gamma-ray source is 4.07 TBq and the absorbed dose rate is 7.2×10^{-3} Gy/s. The energy of the neutrons of FNS has a sharp peak at 14.1 MeV. The flux of fast neutrons is 3.6×10^{9} n/cm^{2}s and the gamma-ray dose rate is low.

6.6.3 Results and Analyses

The transmission loss of all fibers irradiated by gamma-ray and fast neutron became large with similar tendency as the irradiation time elapsed. An example of the irradiation experimental results, the radiation-induced transmission losses of the optical fiber pre-annealed at 180°C under ^{60}Co gamma-ray irradiation are shown in Fig. 6.6-1. This shows that the optical transmission loss at wavelength less than 700 nm is much larger than that in the infrared wavelength range. The increase of the transmission loss in the fused silica optical fiber was caused by the generation of several color centers in silica, and the transmission loss in the visible wavelength range mainly consisted of two components. Optical absorption shorter than 400 nm was ascribed to E' center and that around 630 nm was ascribed to Non

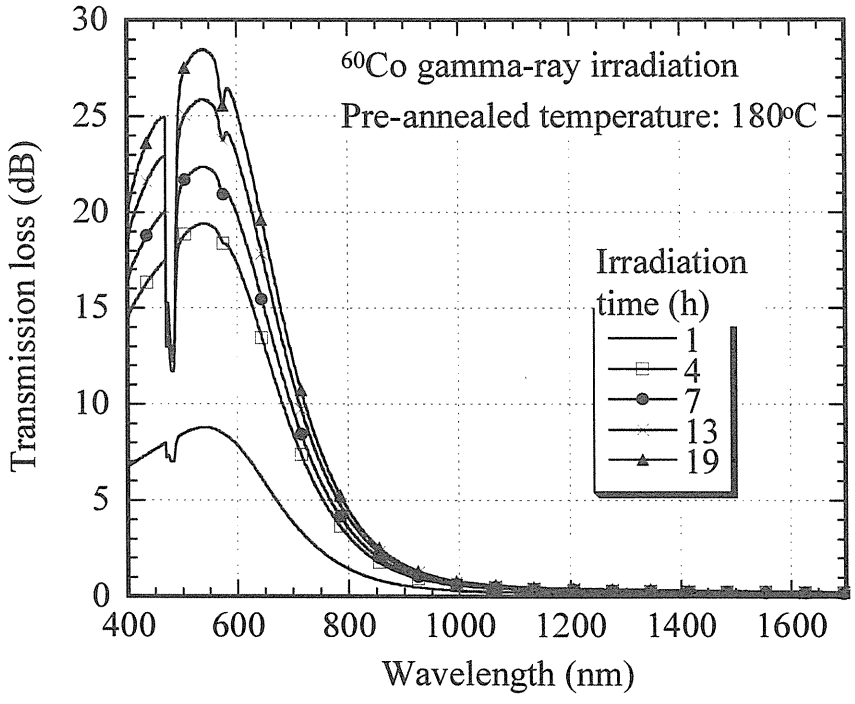

Fig. 6.6-1. Transmission loss of the optical fiber pre-annealed at 180°C under ^{60}Co gamma-ray irradiation.

Bridging Oxygen Hole Centers (NBOHC) [3,4]. Here, the absorption peak of NBOHC was not observed clearly, because the transmission loss of E' center was much larger than that of NBOHC. One can see that Figure 1 has the irregular drop of optical signals around 480 and 570 nm. These irregular signals were not real optical signals caused by physical phenomena of optical fiber but optical noises depending on the optical spectrum analyzer.

Figures 6.6-2 and 6.6-3 show the optical transmission loss by the gamma-ray irradiation as a function of the pre-annealing temperature at 630 nm and 1390 nm, respectively. Figures 4 and 5 show the optical transmission loss by the fast neutron irradiation as a function of the pre-annealing temperature at 630 nm and 1390 nm, respectively. It was obvious from Figs. 6.6-2, -3, -4 and -5 that the transmission loss could be decreased by the annealing treatment before irradiation. Comparison of all temperature conditions, we can estimate that there is an optimum heat-treatment temperature to minimize the radiation induced transmission loss. The mechanism for having the optimum temperature is complicated and not easy. It is considered that the heat-treatment before irradiation could decrease the intrinsic defects. These defects are generated during the drawing process of the optical fiber and act as precursors of the color center. Therefore, the radiation induced transmission loss decrease by heat treatment. And the fibers used in this experiment have the polymer jacket and the jacket can be degraded easily by heat treatment. Therefore, the loss become large as the pre-annealed temperature becomes high.

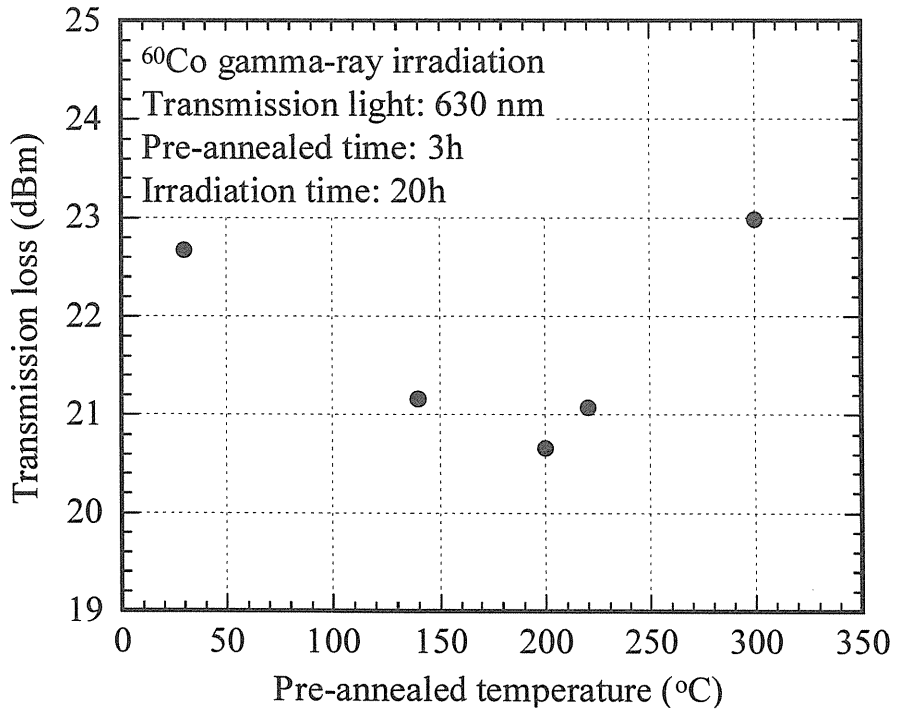

Fig.6.6-2. Pre-annealed temperature dependence of transmission loss of optical fiber at 630 nm under ^{60}Co gamma-ray irradiation.

It was found that the optimum temperature depended on the wavelength of the transmission light. The precursor of color center is defined at the wavelength, for example the peaks at 630 and 1390 nm are attributed to the NBOHC and Si-OH. Therefore, it is considered that the heat treatment effect varies with the kind of precursor of color center.

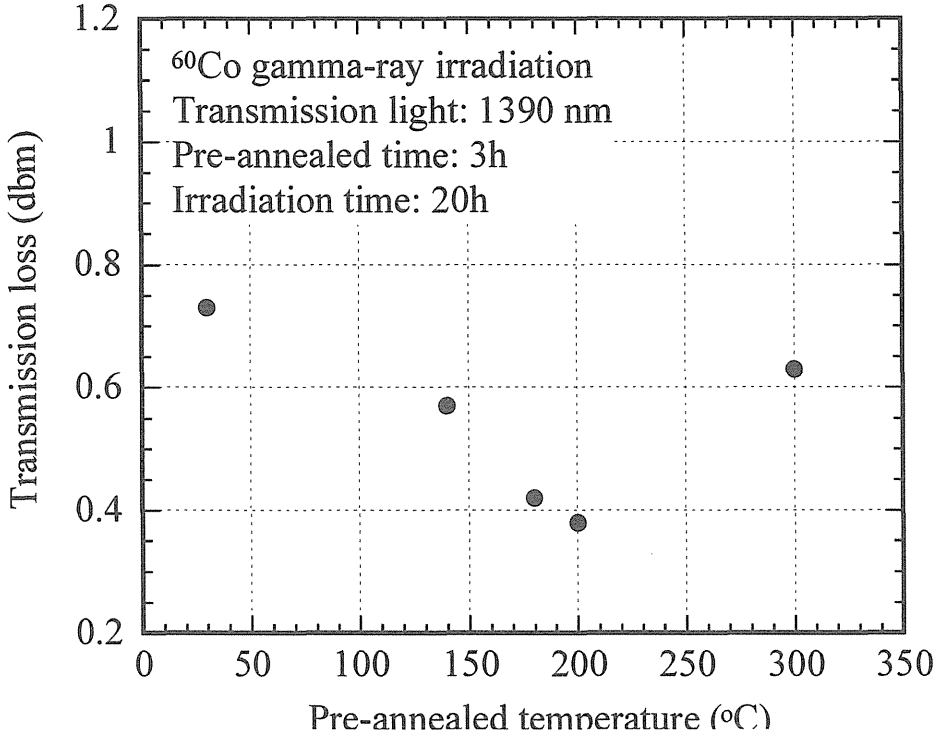

Fig. 6.6-3. Pre-annealed temperature dependence of transmission loss of optical fiber at 1390 nm under ^{60}Co gamma-ray irradiation

The optimum temperature is different between ^{60}Co gamma-ray and fast neutron irradiation, and the temperature might be near 200 and 100°C, respectively. The main gamma-ray energies of Co-60 are 1.17 and 1.33 MeV, and the dominant interaction with optical fiber is the Compton effect. The energy of fast neutron is 14 MeV and the dominant interactions with fiber are the atomic displacement and the knock-on effect. Therefore, I believed that the transmission loss under gamma-ray irradiation is mainly caused by the intrinsic defects of fused silica core fiber, and the loss under fast neutron irradiation is mainly caused by the displacement of the SiO^2 network. In other words, dominant component of precursors under gamma-ray and fast neutron irradiation are intrinsic defect and silica networks, respectively. It is considered that the difference of the optimum temperature arises from the difference of the generation process of transmission loss. However, that process is not cleared. It is necessary to perform more detailed researches used other experimental system, for example electron spin resonance (ESR), etc.

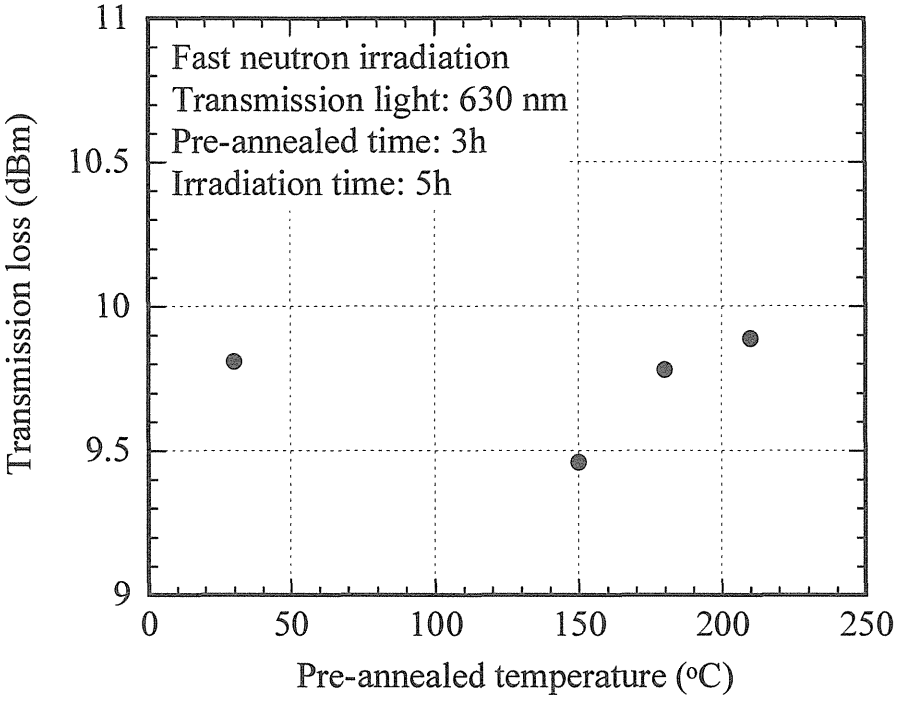

Fig.6.6-4. Pre-annealed temperature dependence of transmission loss of optical fiber at 630 nm under fast neutron irradiation

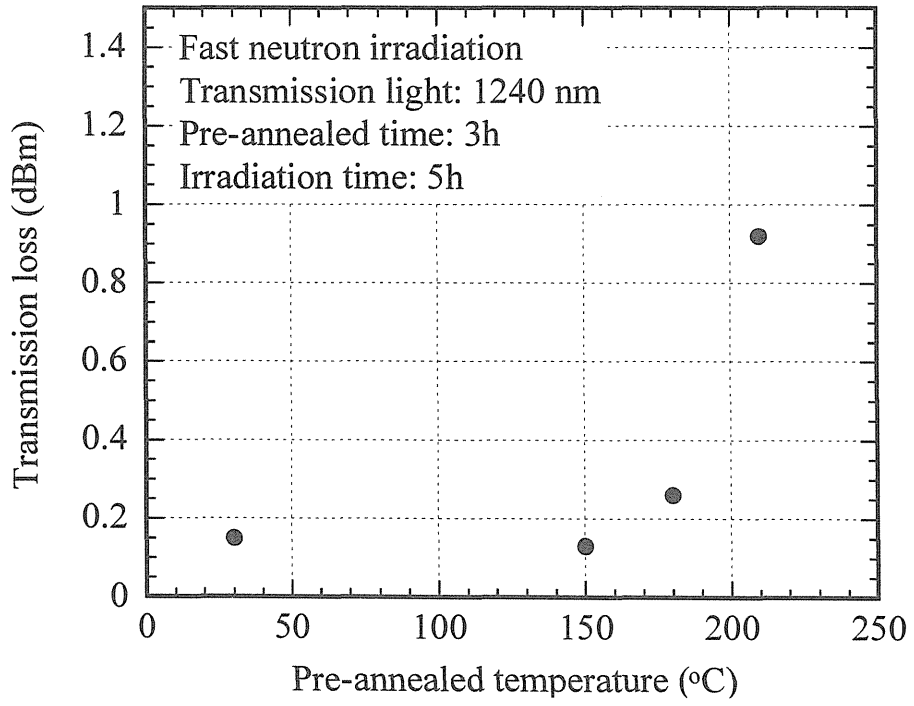

Fig. 6.6-5. Pre-annealed temperature dependence of transmission loss of optical fiber at 1390 nm under fast neutron irradiation.

6.1.4 Conclusion

Pre-annealing effect and the temperature dependence of radiation induced optical transmission loss was investigated using the Co-60 gamma-ray and 14 MeV fast neutron source. The transmission losses in the visible wavelength range were much larger than in the infrared wavelength range, and the loss could be reduced in the whole wavelength range by the heat-treatment before irradiation. The reduction of transmission loss by the heat-treatment after drawing process before irradiation had the temperature dependence. It is found that an optimum temperature to minimize the transmission loss (radiation damage) exists, in other words, the radiation resistance can improve by the heat treatment of a specific temperature. The optimum temperature might be near 200 and 100°C under gamma-ray and fast neutron irradiation, respectively.

References

[1] S. Karasawa, N. Horiuchi, T. Takada, Nucl. Instr. and Meth. B **47**, 404 (1990).

[2] Jong-Won Lee, G.H. Sigel Jr, Jie Li, J. Non-Cryst. Solid. B**239**, 57 (1998).

[3] K. Nagasawa, Y. Hoshi, Y. Ohki, K. Yahagi, Jpn. J. Appl. Phys. **25**, 1224 (1985).

[4] D.L. Griscom, M.E. Gingerich, E.J. Friebele, Phys. Rev. Lett. **71**, 1019 (1993).

6.7 Optical Fast Neutron and Gamma-ray Detection by Radioluminescence

Tatsuo SHIKAMA, Kentaro TOH, Shinji NAGATA, Bun TSUCHIYA, Michinori YAMAUCHI[1], Takeo NISHITANI[1], Tetsuya SUZUKI, Keiji OKAMOTO, Naoki KUBO, Masahiro ISHIHARA[2], Tsunemi KAKUTA[1]

Institute for Materials Research, Tohoku University, Sendeai

[1]*Fusion Neutron Laboratory, Japan Atomic Energy Research Institute, Tokai, Ibaraki*

[2]*Department of JMTR, Japan Atomic Energy Research Institute, Oarai*

6.7.1 Introduction

A possibility of applying a compact optical diagnostics to nuclear systems, such as detecting high energy neutrons in a nuclear fusion system and measuring a high-flux gamma-ray in a fission reactor with a wide dynamic range, has been studied, utilizing radiation resistant optical fibers and radioluminescent (radiation-induced luminescent) materials.

A development of reliable diagnostics of high energy neutrons is one among most important scientific and engineering topics for successful operation of a burning-plasma machine such as International Thermonuclear Experimental Reactor (ITER). Several techniques have been under consideration and some of them were demonstrated their possible feasibility in current machines, but with very low neutron flux&fluence and an associated low gamma-ray flux. A fusion-neutron diagnostic system should operate reliably with a neutron flux up to 10^{13}n/m^{2}s and an associated gamma-ray dose rate up to 1Gy/s, in an ITER-like machine. To be compatible with a realistic and expensive maintenance scenario, a system would better to survive a neutron fluence of 10^{21}n/m^2. Also, it is strongly preferable that a neutron sensing system is position-sensitive with a space resolution as high as possible and is as compact as possible. The optical system examined in the present study was found to satisfy these postulated above, through experiments with fusion-neutrons and gamma-rays.

6.7.2 Experiments

Several materials, which were expected to radiate luminescence, were attached at an end of a radiation resistant optical fiber whose core-diameter was 200μm and were exposed to high energy neutrons generated by the deuterium-tritium (D-T) reaction in the Fast Neutron Source (FNS) of Japan Atomic Energy Research Establishment (JAERI) in Tokai, and to gamma-rays from cobalt-60 sources in the JAERI-Takasaki, at room temperature. The fast neutron flux was in the range of $10^{12\text{-}13}$n/m^{2}s in the FNS and the gamma-ray dose rate was about 5Gy/s in the JAERI-Takasaki gamma-ray facility. An optical signal was guided through a 30 m long radiation resistant optical fiber, which was developed in the ITER-EDA (ITER

Engineering Design Activity) framework for the purpose of applying optical fibers to in-vessel components in the ITER [1,2], to a measuring instrument composed of an optical grating and a CCD, the PMA-11 made by Hamaphoto Co. Ltd.

6.7.3 Results and Analyses

Three materials, silver activated zinc sulfide (ZnS-Ag), copper activated zinc sulfide (ZnS-Cu), and a strontium aluminate doped with europium and dysprosium ($SrAl_2O_4$-EuDy), were found to be radioluminescent, being sensitive to high energy neutrons with a peak position at 450nm, 570nm, and 500nm, respectively, having a half width of 75-150nm. Figure 6.7-1 shows a luminescent spectrum from the ZnS-Ag under a fast neutron flux of about $10^{12}n/m^2s$. The ZnS-Ag had the strongest luminescence among three but its intensity decreased with the increase of neutron fluence, in the meantime, the other two, the ZnS-Cu and the $SrAl_2O_4$-EuDy had relatively weak luminescent intensity but their peak intensity did not change substantially with the fast neutron fluence up to $10^{20}n/m^2$. Changes of the

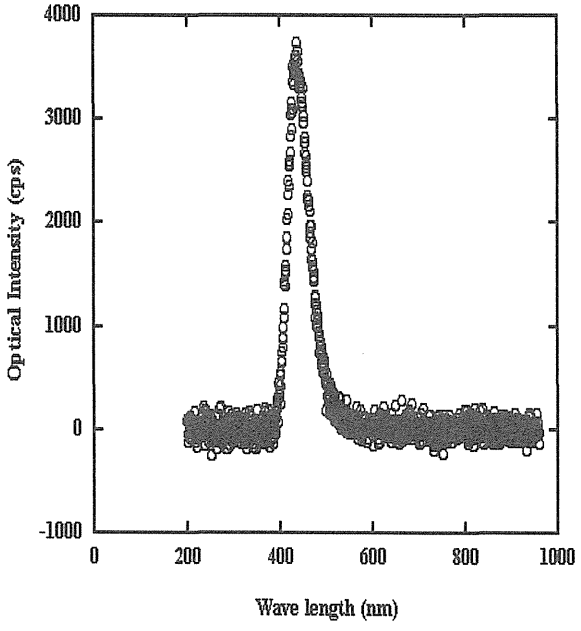

Fig.6.7-1 Radioluminescent spectrum from ZnS-Ag under fusion neutron irradiation.

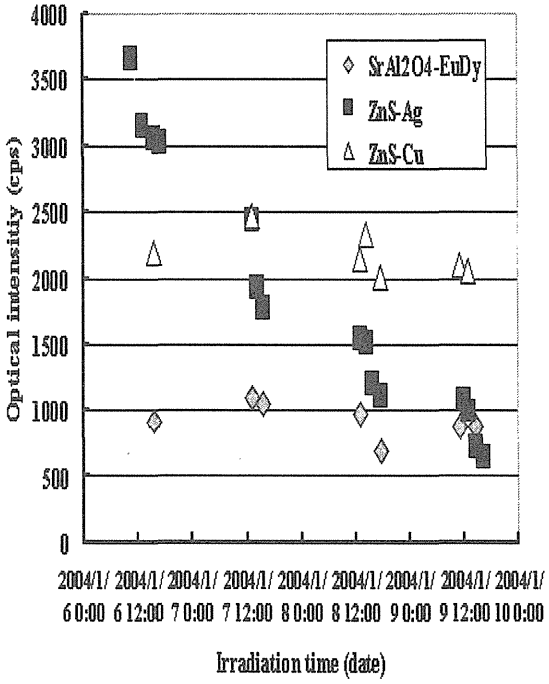

Fig.6.7-2 Change of optical intensity in the course of fusion neutron irradiation at FNS.

luminescent peak intensities are shown in Fig 6.7-2 as a function of irradiation time. For a high sensitivity, the ZnS-Ag is the best among three, but for a long-term stability and being free from frequent re-calibration or replacement, the ZnS-Cu and the $SrAl_2O_4$-EuDy are preferable.

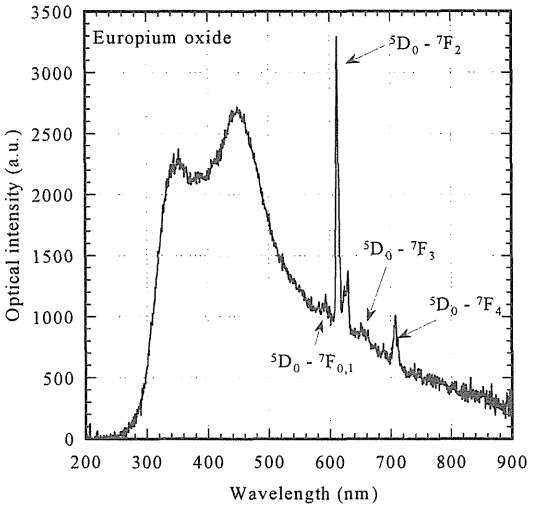

Fig.6.7-3 Radioluminescent spectrum from europium oxdide under gamma-ray irradiation.

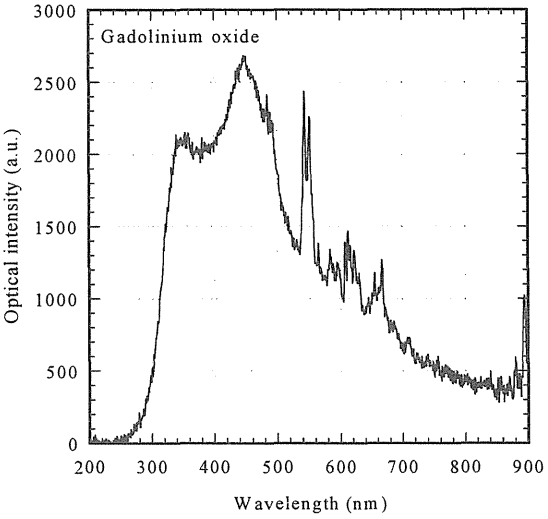

Fig.6.7-4 Radioluminescent spectrum from gadolinium oxide under gamma-ray irradiation

Under the gamma-ray irradiation, only the $SrAl_2O_4$-EuDy showed radioluminescence, but radioluminescent peaks were not detected by the present measuring system in the ZnS-Ag, and the ZnS-Cu. Being insensitive to a gamma-ray will be good in general for neutron diagnostics and the ZnS-Ag, and ZnS-Cu will be preferable to the $SrAl_2O_4$-EuDy. Thus, the ZnS-Cu is the best at present as a sensing element for fusion neutron diagnostics. The ZnS-Cu in the present system can detect the fast neutron flux down to $10^{11}n/m^2s$ with an integration time of 10 s. However, it is estimated that the system can detect a fast neutron flux down to $10^9n/m^2s$ with an integration time less than 1 s, with a photomultiplier system working at a fixed optical wavelength region. A dimension of a sensing element will be in the order of 0.1mmϕ.Thus, the present results showed that the optical fast neutron detecting system with a high space resolution can be composed with a radiation resistant optical fiber and a neutron sensitive ZnS-Cu element, which is compact and easy to install and dismantle in a limited space in a burning plasma machine such as the ITER.

For measuring a gamma-ray flux, several radioluminescent materials are now

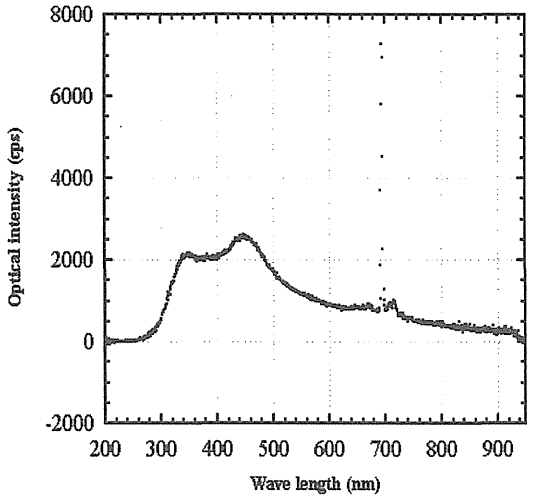

Fig.6.7-5 Radioluminescent spectrum from ruby under gamma-ray irradiation.

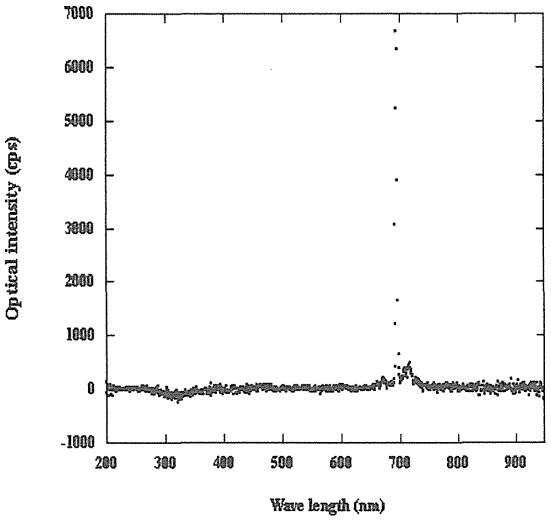

Fig.6.7-6 Spectrum obtained by subtracting radioluminescence from fused silica optical fibers from spectrum shown in Fig.6.7-5

available, such as chromium doped alumina (ruby) (Al_2O_3-Cr), europium oxide (EuO_2), and gadolinium oxide (GdO_2), which are insensitive to neutrons. [3] Figures 6.7-3, -4, and -5 show radioluminescent spectra under the gamma-ray irradiation. Here, it should be noted that the silica core optical fiber itself also generate radiation induced luminescence, which is composed of a peak at 450nm and a Cerenkov radiation in the case of gamma-irradiation. [4,5] However, superimposed radioluminescence from the optical fiber can be easily subtracted from the obtained spectra as shown in Fig.6.7-6 for the case of ruby. The ruby is well-known radeioluminescent material and it can work as a gamma-ray detector with a wide dynamic range from 10^{-3}Gy/s to 10^{3}Gy/s. However, the intensity of its peak at 690nm decreases rapidly with increase of a displacement irradiation dose and with increase of the irradiation temperature as shown in Fig. 6.7-7, because the ruby is a dopant-activated luminescent material. [5,6] In the meantime, intensity of the radioluminescent peaks from the europium oxide and the gadolinium oxide showed more stable behavior with increase of the displacement dose, as they are intrinsic luminescent material. A gamma-ray measuring system with a dynamic range of 10^{-3} - 10^{3}Gy/s could be realized with the gadolinium oxide in a temperature range of room temperature to 300C. The system could be applied not only to a post-irradiation facilities such as a spent fuel handling system and so-called hot cells but also to a core-region monitoring in a power generating fission reactor.

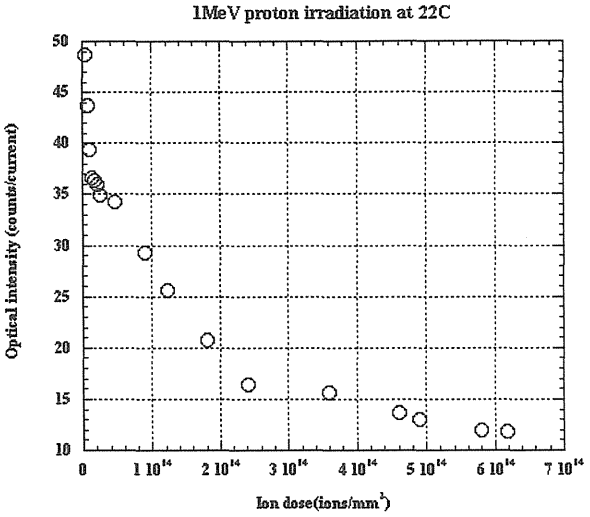

Fig.6.7-7 Optical intensity of radioluminescent peak at 690nm from ruby under proton irradiation [5,6]

6.7.4 Conclusion

Radiation-diagnostics system using radioluminescence sensor was proposed. Radioloumineseece materials responding to gamma-rays and 14MeV neutrons were found and their behaviors were studied under 14MeV neutrons and gamma-ray. The system could be applied to heavy irradiation environments.

References

[1] S.Yamamoto, T.Shikama, V.Beryakov, E.Farnum, E.Hodgson, T.Nishitani, D.Orlinski, S.Zinkle, S.Kasai, Pstott, K.Young, V.Zaveriaev, A.Costley, L.deKock, C.Walker, G.Janeschitz, J. Nucl. Mater., **283-287**, 60-69 (2000).

[2] T.Shikama, T.Kakuta, N.Shamoto, M.Narui, T.Sagawa, Fus. Eng. Design, 51-52, 179-183 (2000).

[3] K. Toh, T. Shikama, S. Nagata, B. Tsuchiya, T. Kakuta, T. Hoshiya, M. Ishihara, Fusion. Sci.Technol. **44**, 475-476 (2003).

[4] T.Shikama, M.Narui, T.Kakuta, H.Kayano, T.Sagawa, and K.Sanada, Nucl. Instr. Methds, B91, 342-345 (1994).

[5] S.Nagata, et al., submitted to J. Nucl. Mater..

[6] S.Nagata, N.Kubo, et al, private communication, to be published.

7. Developments of Measurement Technique

7.1 Micro Fission Chamber for the ITER Neutron Monitor

Michinori YAMAUCHI, Takeo NISHITANI, Kentaro OCHIAI, Junichi HORI[1], Katsuyuki EBISAWA[2]

Fusion Neutron Laboratory, Japan Atomic Energy Research Institute, Tokai, Ibaraki

[1]Kyoto University, Kumatori

[2]Toshiba Co. Ltd., Tokyo

7.1.1 Introduction

Micro-fission chamber is a candidate diagnostic device to measure the fusion power, which is one of the basic control parameters. In present large tokamak facilities such as JET, TFTR or JT-60U, the neutron yield measurement has been carried out using ^{235}U or ^{238}U fission chambers installed outside the vacuum vessel [1-3]. Detection efficiencies in this method are easily affected by surrounding equipment such as other diagnostics or heating systems. Moreover, ITER has thick components as blanket and vacuum vessel that disturb clear signal to arrive there. Therefore, detectors outside the vacuum vessel cannot measure the neutron source intensity with sufficient accuracy. Thus, micro-fission chambers, which are pencil size gas counters with fissile material inside, has been developed as neutron flux monitors in the vacuum vessel of ITER [4-8]. Installing a pair of a ^{235}U micro-fission chamber and a "blank" detector behind the shielding blanket module is proposed. The "blank" detector is a fissile-material-free detector to identify noise issues such as those from gamma-rays. Pulse counting mode and Campbelling mode [9] in the electronics were employed to meet the ITER requirement with respect to the temporal resolution and the dynamic range.

This paper describes the design and the fabrication of a prototype micro-fission chamber and test results under ITER relevant conditions including wide neutron spectrum and intense gamma-rays, and the performance as a ITER power monitor is discussed.

7.1.2 Design of Micro-Fission Chamber

Figure 7.1-1 shows the schematics of a typical micro-fission chamber with wide dynamic range, which is designed for the ITER. In this detector, UO_2 is coated on the outer cylindrical electrode with a coating density of 0.6 mg/cm^2. The active length is 76 mm, and the total amount of UO_2 is 12 mg. The enrichment of ^{235}U is 90%. Thus, the total amount of ^{235}U is about 10 mg. This detector is filled with Ar and 5% N_2 gas at 14.6 atm. The housing material is stainless steel 316L. Electric insulator is alumina (Al_2O_3).

A full body drawing of the fabricated micro-fission chamber and the MI cable is also shown in Fig.7.1-1. Double coaxial MI (mineral insulated) cable is welded directly to the fission chamber. The cable uses SiO_2 as electric insulator with a packing density of 30%. It is filled with Ar at 14.6 atm. The center conductor is insulated not only with the SiO_2 powder but also Ar gas. In case of cracking at the alumina insulator in the detector due to swelling, the Ar gas in the MI cable will prevent the leak of detector gas into the MI cable. The dummy chamber has the same structure as the micro-fission chamber, except no uranium coating on the electrode.

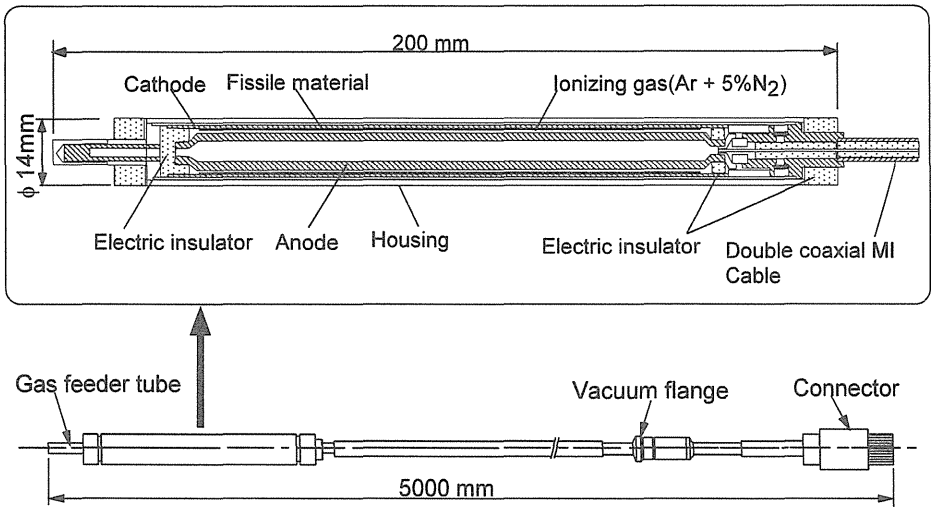

Fig. 7.1-1 Schematics of the structure and the full body of micro-fission chamber and MI cable.

7.1.3 Performance Test

1) Basic Performance

The dummy chamber with MI cable was tested for vacuum leaks at room temperature. We confirmed that the helium leak rate was less than the detection limit, 1×10^{-8} cc/s. In the acceleration test for mechanical shocks, the micro-fission chamber was set on a weighted free-fall table. When the table hit the floor, the acceleration for 30 ms reached 50G at maximum. The test was repeated 10 times. Although a few counts were observed during each mechanical shock, no change appeared in the Campbelling output signal. Neither did in resistance, dimension and vacuum leaks. The resistance between the center conductor and the outer sheath was measured in the range from room temperature (20°C) to 350°C with an impedance analyser. Both detector heads of the micro-fission chamber and the dummy chamber were heated up by a heating apparatus. Although the conductivity is increased by the ionization of alpha particle emitted from the alpha decay of the uranium at low temperature, the change of measured resistances are within the acceptable range for the micro-fission chamber performance.

2) Response for 14 MeV neutrons

The performance tests under 14 MeV neutrons were performed with the target of 80° beam line at FNS. It produces 14 MeV neutrons up to 3×10^{11} n/s. For the sensitivity and linearity measurements, the micro-fission chamber and the dummy chamber were installed just in front of the target as shown in Fig.7.1-2. Both chambers were heated by a ribbon heater from R.T to 250°C.

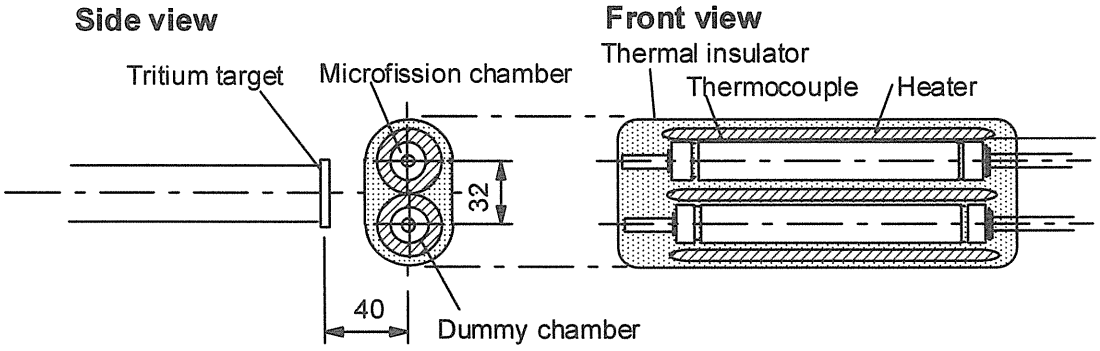

Fig. 7.1-2 Experimental setup of the 14 MeV neutron response measurement at FNS.

The pulse height distributions were measured with a discrimination level of -150 mV. The output voltage of the Campbelling amplifier and the output current of the high voltage power supply were also monitored.

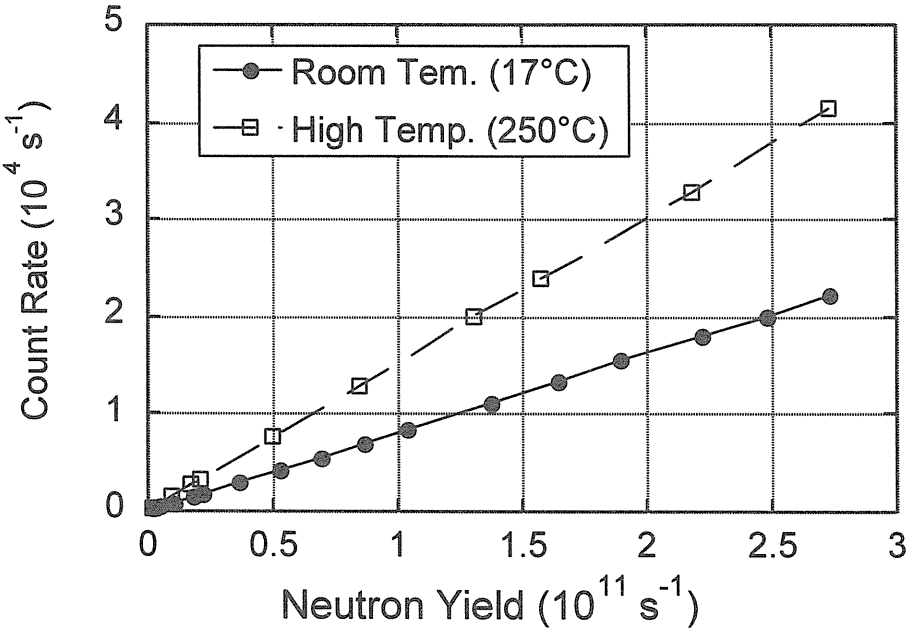

Fig. 7.1-3 Pulse count rates of the micro-fission chamber as a function of the neutron yields.

In the pulse height distributions, shifts of the peak position were observed when the temperature of the chamber was changed. Although the discrimination level was adjusted to

minimize the effect of the peak shift, the temperature-dependence could not be avoided in the present study. The relation between pulse count rates of the micro-fission chamber and neutron yields measured by alpha monitor is shown in Fig.7.1-3. An excellent linearity is observed up to the neutron yield of about 3×10^{11} n/s.

The relation between the squares of the Campbelling output voltages and neutron yields measured by alpha monitor is shown in Fig.7.1-4. An excellent linearity is also observed. The temporal response is shown in Fig.7.1-5. When a neutron pulse in 1ms duration was generated, the squares of the Campbelling output voltage made a curve with 0.98 ms time constant, which means 1 ms temporal resolution could be attained.

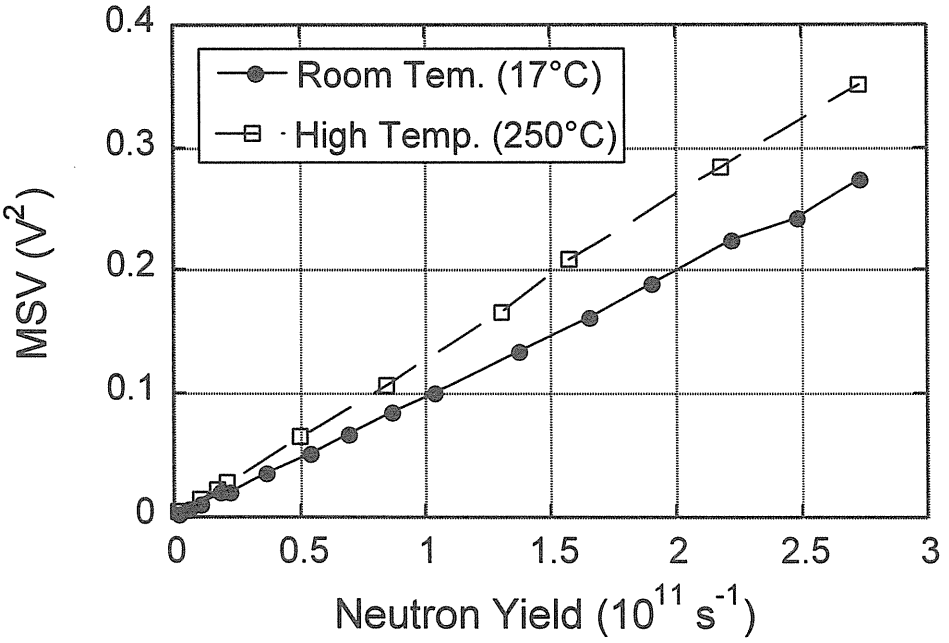

Fig. 7.1-4 Campbelling output voltages of the micro-fission chamber as a function of the neutron yields.

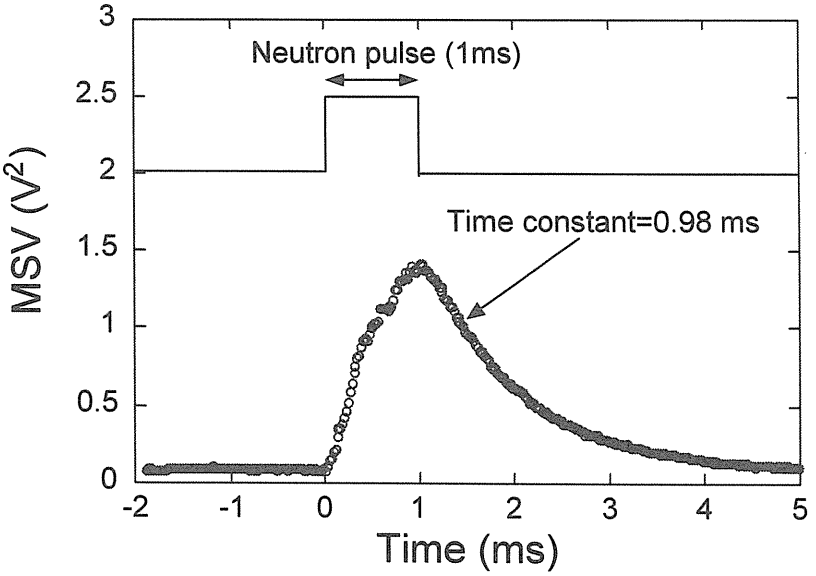

Fig. 7.1-5 Temporal curve of squared Campbelling output response for the 1 ms neutron pulse.

3) Response for gamma-rays

This micro-fission chamber can be operated both in the pulse counting and the Campbelling modes. In the pulse counting mode, current pulse generated by the fission fragments or gamma reaction in the ionizing gas is measured. When a fission reaction releases ~170 MeV as kinetic energy of fission fragments, average energy deposited in the ionization gas is 70 - 100 MeV, while the gamma-ray energy is less than 10 MeV in the chamber. In addition, the Campbell mode is less sensitive to gamma-rays. Therefore, the dummy chamber was employed not only for the gamma-ray compensation but also identification of noise events and radiation induced events such as RIEMF (Radiation Induced Electrical Motive Force).

The dummy chamber was irradiated at the ^{60}Co gamma-ray irradiation facility of JAERI-Takasaki. The gamma-ray dose rate was 4.7Gy/s at the dummy chamber location, which is almost equivalent to the dose rate between the shielding blanket module and the vacuum vessel in ITER, where the micro-fission chambers will be installed. The dummy chamber was irradiated for 19.1 hours, which resulted in the total dose of 0.32 MGy. Compared with the sensitivity for neutrons, gamma-ray sensitivity in Campbelling mode was estimated to be less than 0.1 %.

7.1.4 Conclusion

A micro-fission chamber with 12 mg UO_2 and a dummy chamber without uranium were designed and fabricated for the in-vessel neutron flux monitoring of ITER. The measurement ability was tested with the FNS facility for 14 MeV neutrons and the ^{60}Co gamma-ray irradiation facility at JAERI-Takasaki. Employing the Campbelling mode in the electronics, the ITER requirement for the temporal resolution was satisfied. The excellent linearity of the detector output versus the neutron flux was confirmed in the temperature range from 20°C to 250°. As a result, it was concluded that the developed micro-fission chamber is applicable for ITER.

References

[1] O.N. Jarvis, G. Sadler, P. van Bell and T. Elevant, Rev. Sci. Instrum. **61**, 3172 (1990).
[2] H.W. Hendel, R.W. Palladino, et al., Rev. Sci. Instrum. **61**, 1900 (1990).
[3] T. Nishitani, H. Takeuchi, T. Kondoh, et al., Rev. Sci. Instrum. **63**, 5270 (1992).
[4] V.Mukhovatov, et al., ITER Documentation Series, No.33, IAEA, Vienna (1991).
[5] T. Iguchi, J. Kaneko, M. Nakazawa, et al., Fusion Eng. Design **28**, 689 (1995).
[6] T. Nishitani, K. Ebisawa, T. Iguchi and T. Matoba, Fusion Eng. Design **34**, 567 (1997).
[7] T. Nishitani, et al., Diagnostics for Experimental Thermonuclear Fusion Reactor 2, P.E. Stott, G. Gorini and E. Sindoni ed., Plenum Press, New York (1998).
[8] T. Nishitani, S. Kasai, L.C. Johnson, et al., Rev. Sci. Instrum. **70**, 1141 (1999).
[9] Y. Endo, T. Ito and E. Seki, IEEE Trans. Nucl. Sci. **NS-29**, 714 (1982).

7.2 Cherenkov Detector of the Water Flow Activated by 14 MeV Neutrons

Yury VERZILOV, Kentaro OCHIAI, Chuzo KUTSUKAKE, Takeo NISHITANI
Fusion Neutron Laboratory, Japan Atomic Energy Research Institute, Tokai, Ibaraki

7.2.1 Introduction

The neutron activation of the ^{16}O via $^{16}O(n,p)^{16}N$ reaction and subsequent γ-ray detection of the ^{16}N activity in a flowing fluid was applied for a variety of purposes. Since the threshold energy for the $^{16}O(n,p)^{16}N$ reaction is 10.24 MeV, ^{16}N nuclei is produced only by the 14 MeV neutrons, with water flowing in the vicinity of the D-T neutron source. Thus, a fusion power monitor, based on activation of flowing water, was proposed for ITER, and experimental studies were completed [1,2]. The activation product, ^{16}N, decays by β-emission (100%) with a half-life of 7.13 seconds [3], Table 7.2-1. Presently, activity of the ^{16}N is measured using a γ-ray scintillation detector [1,2]. Such method leads to insufficient time resolution and the delaying of the neutron monitor response, since water has to transfer the ^{16}N from the point of production to the position of a remote γ-detector. In order to overcome these dis-advantages a new approach was proposed. The basic idea of this approach is to utilize the Cherenkov light, produced by β-particles from ^{16}N in water near the neutron source, and then transmit the light by the optical fiber to the remote light detector. To support this idea, several experimental phases were scheduled. The main idea of the first experimental phase is to examine the Cherenkov light measurements using a remotely located water radiator and a light detector. During the second phase the temporal resolution of the proposed technique will be studied comprehensively. In the present paper, theoretical considerations and experimental investigations of the first experimental phase are presented.

Table 7.2-1 Radioactive decay properties* of ^{16}N

Ray	E_β endpoint (keV) / E_γ (keV)	I_β(%) / I_γ(%)	Decay mode
β	1548.1	1.06	β^-
	3303.2	4.8	
	4290.1	66.2	
	10420	28.0	
γ	6128.63	67	
	7115.15	4.9	

* Only branches with intensities of more than 1 % are listed in the table

7.2.2 Theoretical Aspects of a Water Cherenkov Detector

Cherenkov emission is a physical process [4]. Electrons emit light under a

characteristic angle when passing through the medium of the refraction index n, if their velocity exceeds the speed of light in the medium, c/n. For water (n=1.33) the threshold energy for electrons is 0.264 MeV and the emission angle is under 42°. According to the classical description of the Cherenkov effect by Frank and Tamm[5] the number of photons dN emitted per unit path length dx with wavelengths between λ_1 and λ_2 is given by:

$$\frac{dN}{dx} = 2\pi\alpha z^2 \int_{\lambda_1}^{\lambda_2} \left(1 - \frac{1}{n^2\beta^2}\right) \frac{d\lambda}{\lambda^2} \quad (1),$$

for $n(\lambda) > 1$, where z is the electric charge of the particle producing Cherenkov radiation, $\beta = v/c$, and α= 1/137 is a fine structure constant. Assuming that a photomultiplier tube (PMT) with a bialkali photocathode will be utilized for registration of the Cherenkov light, the spectral range of the maximum response was estimated to be as follows. Figure 7.2-1 (curve A) shows the calculated Cherenkov spectrum expressed in terms of the number of generated photons that are proportional to $1/\lambda^2$. Curve B shows the spectral response for the PMT. The product of curves A and B (curve C) shows the number of photoelectrons, liberated at the photo-cathode when Cherenkov light irradiates the cathode. Considering the curve C, it is possible to conclude that the region of the maximum response is estimated to be in the range of 300 – 600 nm. The area under curve C represents the total number of photoelectrons liberated and depends upon initial energy of the particle that generated the Cherenkov light. The intensity of Cherenkov light produced in water by an electron, moderating from E_{max} to the Cherenkov threshold, was estimated by the integration of the equation (1) converted to dN/dE form [6], over the spectral region and energy range. It was integrated numerically and the obtained data is shown in Fig. 7.2-2. The photon output increases rapidly with beta-energy to about 2 MeV, and further increases in energy result in smaller proportionate increases of light output. However, the number of β-particles of sufficient energy to cause Cherenkov radiation in water increases markedly with the increase of maximum emission energy, due to the energy-spectrum characteristics of β-emitters. The ratio of this number and the total number of electrons in the β-spectrum is the Cherenkov

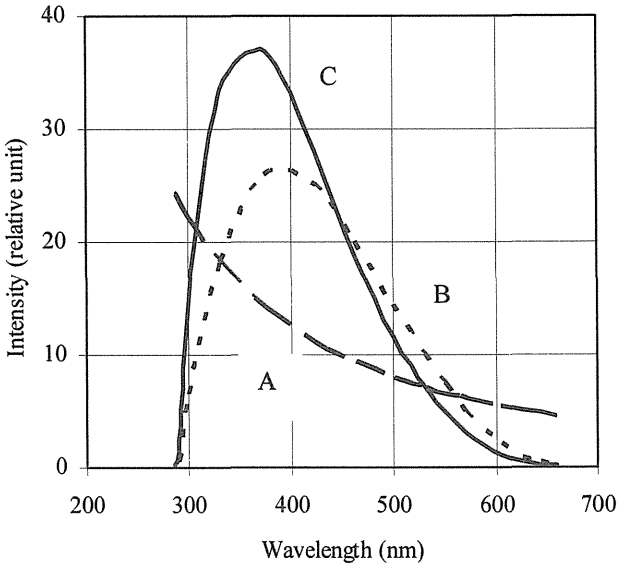

Fig. 7.2-1 A – Cherenkov spectrum, displaying the $1/\lambda^2$ dependence; B – Quantum efficiency of the PMT; C – Response of the PMT to Cherenkov radiation.

yield. The yield calculated for ^{16}N equals 98.6% [6]. Performed analysis has shown [6] that in addition to ^{16}N radionuclide, other radioactive nuclei, which can generate the Cherenkov light, can be produced in the irradiated water. There are radionuclides (^{15}C, ^{17}N, ^{18}N) whose energies are very close to the energy of ^{16}N, but their appearances limit the abundance of the origin nuclide and the nuclear cross section. As a result, contribution of all nuclides to the Cherenkov signal from ^{16}N is less than 0.2%. Since the emitted Cherenkov light is roughly proportional to the beta particle energy, the ^{16}N can be instantly identified. Thus, the Cherenkov counter offers an advantage for counting ^{16}N in water. Explained briefly, it consists of selective detection of large light pulses originating from the passage of high-energy electrons in a volume of water. Utilizing electronic components and altering the desired "window setting" can discriminate against contributions from Compton electrons, produced in the water from γ-ray interactions.

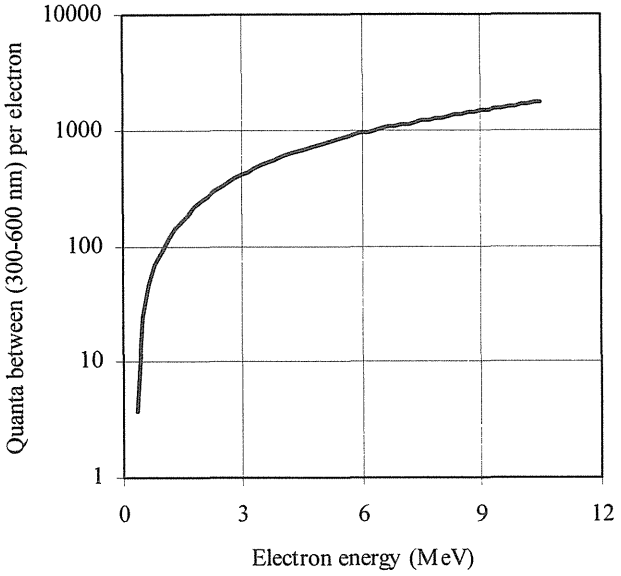

Fig. 7.2-2 The number of Cherenkov photons emitted per electron as a function of energy, calculated for the spectral region 300-600 nm.

7.2.3 Experimental Studies and Results

The experiment was carried out using the FNS facility at JAERI [6]. The ^{16}N radionuclide produced in water near the D-T neutron source, was transported to the chamber of the Cherenkov detector using flowing water in the closed loop, with flow velocity of 2 m/s. The chamber consists of an aluminum cylinder with dimensions of 5 cm in length, a 15 cm diameter, and a glass window. The inside walls were covered with 1mm thick Teflon sheets for light reflection. This chamber was far from the optimum, since the thickness of the reflecting Teflon layer must be about 6 mm for good reflection characteristics, and the material of the window has to be quartz. The PMT, Hamamatsu R1250, was optically coupled to the window chamber. The chamber and the detector were shielded with 10 cm thick Pb blocks. The associated electronic package consists of a high voltage supply, signal amplifiers, and a multichannel analyzer, used for accumulating acquired counts within a selected window.

The ^{16}N radionuclide was generated by D-T neutron irradiation of water flowing next to the source in the position of a neutron flux of about $1 \cdot 10^8$ n/cm^2/s. The transit time to the Cherenkov radiation detector was ~ 6 sec. The identification of the registered Cherenkov signal from ^{16}N was performed using the time decay and pulse height distribution spectrum. During the experimental run, the water flow in the chamber was stopped to estimate the time decay. It fully corresponds to the decay time of ^{16}N. The obtained experimental result is shown in Fig. 7.2-3.

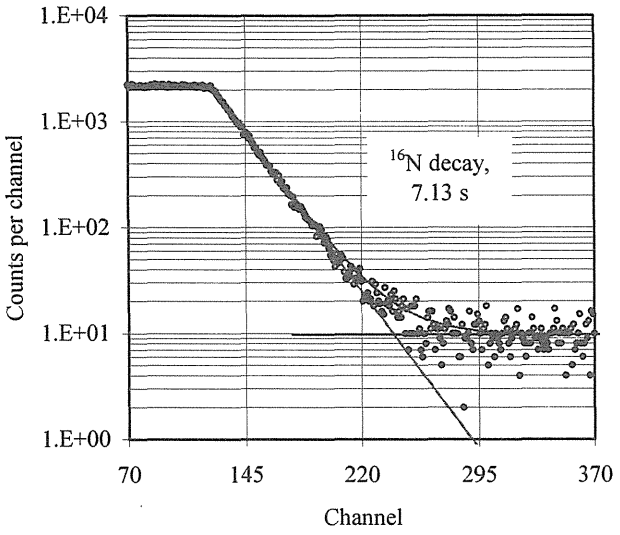

Fig. 7.2-3 Intensity of the Cherenkov signal from ^{16}N as a function of cooling time

A pulse-height spectrum (points) of ^{16}N is shown in Fig. 7.2-4. The slope of the most energetic half of the pulse-height spectrum is a function of the $E_{\beta max}$ for each β-emitter. ^{32}P has only one β-decay branch ($E_{\beta max}$=1710 keV), thus the highly energetic part of the experimental spectrum corresponds to one slope. The result of the deconvolution of ^{16}N spectrum is also shown in Fig. 7.2-4. Two obtained slopes correspond to major β-decay branches of the ^{16}N, with endpoint energies of 4290 keV and 10420 keV.

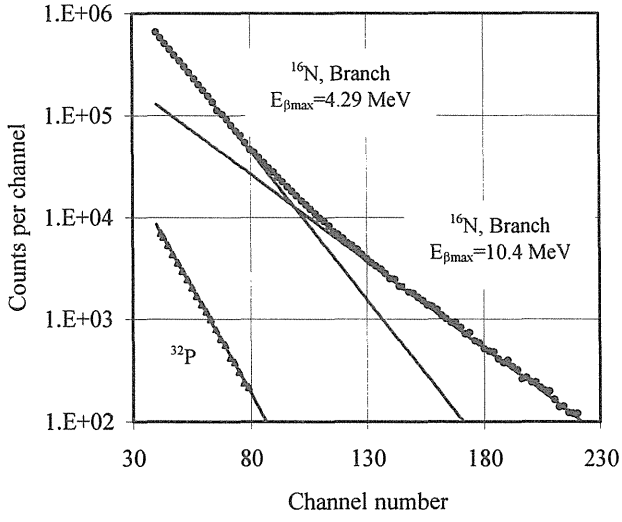

Fig. 7.2-4 The deconvoluted pulse height spectrum of ^{16}N measured by the water Cherenkov detector. ^{32}P is shown for the comparison.

7.2.4 Future Work

In order to complete the feasibility study of the Cherenkov detector as a D-T fusion power monitor for ITER, two more, the second and the third experimental phases are scheduled. The main idea of the second experimental phase consists of studying the temporal resolution of the proposed technique. For purposes of this study, a special Cherenkov detector is to be created, consisting of a water radiator, an optical fiber, and a remotely located light detector. It is

proposed, that the water radiator is to be placed next to the D-T neutron source, and the Cherenkov light generated in the water radiator from the β-rays of the ^{16}N, will be then transmitted by an optical fiber to the remotely located light detector. The third phase consists of finding the optimal solution of transmitting the Cherenkov light in conditions of heavy neutron radiation.

7.2.5 Conclusions

For the purpose of monitoring the D-T neutrons in the system using neutron activation of flowing water, a new approach was proposed. It enables to solve problems associated with the response delay and temporal resolution, which are the most important drawbacks of the previous approach. In support of this idea, the first experimental phase was completed. The response of the detector to the Cherenkov light from the ^{16}N was studied comprehensively. It was concluded, that the water Cherenkov detector is very efficient in measuring the ^{16}N activity, due to: high counting efficiency; absence of the scintillation detector; and simplicity of the method. The present study elaborates upon the feasibility and effectiveness of utilizing the Cherenkov radiation detector in the D-T neutron monitoring system.

Acknowledgments

The authors gratefully acknowledge Mr. S. Tanaka, Y. Abe, M. Seki and Y. Oginuma, for their good operation of the D-T neutron source at the FNS facility.

References

[1] Y. Ikeda, Y. Uno, F.Maekawa, et al., "An investigation of the activation of water by D-T fusion neutrons," Fusion Eng. Design, **37**, 107 (1997).

[2] T. Nishitani, K. Ebisawa, S. Kasai, and C. Walker, "Neutron activation system using water flow for ITER", Rev. Sci. Instrum., **74**, 1735 (2003).

[3] R. B. Firestone, V.S. Shirley (Ed.) Table of Isotopes, 8th Edition, John Wiley & Sons, Inc., New York, (1996).

[4] P.A. Cherenkov, "Visible radiation produced by electrons moving in a medium with velocities exceeding that of light", Phys.Rev. **52**, 378 (1937).

[5] I.M. Frank, I.G. Tamm, "Coherent visible radiation of fast electrons passing through matter", Dokl. Akad. Nauk. SSSR. **14**, 109 (1937).

[6] Y. Verzilov, K. Ochiai, T. Nishitani, Feasibility study of the water Cherenkov detector as a D-T fusion power monitor, JAERI-Research 2003-019, JAERI, (2003).

7.3 Response Function Measurement of Layered Type CVD Single Crystal Diamond Radiation Detectors for 14 Mev Neutrons

Junichi H. KANEKO[1], Tokuyuki TERAJI[2], Yuki HIRAI[1], Kazumasa SHIRAISHI[1], Satoshi. YONEZAKI[2], Souhan KAWAMURA[1], Kentaro OCHIAI[3], Toshimichi ITO[2], Takeo NISHITANI[3], Teruko SAWAMURA[1]

1 Graduate school of Engineering, Hokkaido University, Sappor, Hokkaido

2 Graduate school of Engineering, Osaka University, Suita, Osaka

3 Fusion Neutron Laboratory, Japan Atomic Energy Research Institute, Tokai, Ibaraki

7.3.1 Introduction

A diamond radiation detector has several merits in terms of high radiation resistance [1], high temperature operation [2], high chemical resistance [3], etc. Moreover, a diamond radiation detector can be applied to 14 MeV neutron energy spectroscopy using the $^{12}C(n, \alpha)^{9}Be$ reactions. This method corresponds to neutron energy spectroscopy using the $^{28}Si(n, \alpha)^{25}Mg$ and $^{28}Si(n,p)^{28}Al$ reactions in a silicon surface barrier detector [4]. This capability of a diamond radiation detector was reported by Kovalchuke in 1994 in Ref. 5. The energy resolution of 2% for 14 MeV neutrons was the best result reported in the previous studies using a natural diamond radiation detector [6]. This energy resolution satisfied a required capability of a 14 MeV neutron energy spectrometer for ion temperature measurement for DT plasma. A very compact size of a diamond radiation detector has an advantage in plasma diagnostics that are usually forced strict spatial limitation. Moreover, a diamond radiation detector is at least 100 times tougher than a silicon surface barrier detector in radiation resistance [1]. As mentioned above, a diamond radiation detector has ideal properties for a 14 MeV neutron energy spectrometer for plasma ion temperature measurement. However, it was very difficult to routinely produce diamond radiation detectors that had enough performance, because natural diamond crystals for this purpose were very scarce.

On the other hand, a synthetic technique of diamond has made remarkable progress. The authors reported the first trial of 14 MeV neutron energy spectroscopy using a radiation detector made of a synthetic diamond grown by a high pressure and high temperature (HP/HT) method in Ref. 7. Although the detector succeeded to work as an energy spectrometer, there was severe trapping on electrons [8] and its reduction was indispensable for fruition of a practical detector. Accordingly, characterization of impurities [9], applying of higher purity diamond crystals [10] and estimation of charge trapping mechanism into the HP/HT type IIa diamond crystal [11] were carried out. At the same time, applying of chemical vapor deposition (CVD) diamond single crystal was carried out successfully [12]. However, it was revealed that yield rate of CVD single diamond for energy spectrometer was extremely

poor. Recently, development of a layered type CVD single crystal diamond radiation detector was succeeded [13]; one main motivation of this development was improvement of yield rate. In this article, response function measurement of a layered type CVD single crystal diamond radiation detector for 14 MeV neutrons was described. This experiment was carried out in order to obtain a guide to the next improvement, namely fabrication of a thick sensitive layer.

7.3.2 Detector and experimental setup

7.3.2.1 Layered type CVD single crystal diamond radiation detectors

Figure7.3-1 shows a schematically drawing of a cross section of a layered type CVD single crystal diamond radiation detector. This detector was developed aiming at improvement of poor yield rate of CVD single crystal diamond radiation detectors and fabrication of a thin sensitive layer enough for α particles energy spectroscopy [13]. This detector was fabricated on a cheap HP/HT type Ib diamond single crystal substrate, i.e., yellow diamond. The detector had a layered structure composed by a boron-doped single crystal diamond layer of 0.5 μm in thickness and a non-doped single crystal diamond layer of 20 μm on the substrate. These layers were homoepitaxially grown on (100) surface of the substrate by plasma assisted CVD method in order of boron-doped and then non-doped diamond layers. After crystal growth, a part of the non-doped diamond layer was removed by oxygen plasma etching with a metallic mask; at this part, a Ti/Au electrode was fabricated by evaporation, and the boron-doped diamond layer worked as a back contact. Moreover, an aluminum Schottkycontact was fabricated on non-doped diamond layer by evaporation, too.

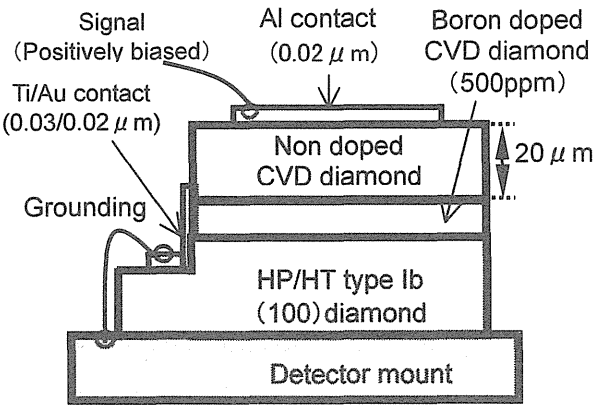

Fig.7.3-1. Schimatic drawing of a cross section of a layered type CVD single crystal diamond radiation detector.

Owing to the boron-doped diamond contact, the detectors had strong rectification properties. The detectors had energy resolution of 2.6 and 2.8 % for 5.5 MeV α particles. These values were far from higher energy resolution of 0.4 % achieved by radiation detectors made of the HP/HT type IIa single crystal diamond [12] and the CVD single crystal diamond [14]. It was already known that quality of the non-doped diamond layers were not so high; it was obvious from their cathode luminescence spectra in which the strong band A luminescence around 420 nm was observed with the free exciton recombination luminescence at 235 nm indicating high quality. It was probably caused mainly by poor crystallinity of the

boron-doped layer owing to growth instrumentation; the boron-doped layer gave a bad influence on crystallinity of the non-doped layer on it. On the other hand, the detector had very thin layer of 20 μm that was very difficult to be fabricated by mechanical polishing and a self standing diamond substrate, thus there was possibility of improvement on suppression of charge trapping on electrons that was big issue on the HP/HT type IIa diamond. Compare with self-standing CVD single crystal diamonds, yield rate of the layered type detector was overwhelmingly high. In this experiment, two layered type CVD single crystal diamond radiation detectors were used.

7.3.2.2 Experimental setup and measurement electronics

Response function measurement experiment for 14 MeV neutrons was carried out at FNS. The diamond radiation detector was set at an exit of a 14 MeV neutron collimator. At the position of the detector, peak energy of neutrons was calculated to be 14.2 MeV, and it had energy broadening of 1.0% in FWHM. The detector was connected with a CANBERRA 2003T charge sensitive preamplifier by cable whose length was 15 cm. A CANBERRA 2021 spectroscopy amplifier and Genie-ESP analysis system were used in this measurement.

7.3.3 Experimental results and discussions

Figure 7.3-2 shows examples of response functions for 14 MeV neutrons obtained by the layered type CVD single diamond radiation detector. Bias voltage of +15V (7.5 kV/cm) was applied to the aluminum contact, and gain and shaping time of the spectroscopy amplifier were 0.6 × 1k and 10 μs, respectively.

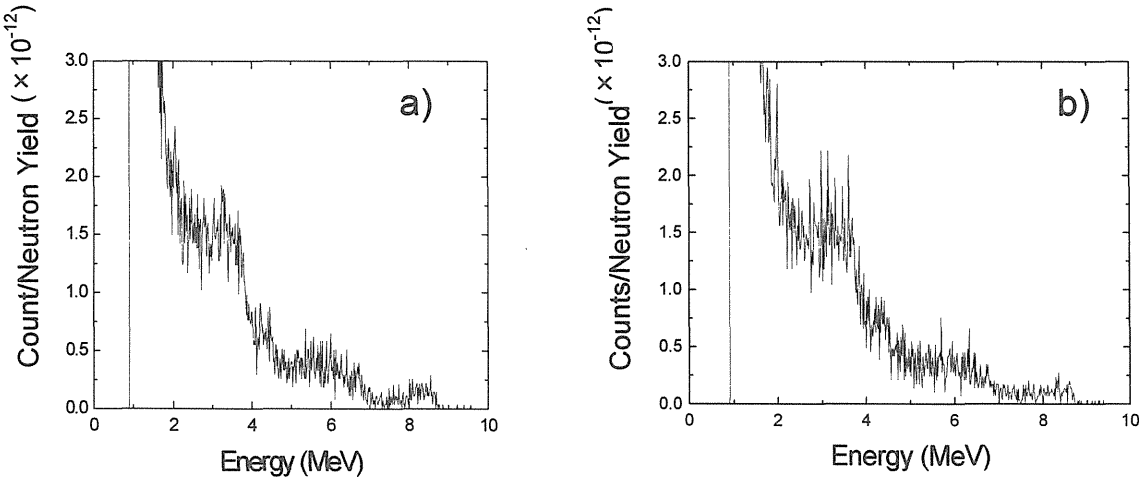

Fig.7.3-2 Change of pulse height distribution spectra obtained by the layered type CVD single crystal diamond radiation detector for 14 MeV neutrons due to measurement time. a) the first (0 - 40 minutes) measurement of series three times measurement in total 120 minutes, b) the third (80 – 120 minutes) measurement.

Continuous measurement of 120 minutes was carried out with counting rate of approximately 20 cps. Figure 7.3-2 a) shows the pulse height spectrum obtained during the first 40 minutes, and Fig. 7.3-2 b) shows the pulse height spectrum obtained during the third 40 minutes, namely from 80 to 120 minutes. In Fig.7.3-2 a), structure caused by the $^{12}C(n, n')^{12}C$, $^{12}C(n, n')^{12}C^*$, $^{12}C(n,n')3\alpha$ and $^{12}C(n,\alpha)^9Be$ reactions was clearly observed. In contrast, the structure was distorted with increase of measurement time as shown in Fig. 7.3-2. It was obvious to get influence of accumulated charge in the detector.

Figure 7.3-3 shows a response function measured by another detector. In this measurement, bias voltage of +25 V (12.5kV/cm) was applied to the aluminum contact. Gain and pulse shaping time constant of the spectroscopy amplifier were 0.6×500 and 6μs, respectively. To obtain this spectrum, six times of a 20 minutes measurement were summed up. Between each measurement, some bias voltage of opposite polarity was applied to the detector in order to remove space charge. As result, the fine spectrum compared with Fig.7.3-2 was obtained. Moreover, energy resolution of 6 % caused by the $^{12}C(n,\alpha)^9Be$ reactions was achieved; it was the best result for synthetic diamond radiation detectors.

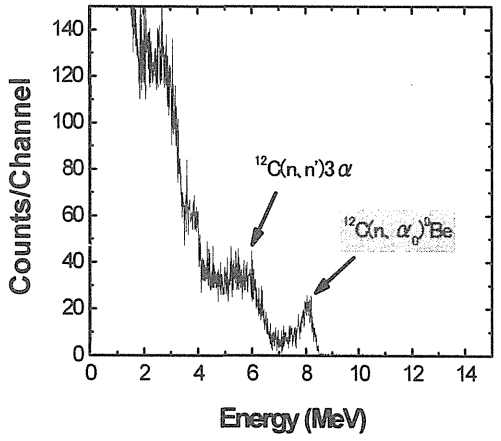

Fig.7.3-3. An example of response function of the layered type CVD single crystal diamond radiation detector for 14 MeV neutrons.

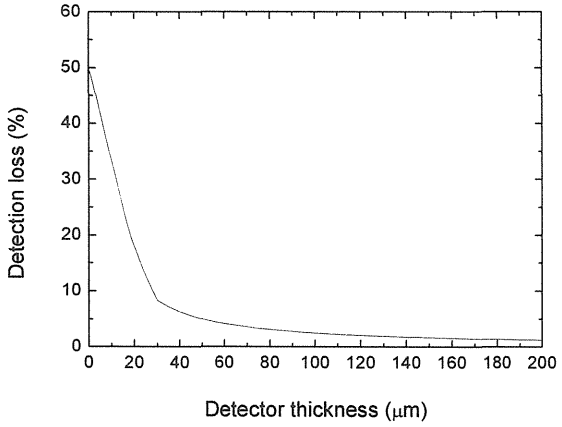

Fig.7.3-4. Dependence of detection efficiency of the $^{12}C(n,\alpha)^9Be$ reactions on thickness of sensitive layer of diamond.

Detection efficiency was 2.8×10^{-7} counts/unit neutron flux for this detector. Figure 7.3-4 shows dependence of detection loss on the thickness of a sensitive layer calculated by analytical approximation. Range of α particles created by the $^{12}C(n,\alpha)^9Be$ reactions was approximately 15 μm in diamond. Thus, for 20 μm in detector thickness, approximately 18 % of counts caused by the $^{12}C(n,\alpha)^9Be$ reactions were not able to deposit all energy to the detector. However, taking into low energy resolution of 3% and broadening of neutron energy of 1%, calculated detection efficiency of 3.2×10^{-7} was almost equal to the experimental result of 2.8×10^{-7}.

For the detectors used in this study, it was difficult to observe transfer properties of electrons and holes separately, because the thickness of the sensitive layers were almost the same length as a range of a 5.5 MeV α particle, i.e., 14 μm. If there was no charge collection loss in the detector, approximately 65 % of pulse height of a signal was composed by motion of electrons for 5.5 MeV α particles. Moreover, the detectors had strong rectification properties, thus it was impossible to change drift direction of electrons or holes by applying opposite bias polarity. As reported in Ref. 13, the experimental results obtained using α particles, the detectors had low charge collection efficiency and slow drift velocity of both charges, i. e., 700 to 2×10^4cm/s. On the other hand, for 14 MeV neutrons, all reactions occurred in the detector homogeneously. Therefore, average contribution to a pulse height of a signal was equal for both electrons and holes. Taking all information described above into account, there were charge losses not only on electrons but also on holes. Probably, there was trapping centers related with bad crystallinity.

In order to improve detector performance, improvement on the boron-doped diamond layer and optimization for growth condition of non-doped diamond layer are indispensable. For the later issue, a growth condition achieving higher growth rate of 4 μm/hour with very high crystal quality was observed. If this growth condition applied to fabrication of the detector, a 100 μm thick detector can be fabricated in 25 hours. Therefore, the authors believe that a practical synthetic diamond radiation detector as 14 MeV neutron energy spectrometer comes true in near future.

References

[1] S. F. Kozlov et al., IEEE Trans. Nucl. Sci., **NS-22**, 160 (1975).
[2] F. Nava et al., IEEE Trans. Nucl. Sci., **NS-26**, 308 (1979).
[3] S. F. Kozlov et al., IEEE Trans. Nucl. Sci., **NS-24**, 242 (1977).
[4] T. Elevant et al., Rev. Sci. Instrum., **57**, 1763 (1987).
[5] V. D. Kovalchuk et al., Nucl. Instrum. and Meth., **A 351**, 590 (1994).
[6] A. V. Krasilnikov et al., Rev. Sci. Instrum., **68(4)**, 1720 (1997).
[7] J. Kaneko et al., Rev. Sci. Instrum., **70(1)**, 1100 (1999).
[8] J. Kaneko and M. Katagiri, Nucl. Instrum. and Meth., **A383**, 547 (1996).
[9] J. Kaneko et al., Diamond and Related Materials **9**, 2019 (2000).
[10] T. Tanaka et al., Rev. Sci. Instrum., **72(2)**, 1406 (2001).
[11] J. H. Kaneko et al., to be published in New Diam. Frontia Cabon Tech.
[12] J.H.Kaneko et al., Nucl. Instrum. Meth., **A505**, 187 (2003).
[13] J. H. Kaneko et al., Submitted to J. Jap. Atom. Energy Eng.
[14] J. Kaneko et al., Nucl. Instrum. and Meth., **A422**, 211 (1999).

7.4 Laser Resonance Ionization Mass Spectroscopy for Very Small Amount Radioactivity

Tetsuo IGUCHI, Kenichi WATANABE, Kazuhiro HATTORI, Yusuke TSUNEKAWA, Jun KAWARABAYASHI, Takeo NISHITANI[1], Michinori YAMAUCHI[1]

Department of Nuclear Engineering, Nagoya University, Nagoya

[1]Fusion Neutron Laboratory, Japan Atomic Energy Research Institute, Tokai, Ibaraki

7.4.1 Introduction

The extensive estimation of radioactivity induced by neutron irradiation is required from the viewpoint of facility maintenance and safety in fusion neutron source facilities, such as fusion reactors and high-energy accelerators. For radiation protection and neutron dosimetry, it should be understood that short-lived radionuclides are important because of their high radioactivity. At the same time, long-lived radionuclides are also important from the aspect of long-term waste management. However, they are difficult to be measured by conventional radiation measurement techniques because of their extremely long half-life or low activity. Consequently, it is desired to directly analyze long-lived radionuclides using high sensitive mass spectrometry techniques, where promising candidates for these applications are accelerator mass spectrometry (AMS), inductively coupled plasma mass spectrometry (ICP-MS) and resonance ionization mass spectrometry (RIMS)[1][2] and so on.

Generally radionuclides produced by neutron irradiation have isobars in a matrix. Therefore, for direct detection of trace long-lived radionuclides, we have proposed to adopt RIMS, because RIMS is the only method having high elemental (isotopic) selectivity, which is the capability of suppressing isobaric interference, high sensitivity and simpleness simultaneously. Furthermore, we have developed resonant laser ablation mass spectrometry (RLA-MS)[3][4] in order to apply the RIMS to solid sample analysis, which is required as a simple and direct analysis method for radionuclides in structure materials. The RLA-MS combines the RIMS and Laser Ablation (LA) technique, which is vaporization procedure, simultaneously with a single laser.

As a demonstration of the detection of trace long-lived radionuclides, we have been attempting the detection of ^{26}Al ($T_{1/2}$: 7.2×10^5 y) produced by ^{27}Al(n,2n) reaction in high energy neutron fields. Aluminum alloys and ceramics are promising low-activation materials for fusion reactors and/or high-energy accelerators. The determination of trace long-lived radionuclide ^{26}Al produced by neutron irradiation is quite important from the viewpoint of high energy neutron dosimetry. For ^{26}Al detection, it is difficult to adopt the direct detection techniques without the elemental selectivity because of the isobaric interference of ^{26}Mg contained in Al material as an impurity.

7.4.2 Experiments

Figure 7.4-1 shows a schematic of our experimental system, which consists of all solid-state high-repetition-rate and short-pulse tunable Ti:Sapphire laser system with a regenerative amplifier and a reflectron TOF mass spectrometer with a field-free drift region approximately 150 cm long and a microchannel plate (MCP) ion detector. The output from this amplifier is frequency doubled using a second harmonic generation crystal (KDP crystal). The bandwidth of the laser was 0.4 cm^{-1}, the laser pulse duration 100 ps and the repetition rate 1 kHz, respectively. The laser output was split into two beams for LA and RIS because the laser power can be separately controlled for LA and RIS to suppress non-resonance ionization on LA and to increase resonance ionization efficiency. The ionization laser pulses were delayed to the LA laser ones for 65 ns, corresponding to a finite time for expansion of the atoms vaporized by LA. In this arrangement, the ionization efficiency to the ablated vapor is quite high because the effective ionization area is as close to the LA spot as possible. The laser beams were focused at an ionization area with a diameter of 50 μm. The laser output energies for LA and resonance ionization were 0.5 μJ/pulse (2×10^8 W/cm^2) and 12 μJ/pulse (6×10^9 W/cm^2), respectively. The laser wavelength was tuned to 457.467 nm corresponding to

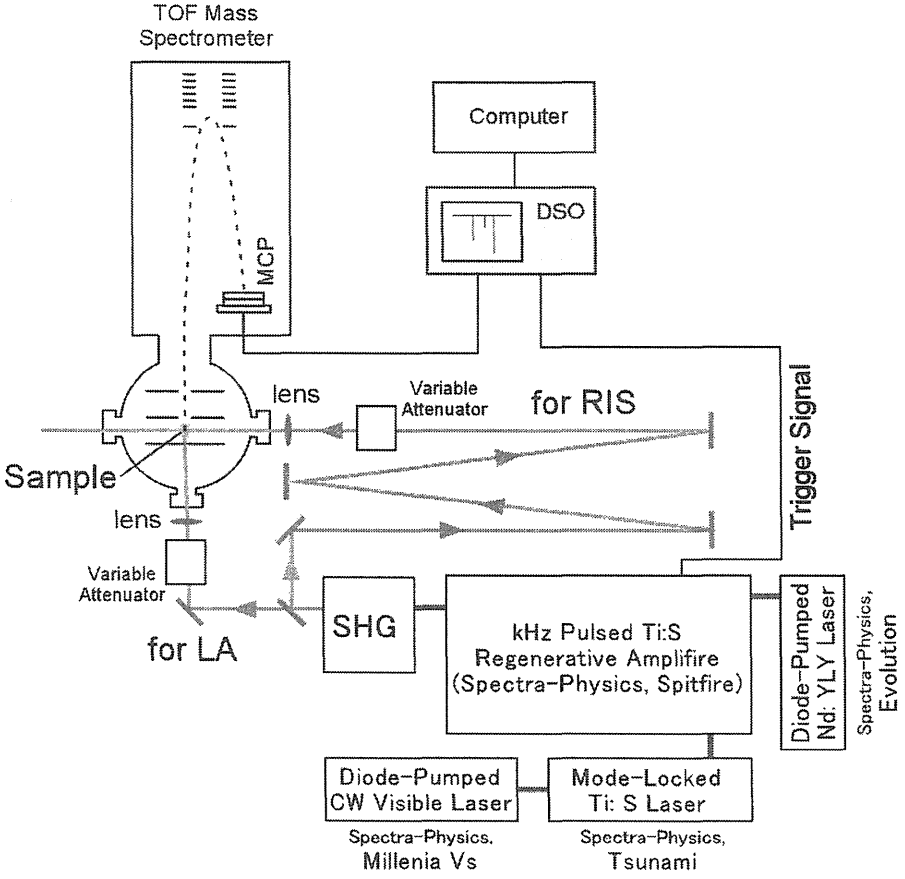

Fig. 7.4-1 Schematic of our RLA-MS system.

the two photons resonance excitation for Al from $3s^2 3p\ ^2P^o_{1/2,3/2}$ to $3s^2 5f\ ^2F^o_{5/2,7/2}$. The TOF data are taken trough a digitizer (Yokogawa, WE7311) to a PC. In the present system, although the repetition-rate of laser pulses is 1 kHz, a maximum data taking rate is 100 Hz, that is to say the data taking efficiency of 10%. As a data processing procedure, we have adopted off-line pulse mode to avoid electrical noise interference.

For a demonstration of the detection of trace ^{26}Al, a high-purity aluminum (99.999%) wire (1 mm dia.×5 mm) was irradiated with the D-T neutrons at JAERI-FNS, when the neutron fluenece was 1×10^{18} n/cm^2 [5]. Figure 7.4-2 shows the gamma-ray spectra obtained from this Al sample by a HPGe detector (relative efficiency 15 %) with the measurement time of 84 hours. The 1809 keV gamma-ray peak of ^{26}Al is obviously detected and the concentration of induced ^{26}Al is estimated to be 7 ppb.

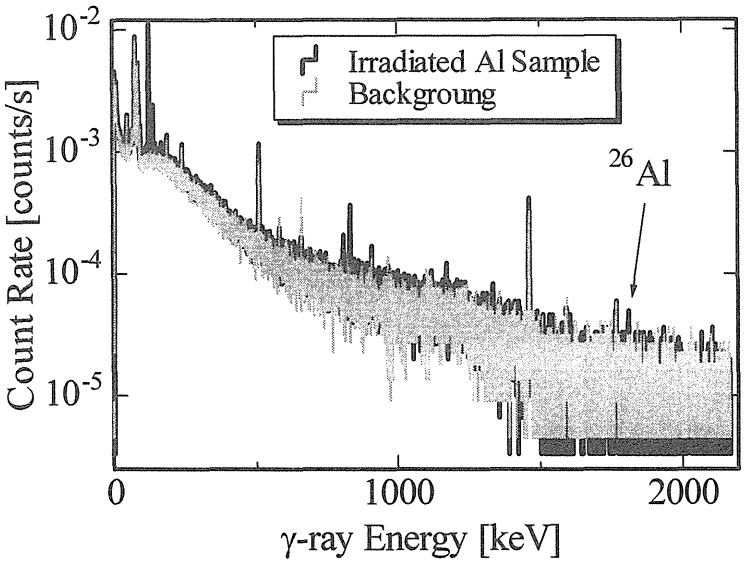

Fig. 7.4-2 Gamma-ray spectra obtained from the irradiated Al sample by HPGe detector.

7.4.3 Results and discussion

The TOF mass spectrum obtained from the irradiated Al sample is shown in Fig. 7.4-3. In this figure, the peak of impurity ^{23}Na and the tail component appears on the left side of the ^{27}Al peak. The tail component is attributed to cluster ions, which have slightly faster velocity than ^{27}Al ions. The clusters, which are defined as an ensemble of atoms such as $^{27}Al_m$, are produced by laser vaporization process and singly or multiply ionized through charge exchange with surrounding ^{27}Al ions. The cluster ions have quite short lifetime and can dissociate during accelerating in an ion extraction field. When the cluster ions $^{27}Al_m^{n+}$ multiply ionized (n>m), which are given higher accelerating force than $^{27}Al^+$ ions, dissociate

in an acceleration region of TOF-MS, the fragment $^{27}Al^{+}$ ions of these clusters have fractional and slightly faster velocity than the normal $^{27}Al^{+}$ ions and form the tail component on the lower mass number side of the ^{27}Al peak in TOF mass spectrum.

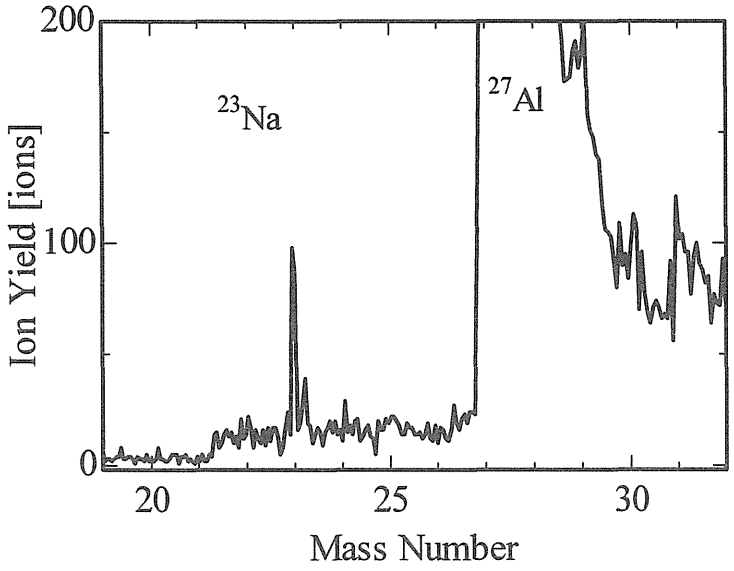

Fig. 7.4-3 RLA-MS spectrum obtained from the irradiated Al sample.

The ^{26}Al peak is submerged in the tail component and can not be found. Although the tail element is based on quite rare events, it is necessary to be suppressed in order to clearly detect ^{26}Al. The $^{27}Al^{+}$ ions dissociated from $^{27}Al_m^{n+}$ (n>m) are given higher kinetic energy in an ion extraction filed than normally accelerated ions so that they are hard to be deflected. If a deflection electrode is installed in a free flight region of TOF-MS, the flight path of the cluster fragment ions has smaller curvature than that of normal ions. Fortunately, the deflection electrode has been already installed into the present reflectron-type TOF-MS in order to change return ion path. Consequently, by adequately installing a slit in front of an ion detector, the tail component would be suppressed.

Figure 7.4-4 shows the mass spectrum for 10^5 laser shots (1000 sec), when using the TOF-MS with the slit of 1 cm width. It is found that the ^{26}Al peak can obviously be detected. The ^{26}Al concentration is approximately estimated to be 3 ppb through comparison with ^{24}Mg yield, where the concentration of impurity Mg is 2 ppm and Al is 600 times higher sensitive than Mg at the present laser power[6]. Considering uncertainty of the impurity Mg concentration, this estimated value is allowable.

Consequently, we have succeeded to demonstrate the detection of trace long-lived radionuclides ^{26}Al. Therefore, it would be concluded that RLA-MS have the capability to directly measure the long-lived radionuclides.

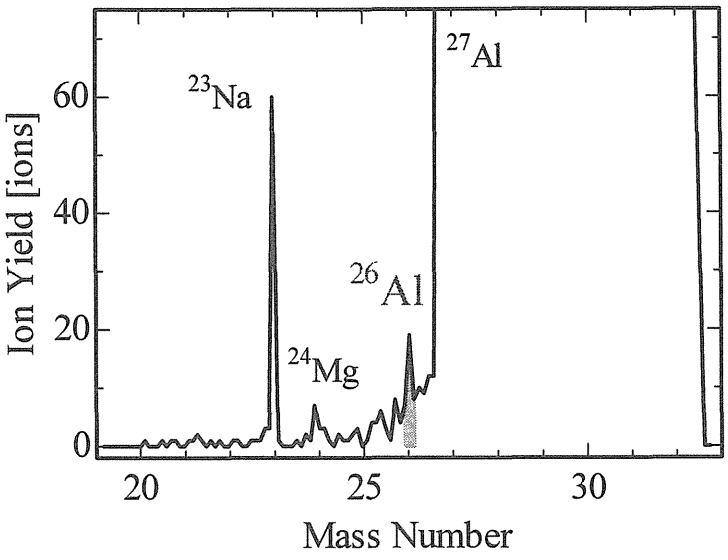

Fig. 7.4-4 RLA-MS spectrum when using TOF-MS installed the slit in front of ion detector.

7.4.4 Conclusion

As a new neutron dosimetry technique, we have proposed to adopt RLA-MS to directly measure the long-lived radionuclides. As a demonstration, we have been attempting to detect trace long-lived radionuclide ^{26}Al produced by DT neutron irradiation. Consequently, we have succeeded to obviously detect ^{26}Al, which has the concentration of 7 ppb, by RLA-MS with the measurement time of 1000 sec. Therefore, we would conclude that RLA-MS have the capability as the new neutron dosimetry technique.

As future works, we will develop a quantitative analysis procedure for RLA-MS and the high resolution and isotopic selective RIMS based on a narrow-band laser, such as laser diodes, in order to improve the ionization selectivity or the signal-to-noise ratio.

References

[1] G. S. Hurst, M. G. Payne, S. D. Kramer, et al., Phys. Today **33**, 24 (1980).

[2] G. S. Hurst, M. G. Payne, S. D. Kramer, et al., Rep. Prog. Phys. **48**, 1333 (1985).

[3] C. G. Gill, A. W. Garrett, P. H. Hemberger, et al., Spectrochimi. Acta B **51**, 851 (1996).

[4] J. E. Anderson, T. M. Allen, A. W. Garrett, et al., AIP Conf. Proc. **388**, 195 (1997).

[5] K. Watanabe and T. Iguchi, J. Nucl. Sci. Technol. **39**, 312 (2002).

[6] K.Watanabe, K.Hattori, J.Kawarabayashi, et al., Spectrochimi. Acta B **58**, 1163 (2003).

7.5 Incident-angle Sensitive Neutron Detector using Scintillating Fibers

Tetsuo IGUCHI, Jun KAWARABAYASHI, Ryoji MIZUNO, Daisuke INUI, Kenichi WATANABE, Takeo NISHITANI[1], Michinori YAMAUCHI[1]

Department of Nuclear Engineering, Nagoya University, Nagoya

[1]Fusion Neutron Laboratory, Japan Atomic Energy Research Institute, Tokai, Ibaraki

7.5.1 Introduction

Neutron measurement in fusion experimental devices is very important for burning plasma diagnostics and control. In particular, neutron emission profile measurement provides useful information on the profile of ion temperatures and densities[2] as well as the time-dependent neutron yield profile[1],[2]. So far several studies have been made on the neutron emission profile monitor, which are almost based on a large number of neutron threshold detectors or neutron spectrometers combined with a massive multichannel neutron collimator[3]. The detectors can provide line-integrated neutron emissivity along the direction of collimator. Neutron emissivity over a poloidal section of plasma is determined by installing a vertical neutron camera and a horizontal neutron camera. However, one of the most serious problems on this type of system is that the spatial resolution is restricted by the collimator design. The restriction of location to install the massive and heavy collimator system is also a difficult problem[4] for the complicated and tight machine integration.

To improve these difficulties, we propose a novel incident-angle sensitive neutron detector using scintillating fibers. In this report, we describe the results on preliminary experiments to confirm the operational principle and basic performance a prototype detector element.

7.5.2 Operational Principle

Figure 7.5-1 shows the configuration of the prototype detector element, which consists of a parallel pair of scintillating fibers equipped with photomultiplier tubes (PMTs) at both ends of fibers. An incident neutron into a fiber is scattered with a constituent hydrogen atoms in the fiber and produces a scintillation light. The neutron incident position in a longitudinal direction of a fiber is determined from a time difference of scintillation light signals to each end of the fiber. When the second scintillating fiber detects the scattered neutron, the scattered neutron energy is determined from positions and a time difference of light emissions in each fiber by a time-of-flight method. If a neutron is elastically scattered, the scattered neutron energy E is given as follow;

$$E = E_0 \cos^2 \theta \qquad (1)$$

where E_0 and θ are the incident neutron energy and neutron scattered angle, respectively. Therefore, if the incident neutron energy is known, the neutron incident direction can be conically determined from the neutron incident positions in each fiber and the scattered neutron energy. Accumulating the conical direction for a number of neutrons, we can estimate the incident neutron direction.

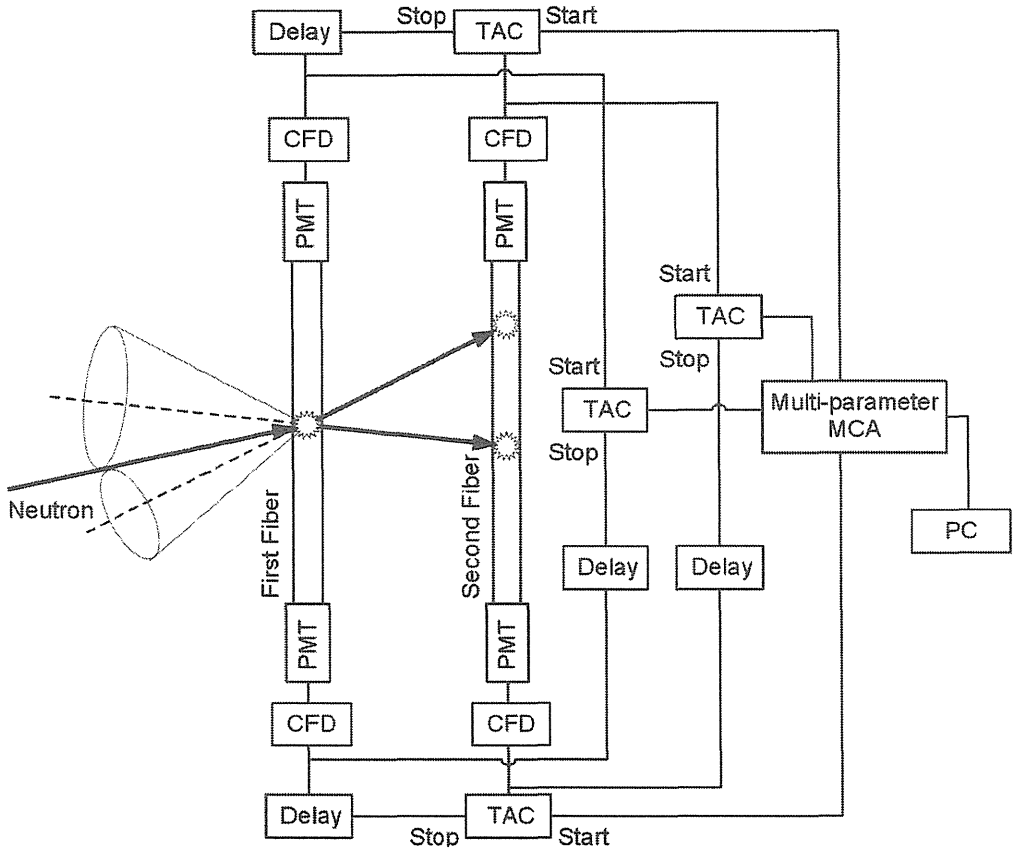

Fig. 7.5-1 Schematic of prototype detector element.

7.5.3 Experimental Setup

The prototype detector element consists of a parallel pair of multi-clad scintillating fiber (BICRON, BCF-20) bundles connected with PMTs (HAMAMATSU, H6612 and R329-02) at both ends of fibers, where the cross sections of the first and the second fibers were 5 mm-squared, 25 mm-squared, respectively, the length of both the fibers 1 m, and the distance between them 30cm. The second fiber was shifted with the angle of 15 degrees from the neutron incident direction to avoid direct irradiation for noise reduction. The time differences between the PMT signals are measured by the ORTEC Model 566 Time-to-Amplitude Converter (TAC) through the ORTEC Model 584 Constant Fraction Discriminator (CFD). Additionally, stop signals for TAC are delayed by a finite time to start

signals. The multiparameter multichannel analyzer system coincidentally records four time differences.

The center position of the first scintillating fiber was irradiated by 14 MeV D-T neutron beams with the flux of 5×10^6 n/cm^2/s at JAERI-FNS. In order to investigate the incident angle dependence of the detector responses, we measured the ones for the incident angles of 0 and 50 degrees to the normal line direction of the first fiber.

7.5.4 Results and discussion

From experimental data of four time differences of the PMTs, we can obtain the information about the neutron incident positions on the first and the second fibers and the flight time of scattered neutron between them. The two-dimensional maps of flight time and flight length of the scattered neutrons are plotted in Fig. 7.5-2. The components with fast and slow flight times are attributed to gamma-ray and neutron, respectively. Therefore, we can discriminate the neutron component from gamma-ray by using the flight time information.

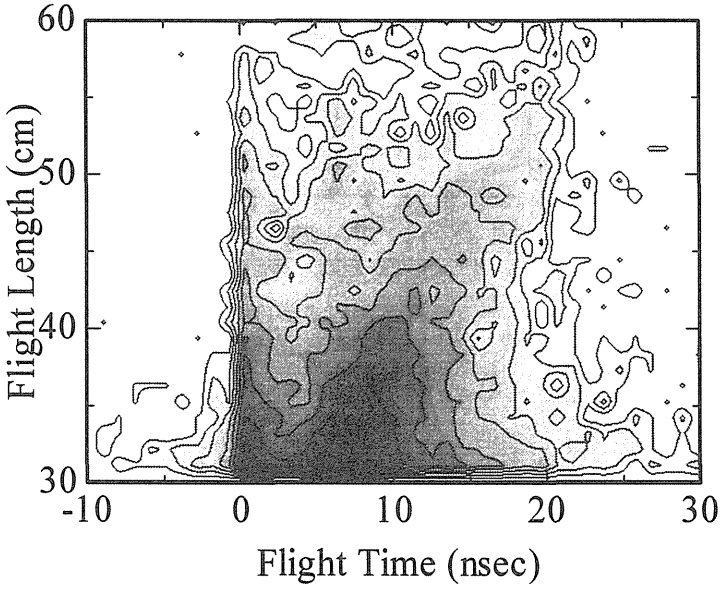

Fig. 7.5-2 Two dimensional map of flight time and flight length of scattered neutrons.

The scattered neutron energy can be determined by the time-of-flight method. Therefore, if the incident neutron energy is known, we can conically determine the neutron incident direction from the neutron incident positions of each scintillating fiber. Accumulating the conical direction for a number of neutrons, we can estimate the neutron incident direction. Figure 7.5-3 shows the neutron incident direction distribution projected on the screen at the distance of 300 mm from the first scintillating fiber, when the incident angles of neutron beam are 0 and 50 degrees. In the case that the incident angle is 0 degrees, the projected position is at (x,y)=(0,0).

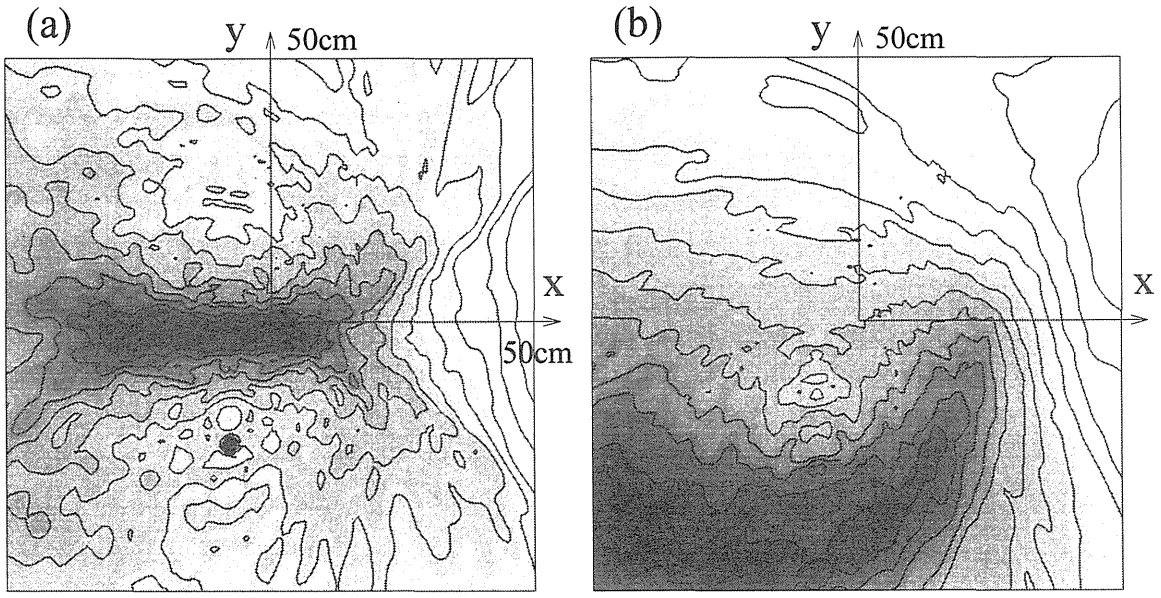

Fig. 7.5-3 Neutron incident direction distribution projected on a screen at the distance of 300 mm from the first scintillating fiber. (a) Incident angle; 0 degree. (b) Incident angle; 50 degrees.

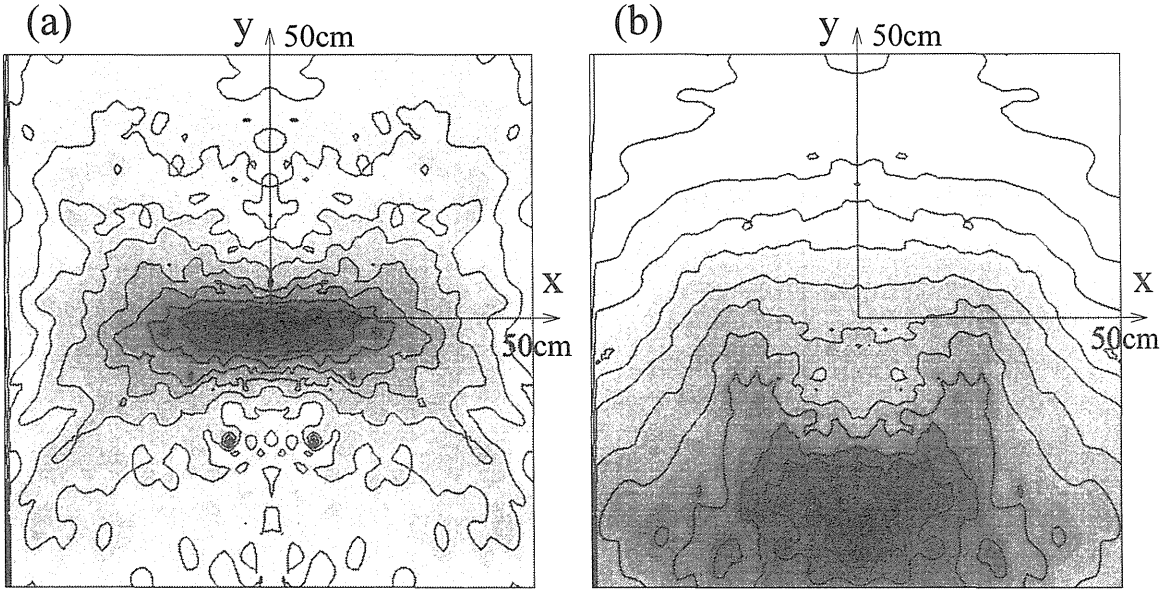

Fig. 7.5-4 Image projected by incident neutron beam overlapping the mirror one.
(a) Incident angle; 0 degree. (b) Incident angle; 50 degrees.

In this figure, a virtual image is created on the opposite side to the plane formed by two fibers because these images are equivalent on the estimation from a scattered angle. To eliminate a virtual image, the detector configuration consisting of multi-second-fibers would be applicable. As an demonstration for this idea, we have virtually overlapped the mirror image to the plane formed by the incident direction and first fiber, that is, the plane of y=0, which means to assume that another second fiber is set on the opposite position to this plane.

Figure 7.5-4 shows the image projected by an incident neutron beam overlapping the mirror one. It is found that the images corresponding to the neutron incident direction clearly appear and the virtual images are eliminated. Additionally, the resolution of the incident angle was estimated around 25 degrees. From these preliminary results, it is considered that the operational principle of the present incident angle sensitive neutron detector has been confirmed.

7.5.5 Conclusion

We have proposed a novel incident-angle sensitive neutron detector using scintillating fibers to improve the difficulties of the neutron emission profile monitor. Through the preliminary e experiments using the prototype detector element, we would conclude that the operational principle of the present detector have been confirmed at least. However, we need further study to improve the basic performance, such as incident-angle resolution, for a practical use by refining the detector configuration design and signal processing system.

References

[1] J. M. Adams et al., Nucl. Instr. Meth. **A329**, 227 (1993).
[2] T. Iguchi et al., Fusion. Eng. Design. **28**, 689 (1995).
[3] O. N. Jarvis et al., Fusion. Eng. Design. **34-35**, 59 (1997).
[4] L. C. Johnson et al., Rev. Sci. Instrum. **68**, 569 (1997).

7.6 Counter Telescope Neutron Spectrometer for Plasma Diagnostics

Takako MIURA, Mamoru BABA, Naoki KAWATA, Masayuki HAGIWARA, Takeo NISHITANI[1], Jun-ichi HORI[1], Kentaro OCHIAI[1]

Cyclotron and Radioisotope Center, Tohoku University, Aoba, Aramaki, Aoba, Sendai

[1] *Fusion Neutron Laboratory, Japan Atomic Energy Research Institute, Tokai, Ibaraki*

7.6.1 Introduction

Measurement of neutrons from fusion plasma provides crucial information on the plasma condition. In particular, the energy spectrum of neutrons or the energy spread of 14 MeV neutrons gives a direct measure of the ion temperature through Doppler broadening. To obtain the information on the ion temperature, the spectrum should be measured with energy resolution better than ~3 % within a limited period of the plasma burst. Therefore, a neutron spectrometer which satisfies good energy resolution and high counting efficiency concurrently is required for the purpose.

For the reason, various types of neutron spectrometers have been proposed as a neutron spectrometer for ion temperature measurement, i.e., a proton recoil counter telescope, a magnetic spectrometer, a time-of-flight method and so on. Up to now, however, no device has succeeded to fulfill the requirement for resolution and efficiency because usually the energy resolution and the detection efficiency conflicts each other in neutron spectrometers by conventional design. To achieve the high performance in both quantities, a spectrometer with special scheme is required.

We have developed a proton recoil telescope which has the capability of particle tracking by two position sensitive detectors and, thereby the potential to achieve high resolution and high efficiency concurrently for 14 MeV neutrons.

7.6.2 Position-Sensitive Proton Recoil Telescope (PSPRT)

Details of PSPRT are described in Ref.1.

The schematic diagram of a position-sensitive proton recoil telescope (PSPRT) is shown in Fig.7.6-1. The PSPRT neutron spectrometer consists of two position sensitive detectors, i.e., a radiator detector (DET.l) and a proton detector (DET.2). DET.1,2 consists of a position-sensitive photomultiplier (PS-PMT; Hamamatsu R2486) coupled to an NE102A plastic scintillator (1 mm thick), and DET.2 consists of PS-PMT and a NElO2A or CsI(TI) scintillator. The PS-PMT (R2486) is of cross-anode type with an effective area of 50 mm in diameter.

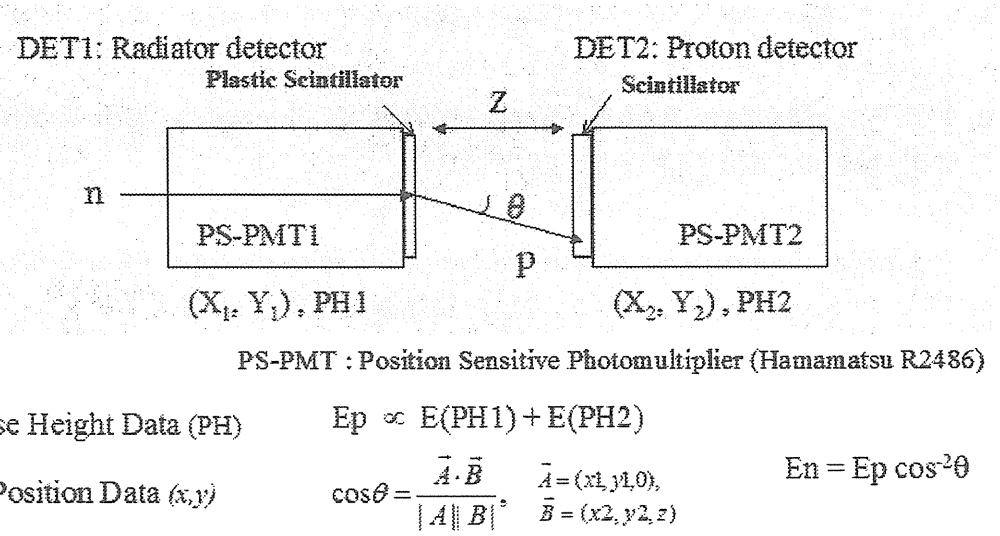

Fig.7.6-1; Schematic diagram of PSPRT

Neutrons enter from backward of PS-PMT of DET1 and ejects proton in the NE102A radiator. Recoil protons from DET.1 are detected by DET.2 in coincidence. In this configuration, the information on both the pulse-height and the position are obtained from both detectors. The proton energy (E_p) is determined by the pulse height, and the recoil angle (θ) by the equation in figure. Consequently, the neutron energy is deduced from the relation $E_n=E_p/\cos^2\theta$ for each event, and the energy loss of recoil protons in DET.1 can be corrected for. By selecting the events only to certain range of the recoil angle, PSPRT can accept larger detector size without degrading energy-resolution. On the contrary, in the ease of conventional PRTs, the sizes of radiator and detector should be small to achieve good energy resolution. Therefore, the detection efficiency of PSPRT becomes higher in proportion to the square of detector radius and much higher than that of conventional PRTs.

The principle of the PSPMT and the way of position sensitivity is illustrated in Fig.7.6-2. As shown in the figure, the position information is obtained by the charge-division method.

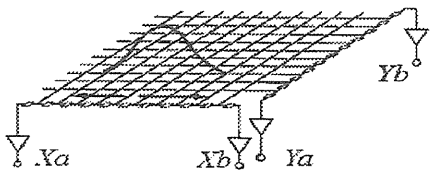

Fig.7.6-2; Principle of position –sensitive photomultiplier

Figure 7.6-3 illustrates the electronics block diagram of PSPRT. Four signals from each photomultiplier were input in ADC and accumulated as pulse-height data using a CAMAC data acquisition system. The pulse-height and position were derived using these signals for each of DET.1 and DET.2. Then, the recoil angle θ and the neutron energy are derived.

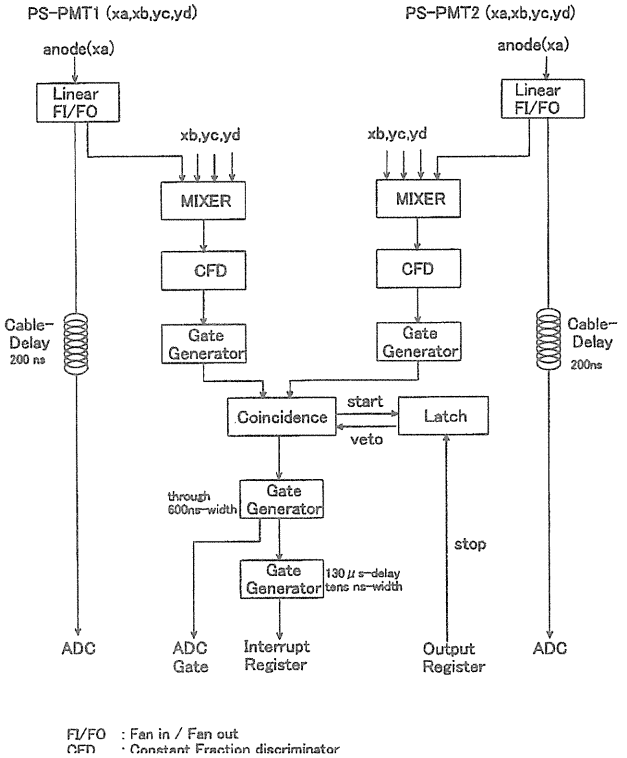

Fig.7.6-3; Electronics block diagram of PRPRT

7.6.3 The performance of PSPRT was tested using 14.1 MeV neutrons

The performance of PSPRT was tested using 14.1 MeV neutrons in Fast Neutron Laboratory (FNL), Tohoku University. The layout of the experiment is shown in Fig.7.6-4.

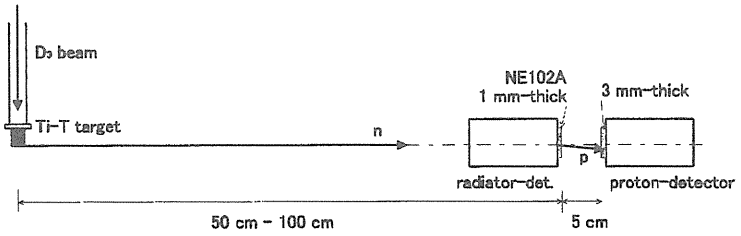

Fig.7.6-4: Experimental arrangement for test of PSPRT

Neutrons emitted to 90 deg. directions were used to minimize the source neutron energy spread (< 100 keV). The radiator was 1 mm thick NE102A plastic scintillator, and the stop detector was also a single NE102A scintillator, 3 mm thick. The side of the scinttilator was painted black to prevent light reflection.

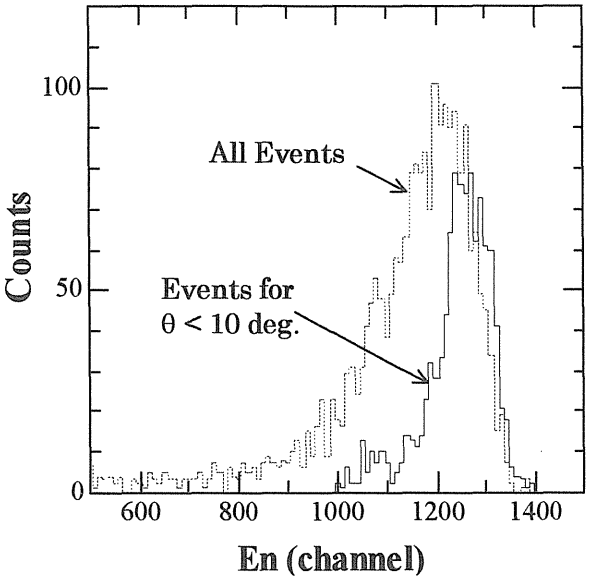

Fig.7.6-5; The response of PSPRT for 14.1 MeV neutrons

The results are shown in Fig.7.6-5. In the figure, two spectra are shown; one is for all events in acceptance angle and the other is for events with recoil angle smaller than 10-deg. PSPRT operated as expected and the effectiveness of angle information is obvious. However, the energy resolution observed (~8 %) is inferior to expected value mainly due to non-uniform sensitivity of PS-PMT. In this case, however, the correction for this effect was difficult to do because the scintillator is a single scintillator for both detectors and because the light transport inside the scintillator. Then, as the stop detector, we decided to employ a mosaic-type (square-rod) scintillator such as used in X-ray CT and PET machines etc.

Then, the stop detector was changed to a bundle of 16 pieces of mosaic-type CsI(Tl) scintillator, $3.75 \times 3.75 \times 30$ mm long to enable the correction for non-uniform anode sensitivity. The side and the top of each scintillator were wrapped with aluminum foil to prevent light interference (cross-talk) among scintillators.

The response of the new detector was measured in the pencil-beam course at Fusion Neutronics Source (FNS) of JAERI, where a neutron beam with energy resolution better than in FNL, Tohoku University could be expected. The experimental arrangement is shown in Fig.7.6.-6. The electronics circuit is same as in Fig.7.6-3.

The experimental result is shown in Fig.7.6-7. In this case, the energy loss in the radiator detector and the effect of non-uniformity of anode sensitivity was corrected for each pixel (scintillator), and the recoil angle is limited up to 5 deg. The spectrum was fitted with Gaussian function to derive the energy resolution. The resolution obtained is 5.2 % and better markedly than 8 % in the detector development. This improvement is due to correction for non-uniform sensitivity. Nevertheless, this value is not enough for actual plasma diagnostic. For further improvement, scintillators with high light output and photomultiplier with higher quantum efficiency are required.

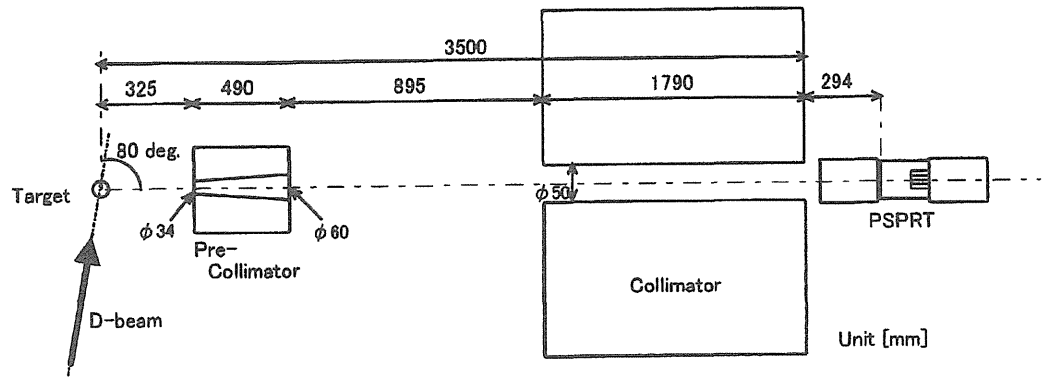

Fig.7.6-6; Experimental arrangement for FNS experiment

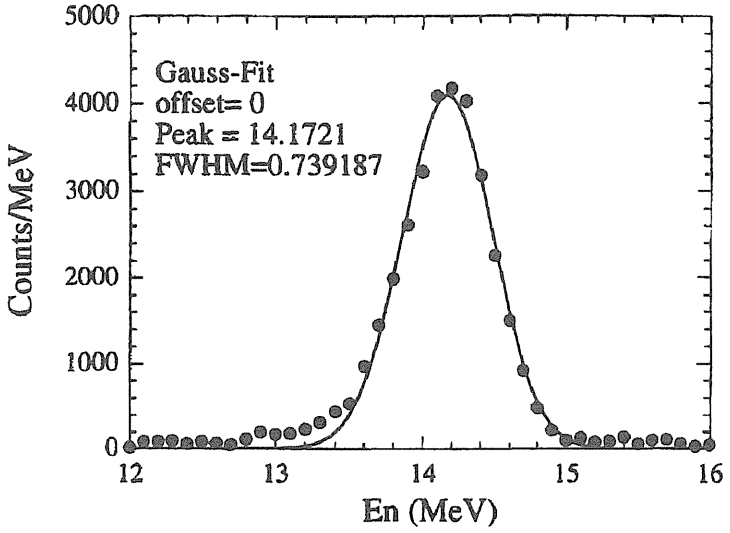

Fig.7.6-7: Experimental result of neutron spectrum measurement at FNS.

7.6.3 Summary

We have developed a position-sensitive proton-recoil-telescope that has potential to fulfill the detector requirement, and will be useful for experiments. The test experiment demonstrated the effectiveness of the present detector but the goal of the detector is difficult to achieve. Further studies will be conducted for further improvement of the detector.

References:

[1] Miura, T., M. Baba et al.; Nucl. Instrum. Methods, **A491**, 99-105 (2002).

[2] J.Olsen et al., IEEE Trans. Nucl. Sci., **40**, 74 (1998).

7.7 Thermal Neutron Profile Measurement using Scintillator Film and Optical Fiber

Toshiro ITOGA, Naoki KAWATA, Masayuki HAGIWARA, Mamoru BABA,
Takeo NISHITANI[1], Kentaro OCHIAI[1], Jun-ichi HORI[1], Makoto NAKAO[1]
Cyclotron and Radioisotope Center, Tohoku University, Aoba, Aramaki, Aoba, Sendai
[1]Fusion Neutron Laboratory, Japan Atomic Energy Research Institute, Tokai, Ibaraki

7.7. 1 Introduction

Measurement of a neutron profile plays an important role in the fusion reactor neutronics studies. Comparison of calculated neutron profile and spectrum with experimental ones provide a means to assess the nuclear data and calculation method employed in the design. Neutron profile measurement also provides useful information for shielding design. It is desirable to obtain the neutron profile in real time with good resolution and minimum perturbation to the neutron filed.

Several methods have been used for the purpose, such as the activation techniques and the position-sensitive counter techniques. The activation techniques give little perturbation and good spatial resolution but are not a real time one. Counters with position sensitivity with good spatial resolution are available like a position sensitive ^{3}He counters, but they are rather massive enough to give significant perturbation.

Mori *et al* reported a method of thermal neutron profiling by scanning the filed with a detector consisting of the ZnS(Ag) scintillator coupled to a photomultiplier with an optical fiber [1]. This method is suitable for our aim in the point of its compact size and the ability to measure in real time. This detector is made of a mixture of ZnS(Ag) and ^{6}LiF and has spatial resolution as high as 3 mm. However, in their detector, discrimination of background components in the lower pulse height region is difficult as shown in Fig.7.7-1, because of the ambiguity in setting the discrimination level. This problem may be due to improper light transmission and non-uniform energy loss of α particles and tritons in the scintillator. Considering such problems, we improved the performance of the detector by employing a combination of a ZnS(Ag) scintillator film and the ^{6}LiF foil coupled to the photomultiplier *via* an optical fiber. As the ZnS(Ag) scintillator film, we employed two types of scintillator; (1) ZnS(Ag) doped on a Mylar film and (2) an NE426 scintillator.

By using this method, we could measure thermal neutron profile in the fusion blanket mockup experiment in real time with high accuracy by rejecting the background components.

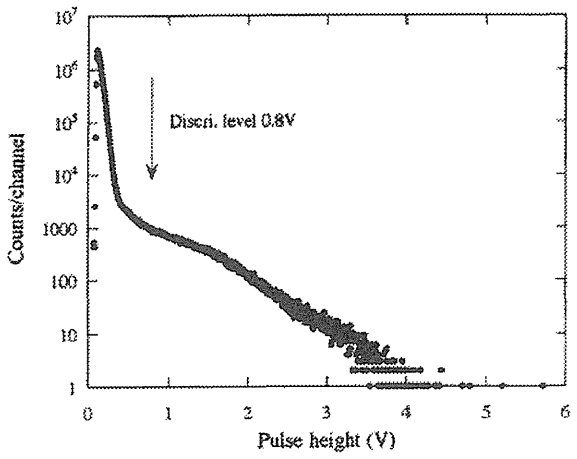

Fig. 7.7-1. Pulse height distribution of ZnS(Ag)-^{6}LiF detector by Mori et al [1].

7.7.2 Development of new detector

Our detector consisted of separate ZnS(Ag) and a ^{6}LiF foil. The ZnS(Ag) scintillator is plated on a Mylar film, 70 μm thick (Instrument Grade Films Co. Ltd) . The ^{6}LiF foil was fabricated with the vacuum evaporation method on an aluminum foil, ~720 μg/cm^2 thick. First, we measured the response of the detector without a fiber using thermal neutrons obtained by moderating 550 keV neutrons produced by the ^{7}Li(p,n) reaction with polyethylene blocks.

Figure 7.7-2 shows the pulse-height distribution by this detector. The separation of neutron events from background components is significantly clearer than in the preview detectors (Fig.7.7-1).

However, there is still an overlap between background components and neutron events. Then, we applied a pulse-shape discrimination (PSD) method based on the zero-crossing technique. In this method, the pulse-shape information was obtained from the zero-cross points of the signal differentiated with the delay-line amplifier. The PSD signal was obtained from the time difference between the anode signal and the zero-cross point. Figure 7.7-3 shows the two-dimensional spectrum for the pulse height *vs.* pulse shape. Neutron events are clearly separated from the background events in the lower pulse-height region which proved to be protons from the Mylar film for ZnS(Ag). Further, triton events and α events are separated each other clearly. Therefore, the PSD technique is effective for the detector to improve the signal-to-noise ratio. We also fabricated and tested a detector using an NE426 scintillator instead of ZnS(Ag). The NE426 scintillator is made of a mixture of ZnS(Ag) and ^{6}LiF, 0.5 mm thick, placed on an aluminum plate. It is fairly stable and easy to fabricate.

We confirmed proper response of the detector using thermal neutrons produced by moderating 8 keV neutrons from the reaction of ^{49}Sc(p,n) [3].

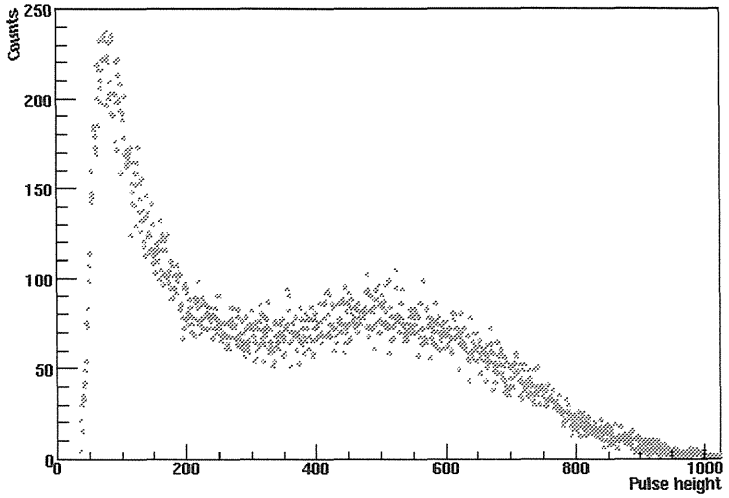

Fig.7.7-2; Pulse height distributions of ZnS(Ag)-^{6}LiF detector

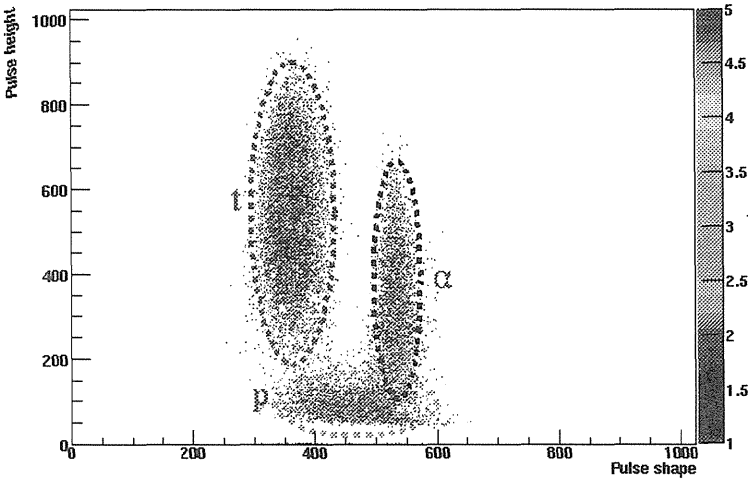

Fig. 7.7-3; Pulse- height vs. Pulse shape for ZnS(Ag)-^{6}LiF detector

7.7.3 Application of the Detector to Fusion Blanket Experiments

Then, we connected the ZnS(Ag)-^{6}LiF scintillator to a photo-multiplier tube with an optical fiber and applied to thermal neutron profile measurement at Fusion Neutronics Source (FNS). We measured the thermal neutron profile in the mockup system of a tritium breeding blanket. The measured thermal neutron profile gives information on the validity of the design calculation. Figure 7.7-4 shows the mockup system we used in this experiment and Fig.7.7-5 illustrates the detector.

First, to confirm the performance of this detector itself, we measured the detector response to thermal neutrons obtained by moderating 14 MeV neutrons with polyethylene blocks, 5cm thick. Figure 7.7-6 shows the result of the response measurement. Thermal neutron events are separated from background events although it α particles and tritons are not separated each other.

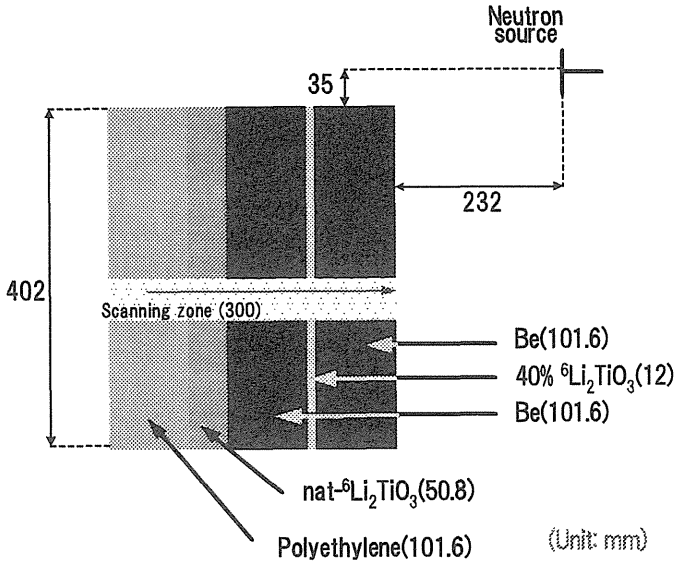

Fig.7.7-4; Configuration for fusion reactor blanket experiment

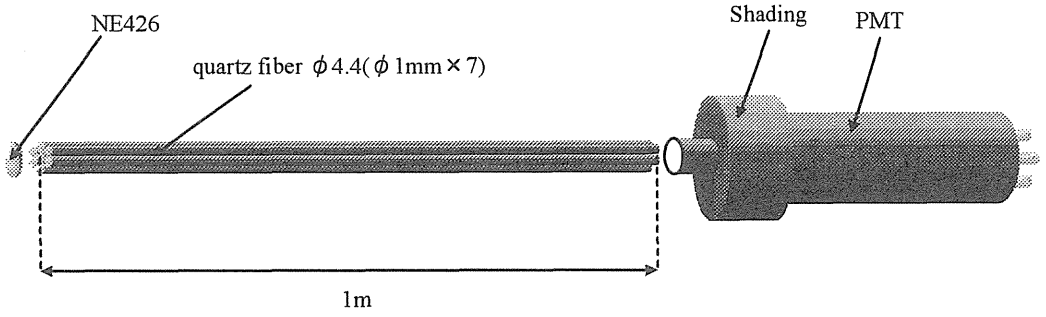

Fig. 7.7-5. Configuration of the ZnS(Ag)-^{6}LiF detector using a fiber

We selected only thermal neutron events by a discriminator and counted only thermal neutron events. Then we counted thermal neutron events continuously by moving the detector for 30 cm in the system using a stepping motor controlled remotely and counted the events rate using a multi-channel-scaler (MCS) as a function of elapsed time.

Figure 7.7-7 shows the result of the thermal neutron measurement. It shows that the thermal neutron spatial distribution reasonably reflects the configuration of the system. Thermal neutrons decreased in the region of the blanket including ^{6}Li and increased in the region of blanket of the polyethylene and ^{9}Be. The thermal neutron profile varies rather smoothly. This is not due to the finite spatial resolution of the detector but the nature of the system as indicated by the fact that in the previous experiment [4] using a thermal neutron field with a sharp edge prepared by a cadmium plate, we achieved a resolution of better than 1 mm.

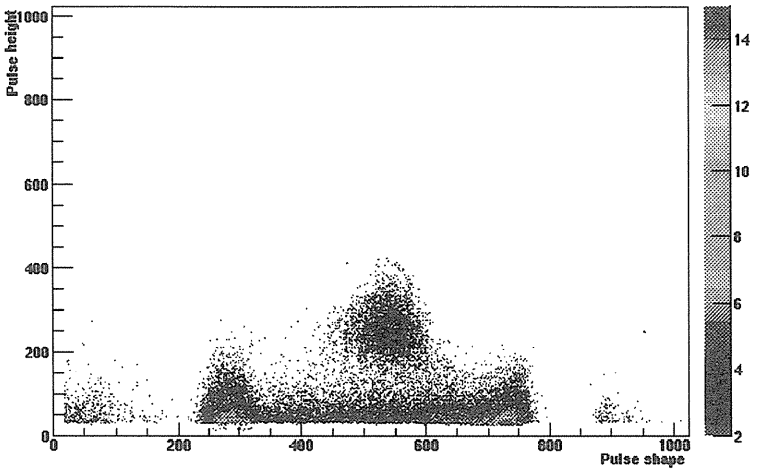

Fig. 7.7-6. Performance of the detector using optical fibers

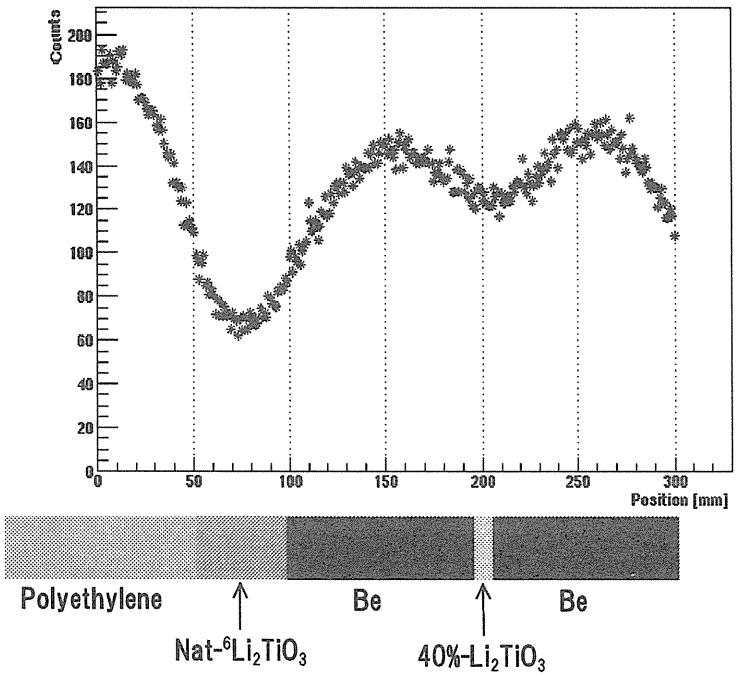

Fig. 7.7-7. Thermal neutron profile in the blanket mockup system

7.7.4 Summary

We fabricated a thermal neutron profile detector using ZnS(Ag) and an optical fiber between the scnitillator and a photomultiplier, and could distinguish thermal neutron events from background components. Using the detector, we could measure the thermal neutron profile in real time in the fusion reactor blanket experiments by scanning the field with the detector. A paper of the subjects has been submitted and will be published soon [5].

Reference

[1] C. Mori et al.: Nucl. Instr. and Methods **A422**, 129-132, (1999)

[2] S. Yasuda et al.: The abstracts of annual meeting of the Atomic Energy Society of Japan, C24, (1998)

[3] M. Baba et al.: Nucl. Instr. and Methods **A376**, 115-123, (1996)

[4] N. Kawata et al.: The abstracts of fall meeting of the Atomic Energy Society of Japan, **E37**, (2001)

[5] T. Itoga., et al., Proc. Int. Symposium on Radiation Safety and Detection Technologies; to be published

8. Skyshine Experiments

8.1 Neutron Dose Measurements and the Analyses

Takeo NISHITANI, Kentaro OCHIAI, Satoshi SATO, Michinori YAMAUCHI,
Makoto NAKAO, Chuzo KUTSUKAKE, Masayuki WADA[1], Shigeo YOSHIDA[2]
Fusion Neutron Laboratory, Japan Atomic Energy Research Institute, Tokai, Ibaraki
[1]*Startcom Co. Ltd., Tokyo*
[2]*Tokai University, Hiratsuka*

8.1.1 Introduction

The evaluation of the radiation exposure outside fusion reactors is very important from the safety point of view. Because the roof of the fusion reactor hall is not so thick compared with the vertical wall, radiation leakage into the environment from the fusion reactor will occur mainly from the roof, which is termed skyshine. Except for the internal exposure of the radioactive gas such as tritium from the stack, the skyshine effect is the most important external exposure source on fusion reactors. The accurate estimation of the skyshine leads to reasonable shielding designs.

There are some studies of neutron skyshine at fission reactors[1,2] and high energy accelerators.[3,4] However, the number of reports on fusion neutron skyshine experiments is very limited. The first experiment of D-T neutron skyshine was carried out at the OKTAVIAN facility of Osaka University, where the neutron dose distribution and the secondary gamma-ray spectra were measured at distances as far way as 600 m from the neutron source.[5-7] The roof of the OKTAVIAN facility is 16 cm thick concrete. The average neutron yield was 8×10^8 n/s in the experiments, which is not strong enough to understand the neutron and secondary gamma-ray behaviors in the region far from the neutron source. Real skyshine measurements were done during the D-T experiments of the Tokamak Fusion Test Reactor (TFTR) at Princeton Plasma Physics Laboratory.[8] Neutron and gamma dose rates were measured in the distance range of 20- 200 m from TFTR.

The major subject of the skyshine experiment is to evaluate the accuracy of the simulation, and to understand the propagation process of the neutron in the air and the secondary gamma-ray production process, which requires an intense neutron source and a well defined source neutron characteristics such as the energy spectrum and the angular distribution. The D-T neutron skyshine experiments were carried out at FNS with a port at the roof in March 2002 and March 2003 [9]. This paper describes mainly the skyshine neutron dose distributions and MCNP analyses of the experiments.

8.1.2 Experiments

FNS is an accelerator based intense neutron source through D-T reactions. Figure 8.1-1 shows a schematic view of the FNS facility. FNS has two target rooms; target room I has a fixed tritium target containing 3.7×10^{11} Bq tritium and the target room II has a rotating tritium target containing 3.7×10^{13} Bq tritium. We used target room I for the shyshine experiments. The target room is 15×15 m^2 wide and 9.1 m high. The thickness of the concrete wall is 1.15 m at the roof and 2 m at the vertical wall. The floor of the target room is an iron grating in order to reduce the neutron scattering from the floor. The tritium target is located 1.8 m above the floor, 5.5 m away from the south wall and 2.75 m from the west wall. The target room has a port in the roof with a size of 0.9×0.9 m^2 which was used for the shyshine experiments. This port is usually closed with a concrete plug. For skyshine experiments, the concrete plug was removed and only 2 mm thick stainless steel plates closed the port in order to keep the reduced air pressure in the target room. The neutron attenuation by 2mm stainless steel plates was negligible. FNS was operated with an acceleration voltage of 360 kV and a target current of 1.4 mA in this experiment. The average neutron yield was $\sim 1.7 \times 10^{11}$ n/s, which was monitored by the associated alpha particle measurement with a silicon surface barrier diode installed in the beam line

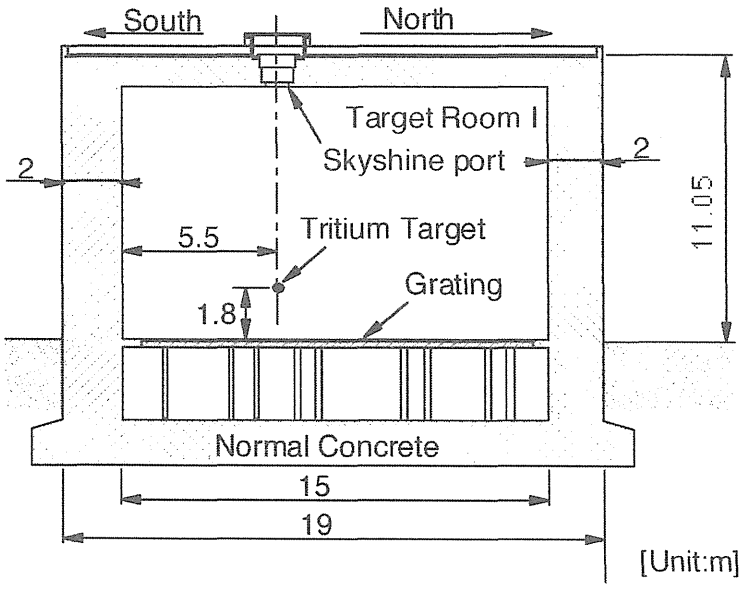

Fig. 8.1-1 Schematic view of the FNS facility

Figure 8.1-2 shows the measurement points around the FNS. FNS is located on a rather flat land only 150 m away from the Pacific Ocean. The north and east sides are surrounded with a forest of pine trees which are about 10 m tall. The neutron dose rates were measured with a spherical rem-counter based on a ^{3}He proportional detector, Fuji Electric NSN10002,

just on the ground at distances from 20 to 400 m in the pine forest and 550 m out of the pine forest along the north direction, and at distances from 20 to 140 m on a road along the south direction.

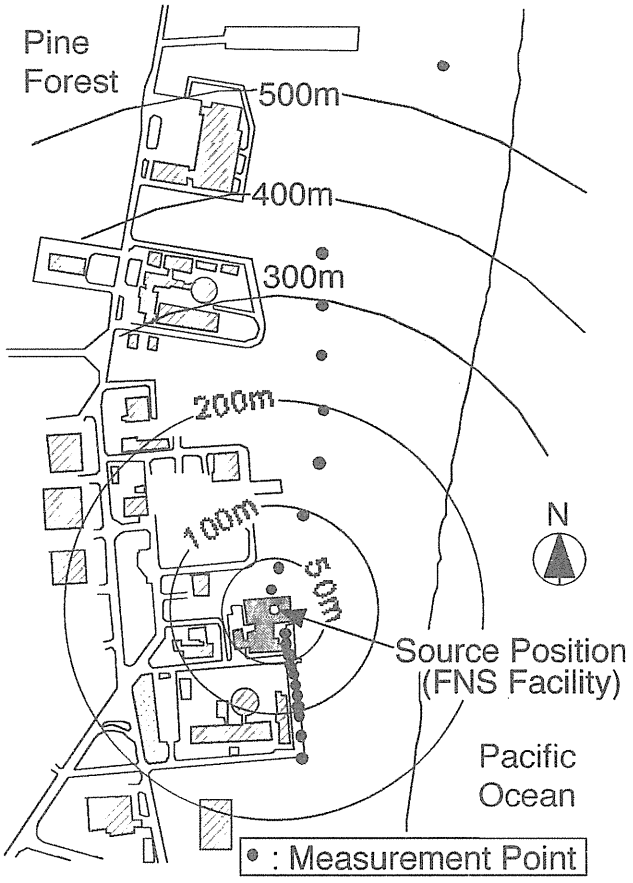

Fig.8.1-2 Measurement points around the FNS building for the skyshine experiment

8.1.3 Results and Analyses

This shyshine experiment was simulated with neutron Monte Carlo calculations using MCNP-4C [10] code and the JENDL-3.2 [11] neutron cross-section library. Figure 8.1-3 shows the MCNP models for the skyshine experiments. For the analysis of the dose distribution in the north direction, the FNS facility was modeled with a simplified cylindrical geometry of 11.5 m in diameter, which was the distance from the source to the north side wall. The pine forest was modeled by homogenized material of $C_6H_{10}O_5$ with a density of 2×10^{-3} g/cm^3, which was determined by an investigation of the average size of pine trees and average number of the trees in the experimental field. The ground was assumed to be concrete with a density of 2.3 g/cm^3. Other buildings were not modeled. In the south direction, the diameter of the FNS facility is 7.5 m. The pine forest was not modeled, because all measurement points

were on the road. The pressure and the humidity of the air were taken into account using measured values.

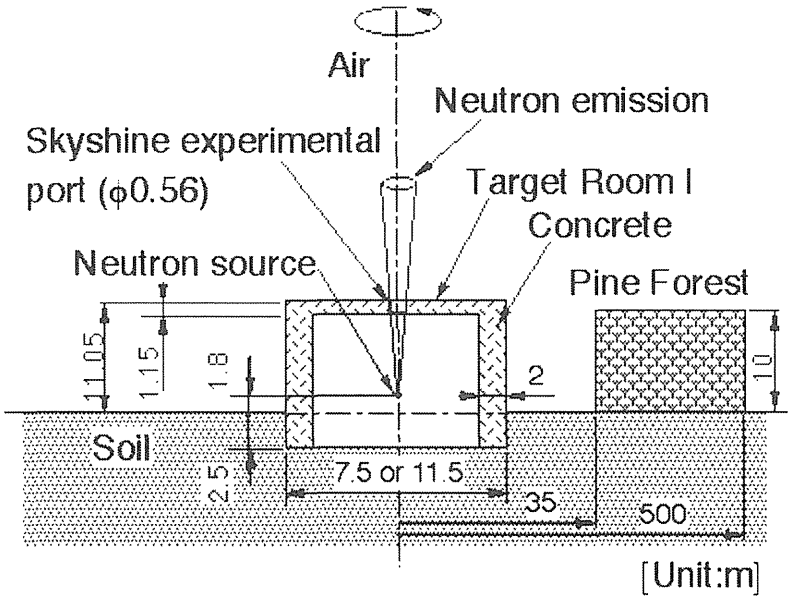

Fig. 8.1-3 MCNP calculation model of the D-T neutron skyshine experiment at FNS.

Neutrons were emitted only toward the skyshine port at the roof from the target in this calculation. The calculation using a 4π emission source was tried to evaluate the contribution of the transmission through the vertical wall and the roof. The typical number of histories is 50,000 and 650,000 for the corn and the 4π sources, respectively. A ring type tally was used in the MCNP calculations.

The neutron dose rate distribution as far as 550 m is shown in Fig.8.1-4. The measured neutron doses in the south direction are about 30% larger than those in the north direction, which is probably because the shorter distance from the source to the wall in the south direction. The background neutron dose rate was 0.004 μSv/hr at the distance of 50 m from the neutron source. Measured neutron dose rates agreed well with the calculation using the 4π source up to the distance of 140 m. In the north direction, the MCNP calculation using the 4π source coincided with that of the corn source at the distance of 200 m. The statistical error of the MCNP calculation with 4π source increases with the distance farther than 250 m. So we adopted MCNP calculations using the corn source for distances farther than 250 m.

8.1.4 Conclusion

D-T neutron skyshine experiments were carried out at FNS with a port at the roof. Neutron and secondary gamma-ray dose rates were measured as far as 550 m and 400 m, respectively.

The experimental results were analyzed with the Monte Carlo code MCNP-4C with the nuclear data library JENDL-3.2, where the FNS building and the measurement field including the pine forest were modeled with simplified cylindrical geometries. The MCNP calculation agreed well both neutron and secondary gamma-ray dose rate distributions within uncertainty of 30%.

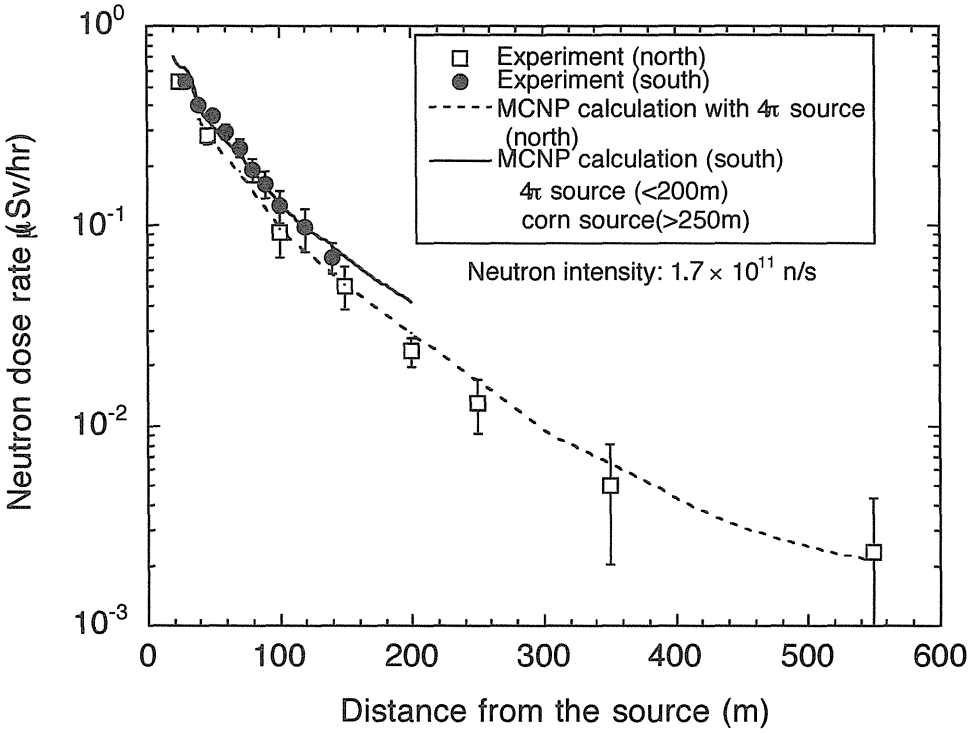

Fig. 8.1-4 Neutron dose distributions in the north and south directions compared with MCNP calculations.

References

[1] A.H. Kazi, C.R. Heimbach, R.C. Harrison, et al., Nucl. Sci. Eng. **85**, 371 (1983).

[2] T. Nakamura and T. Kosako, Nucl. Sci. Eng. **77**, 168 (1981).

[3] T. Nakamura,T. Kosako, K. Hayashi, et al., Nucl. Sci. Eng. **77**, 182 (1981).

[4] K. Hayashi and T. Nakamura, Nucl. Sci. Eng. **87**, 123 (1984).

[5] T. Nakamura, Y. Uwamino, K. Hayashi, et al., Nucl. Sci. Eng. **90**, 281 (1985) .

[6] S. Yoshida, R. Morotomi, T. Kondo, et al., J. Nucl. Sci. Tech. **Suppl.1**, 650 (2000).

[7] M. Ueda, MS thesis, Osaka University, Department of Nuclear Engineering (1984).

[8] H.W. Kugel, G. Ascione, S. Elwood, et al, Fusion Eng. Des. 28, 534 (1995).

[9] S. Yoshida, T. Nishitani, K. Ochiai, et al., Fusion Eng. Des. 69, 637 (2003).

[10] J.F. Briesmeister (Ed.), MCNP - a general Monte Carlo n-particle transport code, version 4C, LA-13709-M, Los Alamos National Laboratory (2000).

[11] T. Nakagawa, K. Shibata, S. Chiba, et al., "Japanese evaluated nuclear data library version 3 reversion-2: JENDL-3.2", J. Nucl. Sci. Technol., **32**, 1259 (1995).

8.2 Secondary Gamma-ray Measurements

Ryohei TANAKA, Shigeo YOSHIDA[1], Isao MURATA, Masayuki WADA[2] and Kentaro OCHIAI[3]
Osaka University, Suita
[1]Tokai University, Hiratsuka
[2]Startcom Co. Ltd., Tokyo
[3]Fusion Neutron Laboratory, Japan Atomic Energy Research Institute, Tokai, Ibaraki

8.2.1 Introduction

In the skyshine experiment, not only the neutron dose but also the secondary gamma-ray dose is important to evaluation the total radiation dose. Previously it was considered that secondary gamma-rays were generated by neutron scattering reactions with air. In the D-T experiments of TFTR [1], however, the secondary gamma-ray dose was comparable to the neutron one in the distance range of 20- 200 m from TFTR, which suggested the contribution of gamma-ray generated by the experimental buildings were significant. Secondary gamma-ray spectra and the doses were measured in the FNS neutron sakyshine experiments (see 8.1) to study the gamma-ray production process

8.2.2 Experimental Setup

The D-T neutron skyshine experiments were carried out at FNS with a port at the roof in March 2002 and March 2003. The setup is described in Section 8.1. Secondary gamma-ray spectra were measured by a high purity Ge detector at distances of 20, 50 and 100 m, and a NaI scintillation detector with a size of 20 cm in diameter by 20 cm long at distances of 200 and 300 m. Also a BGO ($Bi_4Ge_3O_{12}$) scintillation detector with a size of 12.5 cm in diameter and 12.5 cm in length was used for the gamma-ray measurement on the roof and near the wall of FNS. The Secondary gamma-ray dose was evaluated by the gamma-ray spectra derived from the pulse height spectra of NaI scintillation detectors using an unfolding code HEPRO [2].

8.2.3 Secondary Gamma-ray Spectra

Figures 8.2-1 and -2 shows the pulse height spectra measured with the NaI scintillation counter of 125 cm in diameter at the distance of 20, 50 and 100 m, and those with the counter of 200 cm in diameter at the distance of 200 and 300 m, respectively. A natural gamma-ray background from ^{40}K and ^{208}Tl was clearly observed at 1.461 and 2.614 MeV, respectively. A full energy peak from the $^{1}H(n,\gamma)$ reaction and a single escape peak from the $^{56}Fe(n,\gamma)$ reaction are identified at 2.223 and 7.1 MeV, respectively. The origin of those gamma-rays are not

identified, because hydrogen and iron are included in air, soil and buildings. A continuum spectrum in the energy range of 3-7 MeV was enhanced by the shyshine, which is considered to be the convolution of Compton spectra from some neutron capture reactions.

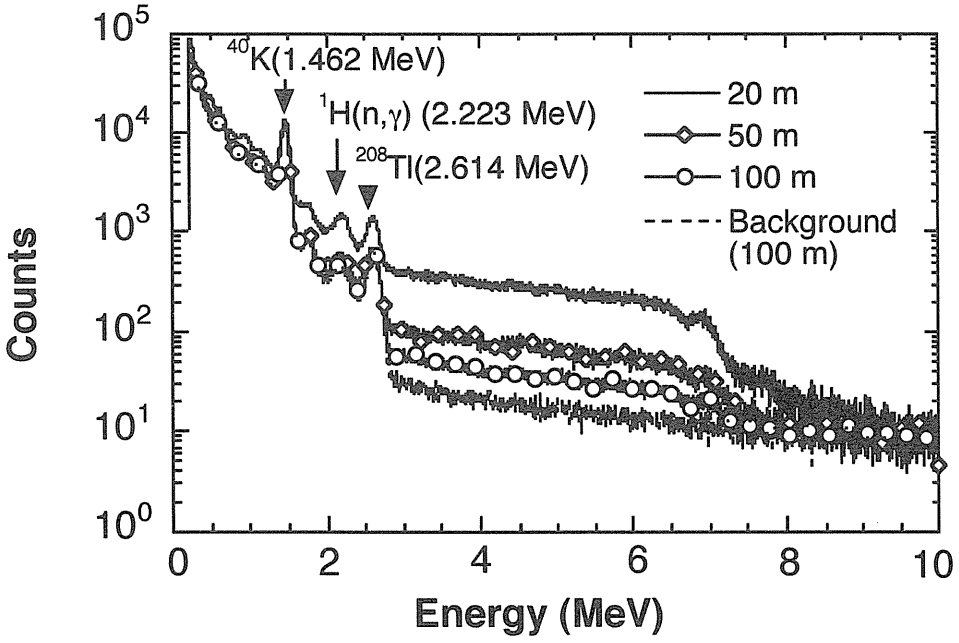

Fig. 8.2-1 Secondary gamma-ray spectra with the NaI scintillation counter of 125 cm in diameter at the distance of 20, 50 and 100 m.

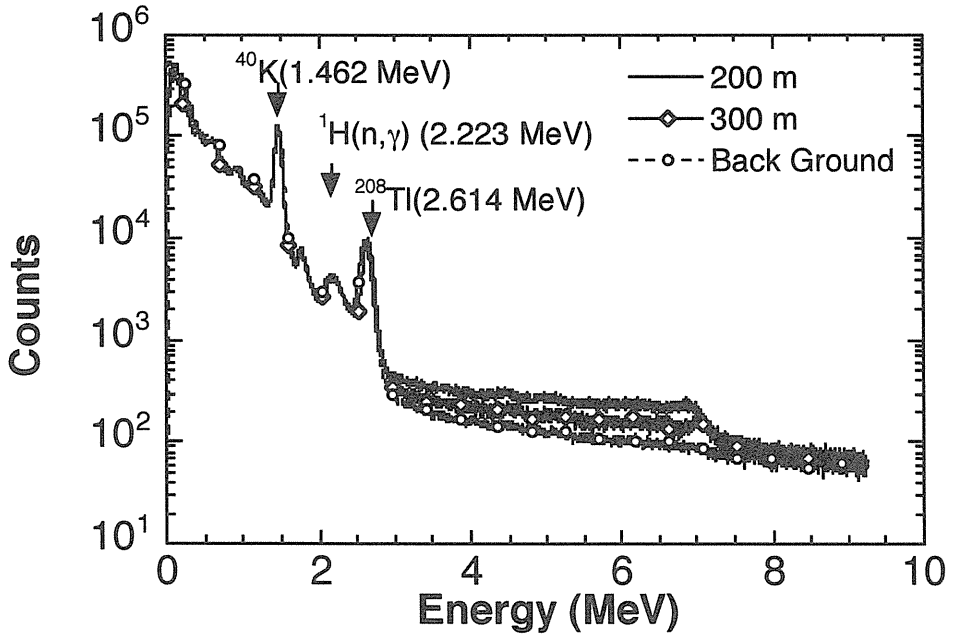

Fig. 8.2-2 Secondary gamma-ray spectra with the NaI scintillation counter of 200 cm in diameter at the distance of 200 and 300 m.

Figure 8.2-3 shows the pulse height spectra measured with the high purity Ge detector at the distance of 20 m from the neutron source. Several peaks of $^{28}Si(n,\gamma)$ and $^{56}Fe(n,\gamma)$ reactions are observed. Those peaks are not observed in the spectra measured at the distance further than 50 m. So those gamma-rays are considered to arise from the FNS building. In the pulse height spectra measured with the BGO scintillation detector, any clear peak except ^{40}K, ^{208}Tl and the peak from the $^{1}H(n,\gamma)$ reaction was not observed on the roof and near the wall of FNS.

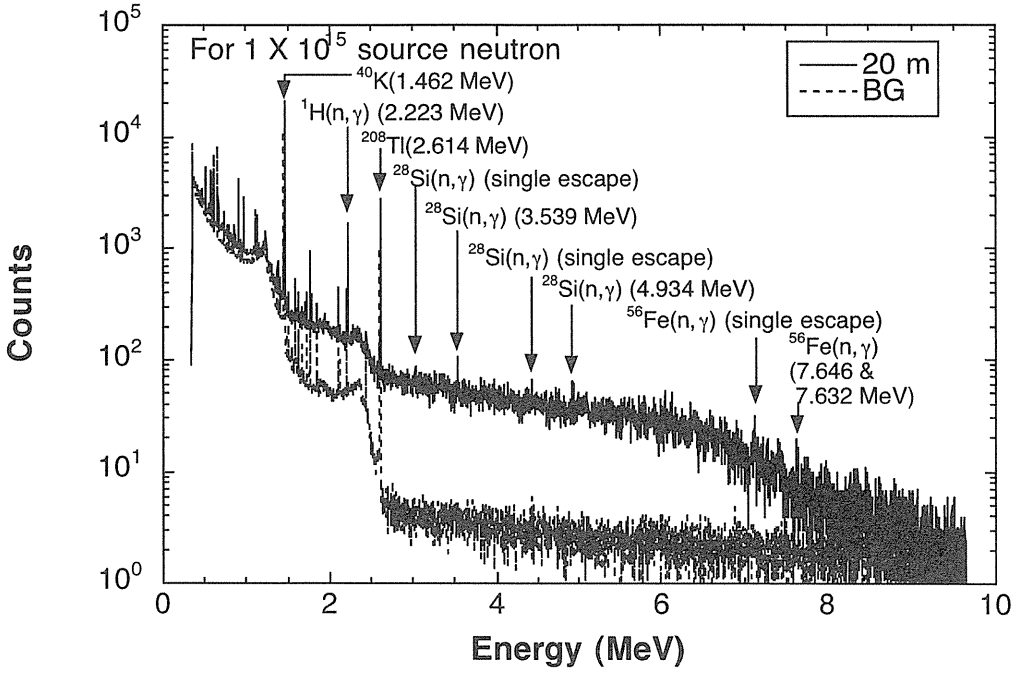

Fig. 8.2-3 Secondary gamma-ray spectra measured with the high purity Ge detector at the distance of 20 m

8.2.4 Secondary Gamma-ray Dose

It was difficult to measure the gamma-ray dose directly by a gamma-ray survey mater. Here the Secondary gamma-ray dose was evaluated by multiplying the dose equivalent conversion factor on the gamma-ray spectra unfolded from the pulse height distribution of the NaI(Tl) scintillation detector using the unfolding code HEPRO. Figure 8.2-4 shows the secondary gamma-ray dose rate distribution. In this experiment, the secondary gamma-ray dose was about 1/100 of the neutron dose. Monte Carlo analysis was carried out based on the model shown in Fig. 8.1-3. The measured dose rate agreed well within 20% of the experimental error with the MCNP-4B [3] calculation with JENDL-3.2 [4].

8.2.5 Conclusion

Secondary gamma-ray measurements were carried out on the D-T neutron skyshine

experiments at FNS by opening the skyshine experimental port at the roof. The Gamma-ray was measured with NaI(Tl) scintillation detectors as far as 300 m away from the D-T target point. The Gamma-ray dose rates were evaluated from the gamma-ray spectra unfolded from the pulse height distribution of the NaI(Tl) scintillation detectors, which agreed well to the Monte Carlo simulation using MCNP-4B code within 20%. Source nuclei of the gamma-rays were investigated around the FNS facility by using a high purity Ge detector, where capture gamma-rays of iron, hydrogen and silicon were identified. The origin of the iron capture gamma-rays is considered to be the concrete of the building. Also gamma-rays of hydrogen and silicon were observed, which suggests that the major source of secondary gamma-rays are from capture reactions of the skyshine neutrons in the soil rather than from scattering reactions in the air.

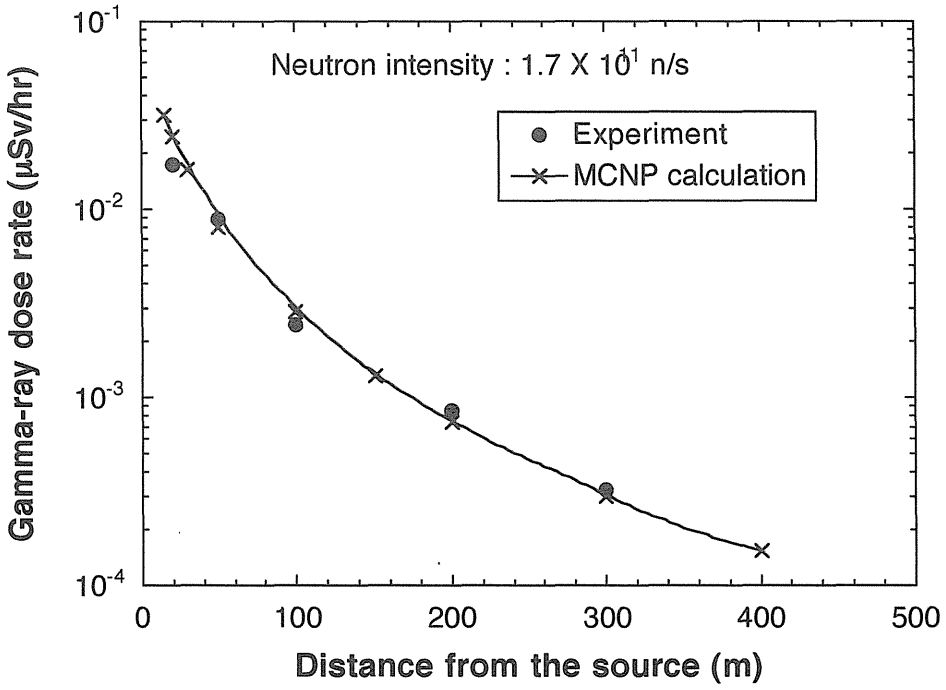

Fig. 8.2-4 Secondary gamma-ray dose rate distribution

References

[1] H.W. Kugel, G. Ascione, S. Elwood, et al, Fusion Eng. Des. **28**, 534 (1995).

[2] M. Matzke, Unfolding of pilse height spectra: The HEPRO program system, Physikalisch Technische Bundesanstalt Report, PTB-N-19, 1994.

[3] J.F. Briesmeister (Ed.), MCNP - a general Monte Carlo n-particle transport code, version 4C, LA-13709-M, Los Alamos National Laboratory (2000).

[4] T. Nakagawa, K. Shibata, S. Chiba, et al., "Japanese evaluated nuclear data library version 3 reversion-2: JENDL-3.2", J. Nucl. Sci. Technol., **32**, 1259 (1995).

8.3 Neutron Spectrum Measurement and Dose Evaluation using Bonner Multi-cylinders

M. Wakisaka[1], Junichi Kaneko[1], Kazumasa Shiraishi[1], Fumiyuki Fujita[1], Akira Homma[1], Teruko Sawamura[1], Kentaro Otiai[2], Takeo Nishitani[2]

[1]*Hokkaido University, Sapporo*

[2]*Fusion Neutron Laboratory, Japan Atomic Energy Research Institute, Tokai, Ibaraki*

8.3.1 Introduction

Energy spectrum was measured by using Bonner multicylinders in the same field described in chap.8.1. In skyshine experiment, a highly sensitive detector is required for measurement of weak radiation fields. In the present experiment a large volume cylindrical ^{3}He proportional counter has been used as a thermal neutron detector. Responses for ^{3}He detector in Bonner Cylinders have been calculated by MCNPX and the energy spectra have been obtained with SAND-II unfolding code. Then the ambient doses have been evaluated. Calculations by MCNPX Monte Carlo code of the energy spectra at the measurement points are shown in Fig.8.1-2. The unfolding multicylinder data up to the distance of 200m from the D-T source are compared with the calculation and a discussion has been done on the results.

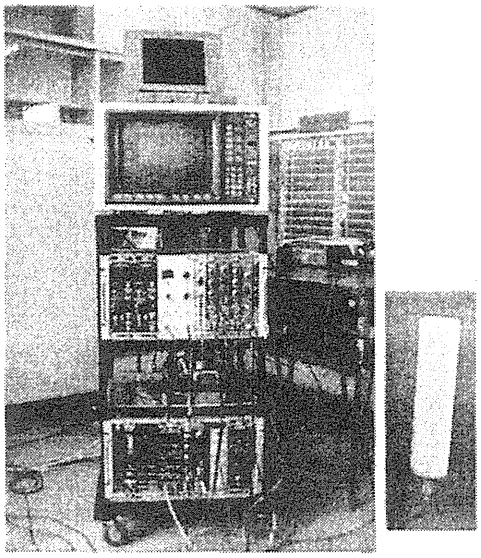

Fig. 8.3-1 counting system, which is set in the monitoring car and the counter with 3cm thickness moderator.

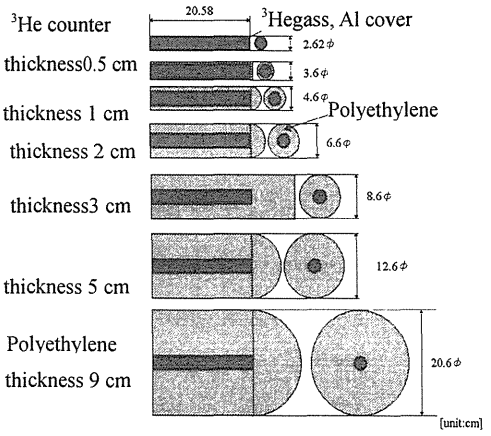

Fig. 8.3-2 Bonner multicylinders: ^{3}He counter with different sizes of polyethylene moderators

8.3.2 Experiments

Fig.8.3-1 shows the counting system and the counter with the 3 cm thickness moderator. The system is set in the monitoring car and brought to the measurement points together with the Bonner cylinders. The ^{3}He counter was set at the center of the cylinders of polyethylene shown in Fig.8.3-2. The sensitive volume and ^{3}He gas pressure of the detector were 89.05 cm^3 and 4.0 atm respectively. The response functions for the ^{3}He counter in

Bonner cylinders are shown in Fig.8.3-3 with moderator thickness as a parameter. The responses are calculated for isotropic incident neutrons directing to the detector center.

Bonner cylinders were vertically set at 1.5 m height from the ground at the measurement points.

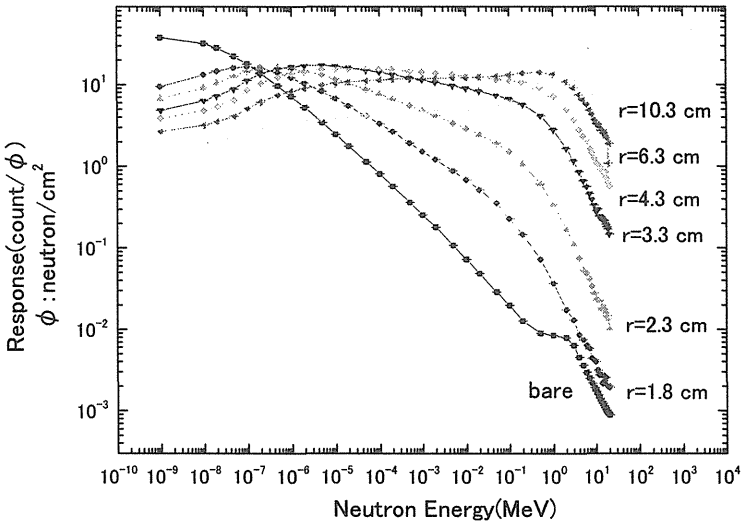

Fig. 8.3-3 Response function of ^{3}Hecounter with different sizes of moderators

8.3.3 Results and discussion

Fig.8.3-4 shows the unfolding spectrum at the center of the skyshine port in Fig.8.1-1. The calculation with MCNPX is also shown in the figure. This spectrum provides an initial guess for unfolding the multicylinder data. The agreement of both spectra is fairly well. At this point, calculated value of dose and evaluated one with unfolding spectrum are 3.84 x 10^4 and 3.34 x 10^4 μSv/h respectively for the source strength of 1.7 x 10^{11} n/s.

The similar spectra at the distances of 46 m and 200 m are shown in Fig.8.3-5 together with unfolding spectra by using another response functions described later. The moderate peak at ~1MeV and the thermal peak become clearer in the spectra, which are thought to be produced by slowing down of neutrons through the shielding wall and during

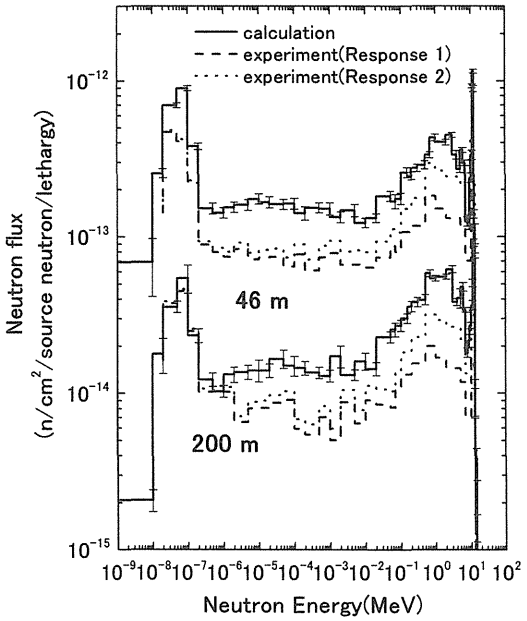

Fig. 8.3-5Neutron energy spectra by calculation and experiment in the north directions. The different response functions are used for unfolding.

propagation through the air and the ground. The deviation of the experimental results from the calculations becomes prominent at intermediate energy region.

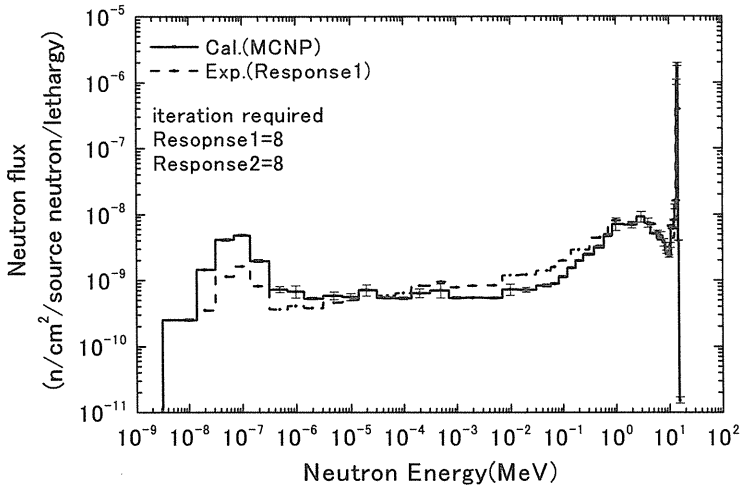

Fig. 8.3-4 Energy spectra by calculation and unfolding at the port center.

One of the reasons for this disagreement might be due to the anisotropic incidence of neutrons to the Bonner cylinder. To investigate this, the response function has been calculated for isotropic incidence neutrons from different directions except the directions through which the neutrons enter the detector-end-surface facing the ground. This means that the skyshine neutrons enter the detector from the top and other sides of the cylinder but not from the ground. We call these response functions Response 2 and those shown in Fig.8.3-3 Response 1. The unfolding spectra by using Response 2 given in the Fig.8.3-5 show better agreement with calculation, which indicate that more detailed treatment of anisotropy of neutrons on the Bonner cylinder is required for more accurate evaluation.

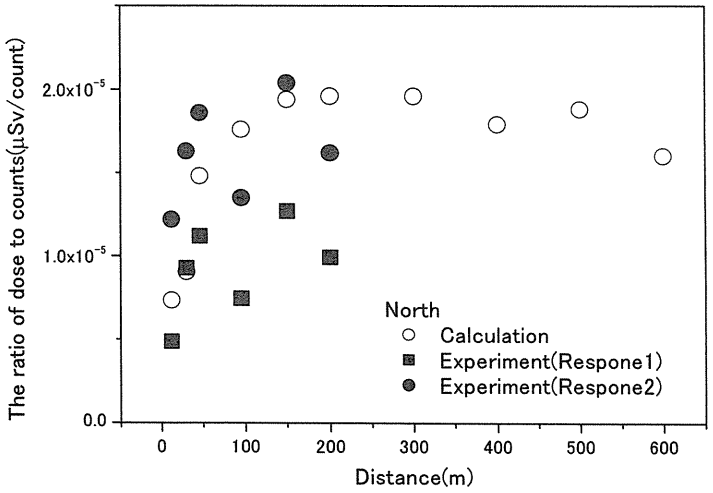

Fig.8.3-6 The ratio of dose to counts by calculation and evaluation with the unfolding spectra.

If the change of the spectrum during the propagation is not so large, a single suitably designed counter can be used to evaluate ambient dose. The counter system with the moderator of 3 cm-thickness was used for this purpose and performed the measurement up to 534 m in North and 135 m in South. The average value of the measured values at different points, the experimental counts is 85% of the calculation in North and 103 % in South. Dose distribution has also been calculated and evaluated by using unfolding spectra. From calculations and experimental evaluation, the ratios of counts to dose have been estimated, which are shown in Fig.8.3-6. The calculation shows that it is almost constant in the region of distance longer than ~100 m. The same tendency appears in the experimental data. Therefore the counter system with 3 cm thickness moderator is used as dosimeter in the longer distance than 100 m. The ratio of dose to counts by 3cm-thickness cylinder is 1.95 x 10^{-5} μSv/h in calculation, 1.06 x 10^{-5} μSv/count by Response 1 and 1.83 x 10^{-5} μSv/count by Response2 in North at 150~200 m. Background count rate was ~200 counts/h, which corresponded to 2~4 x 10^{-3} μSv/h.

8.3.4 Conclusion

Energy spectra of skyshine neutrons from the FNS skyshine port have been evaluated by using Bonner multicylinder and compared with the calculation by MCNPX Monte Carlo code. The spectra at the port center fairly agree with each other however at distant points deviation between those appears. One of the reasons for this deviation is thought to be due to the anisotropy of the incidence neutrons into the Bonner multicylinder. For dose evaluation by a single counter, the ratios of dose to counts by the counter with 3 cm-thickness polyethylene moderator have been calculated and compared with the ratios evaluated by unfolding spectra. The calculation shows that the ratio is fairly constant at the distances longer than 100 m. The absolute values of the conversion factor by calculation agree with the evaluation by Response 2 at 150~200 m.

Bonner multicylinder, using a large volume cylindrical ^{3}He counter as a thermal neutron detector, is advantageous as a highly sensitive spectrometer for skyshine experiment, however, for accurate estimation, more detailed treatment of the anisotropy of neutron field might be needed.

Acknowledgements

The authors want to acknowledge the help of the stuff of FNS for preparation of the experiment and the operation of the accelerator. The assistance of undergraduate students, Mr. S. Kawamura, Mr. K. Tsuji and Mr. S. Tsutida, of Hokkaido University is also acknowledged.

9. Neutronics Analyses and Code Developments

9.1 Modification of ACT-4 for Sequential and Multi-step Reactions

Jun-ichi HORI[1], Michinori YAMAUCHI, Satoshi SATO, Hiromitsu KAWASAKI[2] and Takeo NISHITANI

Fusion Neutron Laboratory, Japan Atomic Energy Research Institute, Tokai, Ibaraki

[1]Present address: Research Reactor Institute, Kyoto University, Kumatori-cho, Osaka

[2]CRC Solutions Corporation, Jonan, Mito, Ibaraki

9.1.1 Introduction

The THIDA-2 system is a comprehensive tool for the calculation of the radioactivity, the decay heat and the dose rate for a fusion reactor [1]. The system consists of three calculation parts for the transport of neutron and delayed gamma ray, induced activity and dose rate. The ACT-4 code is a sub-program and calculates the induced activity, the approximate decay heat and the delayed gamma-ray source after a pulsed operation of the fusion device by means of Matrix Exponential Method to solve the decay chain equations. However, the ACT-4 code has three restrictions of the complexity of the problem: (1) sequential decay of two short-lived nuclei cannot be calculated accurately, (2) the activation of nuclei produced via primary neutron reactions (multi-step reactions) and the activation caused by secondary charged particles (sequential charged particle reactions) are not considered, (3) changes in neutron flux caused by transmutation cannot be treated in a single calculation. It is important for the safety design of a fusion reactor to deal with the multi-step and sequential reactions (SCPRs). In this work, we especially focused on the second restriction and modified ACT-4 code.

9.1.2 Modification of ACT-4 code

In ACT-4 code, Matrix Exponential Method is applied to obtain time dependent nuclide densities and so-called C-matrix is used to solve the problem. The matrix element of C-matrix shows the change of nuclide density via decay or nuclear reaction. The creation or annihilation of nucleus via decay or nuclear reaction is represented by the following term as $\pm\lambda$ or $\pm\sigma\phi$, where λ is the decay constant, σ the reaction cross section and ϕ the neutron flux. The available decay and reaction chains are registered in the CHAINLIB library. The neutron cross-section data corresponding to the reaction registered in the CHAINLIB are also stored in the CROSSLIB library.

In order to treat the multi-step reaction, the number of product nuclei should be renewable in each calculation step cycle. When the function of multi-step reaction is simply

added into the code, the structure of loop becomes more complex and the core memory increases. Therefore, we performed the following modifications and restrain ACT-4 from storing much core memory.

1) All operation schedules are read and set in the element for the first step.
2) The power cycle loop and the step cycle loop are included in the mesh loop and all parameters associated with the creation of nuclei are updated in each step.
3) The exchange of the nuclide vector is carried out in the inner memory region.
4) For each vector, the memory region of working is reserved.

We applied the algorithm of FISPACT code [2] to the consideration of SCPRs. Though the distinction between primary neutron reaction and SCPR is not necessary in C-matrix, the new term $\sigma^{eff}\phi$ should be used in stead of $\sigma\phi$ as a matrix element for the SCPR. The σ^{eff} is called as the effective cross section.

Here, we assume the situation that the *i*'th energy group neutron flux ϕ_i incident on the nuclide A' in a material. The charged particle x is produced by the primary neutron reaction A'(n,x) and the secondary charged particle x may produce the nuclide C via the A(x,n)C reaction. The quantity $N_c(t)$ for the production of nuclide C per unit volume can be represented as,

$$N_c(t) = t_{eff} \sum_{A'} N_{A'} \sum_{i=1}^{I\_max} \sigma_{A',nx,i} \phi_i \Delta E_{n,i} \sum_{j=1}^{J\_max} f_{A',nx,i,j} \Delta E_{x,j} \sum_{k=1}^{j} N_A \sigma_{A,xn,k} \Delta R_{x,k}$$

$$= t_{eff} N_A \phi \sum_{A'} N_{A'} \frac{1}{\phi} \sum_{i=1}^{I\_max} \sigma_{A',nx,i} \phi_i \Delta E_{n,i} \sum_{j=1}^{J\_max} f_{A',nx,i,j} \Delta E_{x,j} \sum_{k=1}^{j} \sigma_{A,xn,k} \Delta R_{x,k}$$

$$= t_{eff} N_A \sigma^{eff}_{A,xn} \phi \qquad (9.1\text{-}1)$$

where,

t_{eff} = effective irradiation time [s]

$N_{A'}$ = number density of the nuclide A' in the target material [/cm^3]

N_A = number density of the nuclide A in the target material [/cm^3]

$\sigma_{A',nx,i}$ = production cross section of charged particle x in the *i*'th neutron energy group [cm^2]

ΔEn,i = neutron energy bin [MeV]

ΔEx,j = charged particle energy bin [MeV]

$f_{A',nx,i,j}$ = normalized emitted spectrum for charged particle x due to the i'th neutron flux [/ MeV]

$\sigma_{A,xn,k}$ = production cross section of the nuclide C via the (x,n) reaction [cm^2]

$\Delta R_{x,k}$ = stopping power of charged particle x in the target material [cm/MeV].

The function to calculate the effective cross-section defined as eq. (9.1-1) was added in ACT-4 code. The additional part consist of one function and four summation loops, namely, the calculation of $\Delta R_{x,k}$ by using the stopping power for each atom in the target material and the loops for *k, j, i, A'*. It should be noted that the effective cross section for the A(x,n)C reaction depends on every elements included in the target material which emits the charged particle x. Therefore, the charged particle production cross-sections, charged particle emission spectra, stopping powers associated with all elements should be given from libraries in order to determine the effective cross section. In this modification, we have made it possible to read the additional libraries that have the same format as the EAF libraries used in FISPACT code. We consider p, d, t, ^{3}He, and α as a charged particle x. The cross sections for the (x,n) reactions, the charged particle emission spectra with the cross sections for producing x, and the stopping powers of x are given in the CROSSXLIB, SPECTXLIB and STOPLIB libraries, respectively. The CHAINLIB library was also modified to include the paths via the sequential reaction.

Table 9.1-1 The induced activities immediately after shut down calculated by the modified and original ACT4.

without SCPR		with SCPR	
nucide	atcivity	nuclide	activity
total	7.49E+10	total	7.49E+10
MN - 56	4.90E+10	MN - 56	4.90E+10
FE - 55	2.03E+10	FE - 55	2.03E+10
MN - 57	2.33E+09	MN - 57	2.33E+09
MN - 54	2.22E+09	MN - 54	2.22E+09
CR - 51	5.31E+08	CR - 51	5.31E+08
FE - 53	3.52E+08	FE - 53	3.52E+08
FE - 59	1.24E+08	FE - 59	1.24E+08
CR - 55	6.47E+07	CR - 55	6.47E+07
MN - 58	4.26E+07	MN - 58	4.26E+07
MN - 58m	1.91E+07	MN - 58m	1.91E+07
CO - 60m	9.34E+06	CO - 60m	9.34E+06
V - 52	8.88E+06	V - 52	8.88E+06
MN - 52m	4.05E+06	MN - 52m	4.05E+06
V - 53	9.90E+05	CO - 56	2.36E+06
H - 3	5.13E+05	V - 53	9.90E+05
MN - 52	5.03E+05	H - 3	5.13E+05
CO - 60	3.77E+05	MN - 52	5.03E+05
TI - 51	3.29E+05	CO - 60	3.77E+05
V - 54	2.25E+05	TI - 51	3.29E+05
CO - 58m	7.83E+04	V - 54	2.25E+05
CO - 58	3.27E+04	CO - 57	1.31E+05
SC - 48	1.12E+04	CO - 58m	7.83E+04
MN - 53	4.48E+03	CO - 58	4.80E+04
CO - 61	7.52E+02	CO - 54	3.01E+04
V - 49	4.25E+02	SC - 48	1.12E+04
MN - 59	1.74E+02	NI - 57	8.73E+03
CR - 56	1.53E+02	CO - 55	4.55E+03
CR - 49	5.86E+01	MN - 53	4.48E+03
SC - 47	8.21E+00	CO - 61	7.52E+02
SC - 50	5.82E+00	V - 49	4.25E+02

9.1.3 Test calculation

The test calculations with the modified and original ACT-4 were carried out to check the additional function, assuming the neutron spectrum of ITER with a first-wall loading of 0.57 MW/m^2 and estimated inventory of 3.926×10^{-2} atoms/barn cm in pure iron. The results obtained by the modified ACT-4 with and without considering sequential reaction are shown in Table 9.1-1. For most of product radioactive nuclei, the agreement of those values is fairly good. On the other hands, it was confirmed that the sequential products such as ^{56}Co were estimated by the modified ACT-4 dealing with SCPR. The activities obtained by the modified ACT-4 dealing with SCPR are also shown as a function of cooling time in Fig. 9.1-1. In the case of iron, the contribution of the ^{56}Co to total activity is much small. However, if long-lived radioactivity is produced in low-activation material, the estimation of sequential reaction product becomes more important.

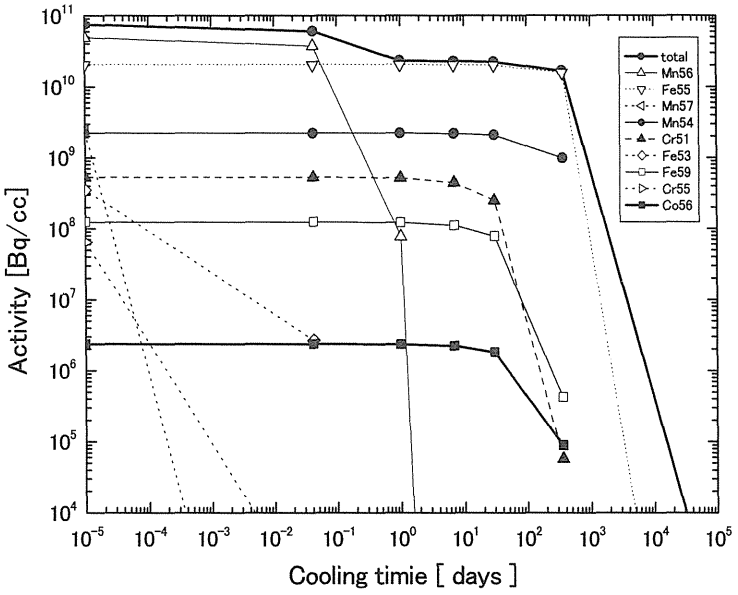

Fig. 9. 1-1 Total activities of several product nuclei as a function of cooling time.

9.1.4 Conclusion

ACT-4 code in THIDA-2 system was modified and made possible to deal with the multi-step and sequential reactions. The test calculations were performed for irradiation iron with neutron spectrum of ITER and we confirmed that the sequential products were estimated by the modified ACT-4 and the other results were agreement with ones obtained by the ACT-4 without option for SCPR.

References

[1] Y. Seki, H. Iida, H. Kawasaki and K. Yamada, JAERI 1301 (1986).

[2] R. A. Forest and D. A. J. Endacott, and A. Khursheed, "FISPACT-Program Manual," AERE-M3655, Atomic Energy Research Establishment (1988).

Appendix Paper List

A.1 List of JAERI report

1) Nishitani, T., Shikama, T., Sugie, T., et al., "Irradiation Effects on Plasma Diagnostic Components (II)", JAERI-Research 2002-007 (2002).

2) Nishitani, T., Ebisawa, K., Walker, C., et al., "Design of In-vessel Neutron Monitor using Micro Fission chambers", JAERI-Tech 2001-066 (2001).

3) Yamauchi, M., Nishitani, T., Ochiai, K., et al., "Performance Test of Micro-fission Chambers for In-vessel Neutron Monitoring of ITER", JAERI-Tech 2002-032 (2002).

4) Nishitani, T., Ebisawa, K., Walker, C., et al., "Design of Neutron Monitor using Flowing Water Activation for ITER", JAERI-Tech 2002-033 (2002).

5) Nishitani, T., Iguchi, T., Ebisawa, K., et al., "Design of Invessel Neutron Monitor for ITER," JAERI-Tech 2002-062 (2002).

6) Iida, T., Tanaka, T., (Nishitani, T.), et al., "Study of Neutron Irradiation Effects on Mineral Insulated Cables for Fusion Reactors," JAERI-Tech 2002-077 (2002) (in Japanese).

7) Terada, Y., Ochiai, K., Sato, S., "Experimental Study of Material Activation of Reduced Activation Ferritic Steel F82H by D-T Neutron Irradiation," JAERI-Research 2002-019 (2002) (in Japanese).

8) Hori, J., Sato, S., Yamauchi, M., et al., "Experimental Study of Sequential Reactions in Fusion Reactor Materials by D-T Neutron Irradiation," JAERI-Research 2003-002 (2003) (in Japanese).

9) Tanaka, R., Ochiai, K., Nakao, M., et al., "Secondary Gamma-ray Measurements on the D-T Neutron Skyshine Experiments", JAERI-Tech 2003-063 (July 2003) (in Japanese).

10) Verzilov, Y.M., Ochiai, K., Nishitani, T., "Feasibility Study of the Water Cherenkov Detector as a D-T Fusion Power Monitor in the System using Neutron Activation of Flowing Water -First Experimental Phase-", JAERI-Research 2003-019 (September 2003).

11) Sato, S., "Study of Shielding Design Method for Radiation Streaming in a Tokamak-Type Fusion Reactor based Monte Carlo Calculation", JAERI-Research 2003-014 (September 2003).

12) Department of Fusion Engineering Research,(Ed. Nishitani, T.), "Report of the 13th IEA workshop on radiation effects on ceramic insulators, December 9, 2003, Kyoto", JAERI-Review 2004-004 (March 2004).

13) Verzilov, Y.M., Ochiai, K., Sato, S., et al., "Analysis of Impurities in Beryllium, affecting Evaluation of the Tritium Breeding Ratio", JAERI-Research 2004-004 (March 2005).

A.2 List of papers published in journals

1) Mitarai, O., Honda, T., Nishitani, T., et al.," Comparative Studies of the dW/dt Effect in the Net Heating Power for Ignition Analysis " Fusion Eng. Design **55**, 477(2001).

2) Nishitani, T., Shikama, T., Fukao, M., et al., "Neutron Irradiation Tests on Diagnostic Components at JAERI", Fusion Eng. Design **56-57**, 905-909 (2001).

3) Uno, Y., Kaneko, J., Nishitani, T., et al.," Absolute Measurement of D-T Neutron Flux with a Monitor using Activation of Flowing Water " Fusion Eng. Design **56-57**, 895 (2001).

4) Maekawa, F., Ochiai, K., Shibata, K., et al.," Benchmark Experiment on Silicon Carbide with D-T Neutrons and Validation of Nuclear Data Libraries" Fusion Eng. Design **58-59**, 595 (2001).

5) Murata, I., Nishio, T., Kondo, T., et al., "Neutron-nuclear Data Benchmark for Copper and Tungsten by Slab Assembly Transmission Experiments with DT", Fusion Eng. Design **58-59**, 617 (2001).

6) Sato, S., Enoeda, M., Kuroda, T., et al., "Characteristic Evaluation of HIP Bonded SS/DSCu Joints for Surface Roughness", Fusion Eng. Design **58-59**, 749 (2001).

7) Konno, C., Maekawa, F., Wada, M., et al., "DORT Analyses of Decay Heat Experiment on Tungsten for ITER", Fusion Eng. Design **58-59**, 961-965 (2001).

8) Klix, A., Ochiai, K., Terada, Y., et al., "Tritium Measurement for ^{6}Li-Enriched Li_2TiO_3 Breeding Blanket Experiments with D-T Neutrons," Fusion Sci. Tech. **41**, 1040 (2002).

9) Kutsukake, C., Seki, M., Tanaka, S., et al., "Tritium Distribution Measurement of FNS Tritium Targets by Imaging Plate,"Fusion Sci. Technology **41**, 555 (2002).

10) Murata, I., Nishio,T., (Ochiai,K.), et al., "(n,2n)Reaction Cross Section Measurement with a Beam DT Neutron Source," J. Nucl. Sic. Technol. Suppl.**2**, 433 (2002).

11) Nishio, T., Terada, T., (Nishitani, T.), et al., "Fusion Neutronics Benchmark Experiment on Structural and Advanced Blanket Materials -Leakage Gamma-ray Spectrum Measurement-," J. Nucl. Sic. Technol. Suppl.**2**, 955 (2002).

12) Murata,I., Kokooo, (Takeuchi, H.), e al., "Fusion Neutronics Benchmark Experiment on Structural and Advanced Blanket Materials -Leakage Neutron Spectrum Measurement-," J. Nucl. Sic. Technol. Suppl.**2**, 978 (2002).

13) Nishitani, T., Uno, T., Kaneko, J., et al., "Fusion Power Measurement Based On $^{16}O(n,p)^{16}N$ Reaction in Flowing Water," J. Nucl. Sic. Technol. Suppl.**2**, 1139 (2002).

14) Ochiai, K., Klix, A., Hori, J., et al., "Neutronics Experiment of ^{6}Li-enriched Breeding Blanket with Li_2TiO_3/Be/F82H Assembly Using D-T Neutrons," J. Nucl. Sic. Technol. Suppl.**2**, 1147 (2002).

15) Maekawa, F., Shibata, k., (Takeuchi, H.), et al. "Comprehensive Activation Experiment with 14-MeV Neutrons Covering Most of Naturally Existing elements – 5 Minutes Irradiation Experiments -," J. Nucl. Sic. Technol. Suppl.**2**, 990 (2002).

16) Sato, S., Iida, H., and Nishitani, T., "Evaluation of Shutdown Gamma-ray Dose Rates around the Duct Penetration by Three-Dimensional Monte Carlo Decay Gamma-ray Transport Calculation with Variance Reduction Method," J. Nucl. Sic. Technol. **39**, 1237 (2002).

17) Miura, T., Baba, M., (Nishitani, T.), et al., "Development of Position-Sensitive Proton Recoil Telescope (PSPRT) ," Nucl. Instrum. Methods, **A-493**, 99 (2002).

18) Hori, J., Maekawa, F., Wada, M., et al., "Radioactivity production around the surface of a cooling water pipe in a D-T fusion reactor by sequential charged particle reactions," Fusion. Eng. Design, **63-64**, 271 (2002).

19) Nishitani, T., Shikama, T., Reichle, R., et al., "In-situ Irradiation Test of Mica Substrate Bolometer at the JMTR Reactor for the ITER Diagnostics," Fusion. Eng. Design, **63-64**, 437 (2002).

20) Morimoto, Y., Ochiai, K., Maekawa, F., et al., "Decay Heat Measurements of Fusion Related Materials in an ITER-LIKE Neutron Field," J. Nucl. Mater. **307-311**, 1052 (2002).

21) Sugie, T., Nishitani,T., S.Kasai, et al., "In-situ Transmissivity Measurement of KU-1 Quartz in UV Range Under 14 MeV Neutron Irradiation," J. Nucl. Mater. **307-311**, 1264 (2002).

22) Kakuta, T., T.Shikama, T.Nishitani, et al., "Round-Robun Irradiation Test of Radiation Resistant Optical Fibers for ITER Diagnostic Application," J. Nucl. Mater. **307-311**, 1277 (2002).

23) Yamauchi, M., Nishitani, T., Ochiai, K., et al., "Development of In-Vessel Neutron Monitor using Micro-Fission Chambers for ITER," Rev. Sci. Instrum. **74**, 1730 (2003).

24) Nishitani, T., Ebisawa, K., and Kasai, S., "Neutron Activation System using Water Flow for ITER", Rev. Sci. Instrum. **74**, 1734 (2003).

25) Kohagura, J., Cho, T., (Nishitani, T.), et al., "Calibration Experiments of ^{3}He Neutron Detectors for Analyzing Neutron Emissivity in The Hot-Ion Mode on The GAMMA 10 Tandem Mirror," Rev. Sci. Instrum. **74**, 1757 (2003).

26) Sato, S., Nishitani,T., "Impact of armor materials on tritium breeding ratio in the fusion reactor blanket", J. Nucl. Mater. **313-316**, 690-695 (2003).

27) Kaneko, J.H., Tanaka, T., et al., "Radiation detector made of a diamond single crystal grown by a chemical vapor deposition method", Nucl. Instrum. Methods in Phys. Res. A **505**, 187-190 (2003).

28) Sato,S., Ochiai, K., Hori, J., et al., "Neutronics Experiments for DEMO Blanket at JAERI/FNS", Nucl. Fusion **43**, 527-530 (2003).

29) Shikama, T., Nishitani, T., Kakuta, T., et al., "Irradiation test of diagnostic components for ITER application in a fission reactor, Japan Materials Testing Reactor", Nucl. Fusion **43**, 517-521 (2003).

30) Yoshida, S., Nishitani, T., K. Ochiai, et al., "Measurement of radiation skyshine with D-T neutron source", Fusion Eng. Design **69**, 637-641 (2003).

31) Morimoto, Y., Ochiai, K., Sato, S., et al., "Shutdown dose evaluation experiment for ITER", Fusion Eng. Design **69**, 643-648 (2003).

32) Tanaka, T., Sato, F., Iida, T., Nishitani, T., et al., "Electrical properties of mineral-insulated cable under fusion neutron irradiation", Fusion Eng. Design **66-68**, 837-841 (2003).

33) Sato, S., Maki, K., "Analytical representation for neutron streaming through slits in fusion reactor blanket by Monte Carlo calculation", Fusion Eng. Design **65**, 501-524 (2003).

34) Hou, L., Ishii, T., Asai, M., Hori, J., et al., "Measurement of $B(M1)$ for the $\pi p_{3/2}\ \nu p^{-1}{}_{1/2}$ doublet in ^{68}Cu", Physical Rev. C **68** 054306 (2003)

A.3 List of papers presented in conference proceedings

1) Reichle, R., Nishitani, T., Hodgson, E.R., et al., "Radiation Hardness Test of Mica Bolometers for ITER in JMTR ", Proc. Of 28th EPS Conf. on Controlled Fusion and Plasma Physics, (Madeira), p.1293 (2001).

2) Sugie, T., Nishitani, T., Kasai, S., et al., "IN-SITU Transmissivity Measurement of KU-1 Quartz in UV Range Under 14 MeV Neutron Irradiation", Proc. of 10th Int. Conf. on Fusion Reactor Materials, (Baden-Baden), p.68 (2001).

3) Sikama, T., Hodgson, E., Yamamoto, S., et al., "Radiation Induced Electromotive Force Induced in Metal/Ceramics Systems for Burning Plasma Diagnostics", Proc. of 10th Int. Conf. on Fusion Reactor Materials, (Baden-Baden), p.69 (2001).

4) Narui, M., Yamasaki, M., Shikama, T., et al., "Dimensional Stability of Mica Film Under Fission Reactor Irradiation", Proc. of 10th Int. Conf. on Fusion Reactor Materials, (Baden-Baden), p.70 (2001).

5) Morimoto, Y., Ochiai, K., Maekawa, F., et al., "Decay Heat Measurements of Fusion Related Materials in an ITER-LIKENeutron Field", Proc. of 10th Int. Conf. on Fusion Reactor Materials, (Baden-Baden), p.242 (2001).

6) Kakuta, T., Shikama, T., Nishitani, T., et al., "Round Robin Irradiation Test of Radiation Resistance Optical Fibers for ITER Diagnostic Application", Proc. of 10th Int. Conf. on Fusion Reactor Materials, (Baden-Baden), p.467 (2001).

7) Murata, I., Nishio, T., Terada, Y., et al., "(n,2n)Reaction Cross Section Measurement with A Beam DT Neutron Source", Proc. of Int. Conf. on Nuclear Data for Science and Technology, (Tsukuba), 1.3-P-50 (2001).

8) Nishio, T., Terada, Y., Murata, I., et al., "Fusion Neutronics Benchmark Experiment on Structural and Advanced Blanket Materials –Leakage Gamma-ray Spectrum Measurement-", Proc. of Int. Conf. on Nuclear Data for Science and Technology, (Tsukuba), 6-P-27 (2001).

9) Murata, I., Kokooo, Nakano, D., et al., "Fusion Neutronics Benchmark Experiment on Structural and Advanced Blanket Materials –Leakage Neutron Spectrum Measurement-", Proc. of Int. Conf. on Nuclear Data for Science and Technology, (Tsukuba), 6-P-19 (2001).

10) Nishitani, T., Uno, Y., Kaneko, J., et al., "Fusion Power Measurement Based on ^{16}O(n,p)^{16}N reaction in Flowing Water", Proc. of Int. Conf. on Nuclear Data for Science and Technology, (Tsukuba), 8-P-6 (2001).

11) Ochiai, K., Markovskij, D.V., Morimoto, Y., et al., "Measurement of Tritium Produced from ^{6}Li-enriched Breeding Blanket Assembly Irradiated with D-T Neutron Source", Proc. of Int. Conf. on Nuclear Data for Science and Technology, (Tsukuba), 8-P-8 (2001).

12) Kutsukake, C., Tanaka, S., Abe, Y., et al., "Tritium Distribution Measurement of FNS Tritium Target by Imaging Plate", Proc. of 6th Int. Conf. on Tritium Science and Technology, (Tsukuba), P.60 (2001).

13) Ochai, K., Klix, A., Terada, Y., et al., "Tritium measurements for the ^{6}Li-enriched Li_2TiO_3 breeding blanket experiments with D-T neutrons", Proc. of 6th Int. Conf. on Tritium Science and Technology, (Tsukuba), P.190 (2001).

14) Tanaka, T., Yonezawa, H., Sato, F., et al., "Electrical Properties of Mineral Insulated Cables under Irradiation", Proc. of 1st iTRS Int. Symposium on Radiation Safety and Detection Technology, (Seoul), P.270 (2001).

15) Tsuchiya, B., Kakuta, T., (Nishitani, T.), et al., "Radiation Effects of 14-MeV Fusion Neutrons on Optical Transmission Properties of Fused Silica Core Optical Fibers," Proc. Int. Symposium on Optical Science and Technology SPIE's 14th Annual Meeting, 210, (Seattle), (July 2002).

16) Ochiai, K., Klix, A., Velzilov, Y. M., et al., "Measurement of Tritium Production Rate for A Modified Lithium-6 Enriched Blanket Assembly with D-T Neutron Source," 22nd Symp. on Fusion Technology, to be published in Fusion. Eng. Design, (Helsinki), (September, 2002).

17) Yoshida, S., Ochiai, Kaneko, J., et al., "Measurement of Radiation Skyshine with D-T Neutron Source," 22nd Symp. on Fusion Technology, to be published in Fusion. Eng. Design, (Helsinki), (September, 2002).

18) Morimoto, Y., Ochiai, Sato, S., et al., "Shutdown Dose Evaluation Experiment for ITER," 22nd Symp. on Fusion Technology, to be published in Fusion. Eng. Design, (Helsinki), (September, 2002).

19) Shikama, T., Nishitani, T., Yamamoto, S., et al., "Radiation Induced Electromotive Force (RIEMF) and Voltage Drift in Magnetic Coil," 22nd Symp. on Fusion Technology, to be published in Fusion. Eng. Design, (Helsinki), (September, 2002).

20) Tanaka, T., Sato F., (Nishitani, T.), et al., "Electrical Properties of Mineral-Insulated Cable under Fusion Neutron Irradiation," 22nd Symp. on Fusion Technology, to be published in Fusion. Eng. Design, (Helsinki), (September, 2002).

21) Sato, S., Ochiai, K., Hori, J., et al., "Neutronics Experiments for DEMO Blanket at JAERI/FNS," 19th IAEA Fusion Energy Conf., IAEA-CN-94/FT/P1-10, (Lyon), (October, 2002), to be published in Nucl. Fusion.

22) Shikama, T., Nishitani, T., Kakuta, T., et al., "Irradiation Test of Diagnostic Components for ITER Application in a Fission Reactor, Japan Materials Testing Reactor," 19th IAEA Fusion Energy Conf., IAEA-CN-94/CT/P-11, (Lyon), (October, 2002), to be published in Nucl. Fusion.

23) Ishii, T., Asai, M., (Hori, J.), et al., "Nano-second Isomers In Neutron-Rich Nuclei around ^{68}Ni", Proc. 3rd Int. Conf. on Fission and Proparties of Neutron-Rich Nuclei," (Sanibel Island, Florida), (November, 2002).

24) Asai, K., Iguchi, T., Nishitani, T., "Design consideration on ex-vessel neutron yield monitor for ITER", 30th IEEE Int. Conf. on Plasma Science, June 2-5, 2002, Jeju, Korea.

25) Nishitani, T., Ochiai, K., Yoshida, S., et al., "D-T Neutron Skyshine Experiments and the MCNP Analysis", 2nd iTRS Int. Symp. on Radiation Safety and Detection Technol., July 24-25, 2003, Sendai.

26) Sato, S., Morioka, A., Kinno, M., et al.,"DT neutron irradiation experiments using the low activation concrete", 2nd iTRS Int. Symp. on Radiation Safety and Detection Technol., July 24-25, 2003, Sendai.

27) Sato, S., Kawasaki, N., Kume, E., Nishitani, T., "Development of combined system of Monte Carlo calculation with activation calculation for evaluation of decay gamma ray dose rate in nuclear fusion reactor", 2nd iTRS Int. Symp. on Radiation Safety and Detection Technol., July 24-25, 2003, Sendai.

28) Morimoto, Y., Ochiai, K., Nishio, T., et al., "Dogleg Duct Streaming Experiment with 14 MeV Neutron Source", 2nd iTRS Int. Symp. on Radiation Safety and Detection Technol., July 24-25, 2003, Sendai.

29) Verzilov, Y., Ochiai K., and Nishitani, T., "A new approach to the D-T neutron monitor using water flow", 2nd iTRS Int. Symp. on Radiation Safety and Detection Technol., July 24-25, 2003, Sendai.

30) Morioka, A., Sato, S., Ochiai, K., et al., "Neutron transmission experiment of boron-doped resin for the JT-60SC neutron shield using 2.45 MeV neutron source", 2nd iTRS Int. Symp. on Radiation Safety and Detection Technol., July 24-25, 2003, Sendai.

31) Nishitani, T., Ochiai, K., Klix, A., et al., "Initial Results of Neutronics Experiments for Evaluation of Tritium Production Rate in Solid Breeding Blanket", 20th IEEE/NPSS Symposium on Fusion Engineering (SOFE2003) October 14 - 17, 2003, San Diego, CA USA.

32) Yamauchi, M., Ochiai, K., Verzilov, Y., et al., "Influence of Impurities in Beryllium on Tritium Breeding Ratio", 6th IEA Beryllium Workshop (BeWS 6) December 3 - 5, 2003, Miyazaki.

33) Nishitani, T., Vayakis, G., Yamauchi, M., et al., "Radiation-mediated thermoelectric potential in the mineral-insulated cable of magnetic diagnostic coils for ITER", 11th International Conference on Fusion Reactor Materials (ICFRM-11), December 7 - 12, 2003, Kyoto.

34) Sato, S., Tanaka, T., Hori, J., Ochiai, K., Nishitani T., and Muroga T., "Radioactivity of vanadium-alloy onduced by D-T neutron irradiation", 11th International Conference on Fusion Reactor Materials (ICFRM-11), December 7 - 12, 2003, Kyoto.

35) Ochiai, K., Hayashi, T., Kutsukake, C., et al., "Measurement of deuterium and tritium retention on the surface of JT-60 divertor tiles by means of nuclear reaction analysis", 11th International Conference on Fusion Reactor Materials (ICFRM-11), December 7 - 12, 2003, Kyoto.

36) Verzilov, Y., Ochiai, K., Klix, A., et al., "Non-destructive analysis of impurities in beryllium for tritium breeding ratio evaluation", 11th International Conference on Fusion Reactor Materials (ICFRM-11), December 7 - 12, 2003, Kyoto.

37) Morioka, A., Sato, S., Kinno, M., et al., "Irradiation and penetration tests of boron-doped low activation concrete using 2.45 MeV and 14 MeV neutron sources", 11th International Conference on Fusion Reactor Materials (ICFRM-11), December 7 - 12, 2003, Kyoto.

38) Narui, M., Yamasaki, M., Shikama, T., Nishitani, T., et al., "Irradiation Effects in Bolometer and Constituting Materials for ITER Application", 11th International Conference on Fusion Reactor Materials (ICFRM-11), December 7 - 12, 2003, Kyoto.

39) Sugie, T., Kasai, S., Taniguchi, M., Nagatsu, M., Nishitani T., "Irradiation Test on Mo- and W-Mirrors by Low Energy Deuterium Ions for ITER", 11th International Conference on Fusion Reactor Materials (ICFRM-11), December 7 - 12, 2003, Kyoto.

40) Toh, K., Shikama, T., Nagata, S., et al., "Optical Characteristics of Aluminum Coated Fused Silica Core Fibers under 14 MeV Fusion Neutrons Irradiation", 11th International Conference on Fusion Reactor Materials (ICFRM-11), December 7 - 12, 2003, Kyoto.

41) Adachi, T., Nagata, S., Tsuchiya, B., et al., "Irradiation Effects on the Electrical Conductivity of Fluorine-Based Polymer Membranes", 11th International Conference on Fusion Reactor Materials (ICFRM-11), December 7 - 12, 2003, Kyoto.

42) Shikama, T., Nishitani, T., Yamamoto, S., et al., "Irradiation Tests of Functional Materials for ITER Plasma Diagnostics", 11th International Conference on Fusion Reactor Materials (ICFRM-11), December 7 - 12, 2003, Kyoto.

This is a blank page.

国際単位系（SI）と換算表

表1　SI基本単位および補助単位

量	名称	記号
長さ	メートル	m
質量	キログラム	kg
時間	秒	s
電流	アンペア	A
熱力学温度	ケルビン	K
物質量	モル	mol
光度	カンデラ	cd
平面角	ラジアン	rad
立体角	ステラジアン	sr

表2　SIと併用される単位

名称	記号
分，時，日	min，h，d
度，分，秒	°，′，″
リットル	l，L
トン	t
電子ボルト	eV
原子質量単位	u

1 eV=1.60218×10^{-19}J

1 u=1.66054×10^{-27}kg

表3　固有の名称をもつSI組立単位

量	名称	記号	他のSI単位による表現
周波数	ヘルツ	Hz	s^{-1}
力	ニュートン	N	$m\cdot kg/s^2$
圧力，応力	パスカル	Pa	N/m^2
エネルギー,仕事,熱量	ジュール	J	N·m
工率，放射束	ワット	W	J/s
電気量，電荷	クーロン	C	A·s
電位，電圧，起電力	ボルト	V	W/A
静電容量	ファラド	F	C/V
電気抵抗	オーム	Ω	V/A
コンダクタンス	ジーメンス	S	A/V
磁束	ウェーバ	Wb	V·s
磁束密度	テスラ	T	Wb/m^2
インダクタンス	ヘンリー	H	Wb/A
セルシウス温度	セルシウス度	℃	
光束	ルーメン	lm	cd·sr
照度	ルクス	lx	lm/m^2
放射能	ベクレル	Bq	s^{-1}
吸収線量	グレイ	Gy	J/kg
線量等量	シーベルト	Sv	J/kg

表4　SIと共に暫定的に維持される単位

名称	記号
オングストローム	Å
バーン	b
バール	bar
ガル	Gal
キュリー	Ci
レントゲン	R
ラド	rad
レム	rem

1 Å=0.1nm=10^{-10}m

1 b=100fm^2=10^{-28}m^2

1 bar=0.1MPa=10^{5}Pa

1 Gal=1cm/s^2=10^{-2}m/s^2

1 Ci=3.7×10^{10}Bq

1 R=2.58×10^{-4}C/kg

1 rad=1cGy=10^{-2}Gy

1 rem=1cSv=10^{-2}Sv

表5　SI接頭語

倍数	接頭語	記号
10^{18}	エクサ	E
10^{15}	ペタ	P
10^{12}	テラ	T
10^{9}	ギガ	G
10^{6}	メガ	M
10^{3}	キロ	k
10^{2}	ヘクト	h
10^{1}	デカ	da
10^{-1}	デシ	d
10^{-2}	センチ	c
10^{-3}	ミリ	m
10^{-6}	マイクロ	μ
10^{-9}	ナノ	n
10^{-12}	ピコ	p
10^{-15}	フェムト	f
10^{-18}	アト	a

（注）

1．表1－5は「国際単位系」第5版，国際度量衡局1985年刊行による。ただし，1 eVおよび1 uの値はCODATAの1986年推奨値によった。

2．表4には海里，ノット，アール，ヘクタールも含まれているが日常の単位なのでここでは省略した。

3．barは，JISでは流体の圧力を表わす場合に限り表2のカテゴリーに分類されている。

4．EC閣僚理事会指令ではbar，barnおよび「血圧の単位」mmHgを表2のカテゴリーに入れている。

換　算　表

力	N(=10^{5}dyn)	kgf	lbf
	1	0.101972	0.224809
	9.80665	1	2.20462
	4.44822	0.453592	1

粘度　1 Pa·s(N·s/m^2)=10 P(ポアズ)(g/(cm·s))

動粘度　1m^2/s=10^{4}St(ストークス)(cm^2/s)

圧力	MPa(=10bar)	kgf/cm^2	atm	mmHg(Torr)	lbf/in^2(psi)
	1	10.1972	9.86923	7.50062×10^3	145.038
	0.0980665	1	0.967841	735.559	14.2233
	0.101325	1.03323	1	760	14.6959
	1.33322×10^{-4}	1.35951×10^{-3}	1.31579×10^{-3}	1	1.93368×10^{-2}
	6.89476×10^{-3}	7.03070×10^{-2}	6.80460×10^{-2}	51.7149	1

エネルギー・仕事・熱量	J(=10^7 erg)	kgf·m	kW·h	cal(計量法)	Btu	ft·lbf	eV
	1	0.101972	2.77778×10^{-7}	0.238889	9.47813×10^{-4}	0.737562	6.24150×10^{18}
	9.80665	1	2.72407×10^{-6}	2.34270	9.29487×10^{-3}	7.23301	6.12082×10^{19}
	3.6×10^6	3.67098×10^5	1	8.59999×10^5	3412.13	2.65522×10^6	2.24694×10^{25}
	4.18605	0.426858	1.16279×10^{-6}	1	3.96759×10^{-3}	3.08747	2.61272×10^{19}
	1055.06	107.586	2.93072×10^{-4}	252.042	1	778.172	6.58515×10^{21}
	1.35582	0.138255	3.76616×10^{-7}	0.323890	1.28506×10^{-3}	1	8.46233×10^{18}
	1.60218×10^{-19}	1.63377×10^{-20}	4.45050×10^{-26}	3.82743×10^{-20}	1.51857×10^{-22}	1.18171×10^{-19}	1

1 cal= 4.18605J（計量法）

= 4.184J（熱化学）

= 4.1855J（15℃）

= 4.1868J（国際蒸気表）

仕事率　1 PS(仏馬力)

= 75 kgf·m/s

= 735.499W

放射能	Bq	Ci
	1	2.70270×10^{-11}
	3.7×10^{10}	1

吸収線量	Gy	rad
	1	100
	0.01	1

照射線量	C/kg	R
	1	3876
	2.58×10^{-4}	1

線量当量	Sv	rem
	1	100
	0.01	1

（86年12月26日現在）

Activity Report of the Fusion Neutronics Source from April 1, 2001 to March 31, 2004